Design, fabrication and characterization of microlasers for data communications

Mattéo Chobe

THÈSE

Pour obtenir le grade de

DOCTEUR DE L'UNIVERSITÉ GRENOBLE ALPES

École doctorale : EEATS - Electronique, Electrotechnique, Automatique, Traitement du Signal (EEATS)
Spécialité : Nano électronique et Nano technologies
Unité de recherche : Laboratoire d'Electronique et de Technologie de l'Information (LETI)

Modélisation, fabrication et caractérisation de microlasers pour les communications de données

Design, fabrication and characterization of microlasers for data communications

Présentée par :

Mattéo CHOBE

Direction de thèse :

Thierry BARON Directeur de recherche, CNRS	Directeur de thèse
Karim HASSAN	Co-encadrant de thèse

Rapporteurs :

Christian SEASSAL
DIRECTEUR DE RECHERCHE, CNRS CNRS DELEGATION RHONE AUVERGNE
Gérard COLAS DES FRANCS
PROFESSEUR DES UNIVERSITES, Université de Bourgogne

Thèse soutenue publiquement le **4 novembre 2024**, devant le jury composé de :

Elise GHIBAUDO, PROFESSEURE DES UNIVERSITES, UNIVERSITE GRENOBLE ALPES	Présidente
Thierry BARON, DIRECTEUR DE RECHERCHE, CNRS DELEGATION ALPES	Directeur de thèse
Christian SEASSAL, DIRECTEUR DE RECHERCHE, CNRS CNRS DELEGATION RHONE AUVERGNE	Rapporteur
Gérard COLAS DES FRANCS, PROFESSEUR DES UNIVERSITES, Université de Bourgogne	Rapporteur
Gaëlle LUCAS-LECLIN, MAITRESSE DE CONFERENCES, Université Paris-Saclay	Examinatrice
Joan Manel RAMIREZ, INGENIEUR DOCTEUR, Nokia France	Examinateur

Invités :

Karim HASSAN
INGENIEUR DOCTEUR, CEA-LETI

Remerciements

Cette page donne l'occasion d'une rétrospective des trois années et quelques mois passés. Que de personnes rencontrées, ayant toutes apportés leur contribution à cette aventure.

En premier lieu, je souhaite remercier Thierry Baron et Karim Hassan, mon directeur de thèse et mon encadrant CEA, pour m'avoir donné l'opportunité et le cadre pour travailler sur ce sujet passionnant et porteur. J'ai ressenti une relation de confiance qui m'as permis de m'épanouir dans ce travail. L'expertise de Karim et sa vision d'ensemble sur les thématiques photonique sur silicium et sources laser III-V sur silicium m'ont été précieuses pour m'aider à m'approprier et développer ma propre expertise sur ces thématiques. Même après avoir été appelé à diriger le LIPS, il a su rester disponible, tout en me laissant gagner en indépendance. Techniquement spécialiste d'un aspect spécifique de la thèse, Thierry m'a apporté sa maitrise sur ce sujet qui m'était initialement obscur, ainsi qu'un regard différent et un recul qui m'ont été précieux, notamment dans certains moments de doute. Merci également à Cécilia Dupré, qui a contribué au lancement de cette thèse m'a co-encadré sur les aspects intégration en son début.

Au LIPS, j'ai eu la chance de faire partie d'une équipe pluridisciplinaire sur laquelle j'ai pu compter pour mener à bien les différents axes de cette thèse. Si tous les membres du LIPS ont joué de près ou de loin un rôle dans ces trois années, il y en a que je souhaite remercier plus spécialement. Il en va de l'équipe filière, et notamment Viviane Muffato, Valentin Ramez, Stéphanie Garcia et Jonathan Faugier pour leur aide au suivi des lots et leurs réponses bienveillantes à mes nombreuses questions sur ce sujet duquel je ne connaissais rien il y a quatre ans. L'équipe caractérisation a également été d'un grand support le moment venu, merci donc pour leur disponibilité et aide à André Myko, Karen Ribaud, Nicolas Dunoyer et Philippe Grosse. Une mention spéciale va à Sylvain Guerber, tant pour son accueil au LIPS en des temps troublés par la pandémie, que pour son aide technique sur un grand nombre de sujets variés (et notamment Lumerical). J'ai eu la chance et le plaisir de faire partie d'un beau groupe de "*jeunes*" : doctorants, CDD et stagiaires, qui m'ont accueilli ou que j'ai pu à mon tour accueillir, et avec qui j'ai partagé de beaux moments au laboratoire et en dehors. Merci donc à vous Josserand, Cyrille, Ismaël, Imène, Warren, Linda, Sara, Louise-Eugénie, Alexis, Xavier, Pierre, Annalara, Baptiste et Guillaume. Je n'oublie pas, bien sûr, mes co-doctorants du bureau C5555, Clément et Valentin, toujours présents dans les meilleurs moments mais aussi dans les moments plus difficiles.

Une double affiliation, c'est deux fois plus de collègues ! J'en profite donc pour saluer les doctorants du LTM, que j'ai côtoyé moins fréquemment mais toujours pour de bons moments, autour d'un café ou aux journées scientifiques du labo.

"*Mes*" plaques ont bénéficié de l'expertise de nombreux technologues du LETI, que je remercie tous sincèrement pour leur implication. Mes remerciements vont à l'équipe MOCVD du LTM : Mickaël Martin, Jérémy Moeyaert, Hadi Hijazi, Léo Mallet et Driss Mouloua aux côtés de Thierry Baron, artistes d'un équipement capricieux. Merci également à l'équipe photonique III-V du LITP, et notamment Romain Thibon, Sophie Barbet et Christophe Jany, à qui j'ai demandé beaucoup de travail pour le développement de ces lasers à la forme si inhabituelle. Je remercie une deuxième fois les membres de la team LITP, que j'ai rejoint cette année, pour leur accueil bienveillant et leur patience alors qu'une partie de moi avait encore la tête à la finalisation de cette thèse. Tant de personnes ont été impliquées sur d'autres étapes de la fabrication et caractérisation in-line et off-line des échantillons fabriqués (je pense aussi à Victor Lumineau). Sans que je ne puisse les citer individuellement, merci donc à toutes ces personnes sans qui il n'y aurait eu que des résultats théoriques.

Mes derniers remerciements sont plus personnels. Ils vont à mes amis de jeunesse, de prépa et d'école, pour les moments de coupure salvateurs passés ensemble, parfois sans parler de la thèse, parfois apportant un regard extérieur sur celle-ci. Merci également du fond du cœur à ma famille et en particulier à mes parents pour leur soutient depuis tant d'années, sans qui je n'aurais pu en arriver là.

Enfin, Marie, pour tout, merci.

Contents

List of Figures

List of Tables

Abbreviations

Abbreviation	Definition
AFM	Atomic force microscope
ASE	Amplified spontaneous emission
BOE	Buffered oxide etch
BOX	Buried oxide
CD	Critical dimension
CMP	Chemical-mechanical polishing
CW	Continuous-wave
DC	Directional coupler
DUT	Device under test
DWELL	Quantum dot-in-a-well
EDX	Energy-dispersive X-ray spectroscopy
ESL	Etch-stop layer
FDM	Finite difference method
FSR	Free spectral range
FWHM	Full width at half maximum
GC	Grating coupler
GS/ES	Ground/excited state
HAADF	High-angle annular dark-field (imaging)
ICP	Inductively coupled plasma
IVBA	Intervalence band absorption
LCI	Lateral current injection
L-I	Light-intensity
OSA	Optical spectrum analyzer
PDK	Process design kit
PECVD	Plasma enhanced chemical vapor deposition
PIC	Photonic integrated circuit
QW/QD	Quantum well/dot
RIE	Reactive ion etching
RMS	Root mean square
RT	Room-temperature
SAG	Selective area growth

Abbreviation	Definition
SAM	Scanning acoustic microscope
SCH	Separate confinement heterostructure
SEM	Scanning electron microscope
SMU	Source measure unit
SOI	Silicon-on-insulator
SRH	Shockley-Read-Hall (recombination)
TLM	Transmission line method
TW	Traveling wave
UID	Unintentionally doped

1

Introduction

This thesis investigates semiconductor microlasers for data communications, with a specific focus on integrated III-V membrane laser sources for silicon photonics. To provide essential context for our work, section 1.1 discusses current trends in electrical and optical data communication, highlighting the role silicon photonics can play in this field. Next, section 1.2 lays the fundamental principles necessary to understand the operation of semiconductor lasers and their integration with silicon photonics. This includes an overview of the state-of-the-art of semiconductor lasers on silicon where we introduce, in particular, III-V membrane lasers. Finally, the goal and outline of this thesis are presented in section 1.3.

1.1. Background

1.1.1. Electrical and Optical Data Communications

Since the mass adoption of smartphones, followed by Internet-enabled high-definition streaming, with ever-increasing resolutions, consumer usage has driven the growth of data communications. Now, cloud-based services, such as Software-as-a-Service, Infrastructure-as-a-Service and Platform-as-a-Service have taken over [1], and Internet-of-Things and machine-to-machine communication, with applications such as connected homes, works, cities, cars or health are expected to drive an explosion of the global Internet traffic [2], [3]. Datacenters constitute an essential infrastructure supporting these applications, and CISCO estimates that almost three quarters of the global data traffic remain within datacenter for storage and processing, or up to 90% if rack-local traffic was taken into account [1]. Besides, data-hungry AI and high-performance computing are leading a steady growth of investments in hyper-scale datacenters.

Subsequently, the matter of the energy consumption of data centers has become increasingly tangible [4]–[6]. Owing to hardware (particularly processor and storage) efficiency gains, and better use of the servers capacity (for instance through server virtualization), it is estimated

that there was just a moderate increase of the global data center energy use between 2010 and 2018, from 194 TWh to 205 TWh, despite greatly increased traffic, storage, and compute instances [4], [5]. Nevertheless, recent simulations predict a swift increase of the datacenter energy needs in the years to come, possibly up to 565 TWh by 2030 [6]. These predictions are based on a slowdown of the efficiency gains, in particular due to the end of Moore's law, and a surge of data volumes resulting from the aforementioned emerging applications [3], [6]. In addition, limitations in speed and energy efficiency of electrical interconnects are leading to a *communication bottleneck*, which was already predicted in the 1980s [7]. The inherent drawbacks of the electrical interconnects result from parasitic capacitance and resistance, leading to power dissipation, losses and signal integrity degradation at high frequencies due to RC filtering, as well as delays and increased surface use, reducing the overall achievable bandwidth density. Optical communications can offer a potential solution to address both the energy consumption and *communication bottleneck* issues [8]–[12]. For distances exceeding a few meters, optical interconnects have already replaced copper-based electrical interconnects, and pluggable 400G optical transceiver modules are already commercially available [13], [14]. However, for shorter distances, the electrical capacitance and resistance are decreased, reducing the power dissipation and signal attenuation of electrical interconnects. As a result, a break-even line between the regions of optical or electrical interconnect superiority can be drawn in the space of interconnect length vs modulation speed. For longer distances and/or higher modulation speeds, optical interconnects exhibit superior performances, while electrical interconnects dominate for shorter link lengths and lower modulation speeds. For commercial applications, cost efficiency should also be taken into account when comparing the performances of electrical and optical interconnects, giving similar trends for their regions of superiority [15]. Of course, the position of the break-even line depends on the optical system efficiency, and in particular on the performances of the laser source [8]. Thus, innovations aimed at improving the performances of optical systems can extend the range of optical interconnects superiority.

1.1.2. Silicon Photonics

Photonic integrated circuits (PIC) have the potential to further improve the miniaturization of optical circuits and components by integrating multiple elements onto a single microchip, and transfer the benefits of photonics to shorter distances. Co-packaged optics and optical network-on-chip aim to bring optical interconnects closer to the ASIC, reducing the length of electrical interconnects [12], [16]. Some advanced systems on a chip also aim at realizing monolithic electronic-photonic integrated circuits by integrating photonics and microelectronics on a single chip fabricated in a CMOS foundry [17]. In particular, silicon photonics, demonstrated in the 1980s [18], is considered an ideal platform for achieving high performance at a low cost [19]. It benefits from mature Si manufacturing, including CMOS fabrication technologies, to enable high throughput, scalability and cost-effectiveness through economies of scale [20]. Si manufacturing also contributed to the availability of large volumes of low cost and high-quality Si and silicon-on-insulator (SOI) wafers used in silicon photonics. With a large index contrast,

the Si/SiO_2 system allows confining light in waveguides that are only a few hundred nanometers thick and wide, enabling improved connection density. Finally, Si exhibits low optical absorption at 1.3 µm (O-band) and 1.55 µm (C-band), and silicon nitride can be used as a complementary material to extend the range of operational wavelengths.

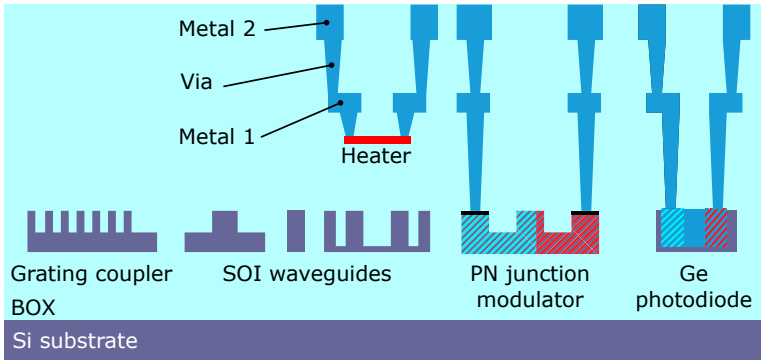

Figure 1.1: Cross-section schematic illustration of some of the main components of the CEA-LETI silicon photonics platform. Adapted from [21].

Fig. 1.1 illustrates a cross-section of some of the main silicon photonics components as processed on the CEA-LETI platform. A PIC for optical communications requires a number of active and passive components [22]. The passive components, fabricated using SOI and/or SiN are the fundamental building blocks of any PIC. Strip and rib waveguides serve the purpose of guiding light to connect the PIC components. Directional couplers, Y-branch and multimode interferometers are employed to couple and split light between waveguides, while grating or edge-couplers are the optical inputs/outputs of the PIC [23]. When wavelength division multiplexing is used to transmit multiple signals in a single waveguide or optical fiber, multiplexers and demultiplexers, such as arrayed waveguide gratings [24] or cascaded Mach-Zehnder [25], are required. In addition, microresonators can be used to generate frequency combs [26]. Electro-optic modulators use thermo-optic, electro-optic or charge effects to convert an electrical signal to an optical signal. They can be fabricated using silicon only, but state-of-the-art modulators benefit from the heterogeneous integration of other materials with stronger electro-optic effects such as SiGe, III-V compounds or barium titanate [27]. Due to silicon being transparent at the application wavelengths, photodetectors also require the heterogeneous integration of other materials, such as III-V compounds or germanium [27]. Last but not least, lasers are possibly the most challenging components to realize on silicon PIC. Methods to fabricate laser sources on silicon will be discussed more specifically in section 1.2.

1.1.3. Requirements of Lasers for Silicon Photonics

Before discussing the fabrication of lasers on silicon in section 1.2, we shall first define the main figures of merits describing their operation and the requirements for co-packaged optics and optical network-on-chip. The figures of merit we consider to be the most important are:

- **Thershold current (I_{th}):** the pump current required to trigger lasing action in a laser

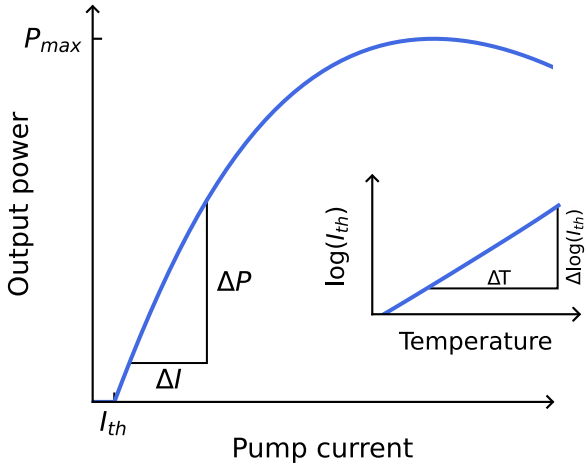

Figure 1.2: Example optical output power versus pump current (L-I) curve of a laser diode illustrating some key figures of merit for continuous-wave operation.

diode. Several indicators can prove lasing action [28]. In particular, it is associated with a kink in the optical power versus pump current curve, as illustrated in Fig. 1.2.

- **Differential (quantum) efficiency (η_d):** the ratio of output photons over input electrons above threshold. Writing ΔP the increase in output power for an increase of the pump current ΔI (Fig. 1.2), we have

$$\eta_d = \frac{q}{h\nu}\frac{\Delta P}{\Delta I} \tag{1.1}$$

with q the electron charge, and $h\nu$ the photon energy.

- **Characteristic temperatures (T_0 and T_1):** respectively describe the threshold current increase and differential efficiency decrease as the laser temperature is increased. The threshold current typically exhibits an exponential dependence on temperature [29], as illustrated by the inset of Fig. 1.2:

$$I_{th} = I_0 e^{T/T_0} \tag{1.2}$$

However, some designs aim at improving the high-temperature operation of laser diodes, breaking this relationship, as will be discussed in section 2.1. In this case, a temperature-dependent characteristic temperature is defined based on the temperature derivative of the logarithm of Eq. (1.2) [30]:

$$\frac{1}{T_0}(T) = \frac{\partial \ln(I_{th})}{\partial T} \tag{1.3}$$

Similarly, T_1 can be defined by

$$\frac{1}{T_1}(T) = -\frac{\partial \ln(\eta_d)}{\partial T} \tag{1.4}$$

- **Maximum output power ($P_{\max}$):** as the pump current is increased above threshold, the output power increases, up to a roll-over of the output power, as illustrated in Fig. 1.2.

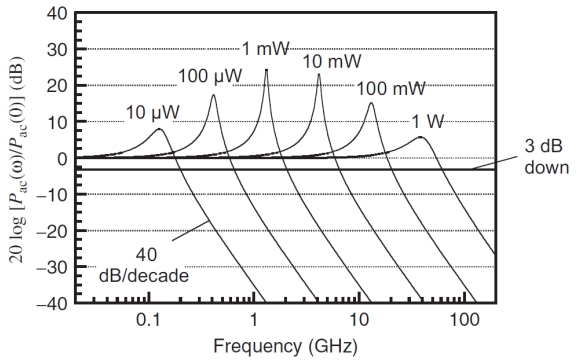

Figure 1.3: Small-signal theoretical modulation response of an idealized laser diode showing the 3 dB bandwidth and its dependence on the optical output power.

This is mainly due to heating and gain saturation, as will be discussed in section 2.1.

- **Side-mode suppression ratio (SMSR):** the ratio of the peak power in the main mode of the laser over peak power in the side modes. The SMSR is often expressed in dB. In wavelength division multiplexing, it is important that the SMSR is high enough (typically above 30 dB) to reduce crosstalk between channels.
- **3 dB modulation bandwidth (f_{3dB}):** instead of combining a laser and an electro-optic modulator, some photonic circuits use directly modulated laser. The 3 dB-bandwidth, as illustrated in Fig. 1.3, is the modulation frequency beyond which the response of the laser diode falls below 3 dB [29]. For a given laser diode, f_{3dB} increases up to a certain point with pump current, before reaching a maximum value. It must be noted, however, that the laser can be driven beyond f_{3dB} while still giving a readable signal [31].

The energy efficiency requirements for optical interconnects are based on the need to provide superior performance as compared to electronics, and on the thermal budget available. Indeed, the maximum amount of heat that can be efficiently extracted from a chip is only a few hundred watts [9]. Among the aforementioned figures of merit, the threshold current and differential efficiency are directly related to the energy consumption and energy efficiency of a laser diode. However, the most relevant figure of metric describing the energy efficiency of a transceiver is its energy cost, expressed in fJ.bit^{-1}. For a directly modulated laser, it corresponds to the ratio of its energy consumption over modulation speed while for systems using optical modulators, the energy consumption of the laser source and modulator must be summed. Depending on the considered application, in particular the distance over which the data needs to be transmitted, the target energy costs ranges from a few tens of fJ/bit to one pJ/bit [9]. Few few fJ/bit directly modulated lasers have already been demonstrated, although with extremely low output powers [32]. The optical power budget and required laser output power depend on the specific application, and in particular on the optical link distance, the use of optical modulators, couplers, or (de)multiplexers for instance. An output power of about 1 mW is generally considered necessary to get a readable signal at the photodetector [22].

For data transfer, the bandwidth density, the ratio of bandwidth to chip perimeter used, can

be seen as more relevant figure of merit than the brute modulation bandwidth per channel. Bandwidth densities of a few Gbps/µm are considered necessary [9]. In addition, while complex data transmission schemes permit high data transmission rates, they can dramatically increase the energy cost of serialization and deserialization [22]. Hence, a high density of 20 Gbps channels for instance, may be more beneficial than a lower density of 100 Gbps channels, both in terms of bandwidth density and energy cost.

1.1.4. Environmental Impact of Data Communication and Silicon Photonics

The environmental impact of information and communication technologies is largely discussed. As we have briefly mentioned in section 1.1.1, data center alone could consume up to 565 TWh of electricity per year by 2030, as illustrated in Fig. 1.4, which is over 2% of the available electricity [6]. However, the environmental impact of digital technologies extends beyond their energy consumption, and digital technologies are sometimes seen as an essential enabler for a sustainable future, for instance, by the European Green Deal [33].

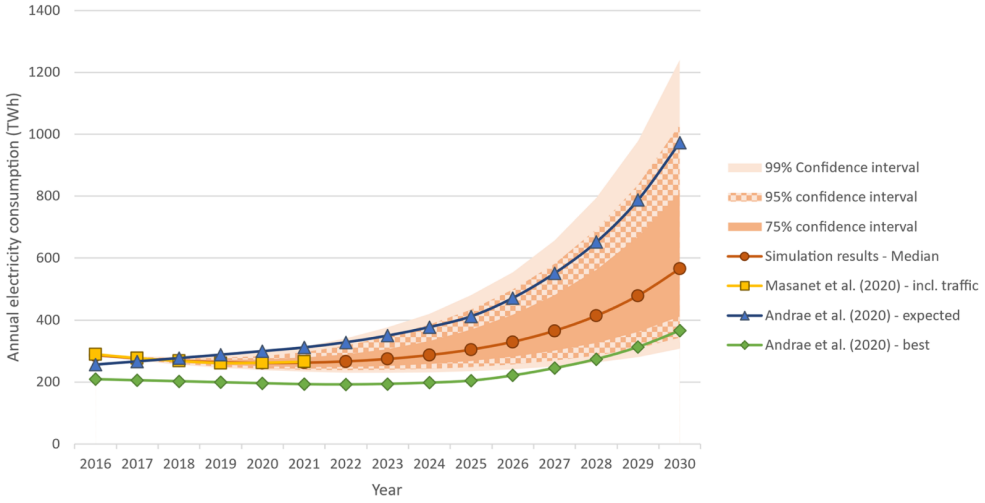

Figure 1.4: Past and forecasted annual energy consumption of data centers, taking into accound the end of Moore's law and the rise of industrial IoT. Taken from [6], with data from [4], [34].

The impact of information and communication technologies is typically separated in direct and indirect effects [35]–[38].

Life-cycle analysis are used to estimate the direct impact of devices manufacturing, transport, use and end of life. This impact is mostly measured in terms of global warming potential and primary energy use, and sometimes also considers water use, abiotic resource depletion and eco-toxicity, which are important factors as well [37]. For both consumer electronics and data centers, manufacturing — in particular of the integrated circuits — represents the major contribution to their environmental footprint [37], [39]. CMOS foundries have a large environmental footprint, considering either energy use, greenhouse gas emissions, or water use. Over time, the energy use and greenhouse gas emissions per wafer area tend to decrease, while the water consumption per wafer area tend to increase. Recently, extreme UV lithography and the higher complexity of

integrated circuits have allowed increasing the density of functionalities per wafer area, but also increased the environmental footprint per wafer area [40]. 60% of the greenhouse gas emissions of CMOS manufacturing result from the energy used to operates machine and maintain a cleanroom environment. This number could be reduced by using renewable energies. Other important contributions result from the chemical and gases used, and perfluorinated compound and diffusive emissions [39]. Because the fabrication of silicon photonics chips relies on the processes of CMOS integrated circuits manufacturing, the aforementioned impacts will also apply to silicon photonics.

Indirect impacts are more diverse, and their overall influence is highly uncertain. Positive aspects include the dematerialization, or tertiarization, of the economy, hoped to decouple economic growth from energy consumption. Another aspect is the optimization of human activities and their energy efficiency, with smart traffic management, smart buildings, smart energy supply or smart production [35]–[38]. Indirect negative impacts result from rebound effects. For instance, despite an increased density of functionalities per wafer area, the total wafers area produced by foundries kept increasing over the years [40]. Similarly, despite improvements in the energy efficiency of information and communication technologies, their energy consumption has increased [37].

Considering all effects, researchers found that digitalization has an overall negative and increasing environmental impact. It could however be positive provided improved efficiencies are associated to a mitigation of the negative direct effects — by stabilizing or reducing the production volume — and if rebound effects are limited [36], [37], [39].

In this thesis, we will primarily focus on enhancing energy efficiency. As previously mentioned, silicon photonics can indeed improve the energy efficiency of data communications [8]–[12]. However, silicon photonics also uses rare materials, such as III-V compounds, and could increase the complexity of chip manufacturing. While fabrication efficiency may not be crucial in the earlier stages of technological readiness, it is essential that designs can be transferred to mature CMOS platforms without introducing unnecessary complexity.

1.2. III-V on Silicon Lasers

Lasers constitute the optical source necessary for any operation performed on a PIC, and integrated lasers leverage the need for the unpractical coupling of light from an external source to the chip.

As illustrated in Fig. 1.5, a laser can be simplified as an optical gain medium in an optical cavity: photons are generated in the gain medium through stimulated emission, while the optical cavity provides the feedback necessary to obtain lasing action. The following subsections will provide a short review of the physics and state-of-the-art of gain media and cavities for lasers on silicon.

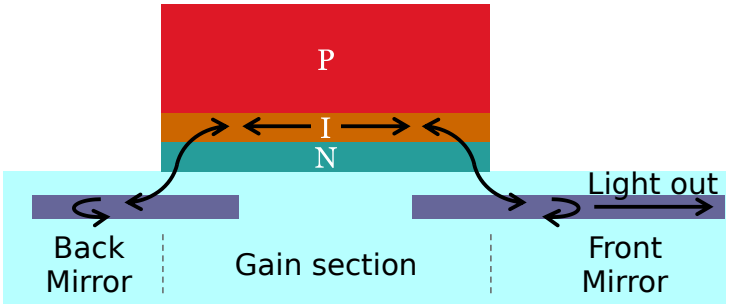

Figure 1.5: Longitudinal cross-section schematic of a laser diode composed of a gain medium in an optical cavity.

1.2.1. Light Emission in Semiconductor Materials

Spontaneous and Stimulated Recombination

In semiconductor lasers, photons are produced from the recombination of free electrons lying in the conduction band with free holes from the valence band. Recombination takes place through several mechanisms, illustrated in Fig. 1.6.

Non-radiative trap-assisted recombination (Fig. 1.6.a) consists of the recombination of free carriers through a defect state in the gap, which can result from crystal defects, impurities, or appear at the semiconductor surface. These should be reduced by improving the crystal quality and through surface passivation. In such recombination, the carrier energy is released in the form of heat transferred to the crystal lattice. The rate of trap-assisted recombination, sometimes referred to as Shockley-Read-Hall (SRH) recombination, writes [29], [41], [42]:

$$R_{SRH} = \frac{np - n_i p_i}{\tau_n \left(n + n_1\right) + \tau_p \left(p + p_1\right)} \tag{1.5}$$

where n and p are respectively the densities of free electrons and free holes, n_i and p_i their intrinsic concentration and n_1 and p_1 would be their equilibrium concentration if the Fermi level was aligned with the trap energy level. $\tau_{n,p}$ are the electron and holes capture lifetimes. Lasers typically operate in the high-level injection regime where $n \gg n_i, n_1$ and $p \gg p_i, p_1$ [29]. In this situation, Eq. (1.5) simplifies to:

$$R_{SRH} = \frac{np}{\tau_n n + \tau_p p} \tag{1.6}$$

Illustrated in Fig. 1.6.b. is the spontaneous recombination of an electron from the conduction band with a hole from the valence band, producing a photon with energy $E_c - E_v = h\nu$. The rate of spontaneous recombination is

$$R_{sp} = Bnp \tag{1.7}$$

where B is the bimolecular recombination coefficient. In conventional lasers, only a small fraction of the photons produced through spontaneous recombination is coupled to the lasing mode. Typical values for this spontaneous emission factor β are close to 1×10^{-5} [29].

In addition to that, the recombination of an electron and a hole may be triggered by an

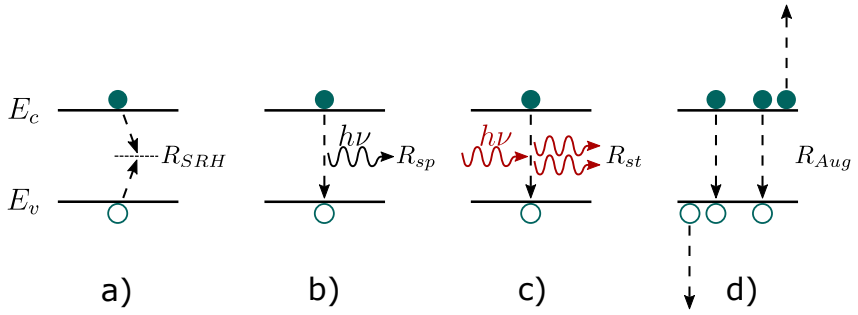

Figure 1.6: Electron-hole recombination mechanisms: (a) non-radiative trap-assisted, or Shockley-Read-Hall recombination (b) radiative spontaneous and (c) stimulated recombination (d) non-radiative Auger recombination

incident photon, generating a photon with the same properties as the incident photon (including energy, polarization and phase). This stimulated emission (Fig. 1.6.c) is the main mechanism for photon generation in lasers. Due to the generated photon having the same properties as the incident photon, it gives the laser its properties of high intensity, monochromaticity, coherence and beam directionality. In an opposite process, the incident photon is absorbed by an electron from the valence band to generate a free electron-hole pair. These two competing processes result in the optical gain g, defined such that the variation of the photon density of the laser mode N_P during propagation along the length of the optical cavity (x-axis) is

$$\frac{dN_P}{dx} = \Gamma g N_P \tag{1.8}$$

Γ is the optical confinement factor, and it is defined as the integral of the Poynting vector of the laser mode on the active medium over the integral of the Poynting vector on the whole space [43]. The optical gain for a given transition is expressed as a function of the occupation probability of the conduction band by free electrons f^e, and of the occupation probability of the valence band by free holes f^h:

$$g = g_{\max}(f^e + f^h - 1) \tag{1.9}$$

where $g_{\max}$ is a material property. If $f^e + f^h < 1$ the rate of absorption is larger than the rate of stimulated emission and the medium acts as an absorber. Upon pumping of the medium to increase the density of free carriers, it becomes transparent when the stimulated absorption and emission cancel out ($f^e + f^h = 1$), and eventually an optical amplifier when the stimulated emission dominates ($f^e + f^h > 1$).

The last recombination mechanism illustrated in Fig. 1.6.d. is Auger recombination, where an electron and a hole recombine non-radiatively by transferring their energy to another conduction band electron (nnp Auger recombination) or valence band hole (npp Auger recombination). Subsequently, the rate of Auger recombination is

$$R_{Aug} = C^n n^2 p + C^p n p^2 \tag{1.10}$$

Where C^n (resp. C^p) is the nnp (resp. npp) Auger recombination coefficient.

Choice of Semiconductor Materials

The band structure of a semiconductor provides valuable information on its potential for being used as a gain material. Fig. 1.7 illustrates the band structure of two common semiconductors, namely silicon and gallium arsenide.

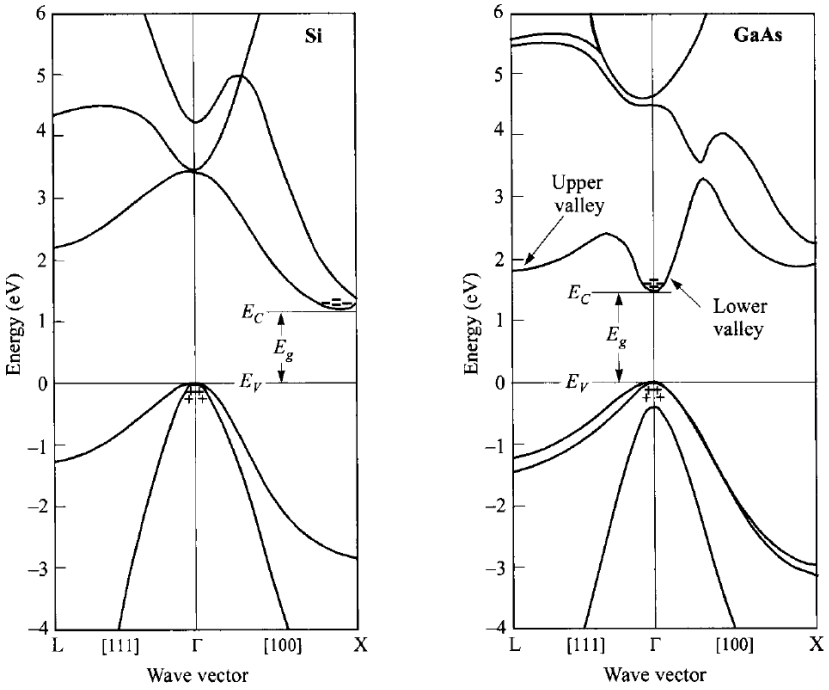

Figure 1.7: Band structure of Si (left) and GaAs (right). The minimum of the conduction band (E_c) of Si is not aligned with the maximum of its valence band (E_v) in the *k*-space. Therefore, Si is said to be an indirect bandgap semiconductor. By contrast, GaAs, a direct bandgap semiconductor, has the minimum of its conduction band aligned with the maximum of its valence band. Taken from [44]

An important parameter to determine if a given semiconductor is a good candidate or not is whether it has a direct or indirect bandgap. Direct bandgap semiconductors, such as GaAs, are those whose conduction band minimum and valence band maximum are aligned in the *k*-space. Because optical transitions must obey the law of conservation of momentum, and this condition is naturally met in direct bandgap semiconductors, such materials exhibit high rates of direct radiative recombination and are good candidates for the realization of optical sources. By contrast, the minimum of the conduction band of indirect bandgap materials, such as Si, is not aligned with the maximum of their valence band. Therefore, radiative recombination requires a third particle to transfer the excess momentum to, greatly reducing the rate at which such recombination happen [29], [45]. Because Si and Ge are both indirect bandgap semiconductors, GaAs or InP-based materials are typically used in laser diodes. Challenges and methods for their integration in silicon photonics are detailed in section 1.2.3.

Another important property is the semiconductor bandgap E_g. It determines the energy carried by the generated photons and thus, their wavelength. Fig. 1.8 presents the bandgap (and corresponding wavelength) of Si, Ge and some common III-V compounds. An additional degree of freedom to reach a continuous span of bandgaps is obtained through the use of III-V

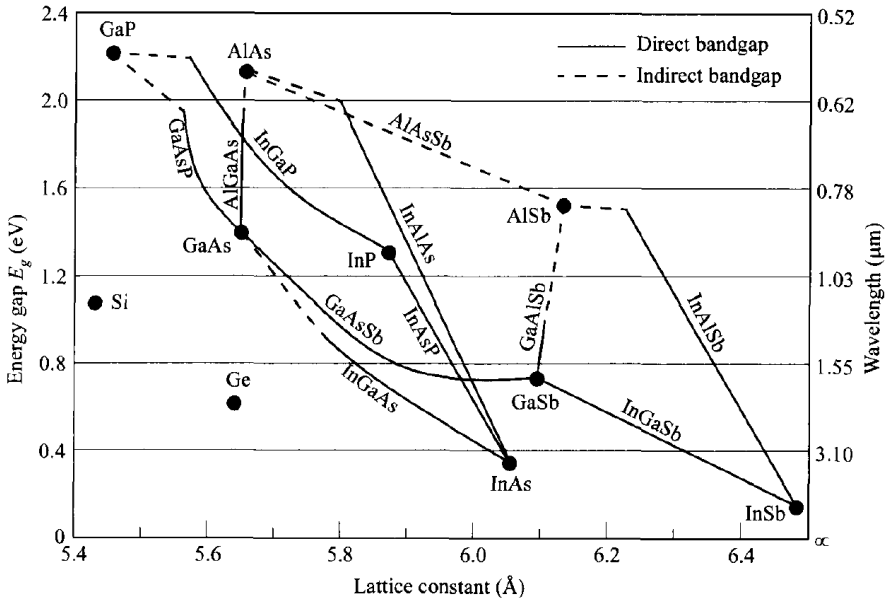

Figure 1.8: Room-temperature energy gap and lattice constant of Si, Ge and some common III-V compounds. Lines connecting binary III-V compounds correspond to their ternary alloys. Taken from [44].

alloys. For instance, the room-temperature (RT) bandgap of GaAs is 1.43 eV, while InAs and AlAs have bandgaps of 0.36 eV and 2.16 eV respectively. Subsequently, the use of GaAs-InAs alloys (written $In_xGa_{1-x}As$ where x is the fraction of InAs) and AlAs-GaAs alloys ($Al_xGa_{1-x}As$) allows spanning a wide range of bandgaps [44], [46].

1.2.2. Semiconductor Heterostructures

The Double Heterostructure

As previously stated, a semiconductor requires $f^e + f^h > 1$ in order to act as an optical amplifier, necessitating the supply of free electrons and holes to the gain medium to meet this condition. In 1963, Z. Alferov and H. Kroemer independently proposed the concept of double heterostructure lasers, greatly facilitating their electrical pumping to achieve the population inversion [47], [48].

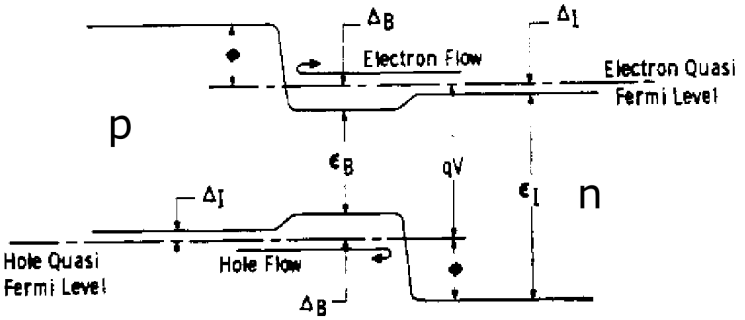

Figure 1.9: Schematic band diagram of a biased double heterostructure laser diode. Taken from the original article by H. Kroemer [48].

Fig. 1.9 illustrates the principle of a double heterostructure laser. The intrinsic gain medium is sandwiched between p and n-doped semiconductors with a larger bandgap. By biasing the

structure, free electrons (resp. holes) can be injected from the n-doped (resp. p-doped) side to the gain medium. In addition, owing to the larger bandgap of the cladding, the free carriers are confined in the intrinsic region of the double heterostructure as shown by the electron/hole flow arrows in Fig. 1.9. Finally, using lower refractive index materials in the doped regions, an optical waveguide is formed, providing optical confinement in the gain medium.

Quantum Confinement in Nanostructures

Besides, heterostructures of the nanoscale use the quantization of energy levels resulting from the spatial confinement of the free carriers to tune their energy levels and modify their density of states. In bulk materials, electrons and holes can move freely along the three dimensions of space. Their energy levels are not quantized and the electronic density of states in the conduction band $N_c(E)$ is

$$N_c\left(E\right) = \frac{1}{2\pi^2}\left(\frac{2m^e}{\hbar^2}\right)^{3/2}\sqrt{E - E_c} \tag{1.11}$$

where m^e is the effective electron mass and $\hbar$ is the reduced Planck constant.

Quantum wells (QW) provide confinement of the carriers along one dimension of space, giving a set of quantified energy levels E_i for movement along this direction. In the simplified case of an infinite potential barrier, the solutions to the Schrödinger equation only exist for the eigenenergies

$$E_i = E_c + \frac{\pi^2\hbar^2 i^2}{2m^e L_z^2} \tag{1.12}$$

where the dependence on L_z, the QW width, gives one degree of freedom to tune the energy levels. Movement along the two other directions is still allowed, and the electronic density of states exhibits a step-like shape (see Fig. 1.10.b) [46]:

$$N_c\left(E\right) = \frac{m^e}{\pi\hbar^2 L_z}\sum_i H\left(E - E_i\right) \tag{1.13}$$

where H is the Heaviside step function. QW are fabricated by growing few nm-thick layers of active material clad between barriers made of a larger bandgap material. Typically used materials are InGaAs on GaAs substrates for emission at 900 nm [49], and InGaAlAs [31] (1.3 μm) or InGaAsP [50] (1.55 μm) on InP substrates.

Quantum wires, which provide 2D confinement of carriers, are not commonly used in laser diodes. Their electronic density of states is plotted in Fig. 1.10.c.

Finally, Quantum Dots (QD) provide quantum confinement of the carriers in all three dimensions of space. As a result, only a discrete set of eigenenergies are allowed [44]:

$$E_{i,j,k} = E_c + \frac{\pi^2\hbar^2}{2m^e}\left(\frac{i^2}{L_x^2} + \frac{j^2}{L_y^2} + \frac{k^2}{L_z^2}\right) \tag{1.14}$$

The electronic density of states writes as a sum of Dirac delta distributions [44]:

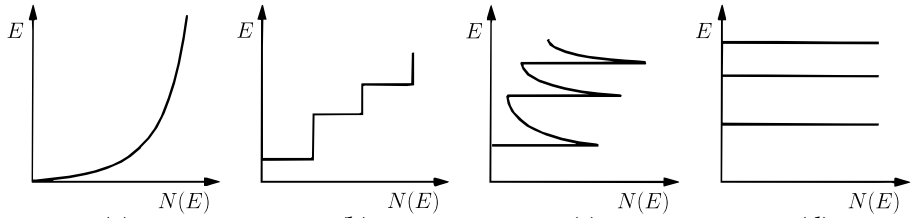

Figure 1.10: Electronic density of states of a (a) bulk, (b) quantum well, (c) quantum wire and (d) quantum dot material. From [44]

$$N_c(E) = \frac{2}{L_x L_y L_z} \sum_{i,j,k} \delta\left(E - E_{i,j,k}\right) \tag{1.15}$$

where $L_{x,y,z}$ are the QD dimensions along the three dimensions. The complete quantization of the energy levels brings benefits in terms of carrier confinement and reduced temperature sensitivity. Indeed, the main cause of the degradation of laser performances with temperature is the thermalization of the free carriers to excited states, which depletes the ground state involved in lasing. Due to the discrete energy levels of QDs, carriers need to have a precise energy to get excited to higher energy levels, which helps to pin the carriers to the ground state. Using InAs QD, Kageyama *et al.* demonstrated the continuous-wave operation of lasers up to 220 ℃ [51]. QD lasers were also shown to exhibit lower threshold currents (due to a smaller active volume), a reduced sensibility to optical feedback and increased tolerance to non-radiative defects (owing to the spatial localization of carriers, isolating them from defects) [52]. For semiconductor laser applications, the most commonly used QDs are InAs QDs grown on GaAs, fabricated through a self-assembly process known as Stranski-Krastanov growth. When growing InAs on a GaAs lattice, after a 1.6 monolayers-thick 2D InAs film (wetting layer) is grown, strain caused by the lattice mismatch between InAs and GaAs is relaxed through the formation of self-assembled 3D InAs clusters. These clusters then grow to become the QDs [53], [54]. Capping of the QDs with a strained InGaAs layer is used to decrease the dots energy levels, thus increasing their emission wavelength up to 1.3 μm [55].

1.2.3. Integration of III-V Materials in Silicon Photonics

As discussed previously in section 1.2.1, Si is a poor candidate for light emission due to its indirect bandgap. Although a number of methods have been employed to realize Si-based light sources, they still suffer from significant drawbacks and in particular, low efficiencies [10]. Therefore, III-V materials are much more commonly used as the active media of light sources on Si. Various methods have been explored to integrate III-V components on Si [10], [56]–[59]. Ideally, these methods should be scalable, provide a high throughput, facilitate the coupling between the III-V and SOI, and be efficient in their use of expensive III-V materials. These qualities are required for low cost and high-performance devices. Fig. 1.11 presents an overview of the existing methods, where two main types of strategies are identified, namely monolithic

and heterogeneous integration. Monolithic integration uses heteroepitaxy, the direct growth of III-V materials on Si substrates, while heterogeneous — or hybrid — integration methods rely on the bonding or transfer of III-V layers or devices grown on a native substrate on a SOI PIC.

Monolithic Integration

The monolithic integration is often considered as the ultimate solutions for light sources on Si. It should meet the needs for scalability, high throughput and low cost [10]. However, a number of crystallographic defects can result from the direct epitaxy of III-V semiconductors on Si. As they form non-radiative recombination centers, they could dramatically hinder the performances of the fabricated devices.

First, antiphase domains are caused by the different crystal structure of Si and III-V materials such as GaAs or InP. While Si has a diamond cubic crystal structure allowing the existence of monoatomic steps at its surface, GaAs, InP and most III-V materials have a zincblende structure which is similar to the diamond structure but with alternating layers of III and V materials. Taking GaAs as an example, Si and As have a higher bonding preference than Si and Ga. Thus, a layer of As first grows on the Si surface before alternating Ga and As layers. Hence, monoatomic steps at the Si surface result in domains with antiphase Ga and As layers, creating defects at the antiphase boundaries [60].

Another source of defects is caused by the difference of lattice parameter. Si has a lattice parameter of 5.431 Å while GaAs and InP have lattice parameters of 5.653 Å and 5.869 Å respectively [61]. During the growth of a crystalline semiconductor on a mismatched substrate, the epi-layer is strained to adapt its lattice to that of the substrate. After a critical thickness is reached, threading dislocations appear to relax the strain. The critical thickness is [44]:

$$t_c \simeq \frac{a_e^2}{2|a_e - a_s|} \tag{1.16}$$

where a_s is the lattice constant of the substrate and a_e that of the epitaxial material. For GaAs and InP epitaxy on Si, the critical thicknesses are respectively 7.2 nm and 3.9 nm, which is impractical for device fabrication.

The thermal expansion coefficient mismatch between Si and III-V semiconductors could be an issue as well since epitaxy is performed at high temperatures. For GaAs, a thickness of 3.0 µm to 5.5 µm can be grown on Si before the creation of cracks [62].

Benefiting from the lower sensitivity of QDs to defects and strategies to reduce the defect density, electrically pumped monolithic QD lasers on Si have already been demonstrated by several groups from the academic research environment [63]–[65]. The most straightforward approach is the blanket heteroepitaxy, where a full-sheet of III-V material is grown on the Si substrate. To reduce antiphase domains, monoatomic steps Si(001) with a 4°–6° offcut have been used [63] but are not the preferred solution since the industry standard is to use on-axis (001) Si wafers. It was also shown that by annealing Si(001) wafers under the appropriate conditions, double-layer steps could be formed, thus preventing the creation of antiphase

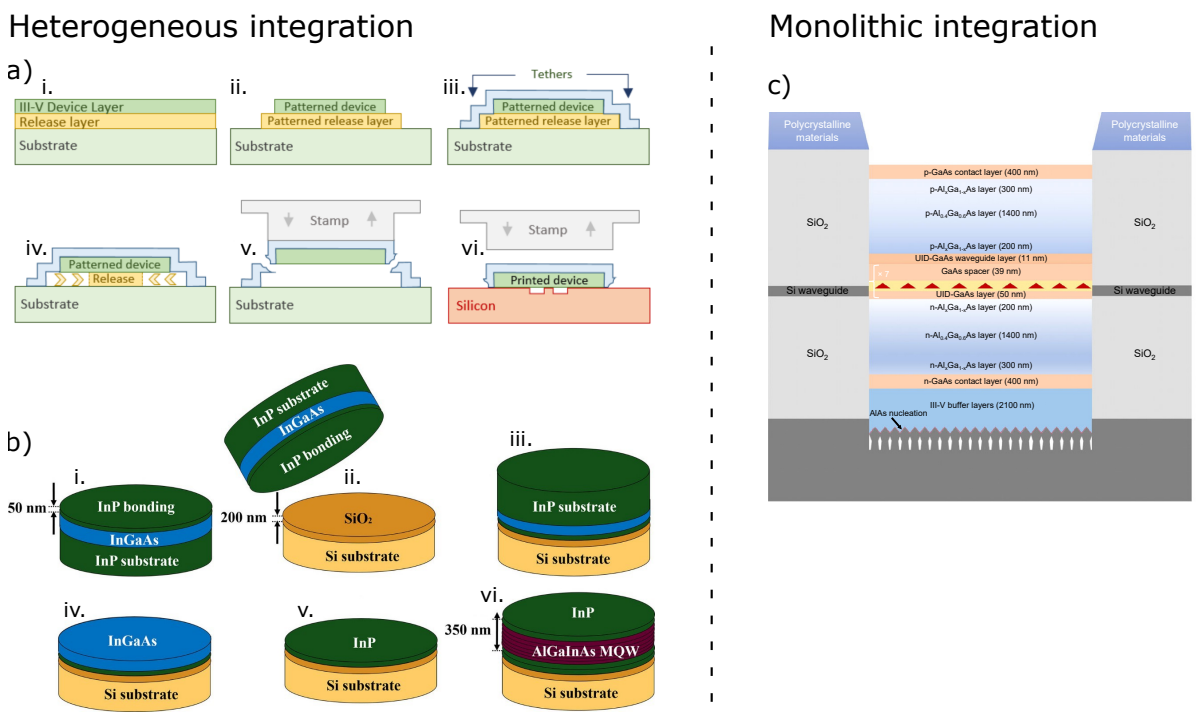

Figure 1.11: Illustration of some III-V on Si integration methods. (a) Micro-transfer printing, from [77]. (b) Direct bonding of an InP thin-film followed by the regrowth of a MQW stack, from [56]. (c) Monolithic epitaxial growth of III-V on SOI substrate to form embedded butt-coupled lasers, from [72].

domains [66]. Double layer steps are also a found on (111)-oriented Si facets. Accordingly, (111)-oriented V-grooves etched on the surface of Si(001) wafers have successfully been used to prevent the formation of antiphase domains [67]. Finally, GaP nucleation layers have been used to annihilate antiphase domains [68]. Regarding threading dislocations, the use of GaAs buffers and strained-layer superlattices was found to efficiently reduce the density of threading dislocations to allow the realization of functional devices [64], [69], [70]. However, these layers greatly increase the stack thickness, making the coupling with Si waveguides challenging. Electrically driven in-pocket and embedded butt-coupled lasers as illustrated in Fig. 1.11.c. were recently demonstrated and offer a promising solution to this issue [71], [72]. Another approach to the suppression of antiphase domains and threading dislocations is the use of the aspect ratio trapping (ART) method. ART uses SiO_2 trenches terminating on the SOI or Si substrate in the form of (111)-oriented V-grooves. III-V nano-ridges are selectively grown in these trenches, so the antiphase domains are prevented due to the (111)-oriented V-grooves, and threading dislocations are trapped in the SiO_2 trenches [62], [73], [74]. Lateral ART [75] and template-assisted selective epitaxy [76] build on the same principles to produce high-quality III-V membranes grown on Si. These approaches facilitate coupling to SOI waveguides as was demonstrated experimentally in reference [65], but the electrical pumping of these structures remains a challenge. Theoretical solutions are discussed in reference [75] for instance, but to the best of our knowledge, no electrically pumped lasers produced by these methods have been demonstrated so far.

Heterogeneous integration

Due to the challenges associated with heteroepitaxy, and in an effort to bring optical sources on the chip, the research and industry have also developed heterogeneous integration methods ensuring an excellent crystalline structure. These approaches also offer better flexibility, are more mature, and are thus currently more favourable for the development of an industrial silicon photonics supply chain [78].

The flip-chip bonding of a laser-diode fabricated on an external platform to the SOI PIC is a well-established technology [79] and it is already used in commercially available SOI PIC [10]. Since the III-V devices and SOI PIC are connected at the packaging stage, the compatibility of their fabrication processes is not a concern. Furthermore, this method allows for the pre-testing of the fabricated devices before bonding, to improve yields. However, the throughput is limited due to the pre-testing of the fabricated devices and their sequential bonding on the PIC. Additionally, the coupling of the bonded device and PIC via a grating coupler requires precise positioning and limits the coupling efficiency [80]. Besides, the flip-chip bonded devices are generally quite large, which limits the scaling of Si photonics and its associated benefits in terms of density, cost, and energy efficiency.

To address these challenges, micro-transfer printing has been proposed as an alternative approach to transfer pre-fabricated electro-optical devices while mitigating the limitations of flip-chip bonding [77], [81]. The basic principle of micro-transfer printing is illustrated in Fig. 1.11.a. It involves the fabrication of a dense array of electro-optical devices on a III-V substrate, on a release layer. Subsequently, an encapsulation layer is deposited to form tethers, followed by selective etching of the release layer. A polydimethylsiloxane stamp is then used to pick multiple devices in parallel and transfer them to the SOI PIC, using alignment marks to properly place the array of devices on the SOI. Because a large number of devices can be transferred at each printing cycle, the throughput is much higher as compared to the flip-chip method. Furthermore, light from the electro-optical devices can be efficiently coupled to the SOI by evanescent coupling, as demonstrated in reference [77]. Finally, this method permits a great efficiency of III-V material use owing to the dense array of devices on the III-V wafer, and the potential for reuse of the III-V substrate after transfer of the devices [10], [59].

Another method is the bonding of unprocessed III-V wafers or dies. The bonded material can consist in a MQW or QDs stack, a complete vertical p-i-n junction or a template or seed for regrowth, with excellent crystalline quality due to being grown on a native substrate [56]. Post-bonding, CMOS processing tools can be used to process the III-V layers, permitting high throughput, volume of production and scalability [10], [56]. In particular, the devices are defined by lithography, giving the best alignment accuracy. This approach allows evanescent coupling with the SOI and the realization of devices with hybrid III-V/Si waveguides combining, for instance, SOI Bragg gratings or ring resonators and a III-V gain medium [82]. This is a proven method: the first electrically pumped hybrid devices using wafer bonding were demonstrated as early as 2006 [83], and it is for instance the method used on the platform commercialized by

Table 1.1: Comparative summary of different III-V on Si integration strategies.

Integration method	Maturity	Crystalline quality	Scaling	Throughput	III-V/SOI coupling	III-V material use efficiency
Flip-chip	Commercial	Native substrate	Limited	Limited	Vertical coupling	Limited
Micro-transfer printing	R&D	Native substrate	High	High	Evanescent, stamp alignment accuracy	High
Wafer/die bonding	Commercial	Native substrate	Best	Best	Evanescent, defined by lithography	Limited
Hetero-epitaxy	R&D	With defects	Best	Best	Challenging, various solutions	High

Intel [84].

Wafer or dies can be bonded using hydrophilic direct oxide bonding processes (Fig. 1.11.b), in which case the III-V and receiver are capped with SiO_2, by deposition or oxygen plasma activation [56], [85]. Next, the wafers are brought in contact in the presence of water. SiO_2 first forms hydrogen bonds with water, before thermal annealing is used to form siloxane (Si-O-Si) bonds from the silanol (Si-OH) groups situated at the surface of each wafer, thus increasing the bonding strength [86], [87]. Hydrophilic direct bonding approaches are attractive since they provide strong and durable bonding interfaces capable of withstanding high temperatures, without introducing auxiliary materials [86]. They require particle-free surfaces with RMS roughness lower than about 0.6 nm. This may be challenging to achieve for academic laboratories, but it is quite standard for commercial foundries and can be obtained using chemical-mechanical polishing of the oxide [57]. Adhesive bonding using polymers such as benzocyclobutene (BCB) as an interfacial material is also used, with the advantage of relaxing the requirements on the initial surface quality [88]–[90]. However, BCB cannot withstand high temperatures, limiting post-processing capabilities. In addition, this bonding is less durable due to the deterioration of the polymer properties over time and stress [56], [88].

Nevertheless, the efficiency of III-V material use is not best in bonding methods since the III-V substrate is generally removed through grinding and wet etching post-bonding, to keep the thin-film of interest only. Due to III-V materials being both rare and expensive, this raises sustainability and economic issues. Works to produce commercial epi-ready III-V on Si large diameter (300 mm) substrates with a better material use efficiency aim at tackling this issue while also allowing economies of scale. The approach to fabricating these substrates is based on the Smart Cut technology already used to fabricate commercial SOI substrates: a III-V donor substrate is bonded to a receiver oxidized Si substrate. Hydrogen ion implantation is used to split the III-V substrate, leaving a thin layer of III-V material on the Si receiver while the

remaining of the donor substrate can be reused. Combined with tiling, this approach allows for the fabrication of large-diameter III-V on Si (or InPOSi) substrates [91].

Table 1.1 summarizes the pros and cons of the different integration strategies discussed in this section. In this thesis, we decided to use the direct bonding approach. It benefits from an excellent crystal quality and great maturity, in particular at CEA-LETI. In addition, it permits great flexibility in the processing of the epi-layers post-bonding.

1.2.4. Types of Laser Cavities

Besides the gain medium, the optical cavity is the second key ingredient of a laser. It provides the feedback necessary for stimulated emission and obtaining lasing action, giving lasers their unique characteristics such as coherence, power density and spectral purity.

Laser cavities can be separated in two main types, namely in-plane and vertical-cavity lasers (VCSEL), depending on whether the direction of light propagation is parallel or perpendicular to the surface of the wafer. Due to the vertical emission, VCSEL are difficult to use in integrated photonics. They have been used in the flip-chip integration, combined with grating-couplers, but suffer from high insertion losses [80].

Subsequently, in-plane lasers appear as a better-suited solution for integrated optics, and will be the only one discussed in the following.

Fabry-Perot Lasers

The two-mirror Fabry-Perot resonator is the simplest form of laser cavity. It consists of a waveguiding structure providing optical gain, confined between two discrete partially transmitting mirrors. It is used in some practical lasers, in particular for the realization of technological demonstrators [63].

The main parameters of any laser cavity can be defined using the example of a Fabry-Perot cavity with a geometrical length L and mirrors reflectivities $R_{1,2}$ as illustrated schematically in Fig. 1.12.

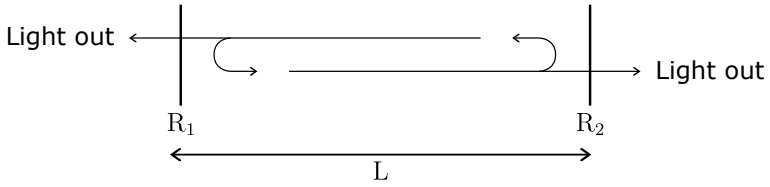

Figure 1.12: Schematic of a Fabry-Perot laser cavity composed of two partially transmitting mirrors of reflectivities R_1 and R_2 separated by a geometrical length L.

The Fabry-Perot cavity can support several standing waves, or longitudinal modes. Like any standing wave, these modes must obey the condition that the cavity length is a multiple of their half-wavelength. As a consequence, the wavelength spacing between two adjacent modes, or free spectral range (FSR), is [29]:

$$FSR = \frac{\lambda^2}{2n_{gr}L} \tag{1.17}$$

with n_{gr} the group effective index. For a non-uniform cavity divided in sections i of length L_i with effective group index $n_{gr,i}$, the product $n_{gr}L$ should be replaced by $\sum_i n_{gr,i}L_i$. The FSR is a key property in the engineering of the emission spectrum of a laser.

The quality factor Q is another important parameter of an optical cavity. It is defined as the ratio of the energy stored in the cavity and dissipated energy per optical cycle [92]. As such, it gives an indication on the photons lifetime in the cavity, τ_p. A long photon lifetime is useful to increase the coherence length of a laser, or decrease its lasing threshold, in particular for lasers with short cavities that cannot provide so much gain per round-trip [93]. However, a long photon lifetime is also detrimental for the modulation bandwidth of directly modulated lasers [29], [94].

Lastly, it is useful to define the mirror losses of a laser cavity. It translates the optical losses due to light being coupled out of the cavity through the mirrors in a term homogeneous to the inverse of a length:

$$\alpha_m = \frac{1}{L} \ln \left(\frac{1}{\sqrt{R_1 R_2}} \right) \tag{1.18}$$

Combined with the propagation losses in the cavity α_i, they determine the linear gain g_{th} necessary to reach lasing threshold, the point when the optical gain overcomes the losses [29]: $\Gamma g_{th} = \alpha_m + \alpha_i$.

Despite its simplicity, the Fabry-Perot cavity suffers from one main drawback, namely that is supports a large number of longitudinal modes, while single-mode lasers are often preferred for data communication applications.

Cavities Based on Bragg Gratings: DBR and DFB Lasers

Distributed Bragg reflectors or gratings (DBR) are a type of spectrally selective mirrors that use weak periodic perturbations of the effective index of the propagation medium to produce distributed small-amplitude reflections. These reflections add-up in phase at a given wavelength only, resulting in a reflectivity peak at this wavelength, while other wavelengths are transmitted. The period of the perturbations of the effective index determines the wavelength at which this reflection peak is found, referred to as the Bragg wavelength. In addition, the bandwidth (reflection peak width) and peak reflectivity of the grating can be controlled by engineering of the amplitude of the effective index perturbations and of the grating length. These aspects will be covered in more details in section 2.4.1.

Owing to their benefits in terms of single mode operation, control of the emission wavelength and mirror reflectivity, Bragg gratings are commonly used in state-of-the-art laser diodes [29]. Lasers employing two DBR located on either side of their gain medium are referred to as DBR lasers. Other lasers are designed with a Bragg grating distributed over the length of the gain section. They are named distributed feedback (DFB) lasers. As will be explained later in section 2.4.3, such lasers support two extended modes by default. A quarter-wavelength defect may then be used, so they instead support a single localized mode. Although such quarter-wavelength shifts are most commonly employed, some advanced DFB lasers use extended

modes to exploit the optical gain provided by the whole active medium length. For instance, in reference [31], workers from NTT used a uniform grating over the active medium length, coupled to an external DBR to select a single mode of the DFB.

Microdisks and Microrings Lasers

Benefiting from the high index-contrast between III-V materials and air or SiO_2, some lasers use microdisks [95] or microrings [96] of III-V material that can support confined *whispering gallery modes* (see Fig. 1.13.b) [97] despite exhibiting diameters as small as 1 µm [98].

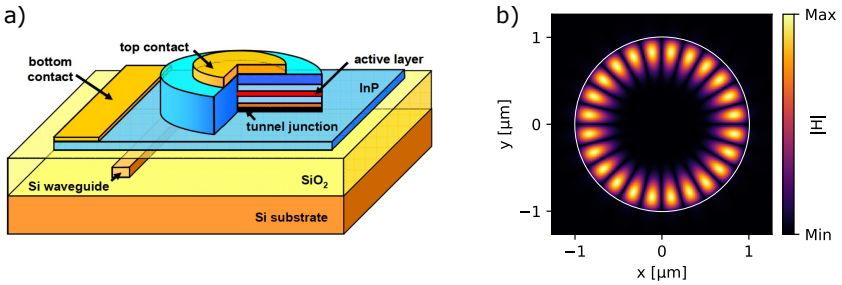

Figure 1.13: Microdisk laser diodes. (a) Schematic of a microdisk laser diode coupled to a SOI waveguide, taken from [95]. (b) Top-view of the magnetic field of the first-order wispering gallery mode of a GaAs microdisc at 1.3 μm, simulated by 2D FDTD. The white circle indicates the GaAs/SiO_2 interface.

Combining high Q-factors in reduced active volumes and a strong optical confinement in the gain medium, microdisk and microring lasers are a solution to realize lasers on silicon with minimal footprint and energy consumption.

Fig. 1.13.a. illustrates an example of electrically pumped III-V on Si microdisk laser coupled to a SOI waveguide from the literature [95]. With a diameter of 7.5 µm, the fabricated laser exhibited a RT threshold of 0.5 mA and single-mode operation with a SMSR of 26 dB at 1.4 mA.

2D Photonic Crystals

2D photonic crystal cavities push even further the combination of a high Q-factor and small active volume. They can be a few microns long and a few hundred microns wide, as illustrated in Fig. 1.14. Such small cavities provide strong light-matter interaction and can enable high Purcell factors, enhancing the rate of spontaneous emission in the cavity mode [29], [99].

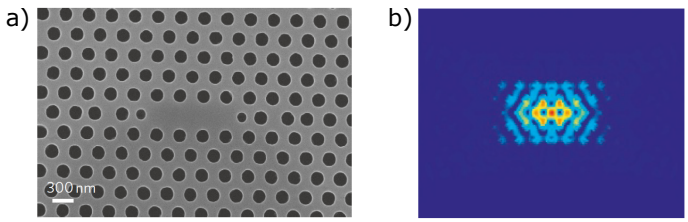

Figure 1.14: 2D three-hole defect photonic-crystal cavity. (a) SEM image and (b) FDTD simulation of the electric field of the cavity mode. Taken from [99].

An electrically pumped photonic-crystal nanocavity laser was demonstrated by J. Vučković and colleagues in 2011 [99], with a threshold as low as 287 nA at 150 K, but could not lase at higher temperatures. In 2013, S. Matsuo and colleagues solved this problem by demonstrating a MQW

photonic-crystal laser with a RT threshold of 4.8 µW and an output power of several µW [32]. These lasers still lacked coupling to a SOI waveguides, which the same group demonstrated in 2021 [100]. Due to coupling with the SOI waveguide, the cavity Q-factor was decreased, but RT operation was still achieved, with a very low threshold of 13.2 µA and an output power of a few µW.

In this thesis, we will explore Fabry-Perot, DBR, DFB and microdisk laser cavities. Despite their potential for the considered applications, 2D photonic-crystal nanocavities are challenging to realize and could only come after the technological developments which will be presented in this thesis.

1.2.5. III-V Membrane Lasers

III-V membrane lasers are a type of in-plane lasers composed of a thin III-V layer, typically 200 nm to 400 nm in thickness, sandwiched between low-index materials such as SiO_2, as illustrated in Fig. 1.15.

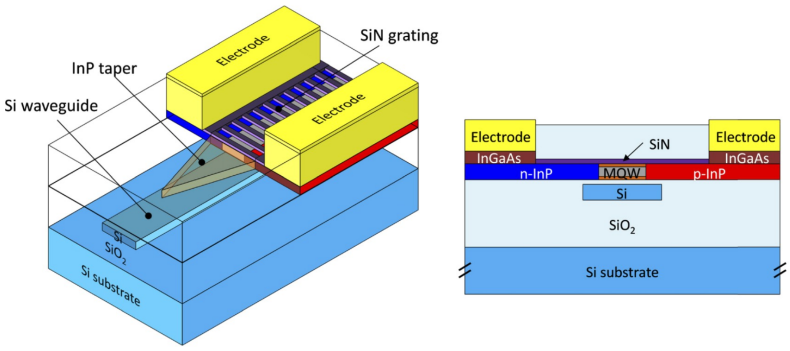

Figure 1.15: Bird's eye view (left) and transverse cross-section (right) schematic of an InP-based membrane DFB laser coupled to a SOI waveguide. Taken from [50].

The large index contrast between the III-V and cladding results in a strong optical confinement in the vertical direction as compared with a conventional double heterostructure laser [101], [102]. For instance, the index difference between GaAs and $Al_{0.4}Ga_{0.6}As$, which are commonly employed in double heterostructure lasers, is 0.20 at 1.3 µm [103], while it is 1.9 for the $GaAs/SiO_2$ system. This allows obtaining high modal gains in reduced active region volumes. As a consequence, lower thresholds — and lower energy consumptions — can be achieved, as well as higher direct modulation bandwidths. S. Matsuo and colleagues have demonstrated state-of-the-art III-V on SiO_2/Si directly modulated membrane lasers with a 60 GHz 3-dB bandwidth and 112 Gbps NRZ modulation, and a RT threshold of 1.1 mA, as illustrated in Fig. 1.16 [104]. Transferring the III-V membrane on a high-termal-conductivity SiC substrate, they were able to push the 3-dB bandwidth up to 108 GHz [31].

Owing to the thinness of the III-V membrane, the effective index of its supported optical mode is lower than that of conventional lasers as will be discussed in section 2.2.2. In particular, by choosing the right III-V membrane thickness, the effective index of the III-V mode can be

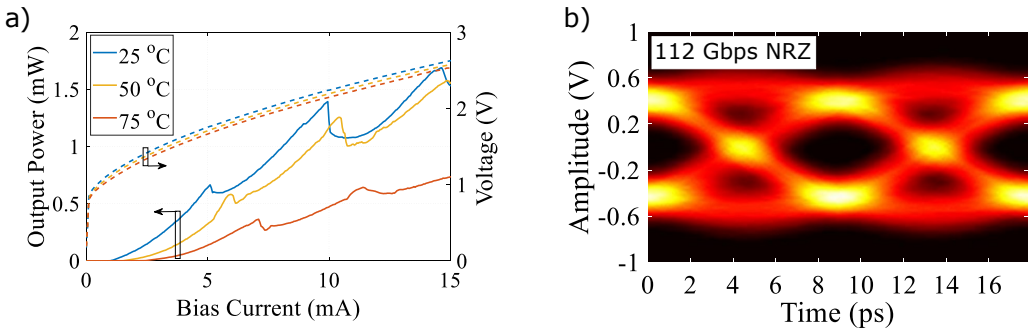

Figure 1.16: Temperature dependence of the L-I-V characteristic of a III-V membrane laser on SiO_2/Si (a) and RT eye-diagram for a 112 Gbps NRZ modulation (pump current 13.9 mA, b). Taken from [104].

close to that of a standard SOI waveguide. This results in hybrid supermodes, which degree of confinement in the III-V or SOI can be tuned by varying the SOI waveguide width [50]. This is by contrast to the thicker conventional lasers, which require approaches such as the localized thickening of the SOI waveguide [105] to be able to evanescently couple the optical field from the III-V to the SOI. This adds further complexity to the fabrication process, and a potential source of optical losses.

Lastly, due to their lower thickness, III-V membranes do not interfere with the back-end-of-line vias as could do thicker III-V stacks. This facilitates the co-integration with microelectronics on a single chip [102].

In vertical p-i-n lasers, a quite thick cladding, typically more than 1.5 µm in thickness, is required to optically isolate the top metal from the active region. Since such claddings cannot be used in III-V membranes, other injection schemes are required. One of them is the lateral current injection (LCI) scheme, with an in-plane p-i-n structure and side metal contacts as illustrated in Fig. 1.15. Vertical diode schemes have also been demonstrated but require thicker III-V membranes, hence lessening their benefits [102]. LCI structures are generally fabricated by etching of an intrinsic III-V membrane comprising the active stack, and lateral regrowth to form the p and n claddings. Hence, a challenge of the LCI comes from the realization of high-quality p-i and i-n interfaces by regrowth. If these interfaces are not good enough, they could lead to voltage drops or surface recombination [102]. A non-uniform distribution of the free carriers over the active region width has also been observed for wide structures, due to the lower holes mobility as compared to electrons. However, it is not an issue when the intrinsic region width is 1 µm or less [106], [107].

Finally, the III-V membrane is a versatile technology. It has already been demonstrated for the realization of 2D photonic-crystal lasers [99] and lasers based on Bragg gratings [31], [50]. In this thesis, we also propose a design of III-V membrane-based microdisk lasers (section 2.4.5). III-V membranes can also be used to realize other silicon photonics active components such as photodiodes or modulators [102].

1.3. Aim and Outline of this Thesis

The aim of this thesis is to provide a new type of laser on silicon, suited for short-distance data communications. This application requires highly energy efficient lasers — *i.e.* with a low threshold and a high differential efficiency. In addition, due to the proximity with the ASIC in the considered applications (co-packaged optics or optical network-on-chip), the laser diode should be able to operate efficiently in high-temperature conditions, typically around 80 °C. We also want to reduce the complexity of the laser integration in the silicon photonics platform. In particular, the proposed solution should allow for the optical coupling between the III-V and SOI without thickening of the SOI, as well as reducing interferences with the standard back-end. Finally, we should avoid adding specific extra lithography levels to the SOI processing.

With this scope in mind, our choice is to focus on III-V membrane laser diodes on silicon, using InAs quantum dots-in-a-well (DWELL) as a light-emitting medium, as illustrated in Fig. 1.17

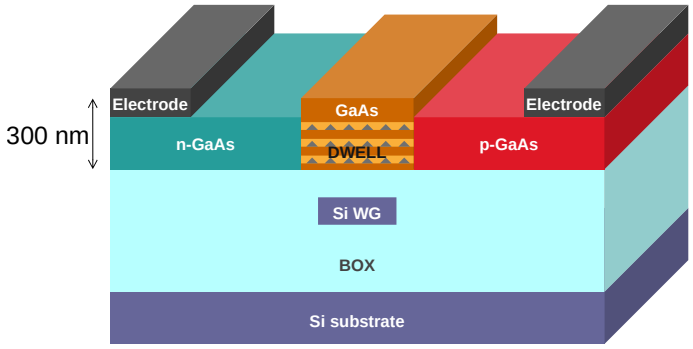

Figure 1.17: Shematic illustration (not to scale) of the InAs DWELL membrane lasers on silicon that we aim at fabricating and modeling in this thesis.

The thesis is structured as follows. Chapter 2 focuses on the modeling of InAs DWELL membrane lasers on silicon, with two main objectives. They are (1) to design such lasers, and (2) to better understand their operation, and in particular the mechanisms affecting their high temperature operation. To this end, we have built a model for the simulation of QD laser, which we benchmarked on state-of-the-art lasers, and later applied to membrane lasers. Besides, the basic theory of waveguides design and coupling, and of Bragg gratings are presented before being used to design laser cavities. In Chapter 3, our developments towards the fabrication of InAs DWELL membrane lasers on silicon are detailed. First, a process-flow for the fabrication of such lasers is proposed, followed by the presentation of our fabrication results. It starts with the development of the essential technological building blocks — such as the realization of horizontal p-i-n structures or the bonding of GaAs on Si — and progresses towards the last generation of prototypes, fabricated on silicon. The fabrication of the SOI circuits is also reported. Morphological characterizations of the fabricated devices are presented in this chapter. The electro-optical characterizations of the fabricated devices are subsequently presented in Chapter 4. Several methods are used to characterize the fabricated devices and gain better insight into their operation.

2

Modeling and Design of Integrated Membrane Lasers

Numerical modeling of integrated membrane lasers is necessary for both understanding their physics and designing devices with the best performances in the view of the prospect applications.

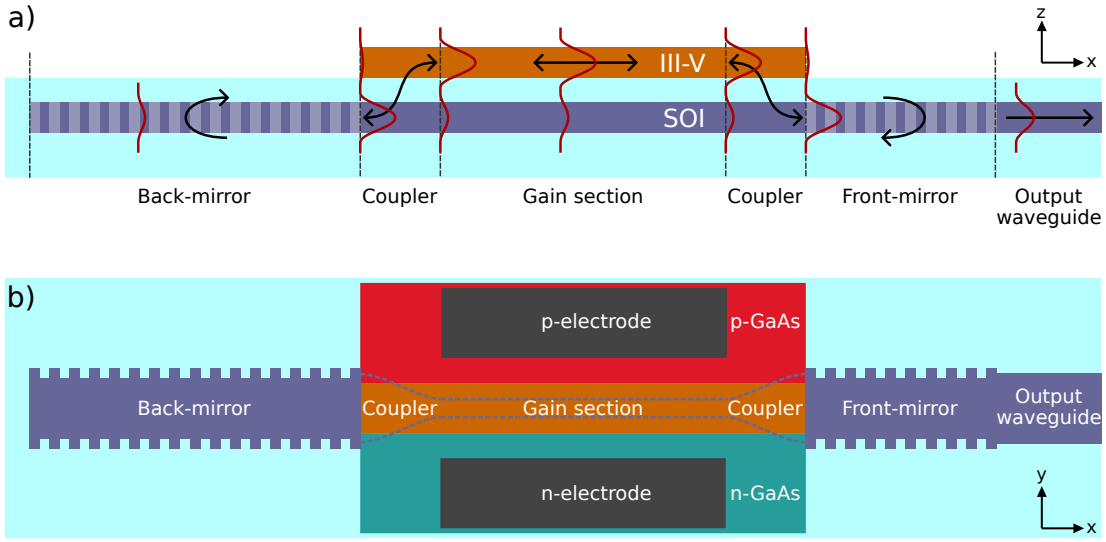

Figure 2.1: Key constituents of a laser diode on silicon illustrated schematically for a longitudinal cross-section (a) and top view (b) of a DBR laser: a gain medium, III-V/SOI optical couplers, two mirrors (which also act as mode selection filters) and an output waveguide.

In this chapter, we present simulation tools and results from commercial software and a house-built model used to study the gain medium and the passive components that constitute a semiconductor laser as illustrated in Fig. 2.1. In section 2.1, we propose a rate equation quantum dot laser model focusing on modeling the thermal behavior of p-doped devices. This model is used to answer the following questions: how does p-doping influence the performance of

quantum dot lasers and how to design energy-efficient quantum dot lasers capable of operating at high temperatures? These questions are of major importance due to the increasing demand for high bandwidth in board-edge, co-packaged optics and future optical network on-chip which will require energy-efficient, small-footprint integrated laser diodes that can operate at high temperatures due to their proximity to the ASIC. Next, in section 2.2 the design of III-V membrane and SOI waveguides is presented, and the coupled modes theory is used to design couplers to transfer light between these waveguides. In particular, we show that the use of a thin III-V membrane allows complete transfer of the optical field to the SOI waveguide while using the standard 305 nm-thick SOI from the CEA-LETI PDK, without requiring additional processing of the SOI to thicken it [105]. Subsequently, in section 2.3, the rate equation model is used with the III-V membrane waveguides designed in section 2.2 to confirm the potential of QD membrane lasers for short-distance optical interconnects. Lastly, in section 2.4 optical cavities for membrane lasers on silicon are designed using Bragg gratings, loop mirrors and microdisks.

2.1. A Rate Equation Quantum Dot Laser Model

This section is taken from our article [108], with a few adaptations.

Rate equation models are commonly used to model QD lasers while providing valuable insight into their physics [109]–[122]. In such a model, a set of coupled differential equations (the rate equations) are used to describe the evolution of the photon density and carrier population among a set of energy levels. The benefits of such a phenomenological approach are an easier implementation and a facilitated comprehension of the various phenomena at stake as compared to an approach using the Maxwell-Bloch equations, for instance, while still providing accurate results [123].

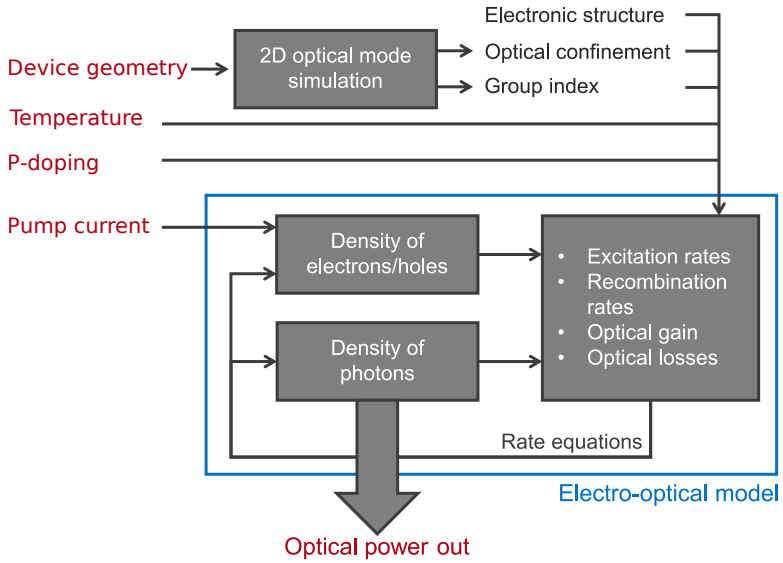

Figure 2.2: Schematic diagram illustrating the basic working principle of a laser rate equation model.

The basic working principle of the model is summarized schematically in Fig. 2.2. The device

geometry, temperature and p-doping are used, along with the density of carriers and photons, to compute the excitation and recombination rates of the carriers, optical gain and optical losses at a given time. Those and the pump current are next used to retrieve the time evolution of the density of carriers and photons — and thus of the optical power — thanks to the rate equations, and so on for the duration of the simulation.

2.1.1. Presentation of the Model

In the model developed in this thesis, five energy levels are considered for each type of carrier (electrons and holes), as shown in Fig. 2.3. Carriers are first injected in the GaAs confinement and spacing layers (spacer) before they can be captured to a bi-quantum-well (QW) level corresponding to the coupled InAs wetting layer and InGaAs capping. Finally, three dots bound states are considered since this best represents the electronic structure studied in reference [124] and thus the temperature behavior of the lasers, as discussed later in this section. The dots *s*-like ground state (GS) shows only spin degeneracy ($\nu_{GS} = 2$) while the *p*-like first excited state (ES1) and the *d*-like second excited state (ES2) are double degenerate, in addition to the spin degeneracy ($\nu_{ES1,2} = 4$) [124].

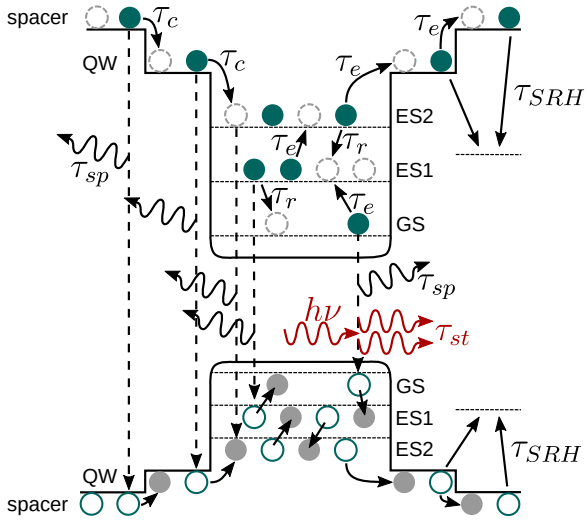

Figure 2.3: Schematic diagram of the energy states in the conduction and valence band considered for the model and of the energy transitions between these states.

In comparison to state-of-the-art QD laser models, two more effects are added to the present work to incorporate the influence of p-doping. It has been shown from the experimental works of Fathpour *et al.* [125] that Auger recombination in the dots plays an important role in the temperature behavior of 1.3 µm QD laser and in particular their high room-temperature (RT) characteristic temperature. Because the Auger recombination coefficients decrease with bandgap [126], [127], these recombination are negligible in higher energy levels. More recently, Norman *et. al* [30] highlighted the temperature dependence of the optical losses of p-doped QD laser, which decrease as the temperature is increased. This behavior is specific to p-doped devices and attributed to intervalence band absorption (IVBA) from holes in the dots levels.

Accordingly, the optical losses term is written as $\alpha_i = \alpha_0 + \sigma_i p$, where σ_i is the IVBA cross-section and p the spatial density of holes among the dots levels. The α_0 term represents other sources of optical losses (mainly scattering and absorption from the doped regions).

The evolution of the surface density of carriers in the bi-QW ($w_{QW}^{e,h}$) and in the spacers ($w_{spacer}^{e,h}$) and of the occupation probability of the dots X state $f_X^{e,h}$ are given by the coupled rate equations (2.1)–(2.5). In these equations, q is the electron charge and other parameters are defined in Table 2.1. The various terms are detailed in the following paragraphs.

$$\frac{\partial w_{spacer}^{e,h}}{\partial t} = \frac{\eta_i I}{qA_{act}} - \frac{w_{spacer}^{e,h}}{\tau_{c,QW}^{e,h}} + \frac{w_{QW}^{e,h}}{\tau_{e,QW}^{e,h}} - R_{spacer}^{SRH} - R_{spacer}^{sp} \tag{2.1}$$

$$\frac{\partial w_{QW}^{e,h}}{\partial t} = \frac{w_{spacer}^{e,h}}{\tau_{c,QW}^{e,h}} - \frac{w_{QW}^{e,h}}{\tau_{e,QW}^{e,h}} - \frac{w_{QW}^{e,h}\left(1 - f_{ES2}^{e,h}\right)}{\tau_{c,dot}^{e,h}} + \rho\nu_{ES2}\frac{f_{ES2}^{e,h}}{\tau_{e,ES2}^{e,h}} - R_{QW}^{SRH} - R_{QW}^{sp} \tag{2.2}$$

$$\begin{aligned}\frac{\partial f_{ES2}^{e,h}}{\partial t} = {} & \frac{1}{\rho\nu_{ES2}}\frac{w_{QW}^{e,h}\left(1 - f_{ES2}^{e,h}\right)}{\tau_{c,dot}^{e,h}} - \frac{f_{ES2}^{e,h}}{\tau_{e,ES2}^{e,h}} - \frac{f_{ES2}^{e,h}\left(1 - f_{ES1}^{e,h}\right)}{\tau_{r,ES2}^{e,h}} \\ & + \frac{\nu_{ES1}}{\nu_{ES2}}\frac{f_{ES1}^{e,h}\left(1 - f_{ES2}^{e,h}\right)}{\tau_{e,ES1}^{e,h}} - R_{ES2}^{sp} - R_{ES2}^{Aug}\end{aligned} \tag{2.3}$$

$$\begin{aligned}\frac{\partial f_{ES1}^{e,h}}{\partial t} = {} & \frac{\nu_{ES2}}{\nu_{ES1}}\frac{f_{ES2}^{e,h}\left(1 - f_{ES1}^{e,h}\right)}{\tau_{r,ES2}^{e,h}} - \frac{f_{ES1}^{e,h}\left(1 - f_{ES2}^{e,h}\right)}{\tau_{e,ES1}^{e,h}} - \frac{f_{ES1}^{e,h}\left(1 - f_{GS}^{e,h}\right)}{\tau_{r,ES1}^{e,h}} \\ & + \frac{\nu_{GS}}{\nu_{ES1}}\frac{f_{GS}^{e,h}\left(1 - f_{ES1}^{e,h}\right)}{\tau_{e,GS}^{e,h}} - R_{ES1}^{sp} - R_{ES1}^{Aug}\end{aligned} \tag{2.4}$$

$$\frac{\partial f_{GS}^{e,h}}{\partial t} = \frac{\nu_{ES1}}{\nu_{GS}}\frac{f_{ES1}^{e,h}\left(1 - f_{GS}^{e,h}\right)}{\tau_r^{e,h}} - \frac{f_{GS}^{e,h}\left(1 - f_{ES1}^{e,h}\right)}{\tau_{e,GS}^{e,h}} - R^{st} - R_{GS}^{sp} - R_{GS}^{Aug} \tag{2.5}$$

The capture and relaxation of carriers are described by the lifetimes $\tau_{c,X}^{e,h}$ and $\tau_{r,X}^{e,h}$ while the reverse excitation processes have lifetimes $\tau_{e,X}$ where the subscript X denotes the energy levels. The latter are expressed as functions of the capture and relaxation lifetimes using the detailed balance condition and Fermi-Dirac statistics, which is the foundation for the simulation of the lasers thermal behavior, as it will be explained in the next subsection (page 30).

The recombination terms considered include bimolecular spontaneous recombination with a rate $R_X^{sp} = B_X w_X^e w_X^h$ (or $R_X^{sp} = B_X f_X^e f_X^h$ for the dots levels) and Shockley-Read-Hall (SRH) recombination $R_X^{SRH} = \left(w_X^e w_X^h\right) / \left(\tau_{SRH}\left(w_X^e + w_X^h\right)\right)$. SRH recombination are considered for the spacer and bi-QW levels only as the spatial localization of carriers in the QDs isolates them from defect states [41], [42], [63], [117]. Auger recombination in the dots are necessary to correctly model the characteristic temperature of p-doped QD lasers, as stated earlier, and yield the term: $R_X^{Aug} = C_X^n f_X^{e^2} f_X^h + C_X^p f_X^e f_X^{h^2}$ [127]. The parameters B_X, $C_X^{n,p}$ and τ_{SRH} are defined in Table 2.1. The optical gain is expressed as a function of the GS population and maximum

Table 2.1: Parameters for the QD laser model used in the simulations. Parameters marked with † are fitting parameters as described in section 2.1.2.

Carrier dynamics parameters	
Injection efficiency	$\eta_i = 0.75$ [128]
Electron capture (relaxation) time	$\tau^e_{c(r)} = 1(2)\ ps$ [112], [129], [130]
Holes capture and relaxation times	$\tau^h_{c,r} = 0.1\ ps$ [112], [129], [130]
Spacer and bi-QW spontaneous recombination coefficients	$B_{spacer,QW} = 50 \times 10^{-7}\ m^2.s^{-1}$
SRH time	$\tau_{SRH} = 130\ ps$ †
Dots spontaneous recombination coefficients	$B_{ES2,ES1,GS} = 5 \times 10^8\ s^{-1}$ [94], [119]
Auger recombination coefficients	$C^{n,p}_{ES2,ES1,GS} = 8 \times 10^9\ s^{-1}$ †
Maximum material gain at lasing wavelength	$g_{\max} = 31.5 \times 10^5\ m^{-1}$ †
Spontaneous emission coupling factor	$\beta = 1 \times 10^{-5}$ [29]
Electronic structure [124]	
$\Delta E^e_{spacer\text{-}QW} = 120\ meV$	$\Delta E^h_{spacer\text{-}QW} = 40\ meV$
$\Delta E^e_{QW\text{-}ES} = 70\ meV$	$\Delta E^h_{QW\text{-}ES} = 10\ meV$
$\Delta E^e_{ES2\text{-}ES1,ES1\text{-}GS} = 70\ meV$	$\Delta E^h_{ES2\text{-}ES1,ES1\text{-}GS} = 10\ meV$
Dots levels degeneracy	$\nu_{ES2,ES1,GS} = 4, 4, 2$
Other Parameters	
Dots density: ρ	Mirrors reflectivities: $R_{1,2}$
Optical confinement factor: Γ	Group index: n_{gr}
Propagation losses: α_0	IVBA cross-section: σ_i
Active region length, width: L, W	Number of DWELL layers: N_{DWELL}
Total DWELL layers area	$A_{act} = W \times L \times N_{DWELL}$

material (QD) gain at lasing wavelength $g_{\max}$:

$$g = g_{\max}\left(f^e_{GS} + f^h_{GS} - 1\right) \tag{2.6}$$

This yields the spontaneous recombination term $R_{st} = v_{gr}\Gamma g N_P V_{mode}/\left(\nu_{GS} n_{dots}\right)$ where v_{gr} is the group index of the optical mode, V_{mode} its effective volume, Γ the optical confinement factor, N_P the photons density and n_{dots} is the total number of dots. It is worth noting that although ES lasing can occur in QD lasers [94], only GS lasing is considered in this work since ES lasing could be prevented practically through spectral engineering of the cavity, benefiting from the quite large energy spacing between the GS and ES1.

The optical gain is also used to compute the evolution of the photons density $N^{\pm}_P$ (where the $\pm$ superscript indicates propagation in the $\pm\, x$ direction, such that $N_P = N^+_P + N^-_P$) through

the rate equation:

$$\left(\frac{1}{v_{gr}}\frac{\partial}{\partial t} \pm \frac{\partial}{\partial x}\right) N_P^{\pm} = (\Gamma g - \alpha_i)\, N_P^{\pm} + \frac{1}{v_{gr}}\beta\frac{R_{GS}^{sp} n_{dots}\nu_{GS}}{V_{mode}} \tag{2.7}$$

Modeling of the thermal behavior

For a given pump current, the output optical power of a laser is greatly influenced by the temperature, as introduced in section 1.1.3. This is explained physically by the Fermi-Dirac distribution of electrons and holes over the available energy levels: as the temperature rises, the probability of occupation of the lower energy levels is reduced as carriers move to higher energy levels, which reduces f_{GS} and subsequently the gain g.

The excitation lifetimes dependence on the energy spacing between the states involved in the transition and on temperature (T) is the key to the simulation of the thermal behavior of the lasers. In our model, the excitation lifetimes are expressed as functions of the capture and relaxation lifetimes and temperature using the detailed balance condition and Fermi-Dirac statistics [122], [131] (more details about their derivation are available in Appendix A):

$$\tau_{e,QW}^{e,h} = \tau_{c,QW}^{e,h} w_{QW}^{e,h} \frac{\sqrt{2}}{t_{spacer}} \left(\frac{\pi\hbar^2}{m^{e,h}k_B T}\right)^{3/2} \exp\left(\frac{E_{spacer} - E_F}{k_B T}\right) \tag{2.8}$$

$$\tau_{e,ES2}^{e,h} = \tau_{c,dot}^{e,h} \rho\nu_{ES2} \exp\left(-\frac{E_{ES2} - E_F}{k_B T}\right) \frac{1}{w_{QW}^{e,h}} \tag{2.9}$$

$$\tau_{e,ES1}^{e,h} = \tau_{r,ES2}^{e,h} \frac{\nu_{ES1}}{\nu_{ES2}} \exp\left(\frac{E_{ES2} - E_{ES1}}{k_B T}\right) \tag{2.10}$$

$$\tau_{e,GS}^{e,h} = \tau_{r,ES1}^{e,h} \frac{\nu_{GS}}{\nu_{ES1}} \exp\left(\frac{E_{ES1} - E_{GS}}{k_B T}\right) \tag{2.11}$$

where t_{spacer} is the spacers thickness, $\hbar$ is the reduced Planck constant, k_B is the Boltzmann constant, $m^{e,h}$ are the electron and hole effective masses, and E_F is the quasi-Fermi level energy.

The temperature of the device is the temperature of its heat-sink plus an onset caused by self-heating. The latter could be estimated theoretically by writing that the electrical power injected in a laser diode (P_{in}) is either converted to output optical power (P_{out}) or dissipated in the form of heat (P_{th}) [29]:

$$P_{in} = P_{out} + P_{th} \Rightarrow P_{th} = P_{in} - P_{out} \tag{2.12}$$

In this equation, the input electrical power may be written as:

$$P_{in} = VI = V_{th}I + R_S I^2 \tag{2.13}$$

where I is the electrical current flowing through the diode and $V = V_{th} + R_S I$ with V_{th} including the ideal diode voltage and other current-independent series voltage and R_S is the diode series resistance. Finally, the temperature increase due to self-heating (ΔT) is the dissipated power

times the thermal impedance of the device Z_{th}:

$$\Delta T = Z_{th} P_{th} \tag{2.14}$$

$$\Delta T = Z_{th} \left(V_{th} I + R_S I^2 - P_{out} \right) \tag{2.15}$$

The dissipated power results in part from Joule heating in the p-doped region due to the lower mobility of holes as compared to electrons [44], [50].This adds more complexity in the determination of the thermal impedance as the sources of heat are distributed. In addition, the thermal conductivity of semiconductors also depends on the temperature — it can be fitted using the power law $K(T) = AT^n$ where, for GaAs for instance, $A = 750 W/cm.K^{0.28}$ and $n = -1.28$ [132]. This adds quite complex thermodynamics considerations to the problem, which we could not delve into within the frame of this thesis.

Experimentally, the relationship between the pump current and the active region temperature increase can be inferred from the wavelength shift of the emission spectrum with pump current [50], [133]. In particular, the data from reference [133] show a slightly superlinear relationship between the temperature increase and pump current ($\Delta T \propto I^{1.2}$). This is sensible considering Eq. (2.15) where the $V_{th}I$ term has a linear dependence on I and the $R_S I^2$ term adds a quadratic dependence on I. To compare the relative contributions of these two terms, let's take the example of the conventional vertical p-i-n laser presented in reference [128]: with $V_{th} = 1.4\ V$ and $R_S = 2.3\ \Omega$, the $V_{th}I$ term dominates over the $R_S I^2$ term for I < 610 mA, which should be compared with the 6 mA threshold. It is quite different for membrane lasers as the thin III-V layers induces larger series resistances. For instance, reference [31] reports $V_{th} = 0.97\ V$ and $R_S = 200\ \Omega$. In this particular case, the series resistance is notably high due to both the membrane design and the extremely short active length (50 µm) and the $V_{th}I$ term dominates up to 5 mA only, to compare with the 2.5 mA threshold.

As a first approximation, in this work, self-heating is implemented through a linear relationship between the temperature increment and the pump current with coefficients based on the measurements from references [133] or [50] depending on the device architecture and corrected for the device length.

To be fully extensive, we should also mention works such as those of A. Uskov [134] aiming at including Auger induced carrier heating in the model through an additional set of rate equations. However, as shown later in this chapter, we find that our model accurately represents the thermal behavior of quantum dot lasers without including this effect.

To conclude this subsection, it should be pointed that while the excitonic approximation is commonly used to simplify the simulation of the dynamics of QD lasers at fixed temperatures [110]–[112], [121], the study of their thermal behavior requires distinguishing between electrons and holes even in the absence of p-doping [117], [134], [135]. While the lasers dynamics is mostly governed by electrons, whose larger energy spacing leads to slower dynamics as compared to holes [121], the narrow energy spacing between the holes states, typically less than $k_B T$ at RT [124], makes them much more prone to thermalization and of main importance in

the thermal behavior of QD lasers. Fig. 2.4.a. presents light-intensity curves simulated using the complete model described here or using the excitonic approximation, showing that the excitonic model fails to represent rollover, as expected. Furthermore, Fig. 2.4.b. illustrates the evolution of the laser threshold current as the heat-sink temperature is increased: while for the excitonic model, temperature has a substantially limited influence on the threshold, the threshold increase with temperature observed in electron-hole simulations is in agreement with experimentally reported results [30], [69].

Numerical resolution of the rate equation model

Three numerical resolutions of the rate equation model detailed above are compared in Fig. 2.4 for an arbitrary example (vertical p-i-n type with L = 750 µm, W = 3.5 µm, $R_1 = 0.30$ and $R_2 = 0.99$).

The most extensive resolution uses a Traveling Wave Finite Difference Method (TW-FDM): the cavity length is sampled in several cells for which the rate equations (2.1)–(2.5) and (2.7) are solved to obtain the variations of carriers and photons densities per time step, including photons propagation from one cell to the next. A simplified resolution (FDM) suppresses spatial sampling by averaging out the densities of carriers and photons over the cavity length. In this case, the density of photons leaving the cavity through a mirror of reflectivity R_i is taken as $N_P ln\left(1/\sqrt{R_i}\right)$ to account for the longitudinal non-uniformity of the photons density in the cavity [29]. As shown in the simulated light-intensity curves of Fig. 2.4.a, the two methods exhibit identical results.

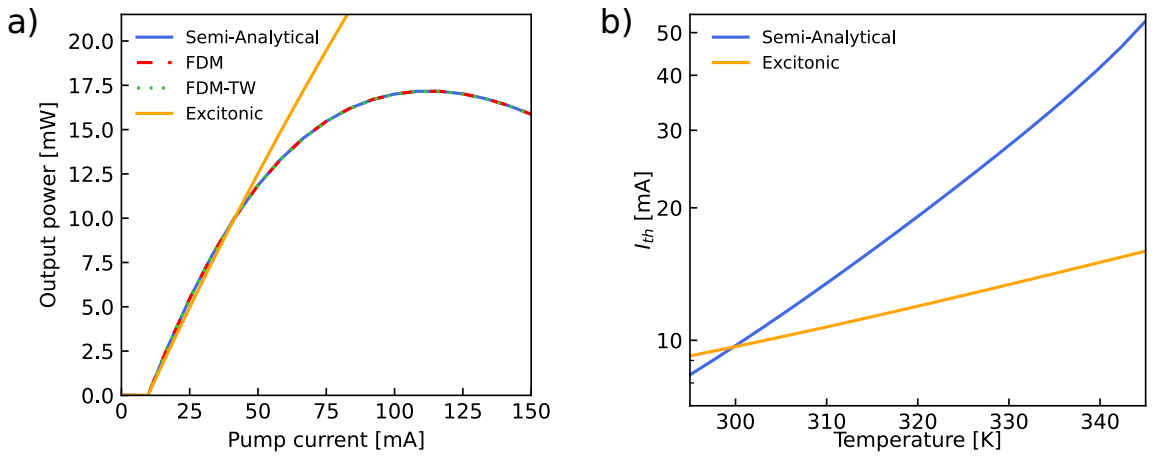

Figure 2.4: a) Comparison of the *semi-analytical* resolution, FDM resolution (with and without traveling wave) and excitonic model for the simulatio of L-I curves. The simulation time for the *semi-analytical*, FDM and TW-FDM resolution are respectively 0.04 s, 54 min and 1 h 41 min (using a 4.6 GHz CPU). b) Threshold current variation with temperature for the electron-hole model and excitonic approximation.

A third resolution is proposed here by considering the steady-state situation where the differential equations (2.1)–(2.5) can be simplified analytically. In this case, the left-hand term of the rate equations vanishes, giving a set of ten non-differential equations. Moreover, the

steady-state gain at or above threshold must equal the optical losses [29], which imposes:

$$\begin{aligned}\Gamma g &= \alpha_i + \alpha_m \\ &= \alpha_i + \frac{1}{L} ln\left(\frac{1}{\sqrt{R_1 R_2}}\right)\end{aligned} \tag{2.16}$$

Together, these constitute a set of eleven equations, which are solved numerically using a Levenberg–Marquardt algorithm [136] to obtain either I_{th} (considering N_P terms negligible at threshold [29]) or N_P for a given pump current. Solving the same equations, this *semi-analytical* simulation offers perfect agreement with the more extensive FDM as visible in Fig. 2.4.a. while being much more computationally efficient (computation time < 0.1 s compared to $\sim$ 1 hour for the FDM).

While this resolution is not able to assess the dynamics of QD lasers, it allows us to produce LI curves with excellent accuracy including thermal effects. Subsequently, all the results presented in the following pages will be obtained from *semi-analytical* simulations. This computation efficiency is of major importance for the simulation of devices as presented in the following sections, and in particular for the design optimization performed in section 2.3.

2.1.2. Assessment of the Model

In this section, the model is applied to lasers described in the literature to adjust a few fitting parameters and assess the model accuracy. Simulation results are analyzed with a focus to better understand the influence of temperature and p-doping on the distribution of free carriers, recombination, optical losses and subsequently, high-temperature operation.

Unintentionally doped lasers

RT transparency current I_{tr} and subthreshold gain measurements, as presented in [128], combined with temperature-dependent threshold measurements allow the determination of the Auger recombination rates (C_X^n, C_X^p), SRH time τ_{SRH} and material gain $g_{\max}$ as fitting parameters. The influence of these parameters can be decomposed as follows.

At transparency, the gain is null so the only channel of carrier loss is through spontaneous recombination (SRH, bimolecular and Auger), which allows for the determination of pairs of Auger-SRH recombination rates solution to the I_{tr} fitting. In addition, τ_{SRH} strongly affects the characteristic temperature T_0 (defined such that $1/T_0 = \partial \ln(I_{th}) / \partial T$ [30]) as increased temperatures lead to carrier excitation to higher energy states where SRH recombination takes place, increasing the threshold. This allows selecting the pair of Auger-SRH recombination rates solution to both I_{tr} and T_0 fitting.

To obtain $g_{\max}$, the subthreshold gain is fitted as [29]

$$g(I) = g_0 ln\left(I/I_{tr}\right) \tag{2.17}$$

where the g_0 coefficient has a direct connection with $g_{\max}$ (from Eq. (2.6)), which is adjusted accordingly.

The numerical parameters used in the simulations are summarized in Table 2.1 (page 29), including fitting values for $C_X^{n,p}$, $g_{\max}$ and τ_{SRH}.

Fig. 2.5 shows the simulated light-intensity (LI) curves of an $8 \times 1340\ \mu m^2$ QD laser with as-cleaved facets ($R = 0.30$) based on those fabricated and characterized in [128], with a confinement factor of 2 % (simulated using Lumerical MODE). The simulated threshold current and differential efficiency at 20 ℃ are 16 mA and 42 %, degraded to 45 mA and 25 % at 50 ℃, while the characteristic temperature in the 20 ℃ to 90 ℃ range is 30 K. We observe proper agreement with experimental reports from reference [128], confirming that our model accurately estimates the steady-state characteristics of QD lasers, both in terms of threshold, differential efficiency and their temperature dependence.

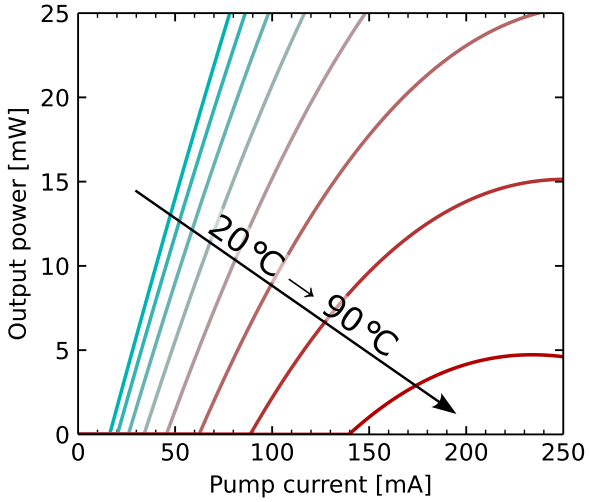

Figure 2.5: Light-intensity curves simulated for various heat-sink temperatures, for a $8 \times 1340\ \mu m^2$ device based on those described in [128]. The characteristic temperature describing the threshold current increase with temperature is 30 K.

Theoretical study of the influence of p-doping

The benchmark is further completed with the study of p-doping, which has not been extensively investigated within the frame of rate equations models so far in the literature. This study is performed through the analysis of the threshold current and its temperature dependence as p-doping is known from experimental works to increase the RT threshold for otherwise identical lasers and reduce their threshold current temperature sensitivity [30], [125], [137]. Fig. 2.6 shows the evolution of the simulated threshold with temperature for an unintentionally doped (UID) laser and lasers with p-doping levels corresponding to 10, 20 and 30 extra holes per dot, based on the devices presented in reference [30], which are identical to the device of Fig. 2.5 except for p-doping and length. Further increasing p-doping would lead to marginal gains on the temperature behavior and greatly reduced differential efficiencies due to IVBA. The simulated p-doped devices exhibit increased RT thresholds and characteristic temperatures, up to 380 K (resp. 120 K) for 30 (resp. 10) holes per dot compared to 48 K for the UID device, in agreement with experimental reports [30], [51], [137]. Such improved characteristic temperatures

allow the threshold current of p-doped lasers to become lower than that of UID laser at high temperatures, which is of major importance for applications where the lasers have to operate in harsh environments.

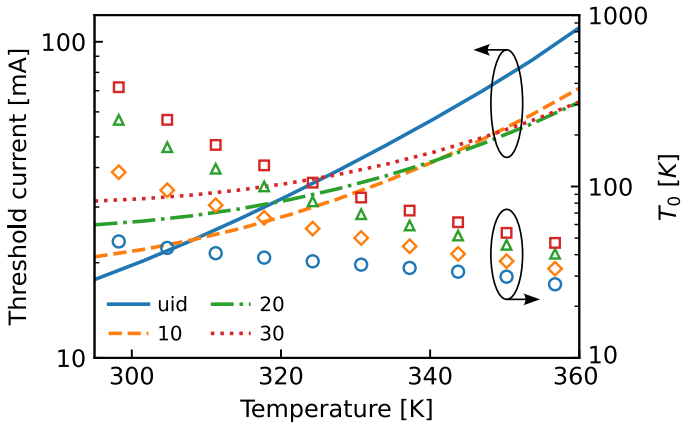

Figure 2.6: Simulated temperature dependence of the threshold currents and corresponding characteristic temperatures T_0 for UID and p-doped devices with doping levels corresponding to 10, 20 and 30 extra holes per dot. Devices are $8 \times 1500\ \mu m^2$ based on the architecture of [30].

To provide a deeper understanding of the physical phenomenon that affect the threshold current and its temperature dependence, the three contributions to the threshold current: radiative (I_{rad}) and Auger (I_{Aug}) recombination in the dots and radiative and SRH recombination in the reservoir — bi-QW and spacers — levels (I_{res}) are isolated for an UID and a p-doped laser as shown in Fig. 2.7.

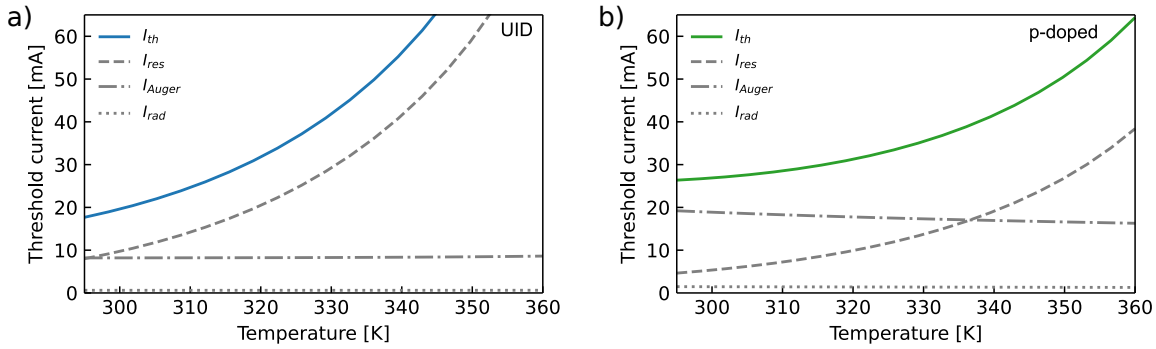

Figure 2.7: Temperature-dependence of the contributions to the threshold current I_{th} from reservoir (bi-QW and spacers) radiative and SRH recombination I_{res}, Auger recombination in the dots I_{Auger} and radiative recombination in the dots I_{rad} compared for the UID (a) and p-doped (20 holes per dot, b) devices of Fig. 2.6.

For the UID laser at RT, the relative weight of contributions from dots Auger and radiative recombination agree with those obtained from hydrostatic pressure measurements [126]. The first thing we want to highlight is how the RT Auger and dot radiative current increases with doping. Indeed, without p-doping, the hole states occupation probability is considerably low, hence hindering recombination, while with p-doping the increased hole occupation probability (see Fig. 2.8) drives up the Auger and radiative recombination rates.

We also observe from Fig. 2.7.b. a moderate decrease of the Auger recombination current as

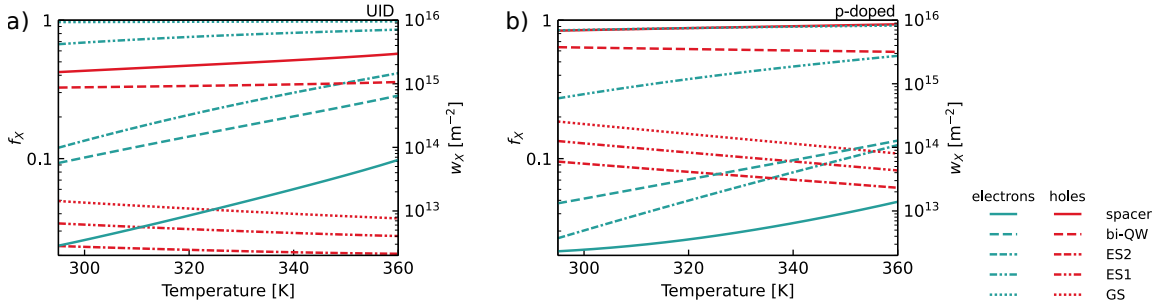

Figure 2.8: Temperature-dependence of the energy levels free-carriers population at threshold compared for the UID (a) and p-doped (20 holes per dot, b) devices of Fig. 2.6.

the temperature is increased for the p-doped laser. This behavior was assessed experimentally and proposed as an explanation for the high characteristic temperature of p-doped InAs QD lasers close to RT [125] and it is assumed to be caused by holes thermalization [138]. To better understand it the two different Auger processes should be considered separately, namely nnp recombination, where an electron and a hole recombine by transferring their energy to another electron (with a rate $C_n n^2 p$ where n and p are respectively the electron and hole densities in the dots) and npp recombination where the energy is transferred to another hole (rate $C_p n p^2$). These two processes exhibit particularly different temperature dependence as the thermalization of holes causes the rate of npp recombination — which depends quadratically on the population of holes — to drop above RT while the electron-dominated nnp term is much less temperature sensitive. However, it is experimentally challenging to distinguish between these two processes and in experiments aiming at estimating the Auger coefficient, the Auger rate is commonly simplified as Cn^3 [125], [127], losing the distinction between C_n and C_p. Experiments performed on 1.5 µm quantum well lasers found npp processes to be predominant in these materials [139] but to the best of our knowledge, no experimental works estimated the relative contribution of the two processes specifically for InAs QD, which led us to use $C_n = C_p$. Assuming the predominance of npp processes would strengthen the Auger recombination decrease with temperature and high RT characteristic temperature of p-doped lasers in our simulations.

The third contribution plotted in Fig. 2.7 corresponds to recombination in the bi-QW and spacers. In opposition to Auger and dots radiative recombination, these decrease with p-doping as the increased density of holes makes the population inversion condition ($f^e_{GS} + f^h_{GS} > 1$) easier to attain at a lower f^e_{GS} and thus a lower overall electron population while without p-doping, the easy thermalization of holes requires f^e_{GS} to be close to 1 which can only be attained through a high population of higher energy levels.

Finally, the evolution of IVBA with doping and temperature cannot be neglected. To the best of our knowledge, the importance of this effect was solely discussed by Shchekin and Deppe and Norman *et al.*, with a rather large range of reported RT optical losses values: between 3.9 cm^{-1} for 104 extra holes per dot (from 1.8 cm^{-1} for an UID device) that have been reported using cutback measurements [137], and up to 40 cm^{-1} using the mode-sum method for a device with 30 extra holes per dot [30]. Given that the optical losses are also linked to the differential quantum

efficiency through the relationship $\eta_d = \eta_i \, \alpha_m / (\alpha_i + \alpha_m)$ [29], the IVBA cross-section can be estimated by using the p-doping dependency of the differential quantum efficiency η_d shown in [30]. Together with η_i from Table 2.1, and calculating $\alpha_m = 760 \; m^{-1}$ with the relationship $\alpha_m = 1/L \times \ln\left(1/\sqrt{R_1 R_2}\right)$ [29] for the devices of Fig. 2.6, we obtain an IVBA cross-section of $\sigma_i = 1 \times 10^{-19} \; m^2$, and $\alpha_0 = 100 \; m^{-1}$. With these parameters the optical losses at threshold reach 15 cm^{-1} at RT for a device with 30 acceptors per dot, well in the range of the values of references [30], [137]. The losses decrease to 10 cm^{-1} at 85 °C due to holes thermalization to higher energy levels, as shown in Fig. 2.9, which is a more limited decrease than reported in reference [30], although it does help increasing the RT characteristic temperature of p-doped lasers to a given extent.

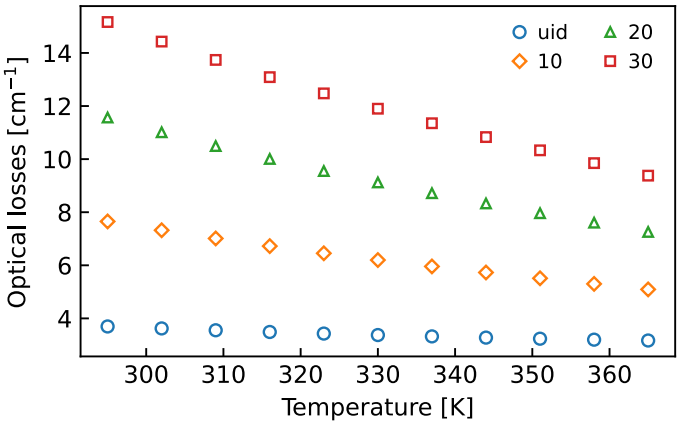

Figure 2.9: Simulated temperature dependence of the optical losses for UID and p-doped devices with doping levels corresponding to 10, 20 and 30 extra holes per dot. Devices are $8 \times 1500 \; \mu m^2$ based on the architecture of [30].

In conclusion, the extra holes added to p-doped lasers, in particular in the dot states, increase RT thresholds due to both increased Auger and spontaneous radiative recombination from dots states and increased losses due to IVBA. At RT, the GS electron population of p-doped devices is lower than for UID devices, for the same optical gain. This leaves room for replacing thermalized holes with new electrons to maintain a sufficient optical gain value as the temperature is increased, thanks to the electrons higher energy spacing and lower effective mass as compared to holes, which makes them less prone to thermalization. As the temperature is increased and the dots hole population is decreased, npp Auger recombination and IVBA decrease. The combination of these two effects reduces the p-doped lasers threshold temperature dependence and plays a role in the high reported T_0. Considering only one of the two effects does not seem sufficient to match experimentally reported characteristic temperatures.

At this stage, our model satisfyingly reproduces experimental data as shown in Fig. 2.6 where a moderate p-doping level (10 holes per dot) provides a satisfying tradeoff between RT and high-temperature performances. In section 2.3, we will apply this model to the study of InAs QD membrane lasers.

2.2. III-V Membrane Waveguides and Coupling with Standard SOI

As discussed in Chapter 1, while SOI is a material of choice for the realization of PIC, benefiting from the CMOS fabrication maturity, its indirect bandgap imposes the use of III-V materials as a gain medium. Laser cavities must then be designed with coupled III-V and SOI and in these works, we chose to use evanescent coupling which allows for low coupling losses and facilitates placing mirrors within the SOI.

Sections 2.2.1-2.2.2 reports on the design of the individual SOI and III-V waveguides before waveguides coupling and couplers design are detailed in section 2.2.3. For the sake of brevity, unless stated otherwise, we will only present the design of III-V waveguides and couplers for 1 µm-wide III-V waveguides, although the same design procedures were also used for wider III-V waveguides.

2.2.1. SOI Waveguides

SOI waveguides are not at the core of this thesis and are only briefly mentioned for the needs of the couplers design. SOI circuits part of MPW wafers processed on the 300 mm platform, benefiting from high-resolution immersion lithography and advanced processing tools.

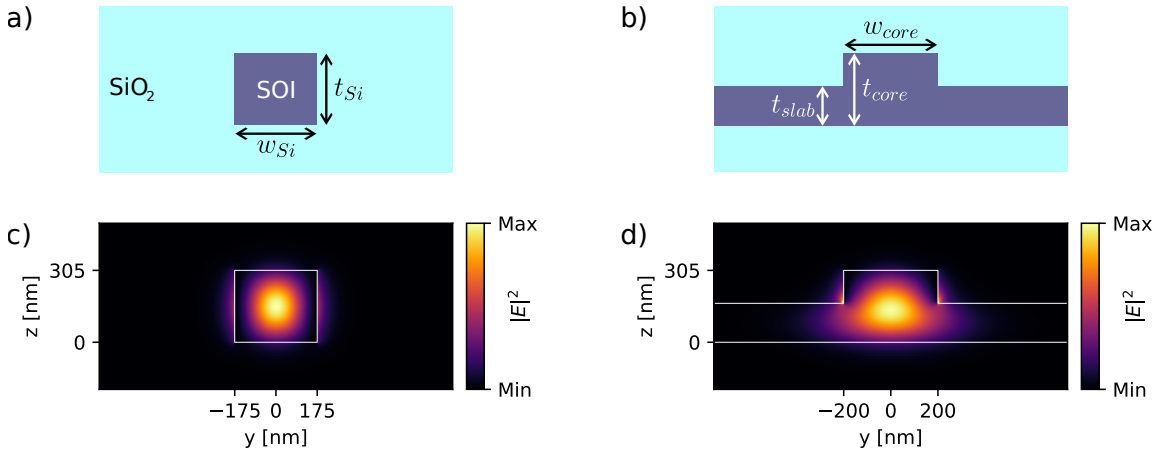

Figure 2.10: Cross-sectional schematic (a, b) and simulated intensity profiles (c, d) of the fundamental TE modes of a strip (a, c) and a rib (b, d) SOI waveguides.

Two types of waveguides are commonly used in silicon photonics, namely strip and rib waveguides. Strip waveguides (Fig. 2.10.a) take the form of a rectangular core of high index material (Si) embedded in a low index material (SiO_2). The high index contrast provides strong confinement, allowing short radius of curvature and remarkable compactness. However, the strong confinement also strengthens the interaction between the optical field and the sidewalls of the waveguide, which roughness caused by the etching process diffracts light and increases propagation losses. Rib waveguides (Fig. 2.10.b) offers a way to reduce the interaction between the optical field and rough sidewalls by only partially etching the SOI around the core to preserve an SOI slab, reducing the effective index contrast and, subsequently, the optical confinement in the horizontal direction. Thanks to the reduced optical confinement and sidewalls height,

propagation losses are reduced [140].

In designing SOI waveguides, their thickness is imposed by the design rules: at CEA-LETI, the SOI used is 305 nm-thick. This sets the thickness of strip waveguides and of the core of rib waveguides. In addition, the etching depth to form rib waveguides is 140 nm, giving a slab thickness of 165 nm. With these constraints, the number of supported modes and their effective indices can be controlled by varying the waveguide width as presented in Fig. 2.11, showing the simulated effective indices of the first TE and TM modes of SOI strip (a) and rib (b) waveguides as a function of the waveguides width. Practically, we exclusively work with the TE0 mode and want to keep the waveguide width low enough so it can only support the fundamental mode, or light could be coupled to higher order TE modes. Subsequently, the nominal width of the SOI waveguides is set to 350 nm. However, in certain cases — for instance in III-V to SOI couplers — it may be necessary to increase the waveguide width to reach larger effective indices, which makes the waveguide able to support higher-order TE modes. In this situation, care must be taken to only use straight waveguides, to avoid coupling light from the fundamental mode to higher-order mode [140].

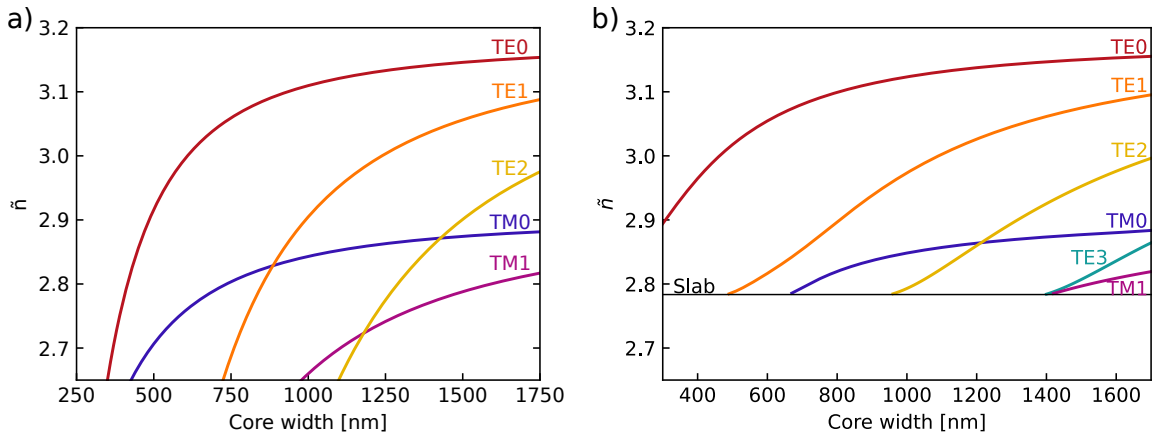

Figure 2.11: Simulated effective indices of the guided TE and TM modes of SOI strip (a) and rib (b) 305 nm-thick waveguides as a function of their width.

From Fig. 2.11, even for the widest 305 nm-thick SOI strip and rib waveguides, the effective index of the TE0 mode has an upper limit of about 3.16. For comparison, the effective index of the TE0 mode of a 2 µm-wide III-V waveguide made from a typical 300 nm-thick InAs DWELL stack clad in the vertical direction by $Al_{0.4}Ga_{0.6}As$ as presented in reference [128] is 3.27. This is why extra technological steps such as a local thickening of the SOI as presented in reference [105] are required to couple light from a conventional vertical p-i-n III-V structure to an SOI waveguide. In the following subsection, we present the design of active III-V waveguides that circumvent such needs.

2.2.2. Design of the III-V Membrane Waveguides

III-V membrane waveguides are represented schematically in Fig. 2.12. When the III-V membrane is reported on SiO_2 (Fig. 2.12.b–c) and capped with a low-index dielectric material (SiN or SiO_2),

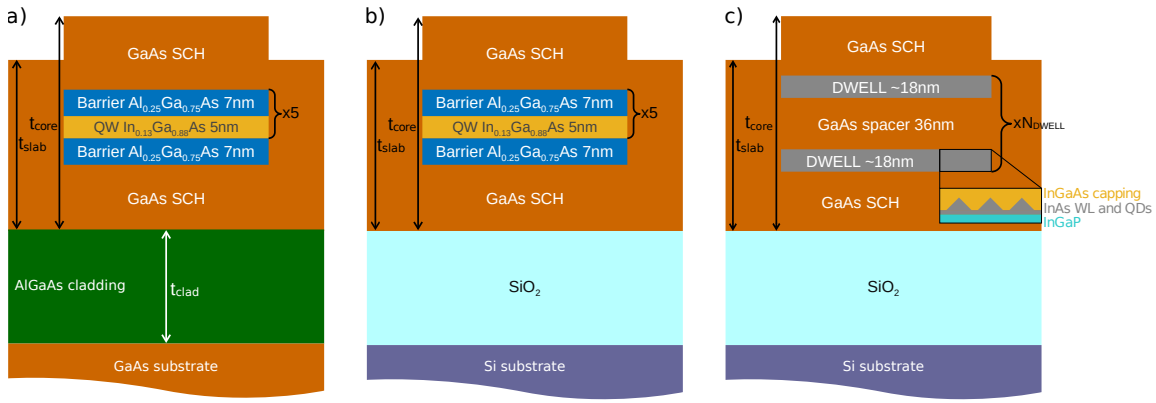

Figure 2.12: Schematic transverse cross-section (not to scale) of the III-V membrane waveguide and InGaAs/AlGaAs MQW stack for emisison at 920 nm on a GaAs substrate with AlGaAs cladding (a) and on a Si substrate with SiO_2 cladding (b), and InAs DWELL stack for emission at 1310 nm on SiO_2 on Si (c). The III-V membrane rib waveguide comprises a core which includes the active stack and a GaAs slab.

those provide a high index contrast and thus a strong confinement in the vertical direction. If the active stack is kept on a native III-V substrate (Fig. 2.12.a), a lower-index AlGaAs cladding is used to isolate it from the substrate. Meanwhile, optical confinement in the horizontal direction is obtained by shaping the III-V in a rib-like structure with the rib core being the active stack (with separate confinement heterostructure (SCH) layers) and the slab corresponding to the p and n-doped regions.

The designs of III-V waveguides presented in the following pages follow the progressive fabrication developments which will be presented later in Chapter 3: first, we designed waveguides comprising a MQW active stack for emission at 920 nm on a III-V substrate, next with the same active stack bonded on oxidized silicon. Then, waveguides based on an active stack comprising InAs DWELL for emission at 1310 nm were designed, anticipating for the coupling to an SOI waveguide.

III-V waveguides operating at 920 nm

The thickness of the III-V active stack of devices emitting at 920 nm (Fig. 2.12.a–b) is not constrained by coupling to the SOI. This gives us the flexibility to set the thickness as needed. In our case, we opted for a value of 400 nm, which is slightly thicker than what is typically used for membrane lasers [50] but offers greater leeway in terms of the actual thickness of the slab, which is challenging to control during fabrication.

With t_{core} being set to 400 nm, the next step is to determine the core-slab thickness difference required to achieve optical confinement in the horizontal direction. Fig. 2.13 shows the simulated optical confinement in the core (Γ_{core}) and $1/e$ radius of the optical mode electric field in the horizontal direction as a function of the core-slab thickness difference. These two metrics are connected but have a somehow different practical influence on the laser performance. While the optical confinement in the core determines the interaction between the optical field and the active medium, and thus influences the modal gain, the mode radius is linked to the field

interaction with the absorbing doped regions and also helps us determine the distance at which the electrodes should be placed from the active region.

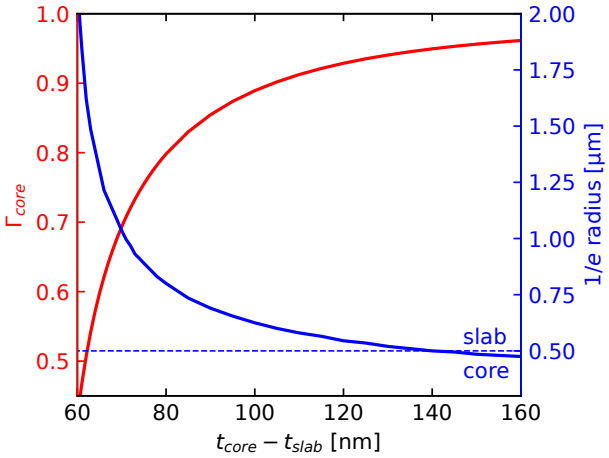

Figure 2.13: Simulated optical confinement in the core and electric field $1/e$ radius of the fundamental TE mode of the GaAs-based rib waveguides presented in Fig. 2.12.b. as a function of the core-slab thickness difference, simulated for a wavelength of 920 nm.

Fig. 2.13 indicates that a thickness difference of at least 60 nm is required to guide the TE0 mode in the III-V rib. The optical confinement rapidly increases for thickness differences of 60 nm to 100 nm and then slowly converges to a maximum value. However, care must be taken as the thickness difference is achieved by decreasing the thickness of the doped regions used for electrical pumping and dissipation of the heat away from the active region due to isolating silica being used as an underlying layer [50]. Thus, a tradeoff must be found between optical confinement and electrical and thermal conductivity. Our choice is to rely on a thickness difference of 130 nm, which provides strong optical confinement and gives us a safety margin of a few tens of nm if the experimental thickness difference is lower than planned. The substrate (GaAs with an AlGaAs cladding or Si with a SiO_2 cladding) has a clearly limited impact on the optical confinement in the horizontal direction so the same designs are used for both substrates.

SiO_2 is used as an underlying cladding and bonding layer when the III-V membrane is reported on silicon. Its thickness is set to 2 µm to be the same as the BOX thickness of 300 mm SOI wafers. Thanks to the large index contrast between the III-V and SiO_2 and the thickness of the oxide layer, the optical mode supported by the III-V membrane is completely isolated from the silicon substrate. However, in the situation of Fig. 2.12.a. with the device on a GaAs substrate, isolating the active waveguide from the GaAs substrate is more challenging. Benefiting from the matching lattice constants of GaAs and AlGaAs, and lower refractive index of AlGaAs (Fig. 1.8), an AlGaAs cladding can be epitaxially grown on the GaAs substrate before the epitaxial growth of the active stack to provide optical isolation. The propagation losses due to substrate leakage were simulated as a function of the AlGaAs cladding thickness for varying Al composition using a finite element method mode solver (Lumerical FEEM). The use of Lumerical FEEM rather than Lumerical MODE — our preferred mode solver for most of the other mode simulations

in this thesis — was motivated by benchmarking for this specific application with data from the literature for an SOI waveguide example [141], [142]. The results obtained with Lumerical FEEM showed better agreement with data from the literature and the losses dependence on the BOX thickness was also more consistent with literature reports. The results are shown in Fig. 2.14: losses decrease exponentially with increasing AlGaAs thickness while an increasing Al fraction in the cladding also strongly decreases losses owing to the increased index contrast. As an example, for a cladding thickness of 600 nm, the loss value simulated for $Al_{0.5}GaAs$, $Al_{0.6}GaAs$ and $Al_{0.9}GaAs$ are respectively 3.2 dB.cm^{-1}, 1.0 dB.cm^{-1} and 0.06 dB.cm^{-1}. With the MOCVD equipment used to perform the epitaxial growths of this thesis, it is difficult to grow layers thicker than 600 nm so we set the thickness of the AlGaAs cladding to this value and aim for the highest Al concentration. With the most aggressive parameters, an Al fraction of 0.6 is obtained, resulting in expected losses due to substrate leakage of 1.0 dB.cm^{-1}, which we consider is about the upper limit of what can be regarded as a reasonable value.

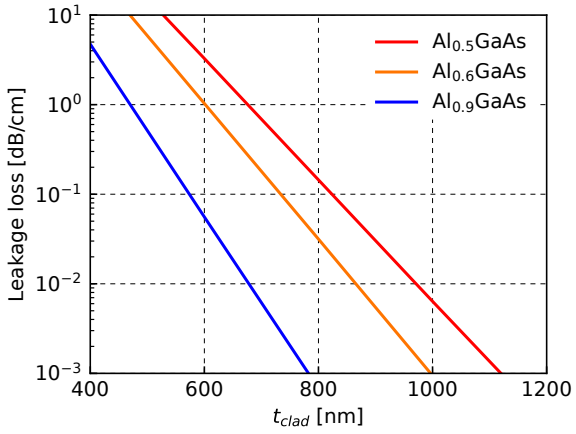

Figure 2.14: Simulated propagation losses due to substrate leakage of the TE0 mode of the structure of Fig. 2.12.a. as a function of the AlGaAs cladding thickness and composition, simulated using Lumerical FEEM.

III-V membrane waveguides for operation at 1310 nm

The following section focuses on the design of III-V membrane waveguides comprising InAs DWELL for emission at 1310 nm as illustrated in Fig. 2.12.c. Thanks to the high index contrast between the III-V and oxide, the membrane is optically fully isolated from the substrate.

As these devices are intended to be coupled to SOI, the thickness of the III-V membrane is chosen to allow mode transfer to the SOI without tapering of the III-V or thickening of the SOI. This is achieved when the III-V waveguide mode has a lower effective index than the SOI waveguide mode (we are still working with TE0 modes), as it will be detailed in section 2.2.3. Fig. 2.15 presents the simulated effective index of the slab mode of a III-V membrane (stack of Fig. 2.12.c, core) as a function of the membrane thickness. For comparison, the range of effective indices covered by the TE0 mode of the SOI strip waveguide for an SOI waveguide width lesser than or equal to 1500 nm is represented by the hatched domain. For a 1500 nm-wide strip SOI waveguide, the condition that the effective index of the III-V slab mode is lower than the

effective index of the SOI waveguide mode imposes a maximum III-V membrane thickness of 360 nm. However, to ensure the most complete transfer of the optical field from the III-V to SOI waveguide it is beneficial to have a larger mismatch of effective indices. Therefore, we decided to work with a III-V membrane thickness of 310 nm, providing an effective index difference of 0.06.

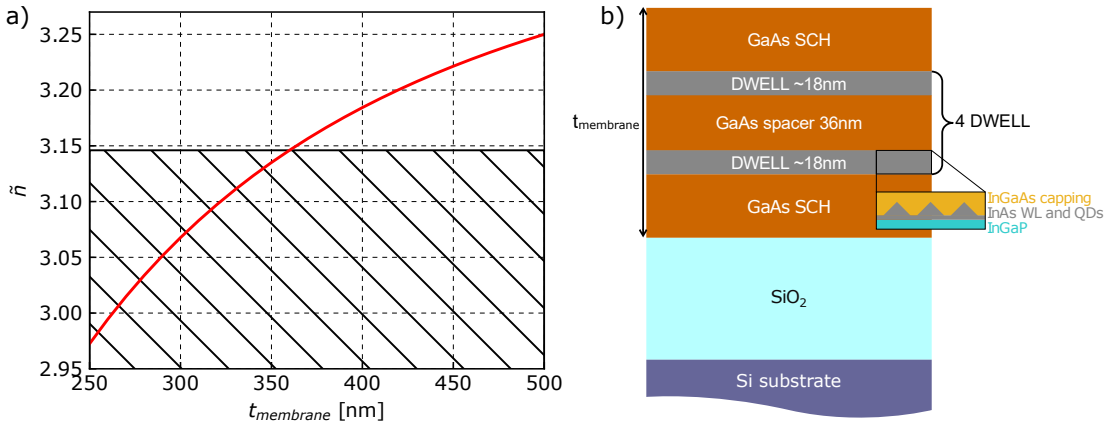

Figure 2.15: a) Simulated effective index $\tilde{n}$ of the slab mode of the III-V membrane (DWELL stack (b)) as a function of the membrane thickness $t_{membrane}$. The hatched domain corresponds to effective indices attainable for the TE0 mode of an SOI strip waveguide as presented in Fig. 2.11 with a width lesser than or equal to 1500 nm.

Optical confinement is achieved through patterning of the III-V in a rib structure, as for the structures presented in the previous section. Fig. 2.16 illustrates the cross-sectional electric field of the III-V rib waveguides TE0 modes for various core-slab thickness differences in the form of intensity maps (c–e) or electric field profile at a given z-position (b). Compared with the InGaAs MQW stack, the thickness difference required to have a guided mode is much lower, down to 10 nm (although the corresponding mode is weakly localized). This is mainly due to the AlGaAs barriers present in the MQW stack that decrease the effective index of the guided mode — and thus require a thinner slab to have a guided mode — but are absent from the DWELL stack.

To provide a more quantitative analysis, similar to Fig. 2.13, Fig. 2.17 displays the corresponding optical confinement factor in the rib core and the $1/e$ radius of the electric field in the y direction as a function of the core-slab thickness difference for the InAs DWELL stack. For this configuration, we opted for a core-slab thickness difference of 50 nm, corresponding to a region of larger derivative of the optical confinement and mode radius as compared to the solution chosen for the InGaAs MQW stack. This means the confinement could have been higher, mode radius lower and fabrication tolerance on the slab thickness improved, however this choice offers a tradeoff for a sufficient electrical and thermal conductance of the doped regions, motivated by the lower III-V membrane thickness.

An alternative solution that we proposed in reference [143] is the use of AlGaAs instead of GaAs to realize the n and p-doped regions. Thanks to its lower index as compared to GaAs, the use of AlGaAs allows the existence of guided modes with a reduced or even null thickness difference between the waveguide core and doped regions. In addition, the larger bandgap of AlGaAs compared to GaAs would prevent the leakage of electrons to the p-doped region which

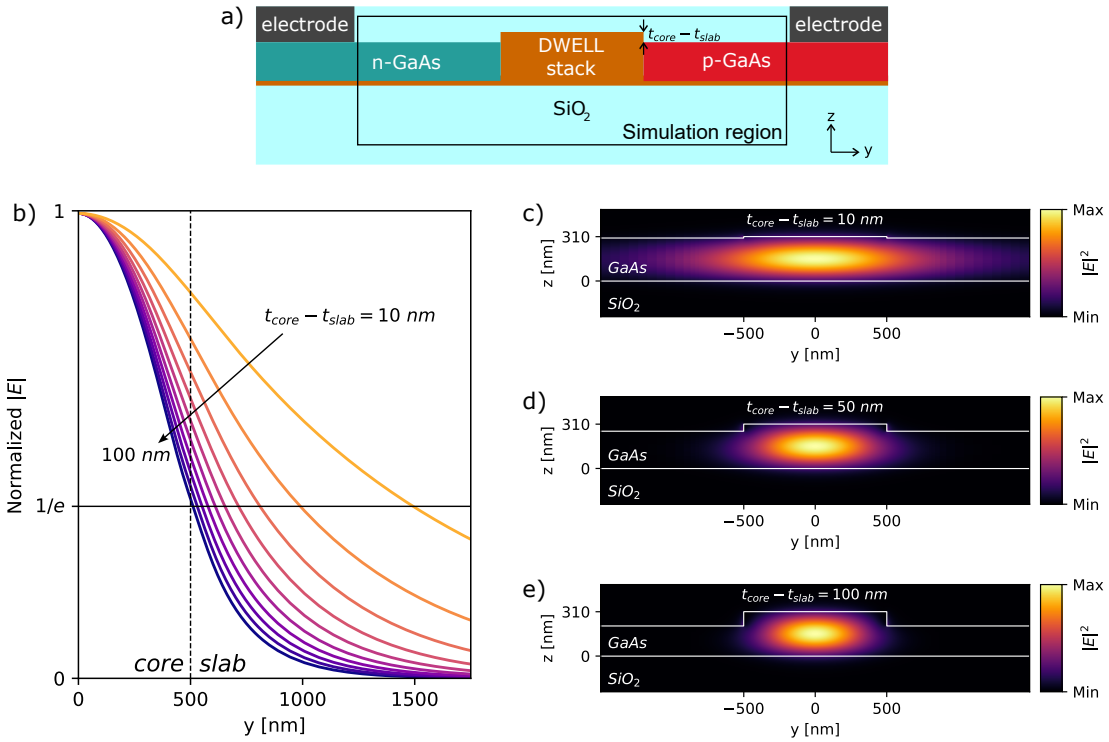

Figure 2.16: Cross-sectional simulation of the TE0 mode of GaAs rib waveguides simulated at 1310 nm. (a) Cross-sectional schematic of the DWELL membrane laser highlighting the simulated structure. (b) Horizontal line electric field profile for core-slab thickness differences ranging from 10 nm to 100 nm by steps of 10 nm. (c-e) Cross-sectionnal intensity profile for core-slab steps of 10 nm (c), 50 nm (d) and 100 nm (e).

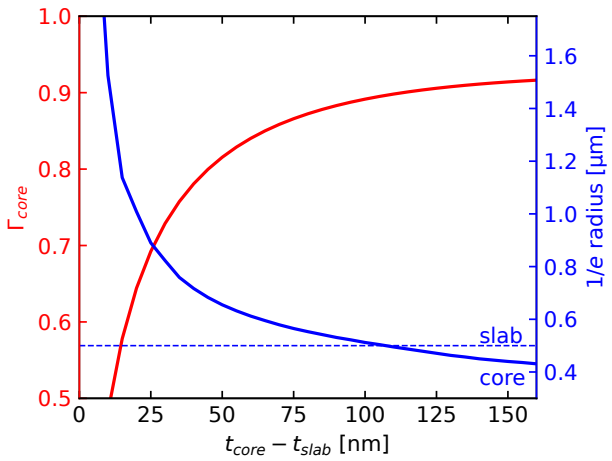

Figure 2.17: Confinement in the core and electric field $1/e$ radius of the fundamental TE modes of GaAs rib waveguides at 1310 nm, as a function of the core-slab thickness difference.

may happen otherwise. From Sargent's rule of thumb of a $4k_BT$ barrier height ΔE_g required to prevent leakage [106], 100 meV (resp. 140 meV) are required at RT (resp. 125 °C), achieved with an Al composition x = 0.06 (resp. 0.09) [61]. This is an extra safety measure regarding the GaAs-AlGaAs junction, but the carriers captured by the DWELL are already more strongly confined. The confinement in the III-V rib core and $1/e$ radius of the electric field simulated as a function of the core-slab thickness difference and for various AlGaAs compositions are shown in Fig. 2.18. The resulting values obtained for a null thickness difference and Al compositions of 0.10, 0.22, 0.34 and 0.41 match those obtained for GaAs doped regions with a thickness difference of respectively 25 nm, 56 nm, 77 nm and 87 nm.

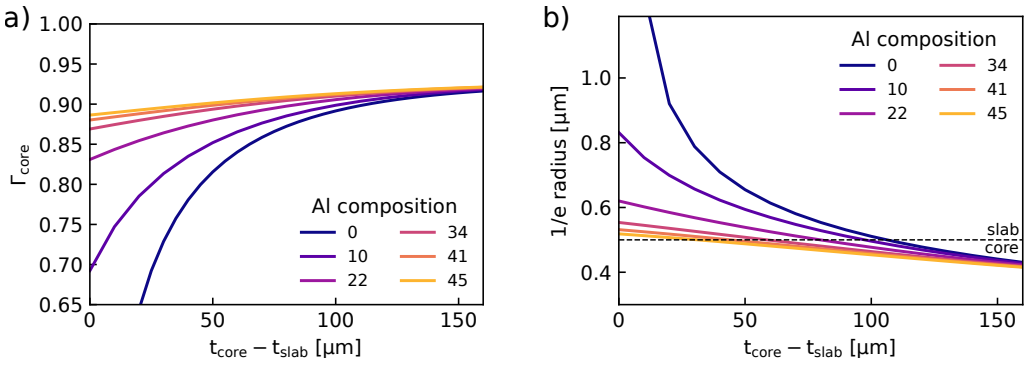

Figure 2.18: Confinement in the core and electric field $1/e$ radius of the fundamental TE modes of III-V rib waveguides composed of a GaAs core and an AlGaAs slab at a wavelength of 1310 nm, as a function of the core-slab thickness difference and for Al compositions ranging from 0% (GaAs) to 45% ($Al_{0.45}Ga_{0.55}As$). AlGaAs refractive indices are taken from [103].

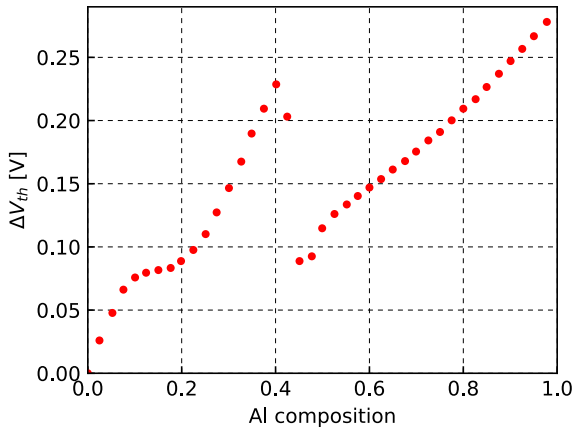

Figure 2.19: Increase in the diode threshold current with Al composition of the doped regions, simulated with Silvaco.

However, a tradeoff must again be sought as there are some drawbacks to an excessive increase of the Al composition. Due to Fermi levels alignment, an heterobarrier appears at the intrinsic GaAs - doped AlGaAs heterojunction [44], resulting in an increase of the diode threshold current as the Al composition is increased, as shown from Silvaco simulations displayed in Fig. 2.19. In addition, increasing the Al composition from pure GaAs leads to decreased carriers mobilities and thus increased diode series resistance due to carrier scattering for both electrons

and holes. The mobility of electrons drops even more sharply from x = 0.3 to x = 0.45 due to the $\Gamma - X$ crossover [61], [144], [145]. The thermal conductivity of AlGaAs also decreases as the Al ratio is increased up to 0.5 [61] which would worsen self-heating. Subsequently, an Al composition of 0.15 to 0.20 is a satisfying tradeoff for optical confinement and satisfying electrical and thermal properties. Due to the extra fabrication complexity caused by the use of AlGaAs — in particular due to residual carbon doping induced by the introduction of Al precursors in our epitaxies — this solution was not tested experimentally within the frame of this thesis.

2.2.3. Design of III-V/SOI Optical Couplers

This section begins with an introduction to the basics of the coupled modes theory applied two coupled waveguides using the formalism developed by A. Yariv [146] and a design criterion for adiabatic coupling between waveguides. Next, this criterion is applied to the design of III-V membrane to SOI couplers.

Coupled-mode theory and an adiabatic coupler

The coupled modes theory is introduced for two coupled waveguides a and b with light propagating in the x direction as illustrated in Fig. 2.20. Considered individually, the two waveguides support optical modes with

$$\boldsymbol{E_a}(x,y,z,t) = A\exp\left[i\left(\omega t - \beta_a x\right)\right]\boldsymbol{e_a}(x,y,z) \tag{2.18}$$

$$\boldsymbol{E_b}(x,y,z,t) = B\exp\left[i\left(\omega t - \beta_b x\right)\right]\boldsymbol{e_b}(x,y,z) \tag{2.19}$$

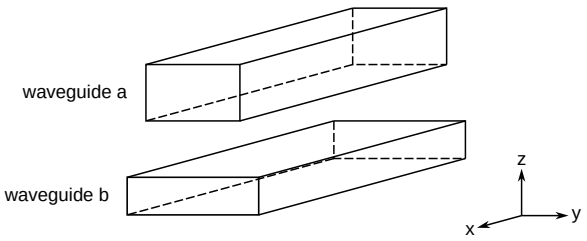

Figure 2.20: Schematic of two coupled waveguides.

Now considering the system constituted of the two coupled waveguides, the optical field may be expressed as a linear combination of two hybrid supermodes and their accumulated phases. The even ($\boldsymbol{e_e}$) and odd ($\boldsymbol{e_o}$) supermodes are written as column vectors which two components correspond to the field in the modes of the individual waveguides a and b [147]:

$$\boldsymbol{e_e}(x) = \frac{1}{\sqrt{2}}\begin{bmatrix}\sqrt{1-\delta/S}\\ \sqrt{1+\delta/S}\end{bmatrix}\exp\left(-i\beta_e x\right) \tag{2.20}$$

$$\boldsymbol{e_o}(x) = \frac{1}{\sqrt{2}} \begin{bmatrix} -\sqrt{1+\delta/S} \\ \sqrt{1-\delta/S} \end{bmatrix} \exp\left(-i\beta_o x\right) \tag{2.21}$$

where $S = \sqrt{\delta^2 + \kappa^2} = (\beta_e - \beta_o)/2$ is the half-difference of propagation constant between the even and odd supermodes with $\delta = (\beta_b - \beta_a)/2$ the mismatch of propagation constant between the modes of the individual waveguides and κ the coupling coefficient between the two waveguides. κ can be decomposed in the form of two coupling coefficients describing respectively coupling from waveguide b to waveguide a (κ_{ab}) and from waveguide a to waveguide b (κ_{ba}) such that [29], [147]

$$\frac{dE_a}{dx} = -i\beta_a E_a - i\kappa_{ab} E_b \tag{2.22}$$

$$\frac{dE_b}{dx} = -i\beta_b E_b - i\kappa_{ba} E_a \tag{2.23}$$

The coupling coefficient κ_{ab} is linked to the interaction between the field of waveguide a and b in waveguide a and is calculated as [29], [65], [148], [149]

$$\kappa_{ab} = \frac{k_0^2}{2\beta_b} \frac{\iint_{WG_a} \left(n^2(y,z) - n_{bg}^2\right) \boldsymbol{e_a^*} \cdot \boldsymbol{e_b}\, dydz}{\iint_{space} \boldsymbol{e_b^*} \cdot \boldsymbol{e_b}\, dydz} \tag{2.24}$$

where $k_0 = 2\pi/\lambda_0$ is the wave vector in vacuum, $n(y,z)$ and n_{bg} are respectively the local and background refractive indices and $\iint_{WG_a} \ldots dydz$ denotes the integral over a y-z cross section of waveguide a. The same applies for κ_{ba} by interverting a and b indices. Subsequently, κ is defined as their average value [29], [150]:

$$\kappa = \sqrt{\kappa_{ab}\kappa_{ba}} \tag{2.25}$$

From this point, it can already be seen from Eqs. 2.22-2.23 that there exist a beats phenomenon with periodic transfer of light from waveguide a to b and back. For two identical (or phase matched) waveguides, complete power transfer from one waveguide to the other is achieved after a length L_c known as the coupling length [29]:

$$L_c = \frac{\pi}{2\kappa} \tag{2.26}$$

This phenomenon is illustrated in Fig. 2.21 for a 1 µm-wide III-V waveguide with InAs DWELL and a 730 nm-wide SOI strip waveguide as defined in the previous sections, separated by a 200 nm-thick oxide layer. For this configuration, the coupling coefficient is 540 cm^{-1} (see more details in the next section), resulting in a coupling length of 29 µm.

Although this codirectional coupling phenomenon can be used to realize couplers, referred to as directional couplers (DC), for instance by ending the III-V waveguide at the position

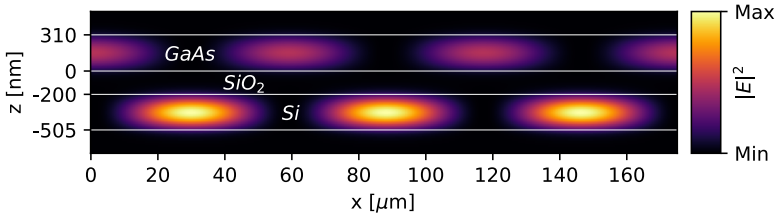

Figure 2.21: Vertical plane longitudinal cross-section of the electric field in a system composed of a 310 nm-thick, 1 μm-wide rib-like III-V waveguide and a 730 nm-wide SOI waveguide (matching propagation constants) as defined in sections 2.2.1-2.2.2 illustrating the phenomeneon of codirectional coupling.

x = 29 µm in the example of Fig. 2.21, such a coupler is difficult to realize practically. Indeed, the requirements on lithographic precision to stop the III-V waveguide accurately at L_c and on the experimental value of κ, which must be precisely known for proper determination of L_c, strongly decrease the tolerance of these couplers to fabrication defects [151].

Following on the coupled mode theory, Sun *et al.* proposed a new design of more tolerant couplers with the goal of transforming the supermodes from being completely localized in one waveguide to being completely localized in the other waveguide while minimizing transfer to the other supermode. Writing ε the fraction of power allowed to be transferred to the unwanted supermode, the shortest coupler matching this condition according to this new design has a length

$$L = \frac{1}{\kappa\sqrt{\varepsilon}} \tag{2.27}$$

and its shape is determined by the criterion

$$\frac{d\gamma}{dx} = 2\kappa\sqrt{\varepsilon}\left(1+\gamma^2\right)^{3/2} \tag{2.28}$$

where $\gamma = \delta/\kappa$ [147].

The solution to the differential equation 2.28 is

$$\gamma = \tan\left[\arcsin\left(u\right)\right] \tag{2.29}$$

with $u = 2\sqrt{\varepsilon}\kappa\left(x - x_0\right)$ if κ can be considered constant along propagation, or $u = 2\sqrt{\varepsilon}\int_{x_0}^{x}\kappa\left(x'\right)dx'$ if it cannot, where x_0 corresponds to the point of matching propagation constants ($\beta_a = \beta_b$).

Application of the adiabaticity criterion to the III-V membrane / SOI system

The following pages are dedicated to the design of III-V/SOI couplers according to the criterion of Sun *et al.* presented just above (Eq. (2.29)). The III-V and SOI waveguides are as described in sections 2.2.1-2.2.2, more specifically a strip SOI waveguide and a III-V waveguide with InAs DWELL (Fig. 2.12.c). This system is presented schematically in Fig. 2.22, showing the two design parameters to work with: t_{ox}, the thickness of the oxide layer separating the two waveguides, and w_{Si}, the width of the SOI waveguide. The value of t_{ox} is fixed by design and is a constant across the full wafer while w_{Si} is defined by lithography and is a variable along propagation.

Our objective is to keep the III-V waveguide width constant over the whole device length to relax constraints on its lithographic definition. Indeed, while the SOI is processed on a 300 mm platform, with access to high-resolution immersion lithography, the III-V is processed on a 100 mm platform without access to this tool. In addition, we will focus on the even supermode with light in the III-V at $x = 0$. Again, for the sake of brevity, designs for 1 µm-wide III-V waveguides only are detailed, but the same procedure applies to other widths.

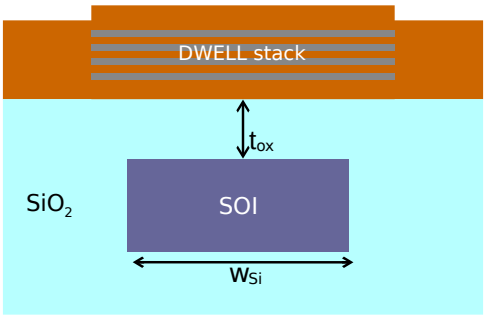

Figure 2.22: Schematic transverse cross-section of the coupled III-V (as defined in section 2.2.2 with an InAs DWELL stack) and SOI waveguides. The III-V waveguide is fixed while the Si waveguide width is a propagation variable .

Using Eq. (2.29) with our system requires knowing the relationship between δ, i.e. $\tilde{n}_{Si}$, and w_{Si}, which we already have from Fig. 2.11, and the relationship between κ and t_{ox}, w_{Si}.

The coupling parameter κ is calculated from Eqs. 2.24-2.25 with the propagation constants and fields of the individual waveguides modes simulated using Lumerical MODE. Fig. 2.23 shows how the coupling coefficient decreases exponentially as the separation between the two waveguides is increased, from 3570 cm^{-1} for t_{ox} = 50 nm, to 540 cm^{-1} at 200 nm and 145 cm^{-1} at 300 nm.

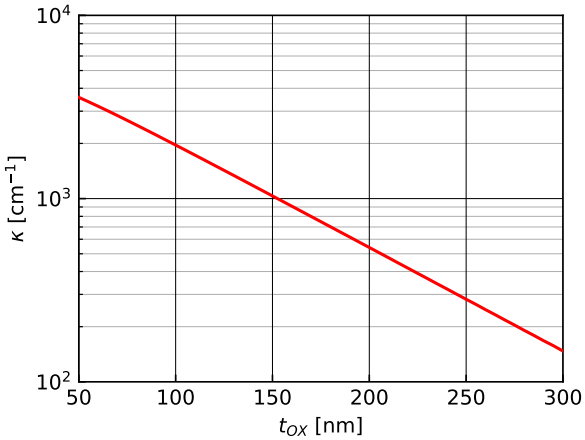

Figure 2.23: Coupling strength κ as a function of the thickness of the oxide layer separating the SOI and III-V waveguides t_{ox}, calculated for a 730 nm wide SOI strip waveguide and a 1 μm wide III-V core (index matching).

The influence of the SOI waveguide width on the coupling coefficient, shown in Fig. 2.24 for t_{ox} = 200 nm, is much different. Although $\kappa_{Si/IIIV}$ and $\kappa_{IIIV/Si}$ strongly depend on w_{Si}, their averaged value κ exhibits a limited variation with values ranging between 540 cm^{-1} and 615 cm^{-1} for $w_{Si} \in$ 400–2000 nm. Sun and Yariv also reported that κ remains almost constant

as the waveguide width is varied, provided that the separation between the two waveguides remains the same [150].

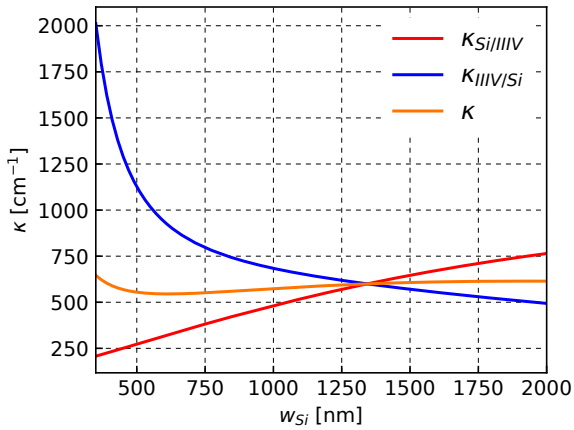

Figure 2.24: Coupling strength κ as a function of the width of the SOI waveguide w_{Si} calculated for t_{ox} = 200 nm using Eqs. 2.24 and 2.25.

The dependence of the coupling coefficients on the waveguides separation and width both agree with the trends reported in reference [152].

Having expressed the dependence of δ and κ on the design parameters, we may now proceed to designing the couplers. We will first set the waveguides spacing and then determine the optimum SOI taper profile and length.

The waveguides spacing t_{ox} (and subsequently κ) influences the coupler performances in two ways. From Eq. (2.27), the lower the coupling coefficient, the longer the coupler needs to be in order to maintain a given ε value, or stated differently: for a given coupler length, the lower the coupling coefficient, the larger the fraction of power coupled to the unwanted mode. Accordingly, reducing the waveguides spacing to minimize the coupler length and fraction of power transferred to the unwanted mode seems appealing. However, the coupler must also achieve the most complete transfer of the optical field to the SOI waveguide which, from Eq. (2.20), is achieved when $\delta/S \to 1$. The normalized fraction of the even supermode intensity supported by the SOI and III-V waveguides modes, $(1 \pm \delta/S)/2$, is plotted in Fig. 2.25 as a function of the SOI waveguide width for various waveguides spacings. While for weakly coupled waveguides (t_{ox} = 200-250 nm), increasing the SOI waveguide width from 500 nm to 1250 nm results in an almost complete transfer of the optical intensity from the III-V waveguide to the SOI waveguide, a complete transfer cannot be achieved for the more strongly coupled waveguides. For instance, for a 50 nm waveguides separation, the power splitting ratio between the two waveguides converges to approximately 80:20 as the SOI waveguide width is increased.

Subsequently, the waveguides separation is set to 200 nm, its lowest value allowing a complete transfer from one waveguide to the other. The width of the SOI waveguide at the input of the coupler is set to 585 nm in order to maximize the fraction of optical power localized in the III-V and thus the modal gain, and to 2000 nm at the output of the coupler. The simulated optical field in the coupled-waveguides system is shown in Fig. 2.26 at the input, phase-matching and

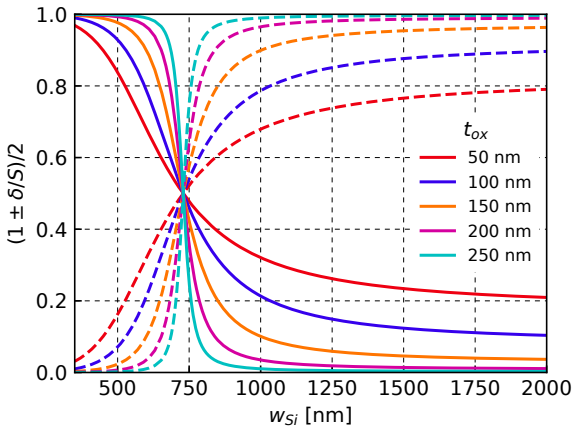

Figure 2.25: Squared modulus of the two components of the e_e vector as a function of the SOI waveguide width, for several t_{ox} values. The solid line represents the first component ($(1 - \delta/S)/2$), corresponding to intensity in the III-V waveguide mode while the dashed line represents the second component ($(1 + \delta/S)/2$), corresponding to the intensity in the SOI waveguide mode.

output positions. With further experience on this topic, I would now recommend a smaller output width considering that 1250 nm would be sufficient for a complete transfer of the optical field to the SOI waveguide, while also mitigating other issues which will be discussed in the next paragraphs.

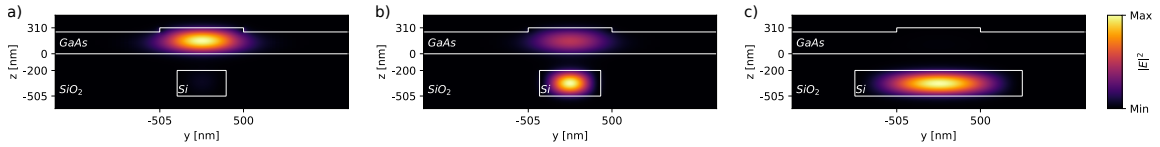

Figure 2.26: Cross-sectionnal III-V/SOI coupler hybrid mode for a III-V rib waveguide with a core width of 1 μm and an SOI strip waveguide width of a) 585 nm, b) 730 nm (matching propagation constants) and c) 2000 nm.

Finally, III-V/SOI couplers were designed according to Eq. (2.29) and with the parameters detailed above. Fig. 2.27 shows the resulting couplers profiles (Si waveguide width as a function of the propagation distance) and transmission simulated using the eigenmode expansion (EME) solver of Lumerical MODE [153]. The accuracy of the EME simulations was benchmarked over FDTD simulations for a set of points, exhibiting satisfying agreement while being much more computationally efficient (both in terms of simulation time and RAM requirements).

Based on both the coupler profile and simulated transmission, it seems correct to consider the coupling coefficient as independent on the SOI waveguide width as the difference in coupler profile is imperceptible. However, we found that the coupler profile calculated from the coupling coefficient obtained from Eqs. 2.24-2.25 resulted in a transmission converging to about 87% for long couplers, while by replacing κ by an arbitrary larger value in Eq. (2.29), the transmission peaked to almost 100%. This can be attributed to the sudden widening of the waveguide obtained with $\kappa = 540$ cm^{-1}. Simulating the transmission along propagation for a 100 µm-long coupler with this profile, we found that the propagation dropped by 10% in the last micron. This could have been mitigated by setting the output coupler width to 1250 nm as it allows

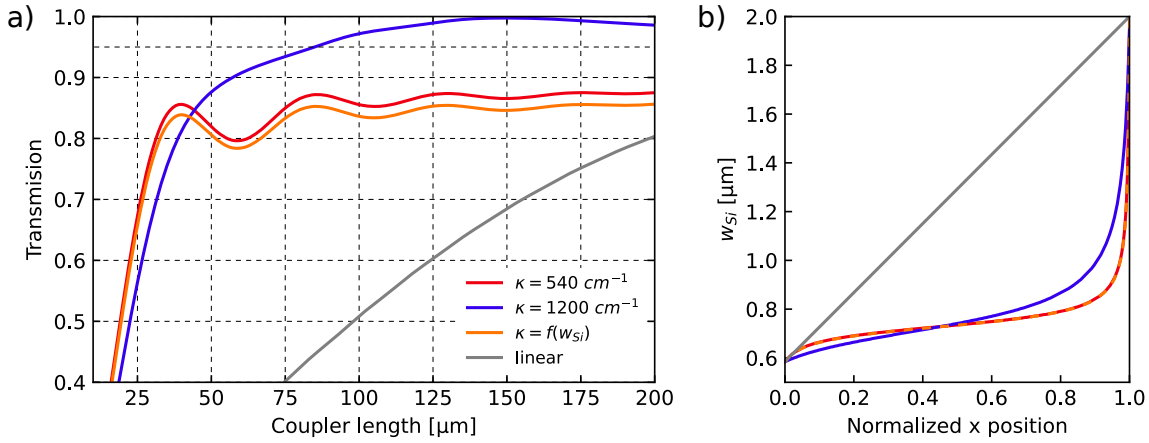

Figure 2.27: Simulation of III-V/SOI couplers. a) coupler transmission simulated (at 1310 nm) as a function of its length for a coupler shape calculated using the adiabacity criterion from [147] approximating κ as a constant with value 540 m^{-1}, an exagerated value 1200 m^{-1} or the Si-width dependent κ calculated from Eqs. 2.24-2.25. b) corresponding Si waveguides profiles.

complete transfer of the optical field to the SOI waveguide, as stated before, while eliminating the abrupt widening of the waveguide at the coupler end. In practice, we found that overestimating the coupling coefficient in Eq. (2.29) resulted in a smoother widening of the waveguide and higher transmission, and designed the couplers accordingly. The coupler length was taken as the shortest value allowing a transmission of more than 97%. Finally, the III-V facet at the coupler extremity is etched with a 7° angle to reduce unwanted reflections as it was done in reference [154] for instance.

2.3. Modeling of Membrane Lasers on Silicon

In this section, the model of section 2.1 is used to assess the potential of InAs QD membrane lasers as a solution for low threshold lasers able to operate at high-temperatures. This section is taken from our article [108], with minor adaptations.

The modeled device is represented in Fig. 2.28.a. It consists of a III-V membrane comprising InAs DWELL, as described in section 2.2.2. For this initial assessment, we do not consider coupling with an SOI waveguide nor the use of integrated mirror yet. Those will be studied in section 2.4 and could further improve the lasers performance. The mirrors reflectivities are set to 30 % for the front-mirror, which corresponds to an as-cleaved GaAs/air interface and the back-mirror reflectivity is set to 95 %, which could be obtained using a HR treatment. The fundamental optical mode supported by this structure is shown in Fig. 2.28.b. for a 1 µm wide active region comprising four DWELL layers. The corresponding confinement factor in the dots is $\Gamma = 1.6\ \%$.

Thanks to its computation efficiency, the *semi-analytical* model is used to optimize the device architecture. The results of parametric studies focusing on the role of the active region length, width and number of DWELL layers are depicted in Fig. 2.29. The figures of merit considered are the threshold current and differential efficiency η_d, which are directly related to the laser energy

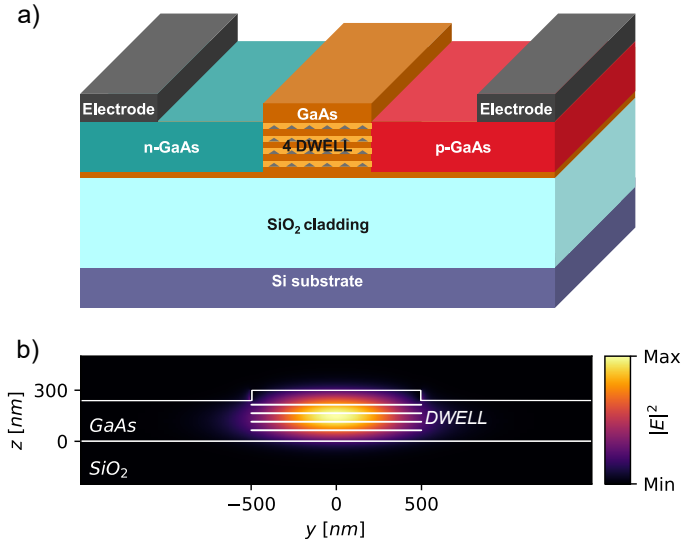

Figure 2.28: Membrane QD laser a) Schematic illustration of an InAs QD membrane laser on SiO_2 on Si b) Simulated cross-section profile of the fundamental TE mode

efficiency. In order for the device optimization to be a tradeoff for both RT and high-temperature conditions, the simulations were performed for heat-sink temperatures of 25 ℃ and 100 ℃.

Increasing the active region length also increases the active volume, thus requiring more carriers to reach population inversion, which results in increased recombination rates. It also increases the round-trip propagation and IVBA losses and thus decreases the differential efficiency. On the other hand, it reduces mirror losses per length unit and increases the maximum round-trip gain. This results in an optimum length to provide enough round trip gain while keeping a limited active volume and moderate round trip losses. P-doping and temperature both influence this optimum length: at RT, the increased recombination rates and IVBA of p-doped lasers result in larger thresholds than for UID lasers at lengths above 550 µm, as discussed in the previous section. However, as the peak gain is increased for moderate doping levels [155], [156], p-doped lasers can be made shorter, eventually reducing the threshold current and increasing the differential efficiency. Thus, for short lasers, the benefits of p-doping are reinforced. As the temperature is increased the escape of carriers to higher energy levels, in particular that of holes, reduces the gain, subsequently requiring longer lasers to keep lasing ability and achieve optimal performances. A length of 300 µm appears as a good tradeoff for best threshold and differential efficiency at RT and high temperature.

Similarly, increasing the active region width increases the active volume with the same consequences as for the length in terms of the number of carriers required to achieve population inversion and subsequent recombination rates. It also increases the mode cross-sectional area and influences the optical mode confinement factor within the active region. This data is simulated using Lumerical MODE: for the narrowest active regions (less than 500 nm), a large fraction of the mode does not overlap with the active region and the confinement factor is reduced, hence reducing the modal gain for a given $f_{GS}^{e,h}$ population and dramatically increasing the threshold current as high populations are required to for the gain to match the losses. Because

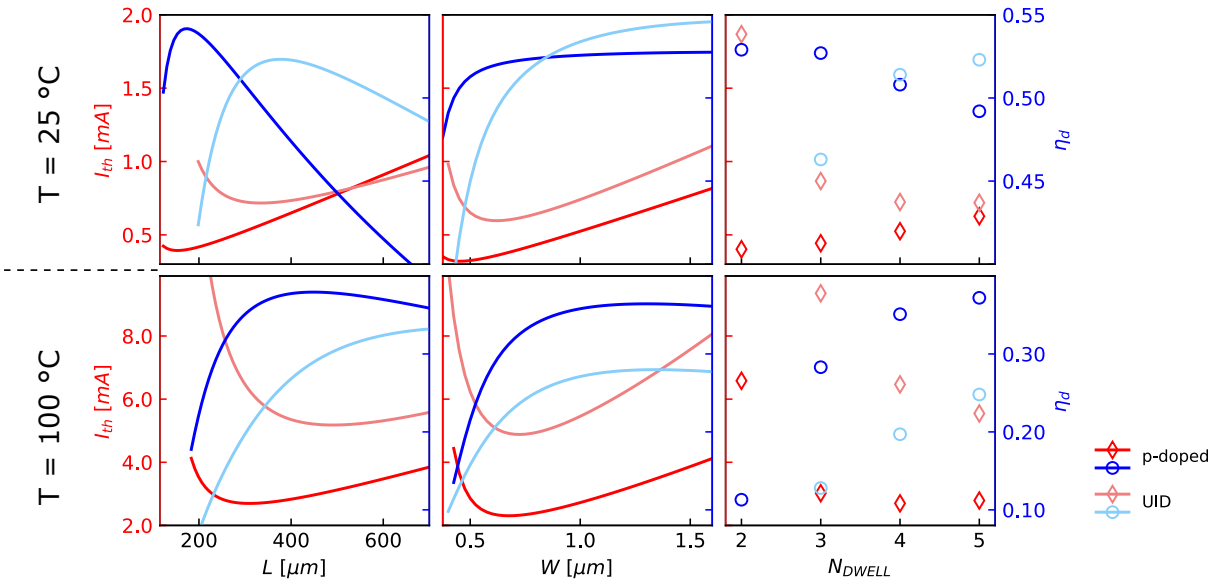

Figure 2.29: Parametric studies on the influence of design parameters (cavity length L, active region width W and number of DWELL layers N_{DWELL}) on the threshold current and differential efficiency η_d of membrane lasers as described in Fig. 2.28, simulated at RT (25 °C, top) and high temperature (100 °C, bottom), for UID and p-doped devices (10 extra holes per dot). When they are not variables, the values of L, W and N_{DWELL} are respectively 300 µm, 1 µm and 4.

the mode overlap with the doped regions is increased, propagation losses are also increased, which further contributes to increasing the threshold current and reducing the differential efficiency for narrow devices. Above 500 nm, the confinement factor keeps increasing, further increasing the modal gain and reducing absorption in the doped regions, eventually converging towards a maximum for widths of 1500 nm and above. Besides, the ratio of confinement to the number of dots peaks at around 500 nm and then decreases. This ratio gives an indication on the relation between the number of injected carriers and the increase in modal gain. An active region width of 1 µm or slightly narrower gives the best tradeoff for low threshold and high differential efficiency at RT and high temperature, while being large-enough to facilitate III-V processing.

Finally, the number of DWELL layers increases both the active volume and the optical confinement without affecting the quality factor of the laser cavity. However, having more dots per laser unit length increases the pump current densities that should be applied to the laser and thus increases self-heating. Besides, the number of DWELL layers is limited by the thickness of the DWELL and spacers between them. With the III-V layer thickness being set to 310 nm, a maximum of five DWELL layers can be used. The best tradeoff is obtained for 4 DWELL layers.

Based on these parametric analyses, the LI curves of a 300 µm long laser with a 1 µm wide active region comprising 4 DWELL layers and a p-doping level corresponding to 10 extra holes per dot are simulated. The device parameters used for these simulations are summarized in Table 2.2 and the parameters from Table 2.1 still holds. As a first assessment and considering a worst case scenario, the SRH time is kept the same as in section 2.1.2 even though longer lifetimes would be expected from QD grown on GaAs substrates. The simulated LI curves are

Table 2.2: Device parameters used for Fig. 2.30.

Device parameters	
$L = 300\ \mu m$	$W = 1\ \mu m$
Number of DWELL layers	$N_{DWELL} = 4$
Total DWELL layers area	$A_{act} = W \times L \times N_{DWELL}$
Mirrors reflectivities	$R_{1,2} = 0.30, 0.95$
Optical confinement factor	$\Gamma = 0.016$
Group index	$n_{gr} = 3.8$
Propagation losses	$\alpha_0 = 100\ m^{-1}$
IVBA cross-section	$\sigma_i = 1 \times 10^{-19}\ m^2$
Dots density	$\rho = 5 \times 10^{14}\ m^{-2}$ [128]
p-doping	10 holes per dot

presented in Fig. 2.30, for heat-sink temperatures ranging from 20 ℃ to 110 ℃. They show that the device could achieve high-temperature operation with a threshold current of 4.4 mA and above 1 mW output power at 110 ℃. Another important feature is the rather low threshold and high characteristic temperature of this laser, as illustrated in the inset of Fig. 2.30: at 20 ℃, the simulated threshold is 0.50 mA and submilliamp thresholds are predicted up to 60 ℃.

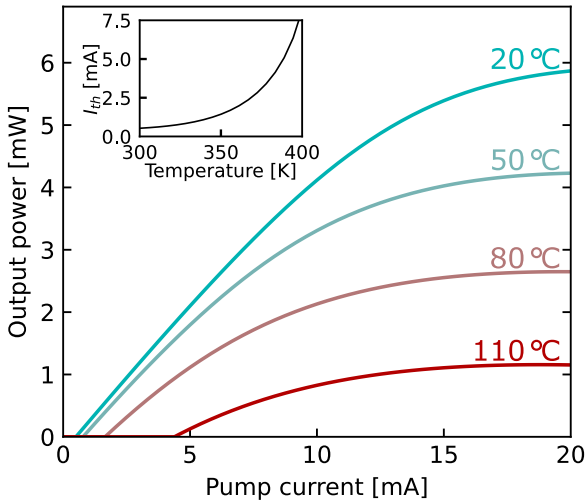

Figure 2.30: LI curves simulated for a QD membrane laser as a function of temperature. The simulation parameters are summarized in tables 2.1 and 2.2. Inset: temperature dependence of the threshold current showing submilliamp operation up to 60 ℃.

This initial assessment indicates that membrane InAs QD lasers are a advantageous candidate for optical on-chip interconnects where limited current and high temperature operation will ease the co-integration with the nearby electronics. For comparison, state-of-the-art MQW-based membrane lasers [31], [50] have RT thresholds close to 3 mA and high-temperature operation was achieved with a 100 ℃ threshold current of 12 mA, which is four times larger than the 2.9 mA expected from the device simulated in Fig. 2.30. State-of-the-art thicker vertical p-i-n

junction QD ridge lasers as presented in [90] or [157] have RT thresholds of 9.5 mA and 4 mA respectively, and could lase up to maximum temperatures of 100 ℃ and 75 ℃. Vertical p-i-n QD ridge lasers optimized for a low threshold using two HR mirrors were reported with threshold currents of 1.5 mA at the cost of below 0.1 quantum efficiencies [158]. Our findings and these values from the literature emphasize that for any configuration (vertical or lateral), a tradeoff is needed between efficiency, threshold and high-temperature operation. More complex integrated cavities — using for instance Bragg reflectors — would permit a finer control of the mirrors reflectivities and spectral filtering for modal engineering.

2.4. Design of Optical Cavities for Membrane Lasers on Silicon

This section reports on the design of optical cavities for membrane lasers on silicon. While section 2.3 presented results for Fabry-Perot lasers with a simple III-V waveguide and either as-cleaved facets (imposing R = 0.30), or having an HR coating, the design of optical cavities benefiting from the heterogeneous integration of III-V and SOI provides more control on the mirrors reflectivities or spectral filtering. This will be detailed for different types of cavities, namely Distributed Bragg Reflector (DBR), Distributed FeedBack (DFB) lasers, Fabry-Perot cavities using loop mirrors and microdisk lasers.

2.4.1. Bragg Reflectors — Basic Principle and Theory

First, we should begin with a brief introduction on Bragg reflectors, which are used in DBR and DFB lasers.

At the interface between two media of different refractive indices — or two sections of a waveguide with different effective indices — n_1 and n_2, an incident optical wave is partially reflected. At normal incidence, the reflection coefficient given by the Fresnel equations is [159]

$$r = \frac{n_1 - n_2}{n_1 + n_2} \tag{2.30}$$

For instance the refractive index of GaAs at 1.3 µm is 3.405 [103], giving a reflectivity R = $|r|^2$ = 0.30, used to realize Fabry-Perot lasers with as-cleaved facets as presented in reference [128] for instance.

The basic principle of Bragg reflectors is to use weak periodic perturbations of the effective index of the medium — as presented in Fig. 2.31 with step-like effective index variations — resulting in a fraction of the incident light being reflected at each index hop. Those distributed reflections add-up in phase and interfere constructively in the contra-propagating direction at the Bragg wavelength

$$\lambda_B = 2\left(L_1\tilde{n}_1 + L_2\tilde{n}_2\right) \tag{2.31}$$

where L_1 and L_2 are the physical length of the segments of effective index $\tilde{n}_1$ and $\tilde{n}_2$ [29].

The general Bragg grating frequency-dependent reflection coefficient (for the field amplitude)

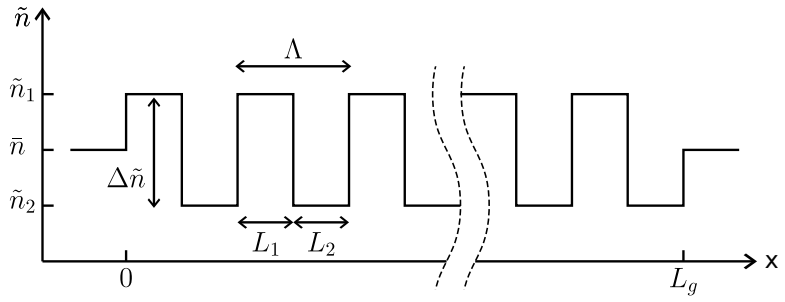

Figure 2.31: Variations of the effective index along propagation in a uniform Bragg grating with step-like effective index variations.

is given by [148]:

$$r(\lambda) = \frac{\kappa \sinh(\gamma L_g)}{\gamma \cosh(\gamma L_g) + i\delta \sinh(\gamma L_g)} \tag{2.32}$$

with κ the coupling factor between the two contra-propagating waves, L_g the grating length, δ the propagation constant deviation from the Bragg wavelength, referred to as the detuning parameter, and γ defined by

$$\gamma^2 \equiv \kappa^2 - \delta^2 \tag{2.33}$$

For step-like effective index variations as presented in Fig. 2.31, the incident wave is subjected to two reflections with $r = \Delta\tilde{n}/(2\bar{n})$ per period length Λ. Hence, the coupling factor is [160]:

$$\kappa = \frac{\Delta\tilde{n}}{\bar{n}} \frac{1}{\Lambda} \tag{2.34}$$

with $\Delta\tilde{n}$ is the effective index contrast between the grating sections and $\bar{n}$ is the average effective index as shown in Fig. 2.31.

In addition, provided that the index variation on the λ_B–λ range is small enough and $\bar{n}$ can be regarded as constant, the detuning parameter is approximated as

$$\delta(\lambda) = \beta(\lambda) - \beta_B \simeq 2\pi\bar{n}\left(\frac{1}{\lambda} - \frac{1}{\lambda_B}\right) \tag{2.35}$$

With these elements, one can compute the power reflectivity (R = | r |) spectrum of a Bragg grating. Some examples are printed in Fig. 2.32, illustrating the influence of the coupling coefficient and grating length on the reflectivity spectra. The modeled Bragg gratings have $\bar{n}$ = 3.16 and $\Lambda = 1310/(2\bar{n})$ nm to obtain λ_B = 1310 nm. Two important figures of merit can be determined from those spectra, namely the peak reflectivity and the bandwidth of the grating.

The peak reflectivity R_p is obtained at the Bragg wavelength. From Eq. (2.32) with $\delta = 0$, it is straightforward that:

$$R_p = \tanh^2(\kappa L_g) \tag{2.36}$$

The grating bandwidth can be defined either from the position of the first zeros or as the full width at half maximum (FWHM) of the reflectivity spectrum. In designing laser cavities,

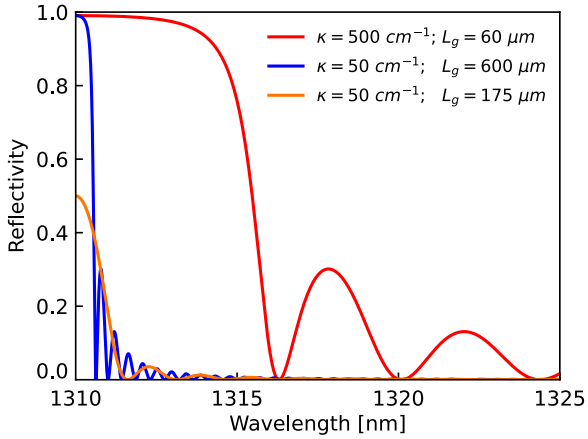

Figure 2.32: Reflectivity spectra of Bragg gratings centered around 1310 nm with coupling factors and lengths indicated in the legend. The peak reflectivity and FWHM bandwidth of the red, blue and orange spectra are respectively R_p = 0.99 and FWHM = 10.9 nm, R_p = 0.99 and FWHM = 1.1 nm and R_p = 0.50 and FWHM = 1.7 nm.

it is more natural to use the FWHM as modes are practically filtered out by limiting their Q-factor. However, an expression for the position of the first zeros is more easily derived and provides a basic understanding of the Bragg gratings filtering properties. The zeros of Eq. (2.32) are obtained for $\gamma L_g = ik\pi : k \in \mathbb{Z}$, giving the bandwidth between the first zeros around λ_B ($k = \pm 1$) [160]

$$\Delta\lambda = \frac{\lambda_B^2}{\pi n_{gr}} \sqrt{\kappa^2 + \left(\frac{\pi}{L_g}\right)^2} \tag{2.37}$$

with n_{gr} the group index.

From Eqs. 2.36-2.37 and the spectra displayed in Fig. 2.32, increasing the coupling coefficient increases both the peak reflectivity and the bandwidth, while increasing the grating length increases the peak reflectivity and decreases the bandwidth. This is well illustrated for instance by the red and blue curves of Fig. 2.32: the blue grating has a coupling coefficient ten times lower than the red one, but is ten times longer. As a result, both gratings have the same peak reflectivity (0.99) but the FWHM of the blue grating spectrum is only one tenth (1.1 nm vs. 10.9 nm) of the red one. Thus, low coupling coefficients are commonly desired in order to realize mirrors acting as spectral filters, but those the tend require larger grating lengths.

The last element needed for the design of optical cavities is the effective mirror location, used to determine the supported longitudinal (or Fabry-Perot) modes. The Bragg grating reflection can be well approximated in both magnitude and phase by a discrete mirror of reflectivity R placed at a distance L_{eff} of the grating origin with [29]:

$$L_{eff} = \frac{1}{2\kappa} \tanh\left(\kappa L_g\right) \tag{2.38}$$

After expressing the basic theory and equations of Bragg gratings, we may proceed to use them for designing laser cavities.

2.4.2. Distributed Bragg Reflector Laser Cavities

The first type of laser cavity investigated is the DBR laser cavity using two Bragg reflectors placed on either side of the gain section to provide feedback and spectral filtering.

In order to simplify the fabrication process and to benefit from the maturity of the CMOS fabrication, we have imposed ourselves the constraints of fabricating the Bragg gratings in the SOI and using only the standard layers of the CEA-LETI PDK, granting access to 305 nm, 165 nm and 50 nm-thick SOI only.

The Bragg grating index contrast is commonly obtained from partial etching of the top of the SOI waveguide — as it was typically done by previous PhD students at CEA-LETI [151], [161]–[163] — or from sidewall corrugations. Because the partial etching of the SOI waveguide is not part of the standard PDK, sidewall corrugations over 305 nm-thick SOI strip waveguides as illustrated in Fig. 2.33.a, c. were used instead. This is permitted by the use of high-resolution immersion lithography which enables us to fabricate relatively low κ sub-lambda structures. However, care must be taken as we have no experience on the design and fabrication of such structures at CEA-LETI yet.

We also experimented with another structure where the strip waveguide is tapered into a narrow core rib-like structure and the contrast index is provided by the presence or absence of the rib core (Fig. 2.33.b, d). For a narrow-enough core, there is no rib-guided mode and the optical mode supported by this structure is the slab mode. Thus, this structure is equivalent to a 165 nm-thick strip waveguide with 305 nm-thick posts.

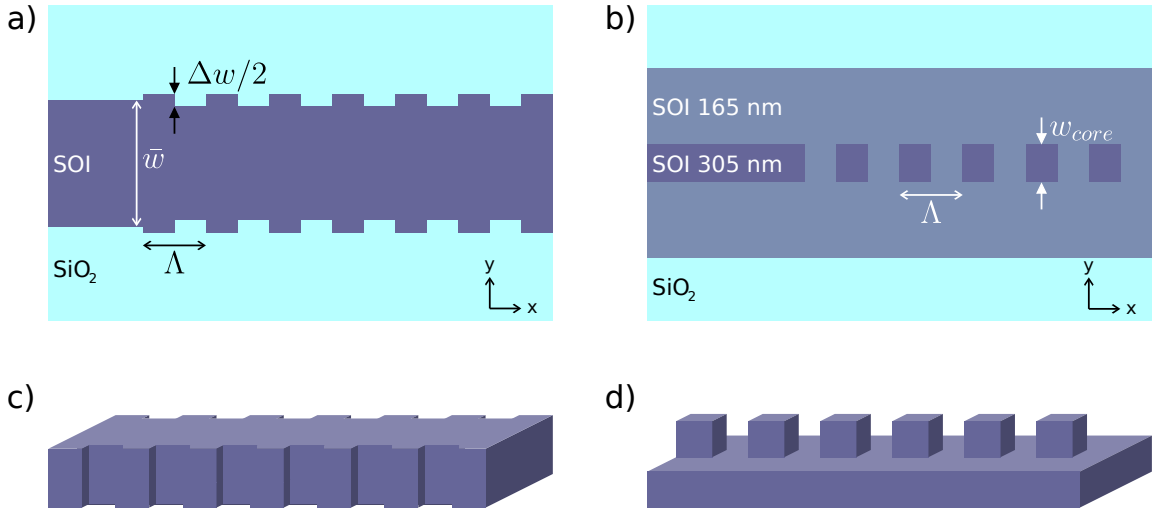

Figure 2.33: Schematic of the designed SOI Bragg gratings. Top-view of the 305 nm-thick strip waveguide with sidewall corrugations (a) and 165 nm-thick strip waveguide with 305 nm-thick posts (b). (c) and (d): bird's eye view of these gratings.

For both types of Bragg grating, we set $L_1 = L_2$ and $\Lambda = \lambda_B/(2\bar{n})$ with $\lambda_B = 1310$ nm. The targeted front and back-mirror peak reflectivities are 50% and 99%, respectively. The configuration using sidewall corrugations theoretically authorizes relatively fine tuning of the coupling factor by varying the corrugation width Δw. This allows adjusting the mirrors bandwidth in order to control the number of longitudinal modes. To achieve its 99% target

peak reflectivity, the back-mirror requires a larger coupling coefficient than the front-mirror if kept short enough for compactness purposes. This combination of a large coupling coefficient and constrained length can result in a too large bandwidth to filter-out unwanted longitudinal modes. In contrast, the front-mirror can achieve its target reflectivity with a lower coupling coefficient and thus, a reduced bandwidth. Consequently, our goal is to achieve a front-mirror FWHM lower than the Fabry-Perot FSR of the cavity for spectral filtering, while allowing a larger bandwidth for the back-mirror so that the main reflection peak of the front-mirror is included in that of the back-mirror.

From Eq. (1.17) with $n_{gr} \leq 3.8$ and $\lambda = 1310$ nm, for a 500 µm-long gain section with two 100 µm-long couplers and combined Bragg gratings effective lengths of 300 µm, a lower bound of the FSR is 0.23 nm, and 0.38 nm for a 100 µm-long gain section.

In the sidewall corrugations configuration, the average width is set to 2 µm, the width at the coupler output, to avoid having to taper the waveguide again. In addition, this is a region of low $d\tilde{n}_{Si}/dw_{Si}$, allowing for lower coupling coefficients as shown in Fig. 2.34. With small corrugation widths, the mode shape is hardly affected by the corrugations and we used the effective indices simulated using Lumerical MODE to calculate the coupling coefficient as a function of the corrugation width.

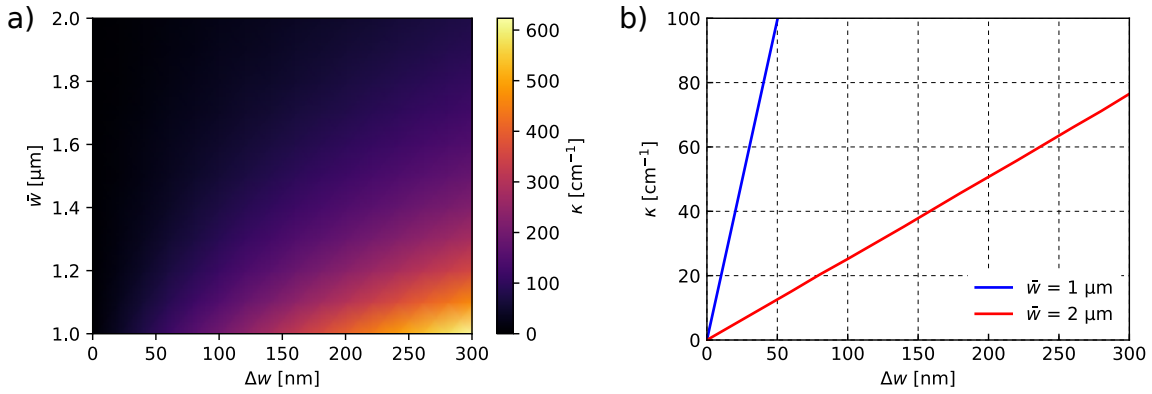

Figure 2.34: Calculated coupling coefficient for the sidewall corrugations configuration: (a) pseudocolor plot of the coupling coefficient as a function of the grating average width and corrugation width and (b) plot of the coupling coefficient as a function of the corrugation width for an average width of 2 µm, as used, and 1 µm for comparison.

Table 2.3: Grating parameters of the designed sidewall corrugations DBR front-mirror (FM) and back-mirror (BM).

	Δw [nm]	L_g [µm]	Λ [nm]	κ [cm^{-1}]	R_p	λ_B [nm]	FWHM [nm]	L_{eff} [µm]
FM	70	500	207	17.4	0.50	1310.1	0.59	202
BM	280	400	207	71.3	0.99	1309.1	1.54	71

The design parameters and calculated characteristics of the designed front and back-mirrors are given in Table. 2.3. The FWHM of the front-mirror (0.59 nm) is larger than the Fabry-Perot FSR but for compactness reasons, we had to set a 500 µm upper limit to the acceptable grating length. The two spectra, calculated from Eq. (2.32) are shown in Fig. 2.35.a.

In the second configuration, due to the posts being centered on the waveguide, the index

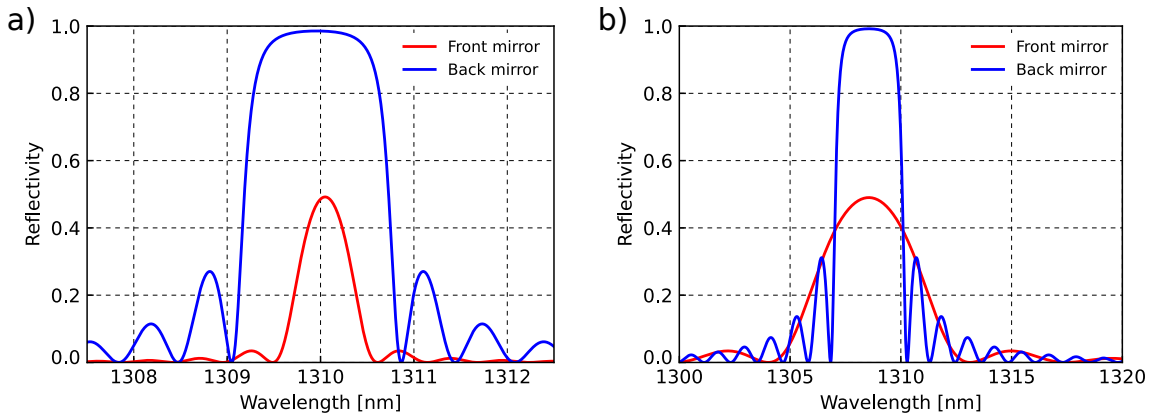

Figure 2.35: Simulated reflectivity spectra of the designed SOI Bragg gratings with (a) 305 nm-thick strip waveguide with sidewall corrugations and (b) 165 nm-thick strip waveguide with 305 nm-thick posts.

contrast is quite strong, resulting in large coupling coefficients and bandwidths. To minimize them, the posts width w_{core} is set to 75 nm, which is the smallest value allowed by design rules. The slab width is 2 µm. From the effective indices simulated using Lumerical MODE, $\bar{n}$ = 2.77 and κ = 125 cm^{-1}. Expecting that the posts might have a non negligible influence on the mode shape, we used the BeamProp tool from RSoft to confirm these values and obtained almost identical results ($\bar{n}$ = 2.78 and κ = 124 cm^{-1}). The front and back-mirrors lengths are set to 70 µm and 250 µm respectively to obtain reflectivities of 50% and 99%. The computed spectra are displayed in Fig. 2.35.b. Due to the high coupling coefficient, large bandwidths are obtained in this configuration: 5.00 nm and 3.03 nm for the front and back-mirrors respectively.

To summarize this subsection, we have designed Bragg reflectors in the SOI using only the standard PDK layers, using two different structures. The first one, with sidewall corrugations theoretically enables a fine control of the coupling coefficient by varying the corrugation width. For the smallest corrugation widths, errors at the fabrication process can be an issue as visible from Fig. 2.34, even though the use of OPC [164] could help mitigating this risk. The second configuration, using 305 nm-thick posts on a 165 nm-thick strip is a priori less exposed to fabrication issues but is associated to high coupling coefficients. We also want to mention other approaches not explored within the frame of this thesis but of relevant interest for the realization of low κ Bragg gratings with better tolerance to fabrication defects. A first solution is to reduce the interaction between the optical field and the index-variation inducing elements by placing them further away from the field maximum, for instance by using rib waveguides with sidewall corrugations of the slab [160], or side posts gratings [165]. Another approach consists of using misaligned sidewall corrugations, which is equivalent to having two gratings with a controlled dephasing depending on the misalignment, resulting in partially destructive interferences in the backward propagating direction [166].

2.4.3. Distributed FeedBack Lasers

Similar to DBR lasers, distributed feedback (DFB) lasers use Bragg reflectors to form the optical cavity. However, for the latter, the Bragg reflector is distributed along the gain section, which modifies the spectra of allowed modes in the cavity. This is best understood from a photonic crystal treatment of the problem, as presented in the book [167]. The Bragg grating can be seen as a 1D photonic crystal, having a periodic structure of period Λ in the x direction as illustrated in Fig. 2.36.a. with the unit cell shown in orange. Its primitive lattice vector is $\Lambda\boldsymbol{x}$, and the reciprocal lattice vector is $2\pi/\Lambda\boldsymbol{x}$, with the Brillouin zone of the reciprocal space being delimited by $-\pi/\Lambda < k_x \leq \pi/\Lambda$. The eigenmodes of this structure must have a phase shift $2k\pi$ over Λ, and their physical wavelength (in the photonic crystal) is 2Λ. Those are the extended modes supported by the system. From the system symmetries, it comes that the nodes of the eigenmodes electric field must be located either at the center of the $\tilde{n}_1$ regions or at the center of the $\tilde{n}_2$ regions, so two eigenmodes are supported by the system. Converting to energy density (Fig. 2.36.c), one mode has its energy mostly concentrated in the high index regions and thus has a lower frequency than the other mode which has a stronger fraction of its energy in the low index regions [167]. No extended mode can exist in between these two frequencies: there is a photonic bandgap.

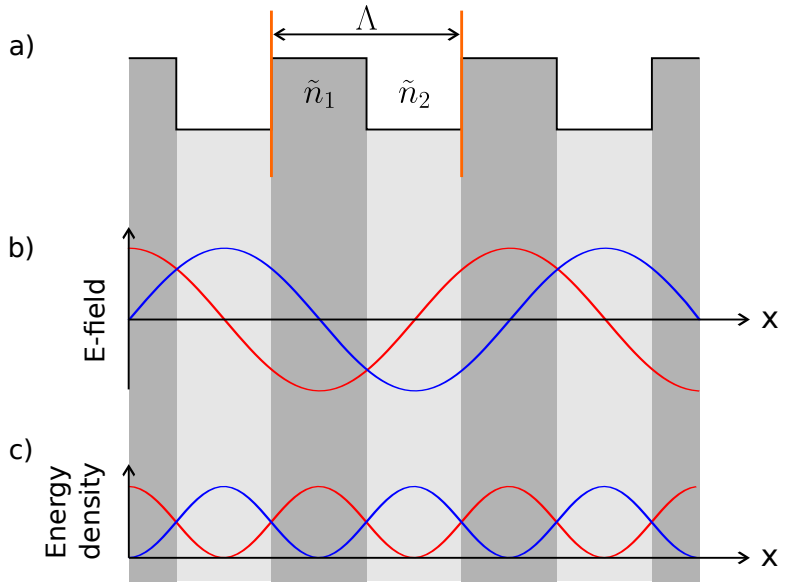

Figure 2.36: Schematic of a one dimensional photonic crystal (a) and distribution of the electric field (b) and energy density (c) of the two associated eigenmodes.

As a consequence, standard DFB lasers support two longitudinal modes. However, in practical lasers, single mode emission is most commonly desired. This can be achieved by introducing a defect in the crystal structure, breaking the translational symmetry of the system responsible for the existence of the two aforementioned modes. In practical DFB lasers, this is typically achieved through the introduction of a quarter-wavelength shift, the lengthening of a $\tilde{n}_1$ or $\tilde{n}_2$ region to create a half Bragg wavelength-long cavity supporting a localized mode which frequency lies inside the photonic bandgap [29], [163], [167]. This is not one of the extended

modes of the crystal so although it can be present into the crystal sections on each side of the defect, its amplitude should decay following propagation in the ±x direction away from the defect, as is the case for light incident onto a DBR. Actually, this new structure can be seen as a half-wavelength-long cavity with a DBR on each side, and will be treated as such in the end of this section.

DFB lasers designed in this thesis are illustrated in Fig. 2.37: they consist in a hybrid structure with coupled III-V and SOI waveguides over the active length, supporting an hybrid mode. Optical gain is provided by the III-V while the Bragg reflectors are fabricated through sidewall corrugations of the SOI waveguide, as for the first DBR lasers configuration studied in the previous section (see Fig.2.33.a). Couplers as designed in section 2.22 are located on each side of the grating to transform the optical mode into being fully localized in the SOI. The III-V waveguides are as presented in section 2.2.2 (Fig. 2.12.c) with a 2 µm wide active core. This was motivated by the need to design devices with a single width to reduce their number and it is the smallest dimension for which we were fully confident in the III-V lithography. The SOI average width over the reflectors sections is 760 nm — resulting in 70% of the hybrid mode optical power being in the III-V mode and 30% in the SOI mode as illustrated in Fig. 2.37.b. — and its corrugation width is determined based on the targeted coupling coefficient. Because the optical mode is only partially localized in the SOI, the coupling coefficient is lower than for the DBR lasers of the previous section for a given set of average width and corrugation width. However, the narrower SOI width as compared to the DBR lasers makes the coupling factor more sensitive to width variations. Due to the SOI width greatly affecting the localization of the hybrid mode in one or the other waveguide, the effective indices simulated with Lumerical MODE in each grating subsection could not be used to estimate the average index and coupling constant of the grating, so the BeamProp tool from RSoft was used instead.

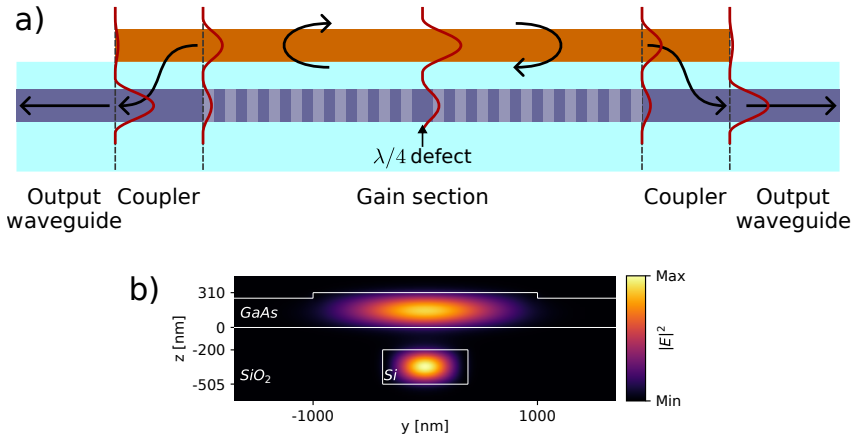

Figure 2.37: Key constituents of a laser diode on silicon illustrated schematically for a longitudinal cross-section (a) and top view (b) of a DBR laser: a gain medium, III-V/SOI optical couplers, two mirrors (which often also act as mode selection filters) and an output waveguide.

Three DFB laser cavities were designed so that the Bragg grating on each side of the quarter-wavelength shift have a 0.8 peak reflectivity and $2L_{eff}$ approximately equal to 75 µm, 150 µm or

350 µm. In addition, variations of those were made by adjusting the gratings lengths to obtain peak reflectivities of 0.7 and 0.9. The corrugations widths, associated coupling coefficients and grating lengths used are given in Table. 2.4 along with the corresponding calculated peak reflectivities and effective lengths. Given that the gratings are distributed over the gain region in DFB lasers, the notions of peak reflectivity and effective length do not directly applies but can still give an estimate of the cavity characteristics.

Table 2.4: Grating parameters of the designed DFB laser cavities.

κ [cm^{-1}]	Δw [nm]	$2L_g$ [µm]	R_p	$2L_{eff}$ [µm]
123	90	203	0.72	69
		242	0.82	73
		305	0.90	78
59	44	406	0.70	141
		484	0.80	151
		610	0.90	160
26	20	947	0.72	320
		1130	0.82	341
		1400	0.91	359

2.4.4. Loop Mirrors

Loop mirrors are another type of mirror used to fabricate Fabry-Perot cavities for our membrane lasers on silicon demonstrators. They consist in a waveguide loop connected to the input and output waveguides through a directional coupler (DC), as illustrated in Fig. 2.38. Light incident from the input waveguide generates two contra-propagating waves in the loop, which then interfere constructively or destructively in the input or output waveguides after passing through the DC again, depending on the followed path. Contrary to Bragg gratings, loop mirrors do not provide spectral filtering but have the benefit of being reliable mirrors as their reflection coefficient solely depends on the splitting ratio of the DC, which is a reliable component from our library.

The output electric field is calculated from the transfer matrix of the DC (**M**) and transmission matrix of the loop (**T**). The incident light E_{in} (from the input port 1 of the DC) goes through the DC, the loop and then the DC again, so that

$$\begin{bmatrix} E_{out,t} \\ E_{out,r} \end{bmatrix} = \mathbf{M} \cdot \mathbf{T} \cdot \mathbf{M} \cdot \begin{bmatrix} E_{in} \\ 0 \end{bmatrix} \tag{2.39}$$

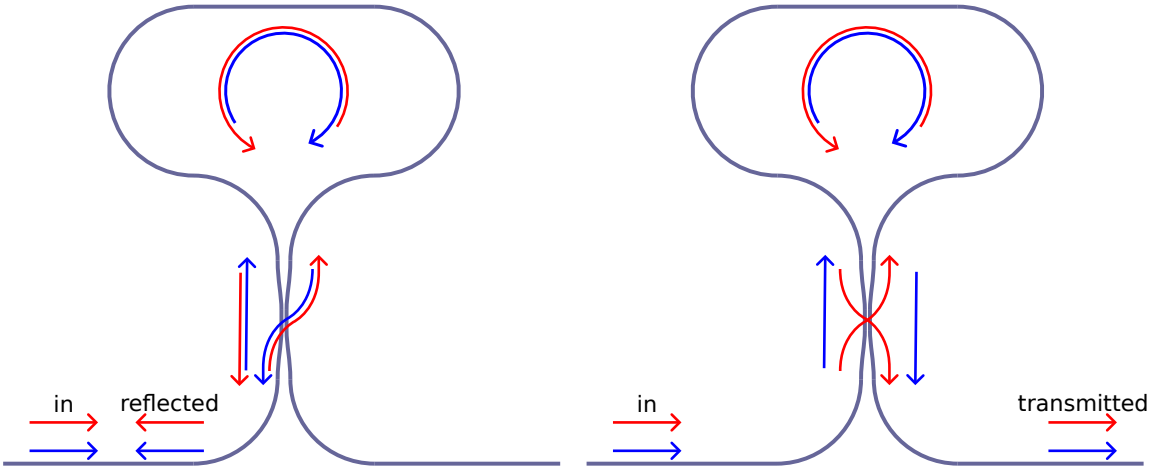

Figure 2.38: Loop interferometer mirror working principle. Left: possible paths for the reflected light. Right: possible paths for the transmitted light.

where for a symmetric DC with power coupling ratio X:Y [168]

$$\mathbf{M} = \begin{bmatrix} \sqrt{X} & -i\sqrt{Y} \\ -i\sqrt{Y} & \sqrt{X} \end{bmatrix} \tag{2.40}$$

The first column of this transfer matrix can be understood as follows: a fraction $\sqrt{X}$ of the field incident from the input port 1 is not coupled to the second waveguide and goes to output port 1, and a fraction $\sqrt{Y}$ is coupled to the output port 2 with a $-\pi/2$ phase shift, and vice-versa for the input port 2.

The transmission matrix of a lossless waveguide of length L and coupling constant β is [29]

$$\mathbf{T} = \begin{bmatrix} e^{i\beta L} & 0 \\ 0 & e^{i\beta L} \end{bmatrix} \tag{2.41}$$

Hence:

$$\begin{bmatrix} E_{out,t} \\ E_{out,r} \end{bmatrix} = \begin{bmatrix} E_{in}e^{i\beta L}X - E_{in}e^{i\beta L}Y \\ -2iE_{in}e^{i\beta L}\sqrt{X}\sqrt{Y} \end{bmatrix} \tag{2.42}$$

Converting to intensity,

$$I_t = E_{out,t} \cdot E^*_{out,t} = E^2_{in}X^2 + E^2_{in}Y^2 - 2E^2_{in}XY = TE^2_{in} \tag{2.43}$$

$$I_r = E_{out,r} \cdot E^*_{out,r} = 4E^2_{in}XY = RE^2_{in} \tag{2.44}$$

where $T \equiv X^2 + Y^2 - 2XY$ and $R \equiv 4XY$.

Those results are shown graphically in Fig. 2.39.

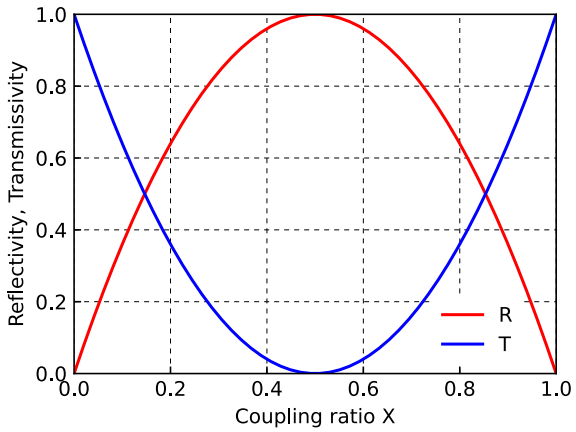

Figure 2.39: Loop mirror reflectivity and transmittance as a function of the coupling ratio of the DC.

The designed loop mirrors use the DC available from the CEA-LETI photonic library with splitting ratio 50:50 (resp. 90:10) for the back-mirror (resp. front-mirror), giving a theoretical R = 1 (resp. R = 0.36). As mentioned in preamble, such mirrors do not provide spectral filtering as the only spectral dependence in the above equations comes from the spectral response of the DC.

2.4.5. Membrane Microdisk Lasers

Microdisk and microring lasers have attracted much interest over the past decades since they allow for the realisation of high Q-factor devices with a reduced active volume [95], [97], [169]. Here, we propose a new design of electrically pumped microdisk lasers relying on our developments on membrane lasers. The design optimization of these devices is still work in progress.

The proposed structure is presented in Fig. 2.40: a microring comprising the DWELL is filled in its inner radius with p-doped GaAs while a n-doped GaAs slab lies at the outside radius of the active ring. The p-doped region may be as thick as the active ring or a few tens of nanometers thinner, while the n-doped slab must be much thinner in order to provide an index contrast necessary to achieve total internal reflection at the disk outer radius. Fig. 2.40.c. shows an expected effective index profile along a cross-section of the microdisk laser. For instance for a 310 nm-thick active stack, 260 nm-thick p-doped GaAs core and 150 nm-thick outer n-doped GaAs slab: $\tilde{n}_1$ = 3.08, $\tilde{n}_2$ = 2.99 and $\tilde{n}_3$ = 2.62. Due to the much lower mobility of holes as compared to electrons, it is important that they are injected through the disk core and not through the thin slab.

Light can be evanescently coupled to an underlying SOI bus waveguide as illustrated in Fig. 2.40.b. and done in reference [95]. Variables affecting the coupling strength include the thickness of the oxide layer or a vertical offset between the ring outer radius and the SOI waveguide edge. Another solution proposed in reference [169] is the use of an SOI ring just below the III-V ring to form a hybrid mode between the III-V and SOI rings, coupled to an SOI bus waveguide. In this solution, the bus waveguide was curved to increase the interaction

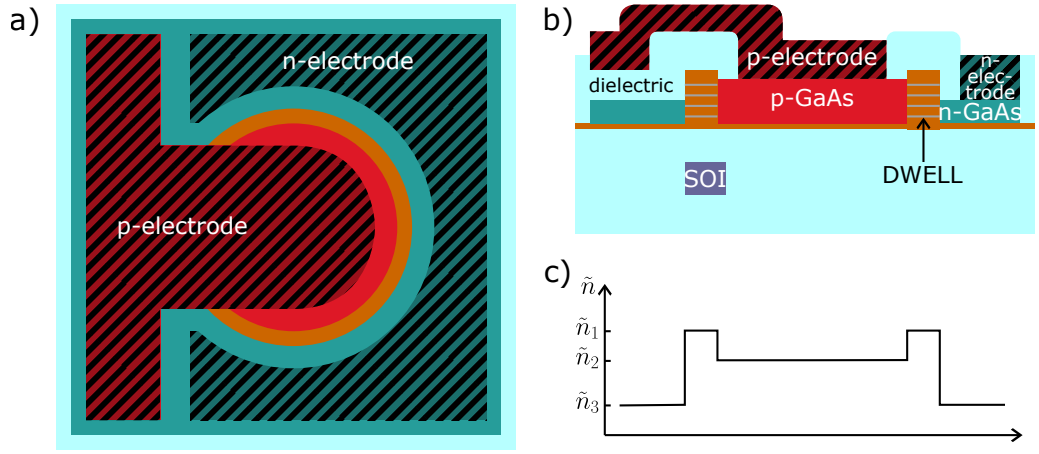

Figure 2.40: Schematic of a membrane microdisk laser a) top view b) cross-section c) effective index cross-section.

length and thus the coupling strength.

2.5. Chapter Summary

This chapter addressed the modeling and design of the building blocks for a laser diode on silicon. A rate equation quantum dot laser model was proposed, emphasizing the role of p-doping on the thermal behavior of QD lasers. The contribution of the extra holes to the optical gain at RT reduces the required electron density to achieve lasing, which gives some leeway for it to be increased as holes thermalize when the temperature is increased. At RT, the rate of npp SRH recombination may be quite high for p-doped devices but it decreases as the temperature increases, setting the optimal p-doping level to around 10 holes per dot according to our simulations. Next, a rib-like patterning of the III-V was proposed to realize active waveguides with either an InGaAs MQW or InAs DWELL-based core. By setting a maximum III-V membrane thickness of 310 nm, light can be transferred to an SOI waveguide with the standard CEA-LETI PDK thickness without additional technological steps. Applying the QD laser model to Fabry-Perot cavity III-V membrane lasers showcases the potential of p-doped InAs QD membrane laser for low-threshold laser sources capable of high-temperature operation. Finally, DBR, DFB, loop mirror and microring laser cavities based on these III-V membranes were designed. In particular, solutions to realize Bragg reflectors in the SOI using only the standard PDK layers were explored. With these constraints, the realization of low κ gratings is challenging and in addition to the sidewall corrugations of a strip waveguide and posts on a thin strip waveguide configurations detailed in this chapter, we recommend exploring configurations using misaligned sidewall corrugations, sidewall corrugations of a rib slab or side posts.

Table 2.5 and Fig. 2.41 summarize the optimum DBR InAs DWELL membrane laser on silicon design parameters, based on the results of sections 2.2, 2.3 and 2.4.2. In the next chapter, we will focus on the fabrication of these devices.

Table 2.5: Optimum DBR InAs DWELL membrane laser on silicon design parameters.

III-V membrane gain medium	
L = 300 µm	W = 1 µm
Active core thickness (t_{core})	310 nm
Core-slab thickness difference (t_{core} - t_{slab})	50 nm
Number of DWELL layers	N_{DWELL} = 4
p-doping	10 holes per dot
SOI waveguide and passive components	
Top oxide cladding thickness (t_{ox})	200 nm
SOI width under the active region (w_{Si})	585 nm
III-V/SOI coupler length (L_c)	100 µm
Front DBR parameters (R_p = 0.50)	κ = 17.4 cm^{-1}; L_g = 500 µm
Back DBR parameters (R_p = 0.99)	κ = 71.3 cm^{-1}; L_g = 400 µm

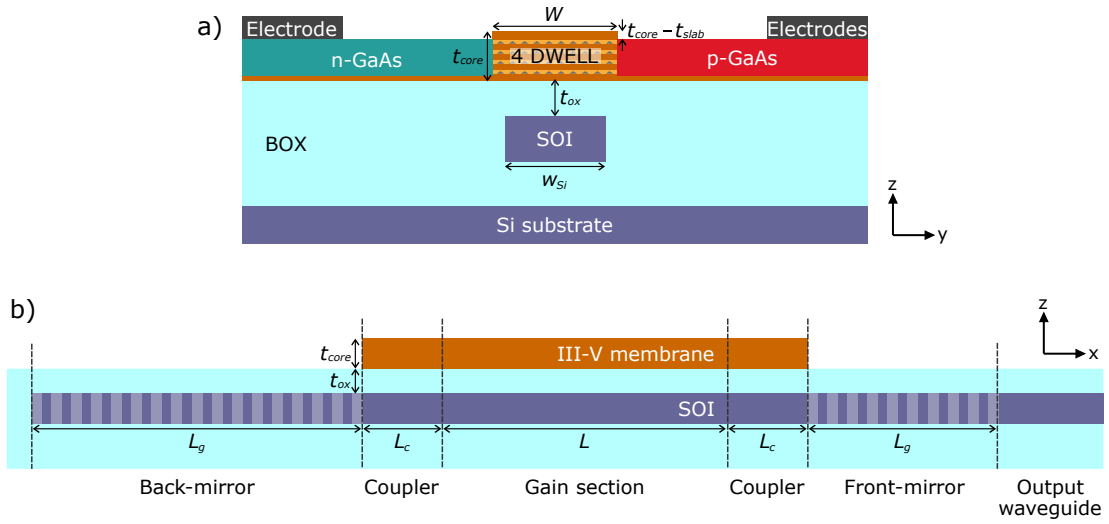

Figure 2.41: Schematic transverse (a) and longitudinal (b) cross-section of the optimum DBR InAs DWELL membrane laser on silicon structure. The numerical values of the shown parameters are given in Table. 2.5

3

Fabrication of III-V Membrane Lasers on Silicon

This chapter reports on the technological developments towards the realization of the InAs DWELL membrane lasers on silicon designed in the previous chapter.

To this end, we begin by proposing a broad process-flow for their fabrication in section 3.1, taking into account the opportunities and constraints of the CEA-LETI platform. The membrane architecture and resulting lateral current injection (LCI) scheme induces major changes to the fabrication of III-V lasers on silicon as compared to the conventional vertical structure. This is due to the horizontal p-i-n structure of LCI devices, which cannot be made by directly growing the n, i and p materials on top of each other as it done for vertical structures. Accordingly, we identified three main challenges in the fabrication of InAs DWELL membrane lasers on silicon, namely:

- The development of processes for the fabrication of thin horizontal p-i-n structures suitable for LCI;
- The bonding of GaAs on Si, a new topic at our laboratory since InP was mostly used so far;
- The combination of these two for the fabrication of III-V membrane LCI devices on silicon. This adds further complexity to the process-flow, in particular due to high-temperature epitaxial growths performed post-bonding, which may create defects at the bonding interface.

To tackle these challenges, we used a step-by-step approach, sequentially adding further complexity to the fabricated devices and parallelizing developments whenever possible. Sections 3.2 to 3.5 of this chapter follow these progressive developments. First, section 3.2 focuses on the development of the primary building blocks, including the bonding of GaAs on Si. In section 3.3, some of these building blocks are used to fabricate a first generation of LCI devices

with an InGaAs MQW-based light-emitting stack, on a GaAs substrate. With these prototypes, we should verify that the first challenge mentioned above is addressed. Next, the process-flows for the bonding of GaAs and for the fabrication of LCI devices are combined to realize III-V on silicon devices (section 3.4), using unpatterned silicon first. Finally, we report on the realization of the silicon photonics circuits in section 3.5. III-V stacks will later be bonded on these SOI wafers, but this was not yet achieved during the time of this thesis.

3.1. Process-Flow for the Fabrication of Membrane Laser on Silicon

This section presents broadly the proposed process-flow for the fabrication of InAs DWELL membrane lasers on silicon, as represented schematically in Fig. 3.1.

It begins with the fabrication of the SOI PIC as part of 300 mm multi-project wafers (MPW), while the III-V stacks are grown separately on 100 mm GaAs wafers with (100) surface orientation from Sumitomo Electric Industries (Fig. 3.1.a). Next, the III-V wafers are bonded on the SOI wafers using a direct oxide bonding process, and the III-V substrates are removed, leaving only the few hundreds of nanometers-thick active stack (Fig. 3.1.b-d). After resizing, the III-V is processed on the 100 mm platform and the laser diode heterostructures are fabricated through two successive cycles of etching of the III-V stack and selective area growth (SAG) of doped GaAs (Fig. 3.1.e-g). Finally, a SiN capping layer is deposited, metal contacts are formed and the mesa is etched (Fig. 3.1.h).

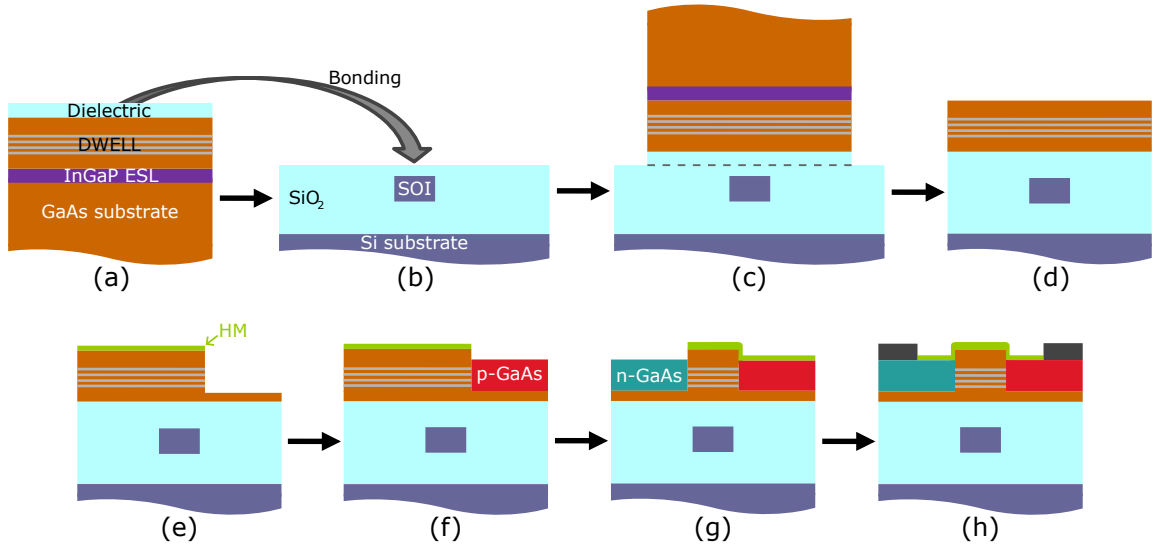

Figure 3.1: Process-flow of the fabrication of InAs DWELL membrane lasers on silicon (cross-sectionnal schematic). a) Epitaxy of an InGaP etch-stop layer (ESL) and of the III-V stack (Fig. 2.12.c) on a 100 mm GaAs substrate, SiO_2 deposition and planarization. b) Direct bonding on a 300 mm patterned SOI wafer capped with planarized SiO_2. c) Bonded wafers. d) GaAs substrate and ESL removal, resizing to 100 mm. e) Hard-mask (HM) deposition and HM and III-V etching. f) Surface preparation and SAG of p-doped GaAs. g) Repetition of steps (e-f) for the SAG of n-doped GaAs. g) Back-end.

3.2. Technological Building Blocks Development

While the vertical p-i-n structure of conventional devices is formed by the successive growth of p-doped, intrinsic and n-doped materials adding-up on top of each other, the lateral p-i-n structure is instead formed by etching and regrowth. Hence, the realization of these structures requires an etching process giving a surface quality compatible with epitaxy. After a brief introduction to the basics of some semiconductor manufacturing processes (section 3.2.1), the aforementioned developments are introduced in sections 3.2.2 and 3.2.3. Section 3.2.4 presents the development of a GaAs on silicon bonding process, conducted in parallel to the fabrication of lateral p-i-n structures.

3.2.1. Basics of Epitaxy and of Plasma Etching

Epitaxy

Epitaxy is the growth of crystalline films on top of another crystalline substrate. Metalorganic chemical vapor deposition (MOCVD) and molecular beam epitaxy (MBE) are two epitaxy methods widely used in microelectronics to grow semiconductor thin films. MOCVD is a chemical deposition method, using metalorganic precursors which are stored in bubblers and carried into the reactor chamber by a carrier gas. In our works, the carrier gas is hydrogen. Trimethylgallium is used as a Ga precursor, trimethylindium or dimethylaminopropyl-dimethyl-indium (DADI) are used for In, trimethylaluminium for Al, tert-butylarsine for As and t-butylphosphine for P. When in the reactor chamber, the precursors diffuse and are adsorbed onto the surface of the heated substrate. Next, the precursors react on the surface of the substrate to form the crystalline semiconductor epi-layers. Gaseous byproducts (resulting from the organic ligands) are also produced and are pumped to the exhaust [170]. MBE, by contrast, is a physical deposition technique. It uses ultra-pure sources of the elements of interest, which are heated to the point where the elements sublime, and then condense on the surface of the target wafer, forming so-called adatoms. Because the substrate is also heated, adatoms of the different elements can still migrate on its surface of and react together to form the epi-layers [171].

Both MOCVD and MBE can be used for the SAG of semiconductor crystals, although through different mechanisms. In both cases, a dielectric (typically SiO_2) mask is used and opened to reveal the semiconductor substrate only where growth is wanted. The selectivity of MBE is mainly a consequence of the increased rate of desorption of the adatoms on the dielectric mask due to a lower sticking coefficient as compared to that on the semiconductor substrate, in particular at high temperatures and low growth rates. In addition, the concentration gradient of adatoms induced by their consumption for epitaxy in the open regions of the mask also leads to a diffusion of the adatoms towards these regions [171]. In MOCVD, surface catalytic reactions facilitate the decomposition of the precursors adsorbed on the semiconductor surface as compared to those on the dielectric mask, lacking these surface catalytic reactions [172]. This in turn induces gradients of concentration of the precursors, leading to their diffusion towards the open areas of the dielectric mask. In this case, both a surface migration — favored by the

lower sticking coefficient of the species on the mask as compared to the semiconductor — of the precursors and a vapor phase diffusion are observed [173]–[175]. Because the MOCVD SAG does not only rely on the sticking coefficient difference between the reactive species and the substrate or mask, but also on surface catalytic reactions linked to its chemical nature, it appears as a better option for SAG than MBE. Another advantage of the MOCVD over MBE is that MOCVD is performed at atmospheric or low pressure while MBE is performed in ultra-high vacuum to avoid incorporating impurities in the epi-layers, increasing the maintenance complexity and cost of MBE tools. Therefore, MOCVD is often preferred in an industrial context.

All epitaxial growths presented in this thesis were realized using an Applied Material 300 mm MOCVD tool. More details about this tool can be found in the thesis of M.-L. Touraton, who previously worked on the SAG of III-V semiconductors at the LTM [62].

Plasma etching

Plasma etching is a widely used type of dry etching, typically allowing for a smaller linewidth and better directionality than wet etching. The used plasma is a partially ionized gas that contains electrons, positively charged ions and neutral free radicals [176]. It is commonly initiated by applying an RF oscillating electromagnetic field to a gas, accelerating the low-mass electrons and resulting in a glow discharge as these electrons collide with neutral atoms. A sample exposed to the plasma is etched by a combination of chemical and physical mechanisms. Free radicals are adsorbed on the substrate surface, reacting with it to create volatile products that desorb and are pumped out of the process chamber. The physical action comes from the negative plasma potential of the substrate or an external bias, leading to a directional acceleration of ions towards the substrate and energetic ion bombardment of the sample surface causing sputtering. Taken alone, the chemical etching lacks directionality while the physical sputtering can be slow and lacks selectivity. However, in the combination of these two mechanisms, the physical ion bombardment enhances the rate of chemical etching by creating active dangling bonds on the sample surface, increasing the rate of reaction with free radicals, and by helping remove the reaction products [177]. Because the etching sidewalls are not exposed to ion bombardment, this tends to an anisotropic etching.

Reactive ion etching (RIE) is a type of capacitively coupled plasma etching where the etching reactor features two electrodes: a larger upper electrode and a smaller bottom electrode (onto which lies the wafer), as illustrated in Fig. 3.2 (left). The upper electrode is grounded while an RF signal is applied to the lower electrode in order to create the plasma and accelerate ions. However, the plasma density of RIE is quite low, in the range of 10^8 – 10^9 cm^{-3}, resulting in quite limited etching rates. This is due to the plasma density and ion energy being controlled by the same RF signal. Therefore, increasing the RF signal magnitude to create a denser plasma also increases the ion energy, resulting in a poor selectivity and damaging the devices.

Therefore, another type of plasma, namely inductively coupled plasma (ICP) is currently more commonly used. The ICP is generated thanks to a coil placed around the top of the reactor chamber and subjected to an RF signal. This creates an alternating magnetic field around the coil

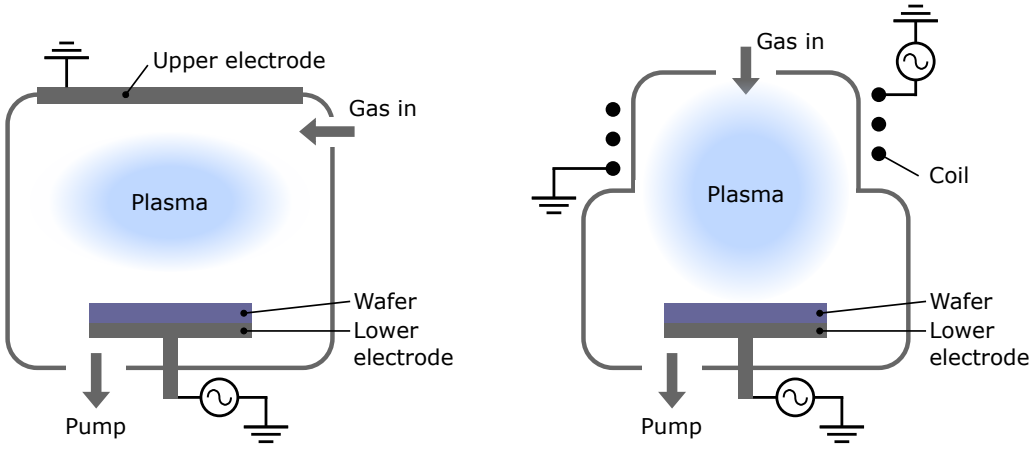

Figure 3.2: Schematic of RIE (left) and ICP-RIE (right) plasma etching reactors.

which in turns induces an alternating electric field in the reactor chamber, used to generate the plasma. An advantage of ICP over RIE is that the magnetic field narrows the plasma, preventing electrons scattering on the reactor walls [178]. In addition, the RF signals used to generate the plasma does not provides bombardment energy to the ions. Therefore, plasma densities of 10^{10} – 10^{12} cm^{-3} can be achieved with ICP.

ICP-RIE reactors, as illustrated in Fig. 3.2 (right), combine a RF generator used to create an ICP at the top of the chamber with a second RF generator connected to the lower electrode onto which lies the sample, to provide energy for ion bombardment. Because the RF signals used to create the plasma and accelerate ions are decoupled, ICP-RIE reactors exhibit high plasma densities and etch rates, along with controlled ion energy.

Dry etchings presented in this thesis are achieved by means of ICP-RIE.

3.2.2. Post-Etching Surface Cleaning of GaAs for Epitaxial Regrowth

The purpose of the first study is to develop a surface treatment to prepare the GaAs surface for epitaxial regrowth after ICP-RIE etching of GaAs, as it will be done to fabricate lateral p-i-n structures (see process-flow Fig. 3.1.d-e.). Indeed, the plasma etching of GaAs can create an amorphous layer or cause roughness at the etched surface [179], [180], which should be cleaned prior to epitaxial regrowth.

To this end, three GaAs wafers were subjected to full-wafer ICP-RIE etching. One of the wafers was treated with an ammonia solution (NH_4OH) to remove the native oxide on the GaAs surface [181]. Another wafer underwent the same NH_4OH treatment, followed by a dry O_3 reoxidation and another NH_4OH oxide removal. The purpose of this is to induce controlled GaAs consumption of a few nanometers without creating surface roughness, to expose a part of the crystal that was less affected by the etching. The third wafer was used as a control wafer and was not treated with the ammonia solution post ICP-RIE etching. Atomic force microscope (AFM) images of the surface of the three wafers following the epitaxy of a 300 nm-thick layer of GaAs are shown in Fig. 3.3. While the control wafer exhibits 3D growth, screw dislocations

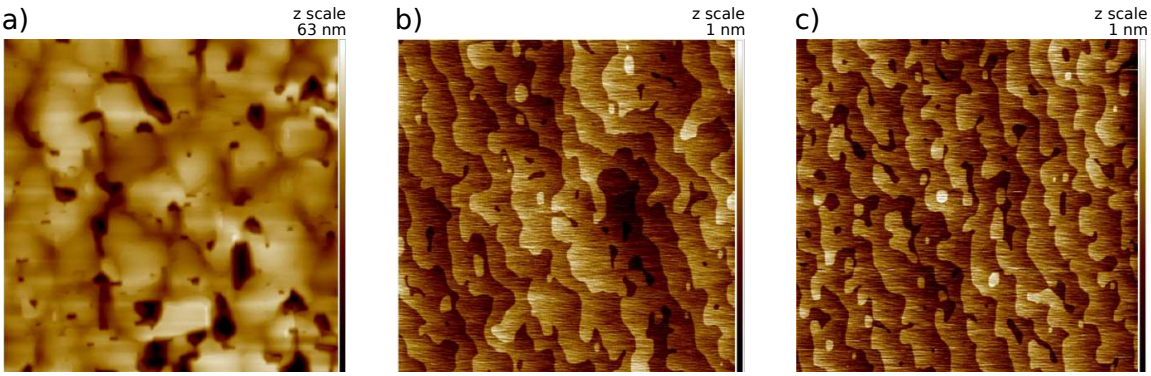

Figure 3.3: 4×4 µm^2 AFM images of GaAs regrowth (300 nm) following full-wafer plasma etching: a) control wafer, no treatment post ICP-RIE etching (RMS roughness R_q = 8.25 nm) b) prepared by NH_4OH deoxidation of the GaAs surface post plasma etching (R_q = 0.16 nm) c) prepared by NH_4OH deoxidation followed by a dry O_3 reoxidation and H_4OH deoxidation post plasma etching (R_q = 0.14 nm).

and high roughness (RMS roughness R_q = 8.25 nm), the two wafers treated with ammonia had visible step edges, characteristic of a step-flow growth of GaAs. The post-epi surface quality is equivalent to that of a raw GaAs substrate (R_q = 0.16 nm and 0.14 nm). This indicates that both treatments can be used for surface cleaning. The single NH_4OH deoxidation is sufficient to restore a good surface quality, and the GaAs consumption caused by the reoxidation and additional deoxidation do not affect the surface topography. To ensure extra safety, the latter surface cleaning was used in the following works.

3.2.3. Selective Area Growth of GaAs Following Ridge Etching

Following works on the full-wafer etching and regrowth, the same processes were applied to the selective area growth (SAG) of GaAs after ridges etching.

6 µm-wide ridges were formed by ICP-RIE etching of a raw GaAs wafer capped with a hardmask, covering the orientations $[0\bar{1}\bar{1}]$, $[0\bar{1}1]$ and in between. A bilayer dielectric hardmask is used for etching and selective growth, and composed of a 30 nm-thick layer of SiN deposited by PECVD (plasma enhanced chemical vapor deposition) at 400 ℃ and a 150 nm-thick layer of SiO_2 deposited by TEOS-PECVD at 400 ℃. Both dielectrics have high stability in NH_4OH, but that of SiN is even higher [182], motivating its use as the first layer to protect the GaAs upper surface. SiO_2 is used as the top layer due to having more experience with using it for SAG at LTM [183].

Cross-sectional SEM images of the ridge sides are shown in Fig. 3.4, following SAG. A small amount (10%)of Al was incorporated in the grown material to provide a refractive index contrast, as proposed in section 2.2.2. The two ridge orientations exhibit very different profiles with an AlGaAs overgrowth on the ridge edge for the $[0\bar{1}\bar{1}]$ orientation, which is absent for the $[0\bar{1}1]$ orientation.

Since the GaAs ridges are used to form optical waveguides, the $[0\bar{1}1]$ orientation without overgrowth should be preferred. According to reference [184], the growth rate on the ridge sidewall in the $[0\bar{1}1]$ orientation is non-null, despite being small, which should be sufficient to

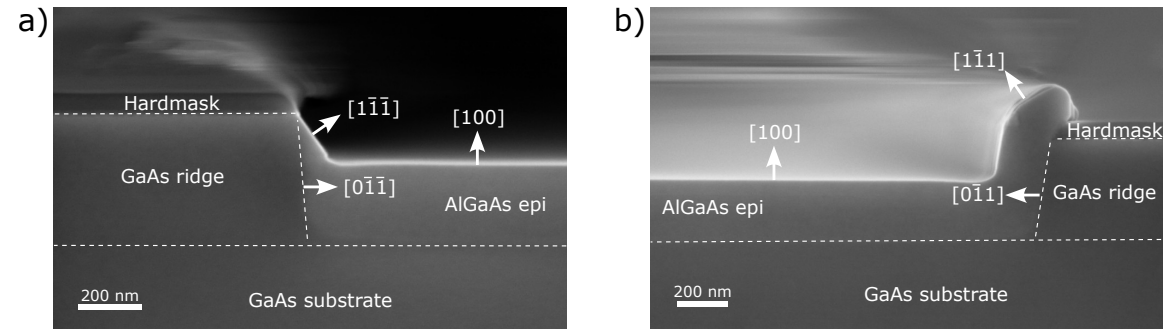

Figure 3.4: Cross-sectional SEM images of the ridge sides following SAG, perpendicular to the ridge direction: a) ridge along the [0$\bar{1}$1] axis and b) ridge along the [0$\bar{1}\bar{1}$] axis

realize a proper junction between the ridge and the SAG material.

3.2.4. Bonding of GaAs on Si

The bonding of GaAs on silicon, key to the integration of III-V on silicon, is realized by means of direct oxide bonding to obtain a transparent bonding interface capable of sustaining high temperatures. On the silicon side, the oxide is quite straightforward to obtain, either by thermal oxidation of the raw wafer, or chemical-mechanical polishing (CMP) of the waveguides capping (for patterned SOI wafers), which is a standard process of the SOI manufacturing. However, the most challenging part is the preparation of GaAs wafers with a low-roughness SiO_2 capping.

Two process-flows have been developed and are presented hereafter. In both case, the GaAs wafer is prepared with an ammonium sulfide ($(NH_4)_2S$) cleaning and scrubbing with NH_4OH prior to SiO_2 deposition, to promote the adhesion of SiO_2. In previous tests, the adhesion of SiO_2 was observed to be the most challenging aspect of this bonding method. Next, the two processes differ in the SiO_2 deposition. In the first case, a 600 nm-thick SiO_2 layer is deposited by PECVD using silane (SiH_4) as a precursor. Following thermal annealing, the SiO_2 is polished by means of CMP down to 300 nm to provide a smooth surface. Attempts to polish it thinner caused delamination of the SiO_2 when its thickness reached about 150 nm. For the other process, the deposited SiO_2 layer is much thinner (50 nm), preserving the original surface smoothness, so that CMP polishing is not required. Following that, the wafers are annealed again to dry them, subjected to a last surface treatment, bonded and annealed at 300 ℃.

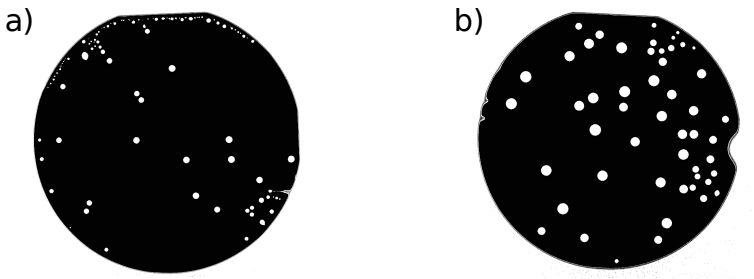

Figure 3.5: SAM images of bonded GaAs on Si wafers. The white spots correspond to bonding defects. a) Process with 600 nm SiO_2 deposition and CMP. b) Process with 50 nm SiO_2 deposition.

Scanning acoustic microscope (SAM) images of the bonded wafers are shown in Fig. 3.5, demonstrating overall good bonding quality with few defects. The process using a thin SiO_2 deposition has the advantage of simplifying the process flow since it does not require CMP and the associated thermal annealing. Given that the SiO_2 CMP is the critical step of the first process-flow and often resulted in delamination of the SiO_2 prior to developing the presented working process-flow, it is strongly beneficial to have a way to do without it. However, from the SAM images, the CMP appears to help reduce the density and size of bonding defects. In addition, in the case where the original wafer surface is too rough for bonding, the thin SiO_2 deposition cannot restore a sufficient surface smoothness. For the first generation of prototypes using a III-V membrane bonded on silicon (section 3.4.1), both bonding processes will be employed to help refine our choice. We will see that the process with CMP gives the best results, in particular when a DWELL stack is employed.

3.3. Prototyping of LCI LED on a GaAs Substrate

In this section, the etching, surface preparation and SAG processes developed in the previous section are used to realize a first generation of LCI devices. This is the first step discussed in the introduction of this chapter, aiming at addressing the challenge of the fabrication of horizontal p-i-n structures suitable for the LCI of free carriers in the active medium. So far, these devices are fabricated on a GaAs substrate with InGaAs MQW as a light emitting medium to mitigate the challenges associated with bonding on silicon and the growth of InAs DWELL. An AlGaAs cladding is used to isolate the active stack from the GaAs substrate, as presented in section 2.2.2.

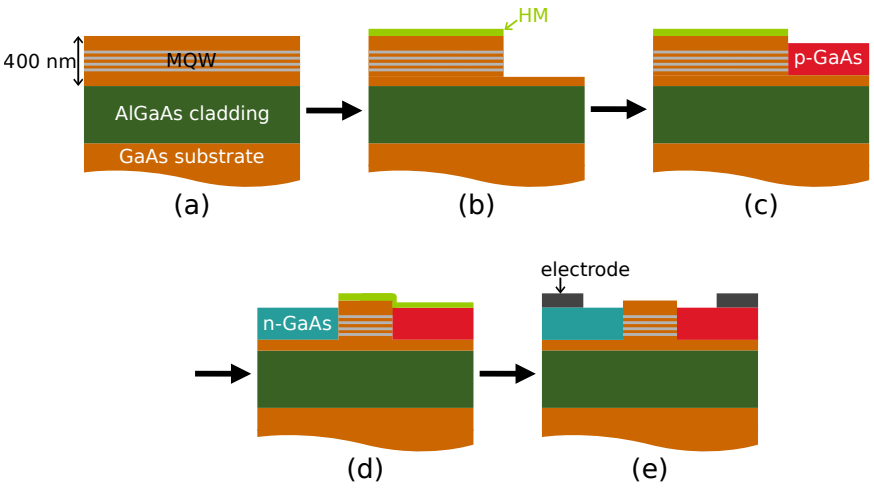

Figure 3.6: Cross-sectionnal schematic overview of the InGaAs/AlGaAs MQW lateral-current injection lasers on a GaAs substrate process-flow. a) Epitaxy of an AlGaAs cladding layer and of the active stack (from Fig. 2.12.a) on a 100 mm GaAs substrate. b) Hardmask (HM) deposition, photolithography, etching of the hardmask and partial etching of the active stack. c) Surface preparation and SAG of p-doped GaAs. d) Repetition of steps (b-c) for the SAG of n-doped GaAs. e) Back-end.

3.3.1. Fabrication

The process-flow for the fabrication of these devices is presented as a schematic cross-section in Fig. 3.6. The lot is composed of three 100 mm GaAs wafers. Device variations covers the length of the active region (1 mm, 1.5 mm, 2 mm and 3 mm), active region width (1 µm, 2 µm, 4 µm, 6 µm, 8 µm and 10 µm) and rib-edge to electrode distance (1 µm, 2 µm, 3 µm and 5 µm).

First, a 600 nm-thick $Al_{0.6}Ga_{0.4}As$ UID cladding is grown on the wafers, followed by a 150 nm UID GaAs SCH, 5 $In_{0.12}Ga_{0.88}As$ QW with $Al_{0.25}Ga_{0.75}As$ barriers and a 185 nm SCH. The total SCH and MQW thickness is 400 nm, and the photoluminescence (PL) peak wavelength of the MQW is 902 nm as illustrated in Fig. 3.7. The difference in thickness of the two SCH is aimed at centering the MQW over the maximum of the optical field, shifted downwards due to the lower cladding (AlGaAs) having a lower index contrast with the active stack than the upper cladding (air). The chosen values were found from Lumerical MODE simulations to yield the highest optical confinement factor in the MQW.

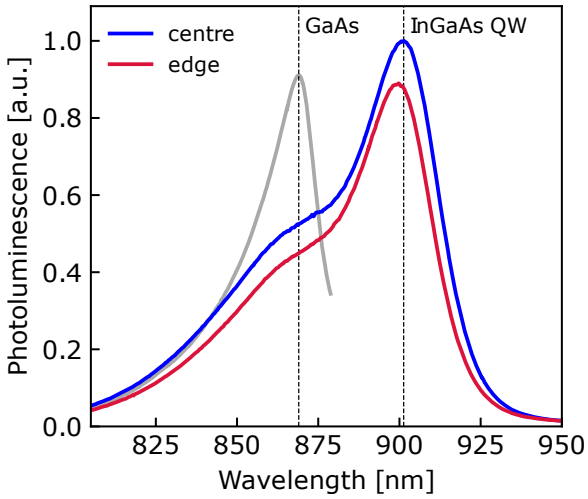

Figure 3.7: RT photoluminescence spectrum of the InGaAs MQW epitaxial stack. Gray is the PL peak for GaAs only, measured from a test wafer.

After that, the bilayer dielectric hardmask as presented in section 3.2.3 is deposited on the wafer. Following coating, exposure and development of a positive photoresist, the hardmask is etched by ICP-RIE using a CHF_3/O_2 gas mixture. Next, the photoresist is stripped and the III-V stack is etched by ICP-RIE using a Cl_2/Ar gas mixture to form reference alignment marks. This step is used to calibrate the rate of III-V etching and its control by laser interferometry. The accurate control of the etching depth during formation of the SAG cavities is of major importance due to the low thickness of the III-V membrane. The etching depth should be as large as possible to allow for a thicker SAG of doped GaAs and reduced electrical series resistance. However, it is also important that the etching stops within the III-V membrane (in particular in later prototypes where the underlying layer is SiO_2), to preserve a seed for the SAG of doped GaAs. In the laser interferometry endpoint detection technique used here, a laser beam (wavelength λ_{laser} = 678 nm for our equipment) is sent onto the etched surface from outside the chamber (Fig. 3.8). Part of the incident light is reflected by the wafer surface, while

another fraction is reflected by the interface with the underlying layer, forming two reflected beams which dephasing depends on the thickness and refractive index of the etched layer. A camera collects the signal resulting from the interference of the reflected beams. The difference of optical path between two maxima of the signal is λ_{laser}, meaning the etch depth during a time period T between these maxima is $\lambda_{laser}/(2n_{layer})$ with n_{layer} the refractive index of the etched layer. Post-process, the etch depth is measured by mechanical profilometer for better accuracy. After calibration, the etch duration is chosen to obtain the target etch depth.

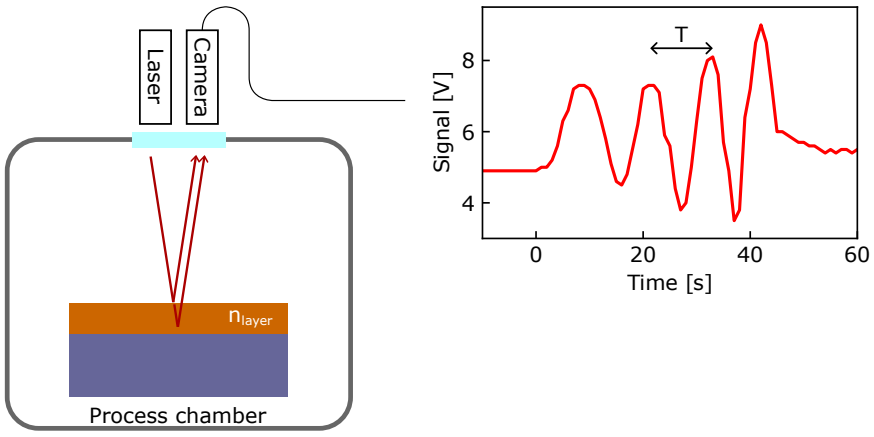

Figure 3.8: Schematic of the Laser interferometry endpoint detection setup and example of recorded interference signal. The signal was recorded for the etching of a 400 nm-thick GaAs membrane on SiO_2/Si. The plasma is turned on at time = 0 s and off at 45 s.

Following that, the hardmask used to form the alignment marks is removed by wet etching using buffered oxide etch (BOE) and a new dielectric hardmask is deposited. Next, the same processes are used with a second photomask to open areas for the SAG of p-doped GaAs. The etching depth for the p-GaAs SAG, measured by mechanical profilometer, is 320 nm for the first wafer and 300 nm for the following ones. ICP-RIE allows for anisotropic etching, so the active core is formed with vertical sidewalls. After cleaning of the wafer using the NH_4OH – O_3 – H_4OH sequence presented in section 3.2.2, p-doped GaAs is selectively grown using Zn as a dopant. The target doping concentrations are 1×10^{19} cm^{-3}, 5×10^{18} cm^{-3} and 2×10^{18} cm^{-3}, and the target thicknesses are 170–190 nm to obtain a thickness difference of 130 nm with the active stack, according to the simulations of section 2.2.2. Due to the device architecture, it is not possible to realize an extra-doped contact layer under the contact only without adding extra technological steps, hence the quite high doping levels used for the first wafer. Lower dopant concentrations are used in other wafers to reduce optical absorption but could result in poor contacts. The doped regions did not use AlGaAs as it had been proposed in section 2.2.2 in order not to add extra fabrication complexity, in particular related to the oxidation of AlGaAs or issues with controlling its doping level.

A photograph of a wafer following the p-doped GaAs epitaxy is shown in Fig. 3.9, along with the corresponding mask. It shows that the selectivity of the GaAs epitaxy is not sufficient, as GaAs has partially grown on top of the dielectric mask, in particular in the wider masked areas corresponding to Hall – van der Pauw measurements structures. While this issue was not

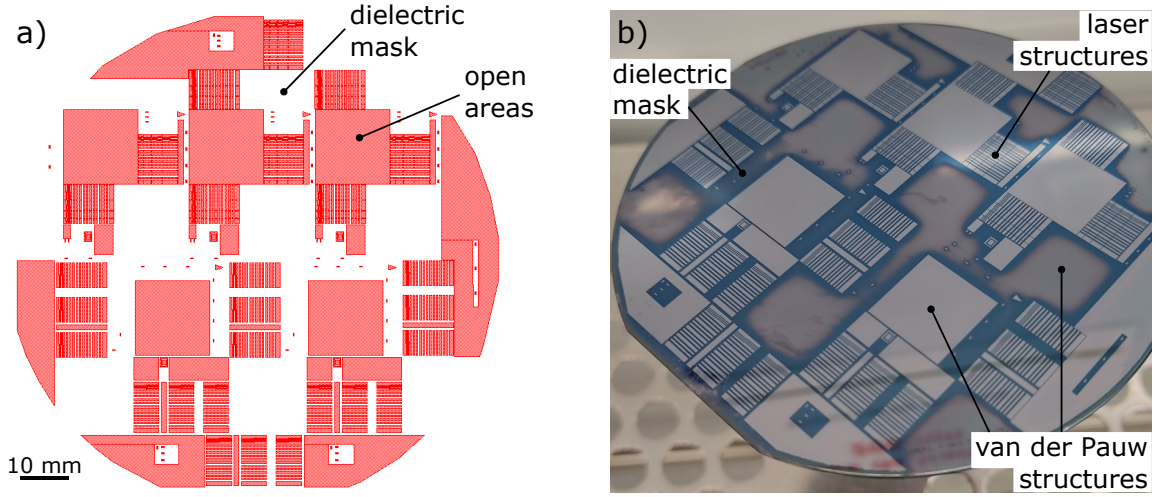

Figure 3.9: SAG of p-doped GaAs. a) Mask of the p-SAG layer. b) Photograph of a wafer following the growth of p-doped GaAs (corresponding to the step illustrated in Fig. 3.6.c). The dielectric mask appears blue while the grey areas correspond to the grown GaAs.

observed in the previous studies (section 3.2.3), we attribute it to the lower fraction of open areas, about 45% compared to 95% in section 3.2.3. Indeed, the lower fraction of open areas locally decreases the precursor consumption and thus increases their local concentration. This explains why the lack of selectivity is particularly visible in the large Hall measurements structures. However, submicron-sized GaAs crystals also grew on the hardmask close to open areas, as exhibited by SEM observations presented in Fig 3.10. Solutions to tackle this issue are explored in section 3.3.3.

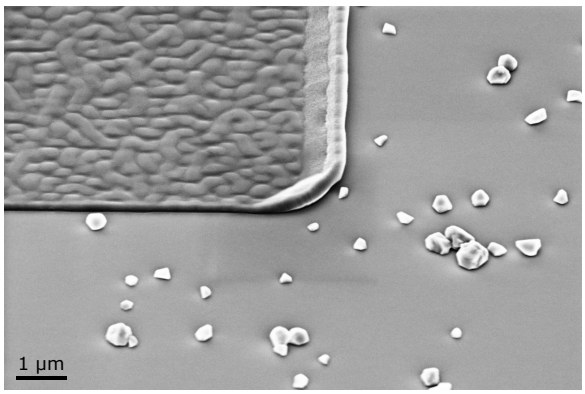

Figure 3.10: SEM image of GaAs grown on the hardmask close to an open region.

Chemical cleaning of the wafers by concentrated hydrofluoric acid (HF) removal of the dielectric was performed to remove unwanted GaAs but did not succeed, and the process was continued with the parasitic GaAs remaining. Hopefully, the density of GaAs crystals close to the areas of interest is low enough not to interfere too strongly with the process.

The next block consists in the realization of the n-doped regions. A new bilayer dielectric hardmask is deposited, and the III-V stack is etched with the same processes as for the etching used to realize the p-doped regions. A III-V thickness of 300 nm was etched on all three wafers.

However, it must be noted that due to the parasitic growth of GaAs on the hardmask, alignment marks were partially covered as illustrated by Fig. 3.11, making it difficult to accurately align the lithographic mask with previous levels.

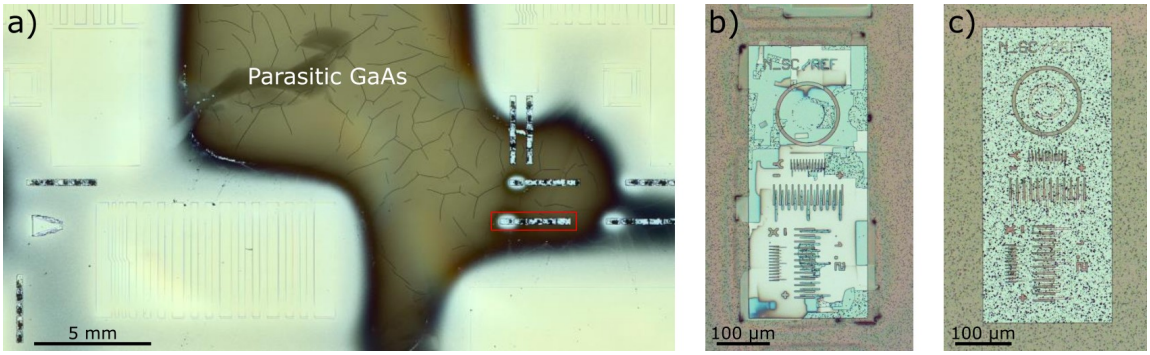

Figure 3.11: Optical microscope images of the wafers following n-SAG lithography. a) Low magnification view of the parasitic GaAs growth. A set of alignment marks is shown in red. Close-up of the n-SAG alignment marks of the first (b) and second (c) wafer.

After surface cleaning, GaAs is grown in the opened areas using silicon as a dopant. The target doping concentrations are 5×10^{18} cm^{-3}, 3×10^{18} cm^{-3} and 2×10^{18} cm^{-3} and the target thickness is 170 nm for all three wafers, to obtain a thickness difference of 130 nm with the active stack.

Following the fabrication of the p-i-n structure, contacts are realized to allow for electrical pumping of the diode. The hardmask used for the SAG of n-doped GaAs is removed using BOE. Both the contacts on the p-doped and n-doped GaAs are deposited by evaporation, patterned by lift-off and then annealed. The metal stack on n-GaAs is Ni/Ge/Au/Ni/Au, and Ti/Pt/Au on p-GaAs. Finally, facets are formed by wet etching using an H_20:H_20_2:NH_4OH (SC1) solution [185].

3.3.2. Morphological Characterization

Further morphological characterizations of the devices were performed at the end of the fabrication process.

A SEM bird's eye view of a fabricated diode is presented in Fig. 3.12. The sample was cleaved perpendicular to the diode to provide a cross-sectional view of the stack.

The p-i-n structure is clearly visible with metal contacts deposited atop the semiconductor, as well as the underlying AlGaAs cladding. A scanning transmission electron microscope image of a sample prepared by focused ion beam (FIB-STEM) is presented in Fig. 3.13 to provide a more detailed view of the interface between the active core and the selectively grown GaAs. This interface appears continuous, with no visible structural defects.

However, several issues can be identified from these images. First, the thickness of the GaAs regrowth is much larger than expected. The total GaAs thickness to the side of the active core is 570 nm, making it 170 nm thicker than the active core when it should have been 130 nm thinner for optical guiding, as shown by the simulations of section 2.2.2. As a consequence, the

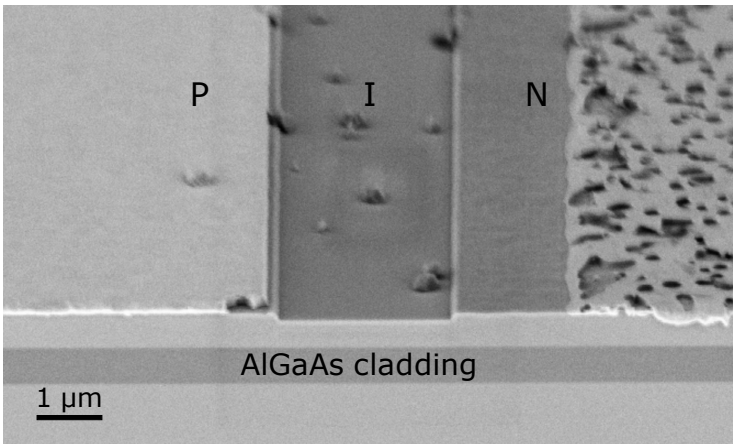

Figure 3.12: SEM bird's eye view of a fabricated diode. Sample prepared by cleaving.

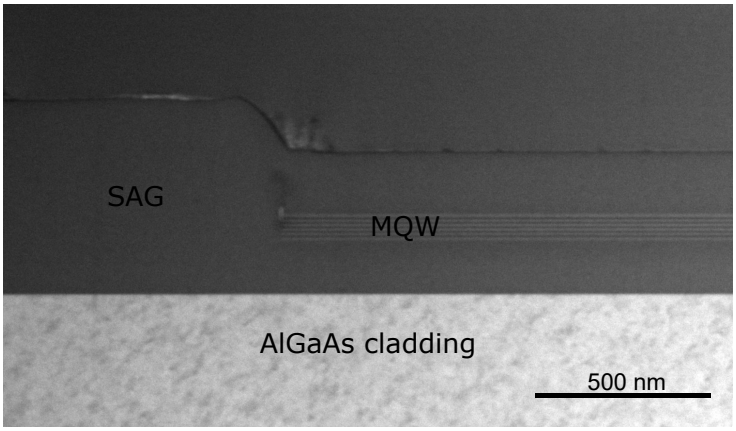

Figure 3.13: FIB-STEM image of a fabricated device showing the selectively grown GaAs.

optical field cannot be guided in the structure, a necessary condition for feedback and light amplification. In addition, submicron-sized GaAs crystals have grown over the masked intrinsic region, as discussed before, and would have diffracted guided light and led to substantial propagation losses. The metal contacts also have some flaws: the edge of the contact on the p-doped GaAs comes very close to the intrinsic core and would have caused huge absorption losses if light was guided in the structure. This is caused by the misalignment of the lithographic mask, due to the parasitic growth of GaAs having damaged the alignment marks and would be solved by fixing the SAG. Depending on the direction, the misalignment can be up to 2 µm. Finally, the metal pads deposited on the n-doped GaAs suffer from a poor structure with a high density of craters. Their consequences on the electrical current injection will be discussed in Chapter 4.

3.3.3. Corrections to the SAG Parameters

As we have just explained, many of the issues observed in the fabrication of this first generation of prototypes arise from the insufficient selectivity of the SAG, and from its growth speed, which needs to be recalibrated for the masks used. This subsection is devoted to fixing the two aforementioned issues.

First, a new set of lithographic masks was designed with the goal of preventing the parasitic growth of the larger GaAs clusters on the hardmask, by filling the whole mask out of the diode and TLM areas with p-SAG and n-SAG dummies forming a checkerboard pattern. A first sample with the MQW stack grown on a raw GaAs wafer was etched with this new mask, then subjected to the usual surface preparation and used for the SAG of GaAs with otherwise identical parameters as the previous samples. Thin AlGaAs markers were incorporated at regular time intervals to help visualize the growth planes and rates. SEM and FIB-STEM observations of this sample are shown in Fig. 3.14. From a bird's eye view of the surface of the wafer, it can

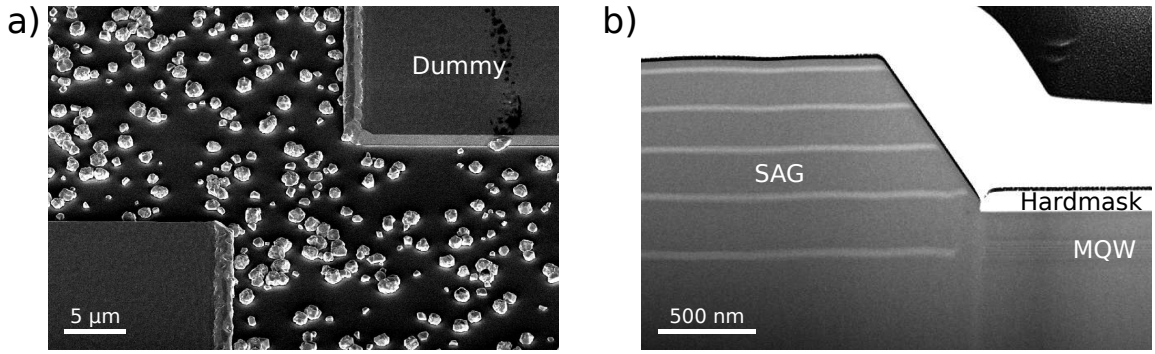

Figure 3.14: a) SEM bird's eye view of the surface of the first sample and (b) FIB-STEM cross-sectionnal image of a $[0\bar{1}1]$ oriented ridge.

be seen that the use of dummies did not solve the selectivity issue. Removing the large Hall measurement structures prevented the growth of a continuous polycrystalline GaAs layer in these regions, but small crystals still grew on the wafer surface. From Fig. 3.14.b, a decrease in the growth rate during epitaxy is observed. The thickness of the GaAs layers between two

AlGaAs markers decreases from 262 nm for the first one to 173 nm for the last one, despite using the same growth parameters, including duration. We estimate that this indicates that in the first phase of the growth, the MOCVD precursors are primarily consumed by the SAG. However, as GaAs crystals begin to appear and grow in size on the hardmask, they also contribute to the precursor consumption, hence reducing the SAG rate.

A second sample was grown, reducing the susceptor temperature from 640 ℃ to 600 ℃ to improve the growth selectivity. In addition, the hydrogen dilution flux was increased by a factor 4.5 to further improve selectivity. The result is shown in Fig. 3.15.a, with no GaAs grown on the hardmask over the whole surface. With these new growth conditions, the desired growth selectivity is achieved. Finally, a third sample was used for calibration of the epitaxial growth rate (Fig. 3.15.b), only changing the growth duration.

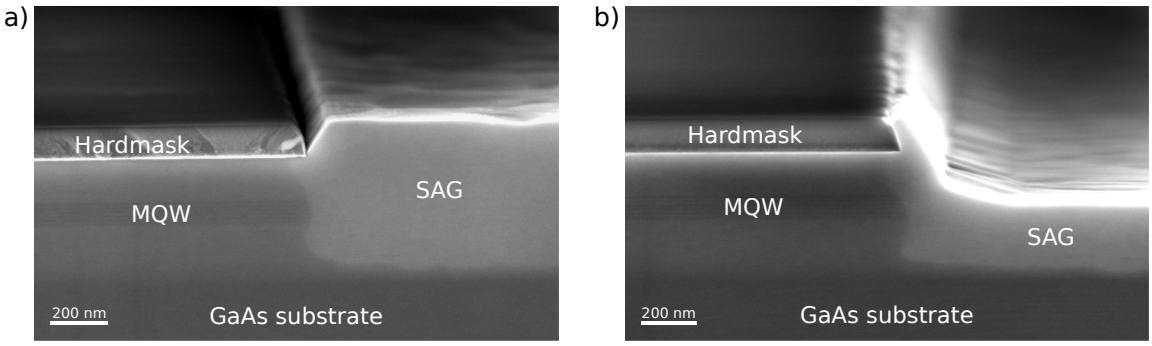

Figure 3.15: Cross-sectionnal SEM images of the second (a) and third (b) samples.

3.4. Prototyping of III-V Membrane Lasers on Oxidized Silicon

Following the realization of LCI devices on a GaAs substrate, the correction to the SAG conditions and the development of a process-flow for the bonding of GaAs on silicon, the next step was to combine these to realize LCI prototypes on silicon as illustrated schematically in Fig. 3.16.

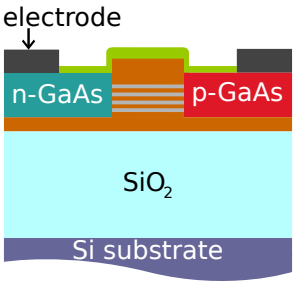

Figure 3.16: Schematic cross-section of one diode of the prototype design.

As an intermediary step towards the fabrication of lasers coupled with a SOI circuit, this generation of devices is fabricated by bonding the III-V on a bulk oxidized silicon wafer. These prototypes aim at demonstrating the regrowth of GaAs following bonding on silicon and integrating the corrections to the SAG in the fabrication of a complete structure. In addition,

the SiO_2 layer under the III-V membrane could already provide benefits in terms of optical confinement in the vertical direction.

3.4.1. Fabrication

This section is dedicated to the fabrication of the aforementioned prototypes. A great part of the fabrication process-flow is identical to the one presented in section 3.3.1 with the process corrections presented in section 3.3.3, so these aspects will be covered briefly so we can focus on the specifics of bonding and fabrication on silicon.

The process-flow for the fabrication of these devices begins with the growth of the III-V stack on a 100 mm GaAs substrate (Fig. 3.18.a). The III-V stack includes a 100 nm-thick InGaP etch-stop layer (ESL) grown on the GaAs wafer just before growing the active stack. Active stacks with five InGaAs QW or four InAs DWELL, as presented in section 2.2.2, are used. The photoluminescence peak wavelength of the MQW and DWELL stack are respectively 915 nm and 1.27 µm.

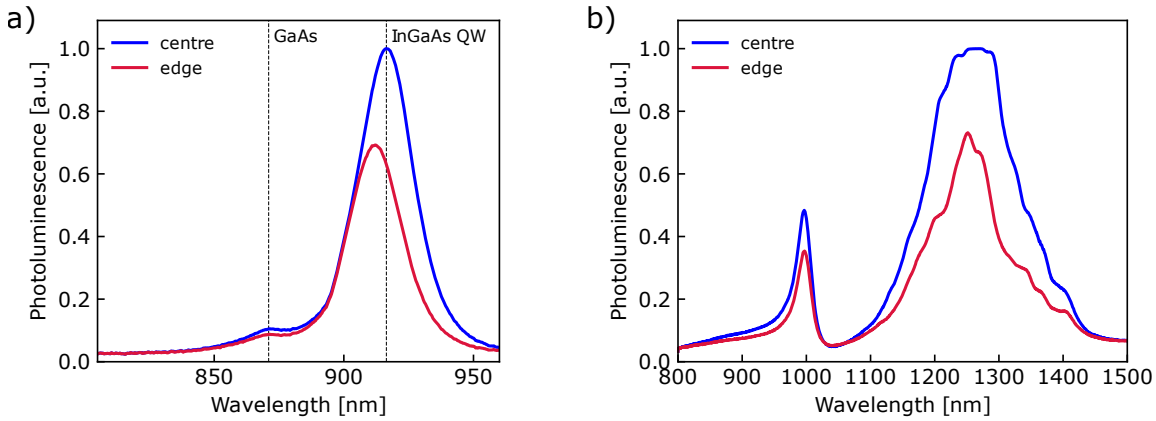

Figure 3.17: RT photoluminescence spectra of the InGaAs MQW (a) and InAs DWELL (b) epitaxial stack.

The two bonding process-flows presented in section 3.2.4 and illustrated in figures 3.18 and 3.20 are used with both types of active stack (MQW and DWELL).

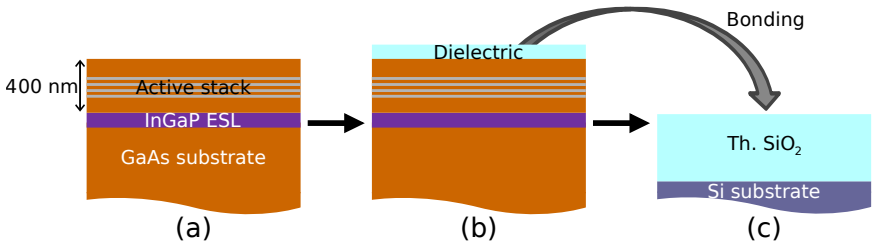

Figure 3.18: Cross-sectionnal process-flow overview of the oxide bonding of GaAs-based III-V stacks (a) on silicon using a 50 nm-thick SiO_2, or 10 nm SiN + 40 nm SiO_2 deposition (b) followed by direct bonding (c).

In addition to the results presented in the initial study (section 3.2.4), some samples were prepared with a thin (10 nm) SiN film deposited on GaAs before the SiO_2. This is to benefit from the high interfacial adhesion of the SiN/GaAs system [186] and prevent delamination during wafer processing (in particular during CMP) or with aging. The silicon receivers are

prepared by thermal oxidation of 100 mm wafers at 1050 ℃ for 13 hours in water vapor (ultra high purity steam) to produce a 2 µm-thick oxide.

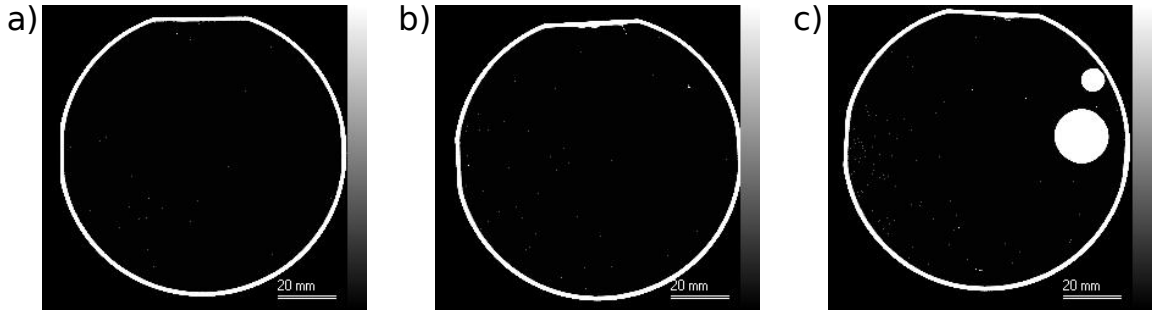

Figure 3.19: SAM image of the bonded GaAs on Si wafers. b) has the SiN layer on the GaAs while a) and c) do not.

SAM images of three wafers post-bonding are presented in Fig. 3.19. The overall bonding quality for the MQW stack is excellent, whether a SiN was used (Fig. 3.19.b) or not (Fig. 3.19.a). Only one wafer had two large localized bonding defects (Fig. 3.19.c). However, one wafer with the DWELL stack was included in this lot but could not be bonded. Indeed, due to their 3D structure, QDs induce surface topography which is propagated to the dielectric capping, causing surface roughness that prevents bonding.

Another lot was run in parallel, using the bonding process-flow with a thicker dielectric deposition and polishing (Fig. 3.20). Once again, a set of wafers used a 10 nm-thick SiN adhesion-enhancing layer before deposition of the SiO_2 to help prevent its delamination.

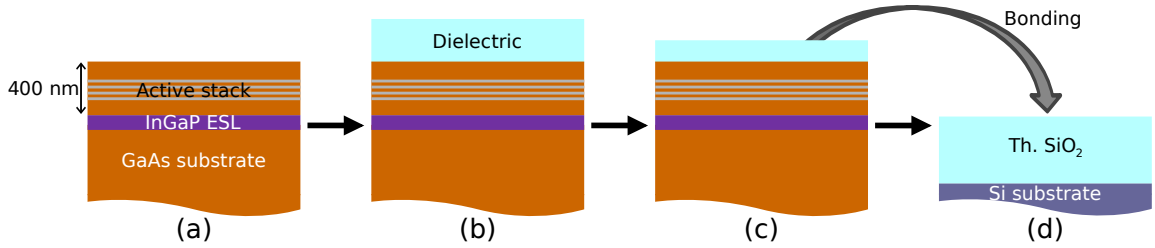

Figure 3.20: Cross-sectionnal process-flow overview of the oxide bonding of GaAs-based III-V stacks (a) on silicon using a 600 nm-thick SiO_2, or 10 nm SiN + 590 nm SiO_2 deposition (b) followed by CMP to produce a low-roughness surface (c).

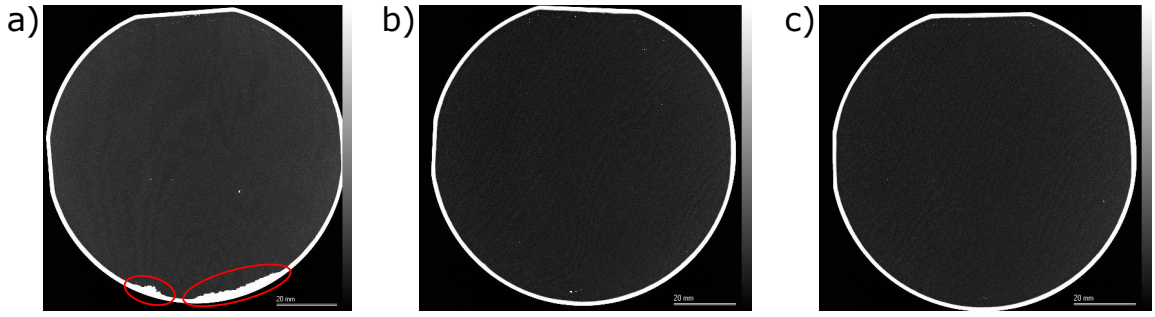

Figure 3.21: SAM image of the bonded GaAs on Si wafers. a) MQW stack without the SiN adhesion-enhancing layer. b) MQW stack with the SiN adhesion-enhancing layer. c) DWELL stack without the SiN adhesion-enhancing layer.

SAM images of the wafers following bonding are presented in Fig. 3.21. As for the previous

bonding process-flow, the overall bonding quality for the MQW stack is excellent with the only flaws occurring on the edge of the wafer (Fig. 3.21.a). This is caused by delamination of the SiO_2 layer during CMP as can be seen from the comparison of the photograph of a III-V wafer following CMP (Fig. 3.22), just before bonding, and the corresponding post-bonding SAM image (Fig. 3.21.a). The areas with visible SiO_2 delamination correspond (circled in red) to the bonding defects evidenced by the SAM. The wafer illustrated here did not use the SiN adhesion-enhancing layer.

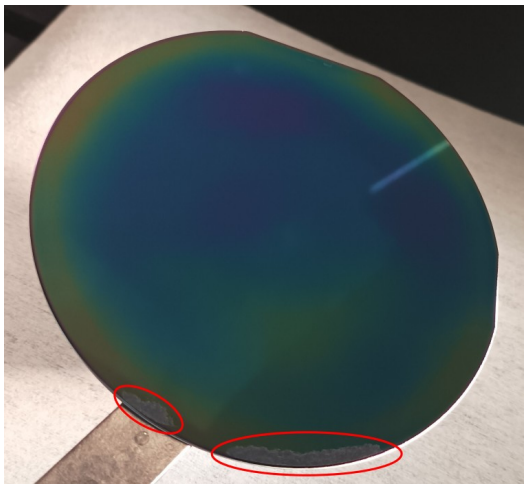

Figure 3.22: Photograph of a III-V wafer capped with SiO_2, without the SiN adhesion-enhancing layer, following CMP. Delamination of the SiO_2 (blue-green hue) is visible on the edge of the wafer (bottom of the picture, exposed gray GaAs), leading to matching bonding defects visible in Fig. 3.21.a.

We observed that all three wafers with the MQW stack and without the SiN adhesion-enhancing layer exhibited approximately the same extent of delamination. Meanwhile, one wafer of this lot used the MQW stack and the SiN adhesion-enhancing layer and did not suffer from SiO_2 delamination (Fig. 3.21.b). Two wafers with the DWELL stack were also included in this lot, one with the SiN adhesion-enhancing layer and one without (Fig. 3.21.c). Both were successfully bonded with an excellent bonding quality.

To summarize the bonding results, we have successfully bonded GaAs wafers with an active stack on oxidized silicon using two process-flows and introducing a new variant in each of them, namely the use of a SiN adhesion-enhancing layer on the GaAs before SiO_2 deposition. The process-flow without CMP has the advantage of reducing the number of technological steps and was successfully used to bond wafers with the MQW stack. However, it failed at bonding wafers with the DWELL stack due to the roughness induced by the QD. The process with CMP allowed for smoothing the roughness caused by the QD, permitting bonding of the wafers with the DWELL stack. Regarding the usefulness of the SiN adhesion-enhancing layer, it seems unnecessary for the process-flow without CMP. However, for the process-flow with CMP, the SiN layer appears to have helped prevent SiO_2 delamination otherwise occurring on the edge of the wafer with the MQW stack. Although the delamination of SiO_2 was quite limited for this lot, it could become more of an issue as thinner oxide layers will be required when coupling

light with an SOI waveguide, reinforcing the usefulness of a SiN adhesion-enhancing layer.

After bonding, the GaAs substrate is thinned down to 100 µm by grinding and the remaining substrate is removed by wet etching using an SC1 solution stopping on the InGaP ESL, much less reactive to SC1. Next, the InGaP ESL is etched using HCl:H_3PO_4 so only the active stack remains on the silicon substrate.

From this point on, the process-flow is the same as for the devices fabricated on a GaAs substrate (Fig. 3.6) but only the wafers bonded without CMP were processed due to fabrication delays for the CMP lot. The p-i-n structure is fabricated by two cycles of etching, surface preparation and SAG of doped GaAs. To ensure the best SAG results, the new parameters of section 3.3.3 were used and a test wafer was used for both SAG to measure the growth rate and adjust the growth duration accordingly. Preventing the growth of GaAs on the hardmask resulted in preserved alignment marks, allowing for a facilitated and more accurate alignment of the photolithography mask for all subsequent layers. SEM images of a device following etching of the epitaxial stack for the realization of the n-doped SAG are provided in Fig. 3.23, illustrating the p-doped GaAs, the etched area where n-doped GaAs will be grown, and in between, the epitaxial stack ridge. The etching sidewalls are quite rough, hence the NH_4OH – O_3 – NH_4OH surface preparation.

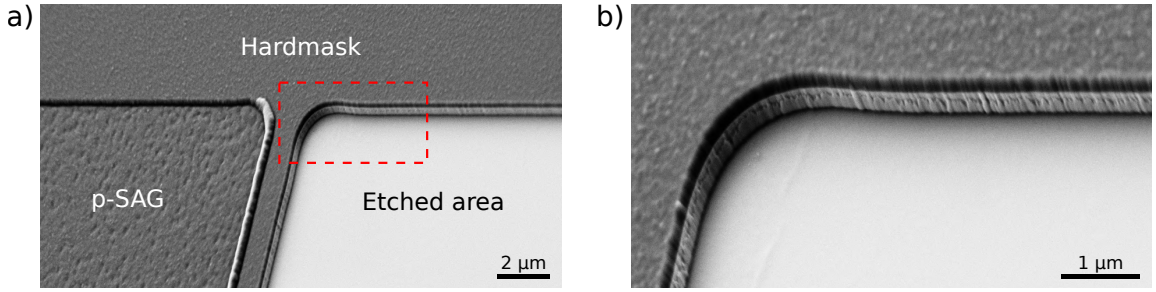

Figure 3.23: SEM image of the III-V openings for the SAG of n-doped GaAs, post-etching. a) General view. b) Close-up of the etch sidewalls.

Following the growth of n-doped GaAs, a SiN capping layer is deposited on the wafer. One more photolithography was used to open the capping layer and form the metal contacts on the p-doped GaAs by evaporation and lift-off, and repeated for the metal contact on the n-doped GaAs. The Au thickness was increased as compared to the previous lot to solve issues observed with the n-contact.

Finally, the facets were formed by wet etching using an SC1 solution, as for the previous lot, or by cleaving.

3.4.2. Morphological Characterization

The fabricated devices were observed by SEM and high-resolution FIB-STEM. Fig. 3.24 presents a SEM bird's eye view of one end of a diode, showing the p-i-n structure with the active core, the selectively grown doped GaAs and the electrodes. A facet etched using the SC1 solution is also visible. Thanks to the improvements in the SAG parameters, no GaAs has grown on

top of the hardmask, and the alignment marks were preserved. Owing to this, the geometry of the fabricated device exhibits much better agreement with the designed masks in terms of active core width and distance of the electrodes. This should be compared with the previous lot, showing asymmetrical and possibly too close placement of the electrodes with the active core (see Fig. 3.12). Both electrodes have a faultless morphology without craters as observed in the previous lot.

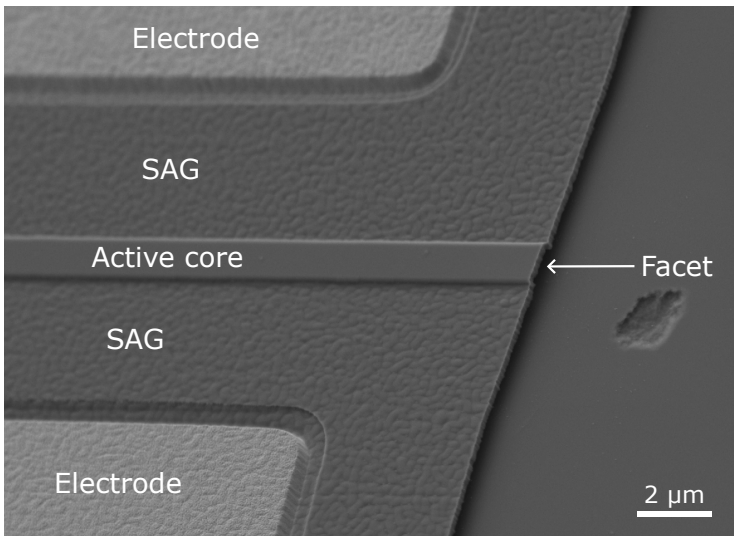

Figure 3.24: SEM bird's eye view of a fabricated device.

A sample was prepared by means of FIB to realize atomic-resolution high-angle annular dark-field (HAADF) STEM images of the active core-SAG interface and of the bonding interface. HAADF is a STEM method where an annular detector is used to collect electrons scattered at a high angle. This allows for a high resolution and high atomic number contrast since the HAADF signal is strongly dependent on the atomic number of the element under the incident electrons. A large-scale image of the sample is shown in Fig. 3.25.

Fig. 3.26 focuses on the interface between the active stack and the selectively grown doped GaAs. In particular, Fig. 3.26.b. presents a close-up of this interface at the intersection of the MQW stack, upper SCH and SAG. The atomic resolution obtained with this image allows us to observe the flawless continuity of the crystal structure at the interface between the initial epitaxy and the doped GaAs regrowth, with no structural defects. This indicates that the NH_4OH – O_3 – H_4OH surface preparation restores a clean, defect-free surface, ready for epitaxy.

Fig. 3.27.a. presents a zoomed-in view of the interface between the crystalline GaAs and amorphous SiO_2 bonding layer. The thickness of the visible oxidized interface layer is about 2.5 nm. The wafer represented in this picture did not use the SiN adhesion-enhancing layer. In addition, an energy-dispersive X-ray spectroscopy (EDX) profile of the present elements, measured on a line perpendicular to the interface is shown in Fig. 3.27.b. According to reference [187], this interface layer consists of GaAs oxide and amorphous arsenic.

To summarize this section, we have fabricated LCI devices by bonding GaAs on oxidized

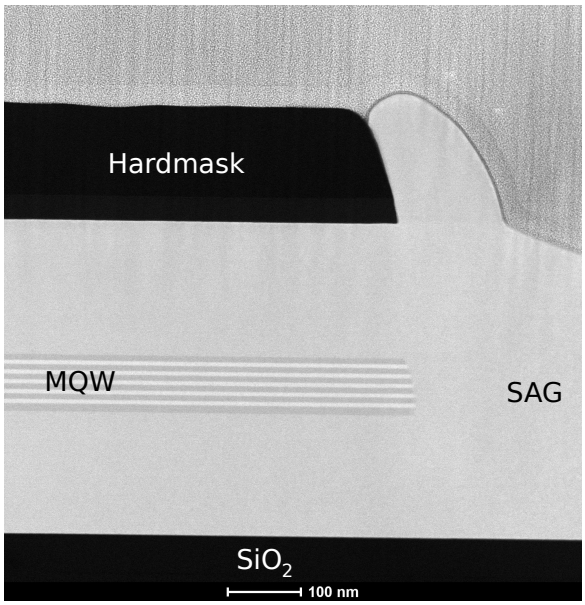

Figure 3.25: HAADF STEM image of a fabricated device.

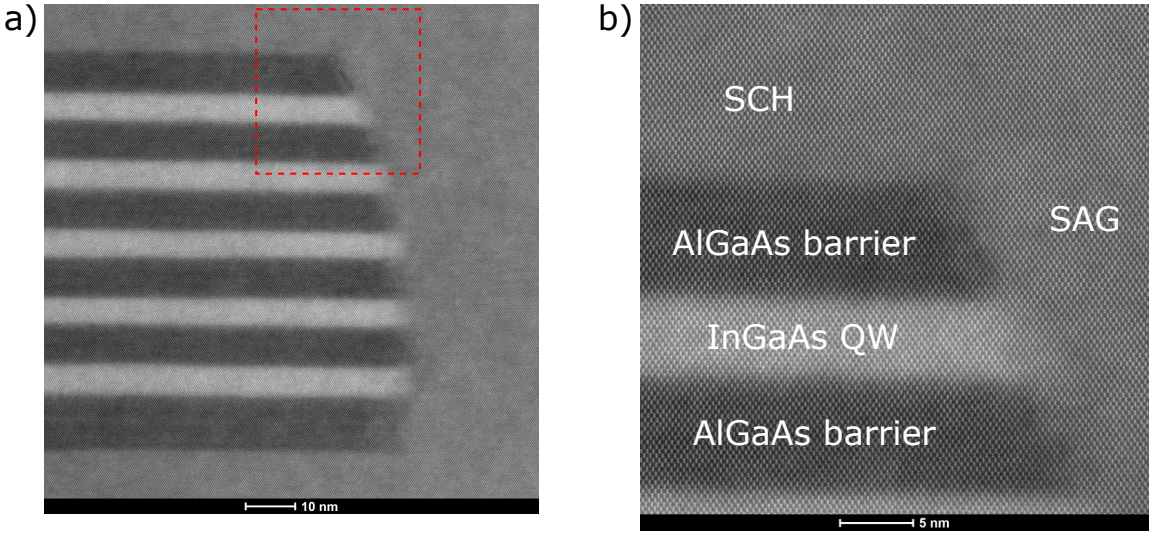

Figure 3.26: Atomic-resolution HAADF STEM image of the SAG interface (a) and close-up view of area enclosed in red (b).

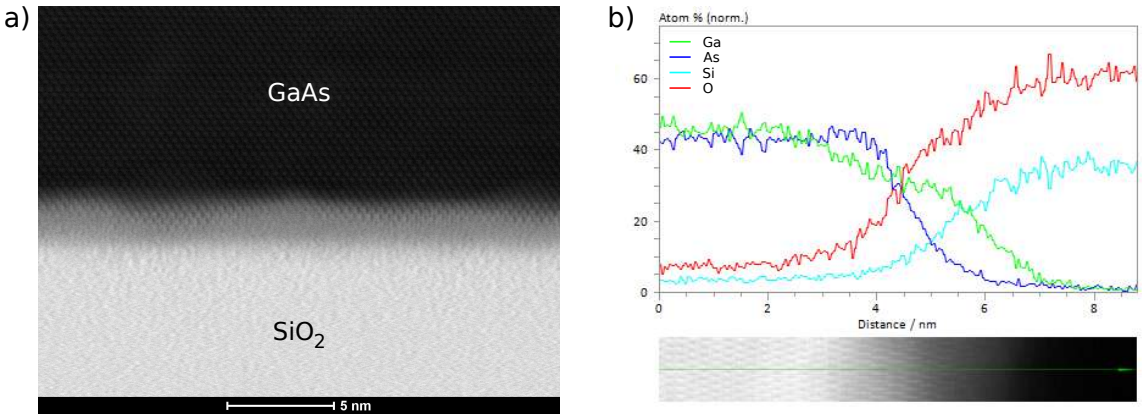

Figure 3.27: Bright-field (BF) STEM image of the GaAs-SiO_2 interface (a) and EDX profile along a vertical line (b).

silicon by two direct oxide bonding processes. Wafers with MQW were perfectly bonded by any of the two processes, while the DWELL stack required using the process-flow with CMP to reduce surface roughness. CMP caused delamination of the SiO_2 capping on the edge of the wafer, which could become a serious issue when thinner oxide layers will be required. A SiN adhesion enhancing layer has been used to improve SiO_2 adhesion on GaAs and suppressed delamination for the prototypes using it. Following substrate removal, the diode was fabricated by a process-flow similar to the one of section 3.3.1, with the corrections proposed in section 3.3.3, greatly improving the morphology of the devices. In particular, atomic-resolution STEM images show the continuity of the crystalline structure at the interface between the initial epitaxy and the selectively grown GaAs. Electro-optical characterizations of these devices are presented in the next chapter, section 4.4.

3.5. Fabrication of the Silicon Photonic Integrated Circuit

This section is dedicated to the fabrication of the SOI PIC. They are fabricated on the 300 mm CEA-LETI platform, using mature processes.

3.5.1. Fabrication

The fabrication process begins with commercial raw 300 mm SOI wafers with a 310 nm-thick SOI atop a 720 nm BOX (Fig. 3.28.a). The top of the SOI is oxidized to obtain the target thickness, and

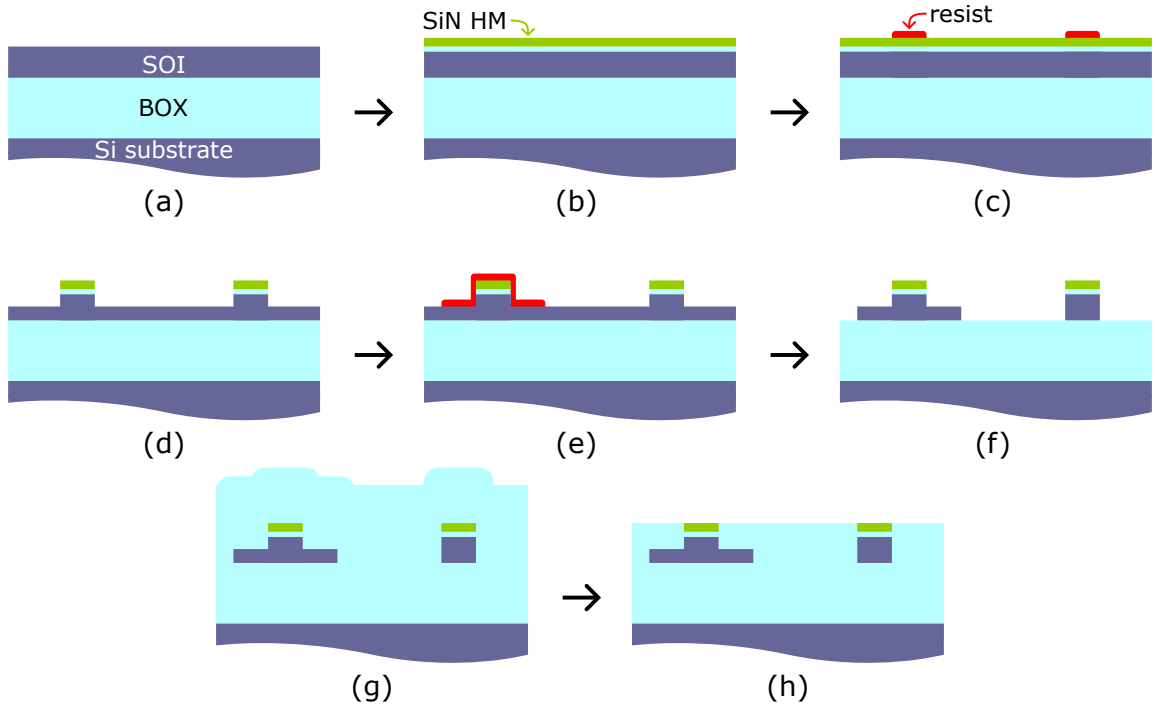

Figure 3.28: Cross-sectionnal schematic of the process-flow for the fabrication of the SOI PIC. a) Raw SOI 300 mm wafers. b) Oxidation of the top of the SOI and SiN hardmask deposition. c) Resist coating, exposure and development. d) Partial etching of the SOI, preserving a 165 nm-thick slab. e) Resist coating, exposure and development (second mask). f) Etching of the SOI down to the BOX. g) SACVD-TEOS capping of the waveguides. h) CMP planarization of the SiO_2 capping.

after etching of alignment marks (not detailed here), a SiN hardmask is deposited by PECVD to protect the SOI (Fig. 3.28.b). Next, a multilayer lithography stack is coated on the wafers, consisting of a spin-on-carbon (SOC) underlayer with planarizing properties and high etch selectivity, a silicon containing anti-reflective coating (SiARC) and finally, a thin (100 nm) layer of positive photoresist. The multilayer system allows for the use of a thin resist layer, necessary to achieve the best focus during exposure. The photoresist is exposed to deep ultraviolet light using an immersion lithography scanner, everywhere except where 305 nm-thick SOI is wanted, and the exposed photoresist is developed (Fig. 3.28.c). Following that, dry etchings are used to etch the multilayer, SiN, thin oxide layer and to partially etch the SOI, leaving a 165 nm-thick slab, and the multilayer is stripped (Fig. 3.28.d). The 165 nm-thick slab corresponds to the slab of rib waveguides and corrugations of the grating couplers. However, at this point it is present everywhere except where 305 nm-thick SOI is wanted (strip waveguides, core of rib waveguides and thicker sections of grating couplers).

After that, a second multilayer is coated and exposed in all areas outside of the rib waveguides and grating couplers, using another photomask (Fig. 3.28.e), and the remaining 165 nm-thick SOI is dry etched with endpoint detection to stop the etching process when the BOX is exposed. This etching is used to form the rib waveguides and grating couplers by removing the slab in all other areas (Fig. 3.28.f).

Finally, the waveguides are capped with 900 nm of SiO_2 by means of sub-atmospheric chemical vapor deposition (SACVD) of TEOS, having superior planarization abilities [188]. After annealing, the SiO_2 capping is planarized by means of CMP, stopping on the remaining SiN hardmask, to obtain a flat surface.

The use of deep ultraviolet immersion lithography at all photolithography steps, combined with OPC methods in the mask design [164] allows for critical dimensions (CD) of about 70 nm.

Due to delays in the fabrication process, we could not bond and process the III-V on these wafers during the time of the thesis.

3.5.2. Morphological Characterization

SEM images were realized prior and post-encapsulation to evaluate the SOI components morphology.

Fig. 3.29 presents a cross-sectionnal SEM image of a strip waveguide, the most basic component of silicon photonics, post-encapsulation and CMP. Due to the fabrication process, the strip waveguide exhibits a trapezoidal shape, an usual feature of silicon photonics waveguides [140].

It can be seen that despite the CMP stopping right on the SiN layer (Fig. 3.29.b), the surface topography is not perfectly flat. This is due to the SiO_2 capping being partially etched around SiN-covered areas due to the partly chemical nature of the CMP process. Profilometer measurements show a step of 5 nm around waveguides at the center of the wafer (12 nm at the wafer edge), and much higher around larger components from other projects of the MPW, such as 23 nm (resp. 45 nm) for echelle gratings at the center (resp. edge) of wafer.

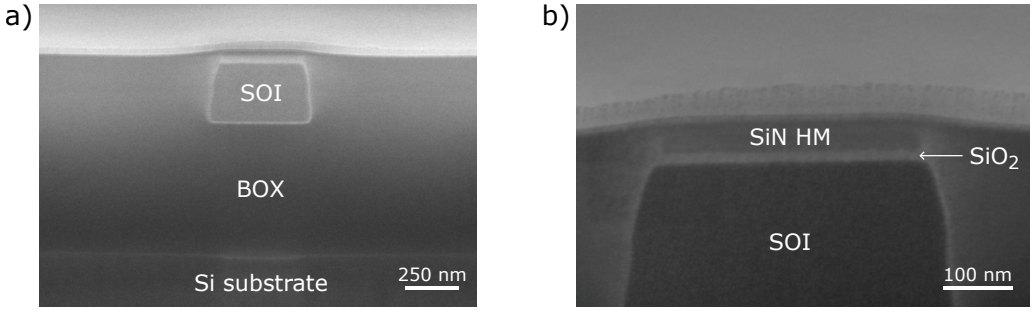

Figure 3.29: Cross-sectionnal images of a SOI waveguide post-encapsulation and CMP, obtained by FIB-TEM. a) General view of the SOI waveguide with BOX and Si substrate. b) Close-up of the top of the waveguide, showing the SiN hardmask.

Bragg reflectors were also put under scrutiny. The constraint we imposed ourselves to fabricate them using only standard PDK layers to facilitate fabrication led to designs with aggressive critical dimensions (CD).

SEM images of the DBR cavity back-mirror made from sidewall corrugations of a strip waveguide are presented in Fig. 3.30, along with the corresponding section of the GDS. In design, this grating has an average width of 2 µm, with 280 nm corrugation width (see Table. 2.3 of section 2.4.2). The fabricated structures seem to exhibit good agreement with the design.

For the front-mirror, observed in Fig. 3.31, the corrugation width is 70 nm, that being 35 nm on each side. This dimension is tiny and resulted in ripples of approximately the right extension in fabrication.

The last illustrated structure is the DBR consisting of a 165 nm-thick strip waveguide with 305 nm-thick posts. The width and length of the posts on the mask are 75 nm and 118 nm respectively, close to the minimal extension allowed by the PDK. Still, all posts were correctly fabricated, even though they exhibit a rather conical shape as it is clearly visible in Fig. 3.33.

3.6. Chapter summary

In this chapter, we have sequentially presented our developments towards the realization of integrated III-V membrane lasers for silicon photonics. A process-flow was proposed, and three main challenges associated with this process flow were identified. They are: the fabrication of thin horizontal p-i-n structures for LCI, the bonding of GaAs on Si and the combination of these two for the fabrication of III-V membrane LCI devices on silicon.

In section 3.2, we tackled the fundamental building blocks required to address the aforementioned challenges. Two surface preparation processes using NH_4OH were found to restore an epi-ready surface, following the ICP-RIE of GaAs. The most aggressive one was combined with ICP-RIE etching of GaAs ridges to perform SAG of GaAs around GaAs ridges, showing the influence of the ridge orientation on the overgrowth of GaAs on the edge of the ridge. In parallel, two process-flows for the direct oxide bonding of GaAs on Si were demonstrated. One uses a simple thin (50 nm) deposition of SiO_2 on GaAs as a bonding layer, while the other one uses a thicker (600 nm) SiO_2 layer later polished by means of CMP to obtain a smooth surface.

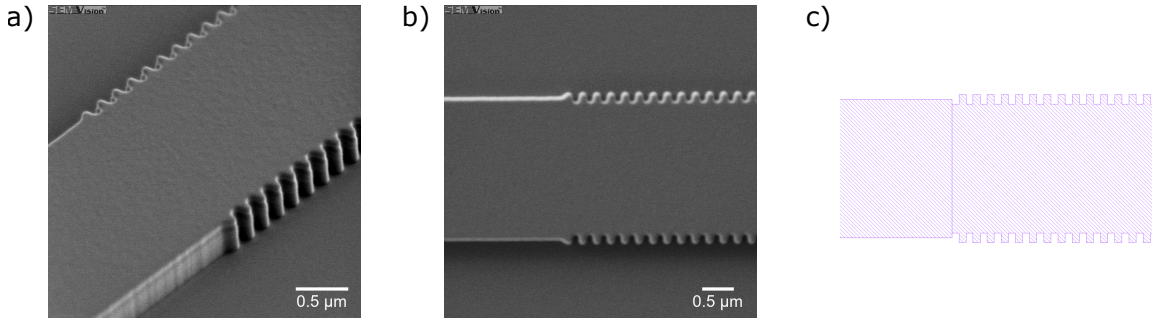

Figure 3.30: SEM images of the sidewall corrugations back-mirror Bragg reflector prior to encapsulation. a) Bird's eye view. b) Top view. c) Corresponding mask layout.

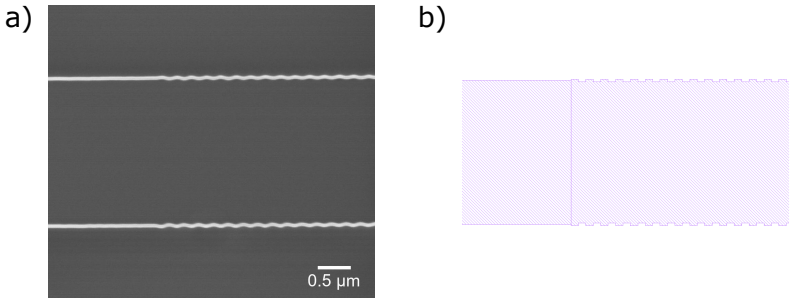

Figure 3.31: SEM images of the sidewall corrugations front-mirror Bragg reflector prior to encapsulation. a) Top view. b) Corresponding mask layout.

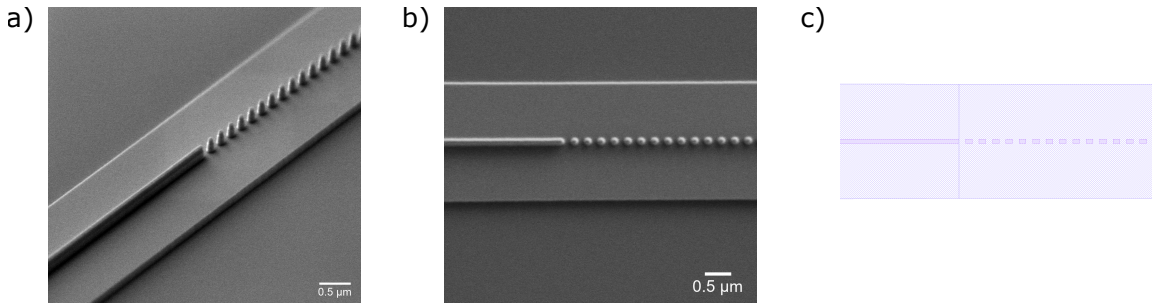

Figure 3.32: SEM images of the Bragg reflector consisting of a 165 nm-thick strip waveguide with 305 nm-thick posts. a) Bird's eye view. b) Top view. c) Corresponding mask layout.

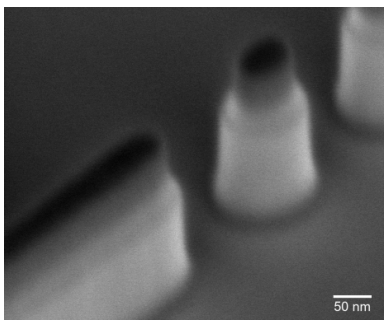

Figure 3.33: SEM zoomed-in image of the Bragg reflector posts. The darker capping corresponds to the HM. The posts exhibit a rather conical shape, with their base being wider than the pattern reported on the HM.

Next, we fabricated LCI devices on a GaAs substrate, to demonstrate a first generation of LCI devices without the extra complexity caused by bonding. Despite promising results, this lot suffered from issues mainly associated with the selectivity and rate of the GaAs SAG when using the functional masks. However, with a short-loop lot, we were able to tune the growth parameters to improve selectivity and decrease and recalibrate the growth rate.

After that, we transferred these developments to III-V on SOI. GaAs wafers with a MQW or DWELL active stack were bonded on oxidized Si wafers. While wafers with the MQW stack could be bonded by any of the two process-flows presented earlier, DWELL required polishing the SiO_2 layer by means of CMP to obtain a smooth surface compatible with bonding. We also introduced a SiN adhesion-enhancing layer on the GaAs, deposited prior to SiO_2 deposition, which can help prevent delamination of the SiO_2 during CMP. After bonding and substrate removal, the process was similar to that on a GaAs substrate, but owing to the improvements to the SAG parameters, the morphology of the fabricated devices was much better. In particular, atomic-resolution FIB-STEM images showed the continuity of the crystalline structure from the active stack to the doped regions. The bonding interface perfectly handled the high temperatures it was exposed to during epitaxy of the doped GaAs.

In parallel, SOI PIC were fabricated as part of MPW on the 300 mm platform, but due to fabrication delays, integration of the III-V with these SOI PIC could not be achieved during the time of this thesis. The SOI PIC included our first Bragg reflectors fabricated using only the standard PDK layers. Despite having aggressive CD, SEM images indicate a fairly good agreement with design.

4

Electro-Optical Characterization

All happy families are alike; each unhappy family is unhappy in its own way.

Leo Tolstoy, in *Anna Karenina*

All lasing lasers are alike; each non-lasing laser is non-lasing in its own way.

A free inspiration based on the quote from Leo Tolstoy.

In this chapter, we focus on the characterization of the fabricated lots from an electrical and electro-optical perspective. These characterizations aim at quantifying the performances of the devices as well as providing insights into their operation.

Section 4.1 provides an introduction to the characterization setup and the methods used in the subsequent sections. Then, the optical characterization of the passive SOI components is discussed in section 4.2. Following that, sections 4.3 and 4.4 cover the electro-optical characterization of the active lateral current injection devices fabricated respectively on a GaAs substrate or with a III-V membrane bonded on oxidized silicon.

4.1. Characterization Methods

This section introduces the various electrical, optical, and electro-optical characterization methods used in the later sections so they can be directly referred to. The characterizations setups and methods are presented, along with their purpose in understanding the functioning of the fabricated devices.

4.1.1. Characterization Setup

The passive and active devices are characterized using a Cascade Microtech Elite 300 probe system, as shown in Fig. 4.1. For the characterization of passive devices (Fig. 4.1.b), light

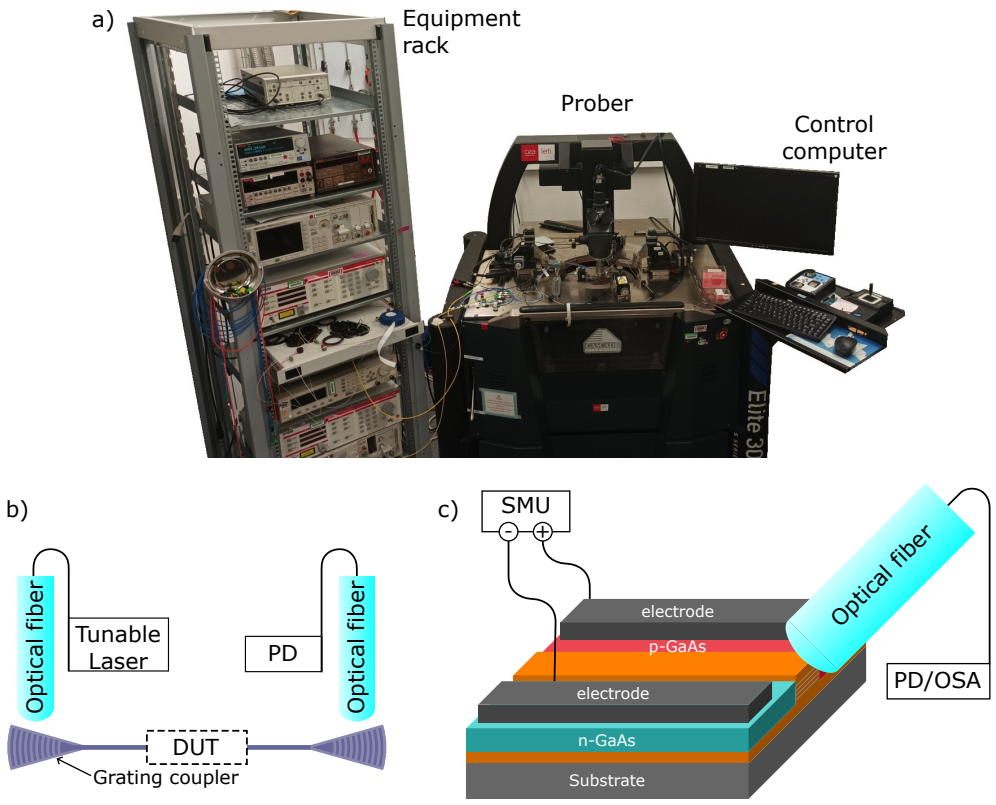

Figure 4.1: Electro-optical prober measurement setup photograph (a) and schematic for passive (b) and active (c) devices characterization. The position of the optical fibers is controlled by micropositioners.

from a tunable laser is fed to the device under test (DUT) via an optical fiber and a grating coupler (GC). The output signal is collected by an optical fiber through a second grating coupler, and measured by a photodiode (PD). To ensure optimal coupling between the optical fibers and grating couplers, the positions of the fibers are automatically adjusted for each device by scanning the space step-by-step in the two in-plane dimensions to find the maximum of the coupling through a Gaussian fit. Active devices (Fig. 4.1.c) are electronically controlled by probes connected to a source-measure unit (SMU). When these devices are not coupled to grating couplers, such as lasers with cleaved facets, an optical fiber connected to a photodiode or optical spectrum analyzer (OSA) collects a small part of the scattered light, as depicted in Fig. 4.1.c. These systems allow for the semi-automatic measurement of several dies and devices from each wafer, by scanning the positions of the chuck holding the wafer.

SMF-28 single-mode fibers are the most commonly used for light injection and collection. In addition, multi-mode fibers (MMF) are used for collection under certain conditions, when the light is not suitably shaped by a grating coupler. Due to their larger core diameter, MMF can collect a larger amount of light. Depending on the measurements being performed, the collecting fiber can be connected to a photodiode (PD) or an optical spectrum analyzer (OSA).

4.1.2. Transmission Line Method

Transmission line method (TLM) measurement are electrical measurements used to evaluate the semiconductor sheet resistance (R_{sh}), contact resistance (R_c), and contact resistivity (ρ_c) of semiconductor layer-contact systems. These parameters directly affect the diode series resistance and thus, its electrical power consumption and self-heating.

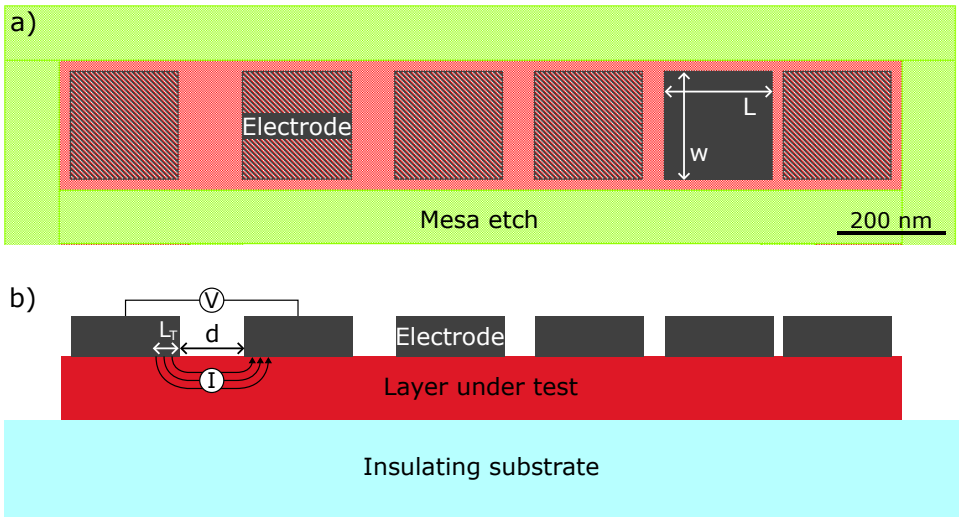

Figure 4.2: Experimental structure for TLM measurements illustrating the design and measurement parameters. a) Layout of a TLM measurement structure consisting of a line of metalic electrodes with varying separation on a mesa of the layer under test. b) Longitudinal cross-sectionnal schematic of this structure.

A typical TLM measurement structure is illustrated in Fig. 4.2: a set of contacts with given width (w) and length (L) are formed on the layer under test, being separated by varying distances d. The total resistance R_t between two adjacent electrodes is measured by passing a current between these electrodes and fitting the resulting current-voltage relationship. For an ohmic contact, the I-V curve is linear and crosses the axes origin. R_t increases as the electrodes separation is increased, and it is related to R_c and R_{sh} by the relationship [189], [190]:

$$R_t(d) = 2R_c + \frac{R_{sh}}{w}d \tag{4.1}$$

Subsequently, R_c and R_{sh} are determined from a linear fitting of $R_t(d)$.

Furthermore, it is often more relevant to know the contact resistivity, sometimes also referred to as the specific contact resistance ρ_c, which is independent of the electrode geometry. The contact resistivity is defined by $\rho_c = dV/dJ$ where, due to the non-uniform current density across the electrode-semiconductor interface, the current density J must be considered only for the area through which the majority of the current flows. The distance from the edge of the contact through which most of the current flows through, referred to as the transfer length, is written L_T (Fig. 4.2.b). It is linked to R_c and R_{sh} by the relationship:

$$R_c = R_{sh}\frac{L_T}{w}\coth\left(\frac{L}{L_T}\right) \tag{4.2}$$

This relationship is best understood intuitively in the case where L $\gg$ L_T and $R_c \simeq R_{sh}L_T/w$.

Next, ρ_c is calculated from R_{sh} and L_T according to [189], [190] :

$$\rho_c = R_{sh}L_T^2 \tag{4.3}$$

Experimentally, the TLM structures are fabricated during the same step as the contacts of the functional devices are formed, on a region of the mask dedicated to measurement structures. The electrodes are squares with w = L = 200 µm, and their separation ranges between 20 µm and 120 µm. In addition, a mesa is etched as illustrated in Fig. 4.2.a. to ensure omnidirectional flowing of the electrons. When measuring the current-voltage relationship for a set of adjacent electrodes, two probes can be used (one per electrode) for both current injection and voltage sensing. However, the resistance between the probe and electrode sometimes cannot be neglected, in which case better measurement accuracy is achieved with a four probes setup, using separate probes for current injection and voltage measurement.

4.1.3. L-I-V Characteristic

The study of the light-intensity-voltage (L-I-V) characteristic holds great importance as it offers a direct evaluation of some of the key figures of merit of laser diodes as discussed in section 1.1.3. To plot the L-I-V characteristic of a device, a source-measure unit is used to inject a given current through the device and read the corresponding voltage, while the output optical power is measured for each pump current using a photodiode.

The I-V characteristic of a laser diode is that of an ideal heterojunction diode in series with a parasitic series resistance [29]. Consequently, the diode threshold voltage and series resistance can be determined from the I-V curves. The parasitic series resistance consists of various contributions including the contact resistance and doped regions sheet resistance, which can be determined separately by TLM measurements. The threshold voltage and series resistance of a diode are critical in determining its electrical power consumption. Moreover, high series resistances can lead to substantial self-heating of a laser diode: the increase of its active region temperature with electrical pump current. As stated in Chapter 2, self-heating depends on the dissipated power and thermal impedance of the laser diode and can degrade its performance at high injection currents.

The L-I curves of laser diodes were already discussed in section 1.1.3. A kink in the L-I curve signifies the lasing threshold has been attained, while its slope above the lasing threshold is directly related to the quantum efficiency (η_d) of the laser diode. The L-I curve also indicates the maximum optical power a laser diode can deliver before roll-over. These are crucial figures of merit for optical sources aimed at being used in data communications. For non-lasing LED, L-I curves can be used to determine the device under test external quantum efficiency and provide insights into the recombination mechanisms involved. A linear relationship between the output optical power and pump current indicates that radiative recombination predominates in the device operation, while a quadratic relationship signifies that non-radiative recombination

are the most important. In particular, non-radiative recombination centers can hinder light emission at low currents but saturate a higher currents, resulting in two distinct regions in the L-I curves [191].

4.1.4. Electroluminescence Spectra

The electroluminescence spectra of a fabricated device provide valuable information on the light emission mechanisms in play in the device operation. They can give a deeper insight on the device functioning than the L-I curves do. The wavelength, or energy, of photons for instance, indicates in which material the electron-hole recombination having produced them took place.

Furthermore, in addition to a kink in the L-I curve, lasing action can also be determined from the emission spectra. At low pumping levels, spontaneous emission predominates, resulting in a broad emission spectrum. However, thanks to the feedback provided by the laser cavity, the relative contribution from stimulated emission increases for the cavity modes as the pump power is increased. As one or a few modes reach their lasing threshold, stimulated emission becomes significantly predominant for these modes, leading to the existence of one or several sharp peaks in the emission spectrum [28]. The side-mode suppression ratio (SMSR), the ratio of the peak intensity of the main mode to the side modes, an important figure of merit for data communications, is also determined from the emission spectrum of the laser.

Electroluminescence spectra can also be used to assess the device self-heating. A first method is to measure the shift of the lasing wavelength of a laser with controlled baseplate temperature at a given moderate pump current, and separately measure the shift of the lasing wavelength with pump current. The active region temperature increase versus pump current is obtained by comparing the results of the second and first measurements, as done for instance in reference [50]. In this case, the wavelength shift is mainly caused by (1) the thermo-optic effect, the change of a material refractive index with temperature, and (2) thermal expansion, affecting the effective period of Bragg gratings used to form the cavity [192].

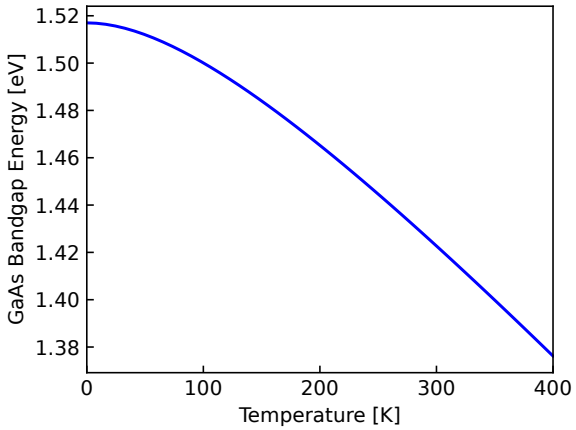

Figure 4.3: GaAs bandgap as a function of temperature, calculated from the Varshni equation (4.4) with the parameters given in reference [193].

Alternatively, temperature also affects the bandgap of semiconductors. This effect is described

by the Varshni empirical equation, stating that the bandgap E_g of a semiconductor at a given temperature T is [194]:

$$E_g(T) = E_0 - \frac{\alpha T^2}{\beta + T} \tag{4.4}$$

with E_0 its bandgap at 0 K, and α and β two fitting parameters. For GaAs for instance, E_0 = 1.517 eV, α = 0.55 meV.K^{-1} and β = 225 K [193], giving the E_g(T) curve plotted in Fig. 4.3.

In the following, when applicable, we use the Varshni equation to directly link the position of the maxima of spontaneous emission peaks with the III-V active region temperature.

4.2. Characterization of the Silicon Photonics Passive Components

This section is dedicated to the characterization of the passive SOI components, and in particular Bragg and loop mirrors. Nine dies from one 300 mm SOI wafer were characterized prior to bonding of the III-V stack, as illustrated in the wafermap of Fig. 4.4.

Some standard components from the photonic PDK were characterized, but since they are not at the core of this thesis, their characterization results are simply briefly specified in this paragraph. The grating couplers have a central wavelength of 1322 nm (standard deviation 1.2 nm) and coupling losses of 2.78 dB (standard deviation 0.07 dB). The standard rib and strip waveguides respectively exhibit losses of 0.47 dB/cm (standard deviation 0.1 dB/cm) and 1.37 dB/cm (standard deviation 0.07 dB/cm). In addition, the measured coupling coefficients of the 50:50 and 90:10 DC at 1310 nm are respectively 44.1:55.9 and 89.8:10.2.

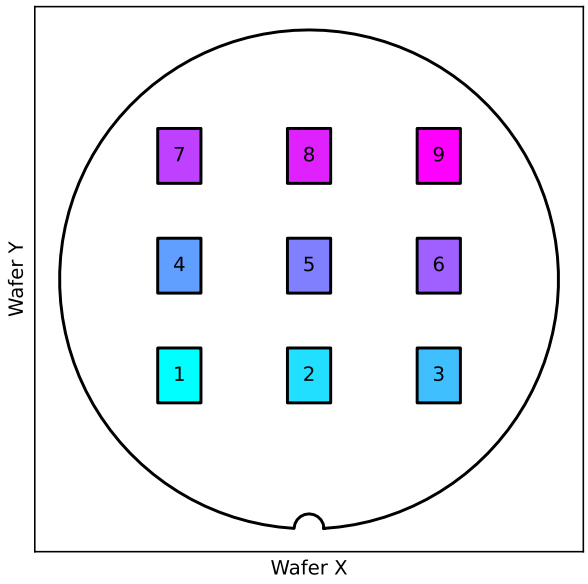

Figure 4.4: Wafermap of the tested dies.

Two types of mirror characterization structures were included in our designs, as illustrated in Fig. 4.5. In the first one (Fig. 4.5.a), the device under test is connected to two grating couplers by a straight waveguide. Light from an external tunable laser is injected in the structure by a SMF and a grating coupler, and the transmittance spectrum is measured from the optical power

collected by a second SMF through the output grating. The measurements are compared with those of a straight waveguide for reference and de-embedding. The automated procedure for the alignment of the optical fibers with respect to the grating coupler is repeated for each device to ensure the measurements reliability. In addition, a three-paddle ("bat ears") polarization controller is used to inject light from the TE0 mode only. Owing to its simplicity, reliability and small footprint, this method is the most commonly used for characterizing silicon photonics mirrors. However, it only allows for measuring the transmittance spectra of the device under test.

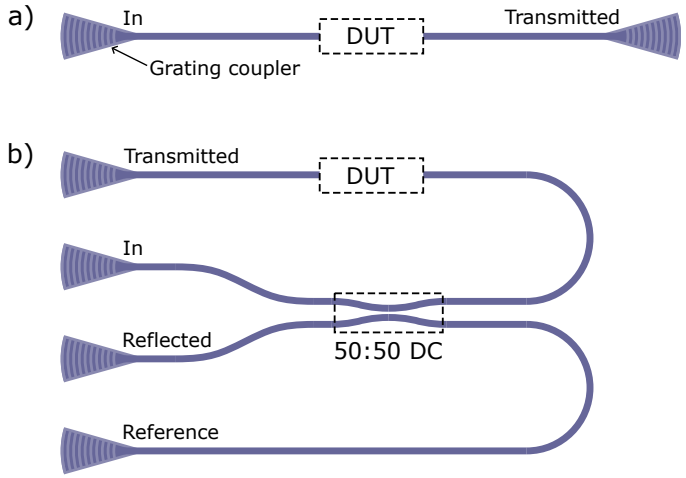

Figure 4.5: Schematic diagram the mirror characterization structures. a) Structures for transmission measurement only. b) Four-channel fiber-array measurements for the simultaneous measurement of the reflection and transmission spectra.

The reflectivity and transmissivity should be linked by the relationship R + T = 1, but diffraction or mode transformation for instance, could break this equality. Accordingly, a second structure, allowing for the simultaneous measurement of both the transmittance and reflectivity spectra is proposed in Fig. 4.5.b. The light in is split between two waveguides using a 50:50 DC, one channel being used as a reference and the other one supporting the device under test so the transmitted signal can be compared with the reference. In addition to the transmittance spectrum, the reflectivity spectrum is obtained by measuring the light reflected by the device under test, traveling back to the DC and collected through the grating coupler labeled as "*reflected*". A fiber-array is used to simultaneously inject light into the structure and read the three output signals. Despite allowing for the direct measurement of the reflectivity spectrum, this setup has two main limits. First, conventional DC are not broadband and the 50:50 splitting ratio is valid for a given wavelength only. The bandwidth for the imbalance to be less than 40:60 is 60 nm, as measured in reference [195]. Provided that both the DC and the DBR are adequately centered at 1310 nm, the imbalance is not an issue since the DC bandwidth is much larger than the FWHM of the DBR. However, if one of them is shifted, or for the characterization of broadband loop mirrors, this can become more of an issue. This issue could be mitigated by using broadband DC as presented in reference [196] for instance. Secondly, this setup requires the coupling efficiency between all grating couplers and optical fibers to be the same for the

results to be consistent, which can be challenging to achieve.

The next subsections present the characterization results of the the posts and sidewall corrugations DBR, and of the loop mirrors. For compactness reasons and due to the four-channel fiber-array measurement setup using a large surface on the masks, only the sidewall corrugations DBR and loop mirrors were tested with this setup while the posts DBR were tested with the transmission setup.

4.2.1. Characterization of Bragg Reflectors for Membrane Lasers

The characterization results for the posts DBR are presented first. Due to errors in coding the photomasks, the actual gratings lengths are 25 µm and 100 µm for the front and back-mirror respectively, when according to the simulations of section 2.4.2, they should have been 70 µm and 250 µm to provide peak reflectivities of 50% and 99%. Fig. 4.6 presents the measured transmittance spectrum of a back-mirror posts DBR, as well as that of a straight waveguide for reference. Two transmission drops can be observed, one at 1304 nm, and another one at 1278 nm. To the best of our knowledge, this was not observed elsewhere in the literature, except for intentional multiple-period gratings [160], [197]. This should indicate a dual-period phenomenon in our structures, which origin we could not elucidate.

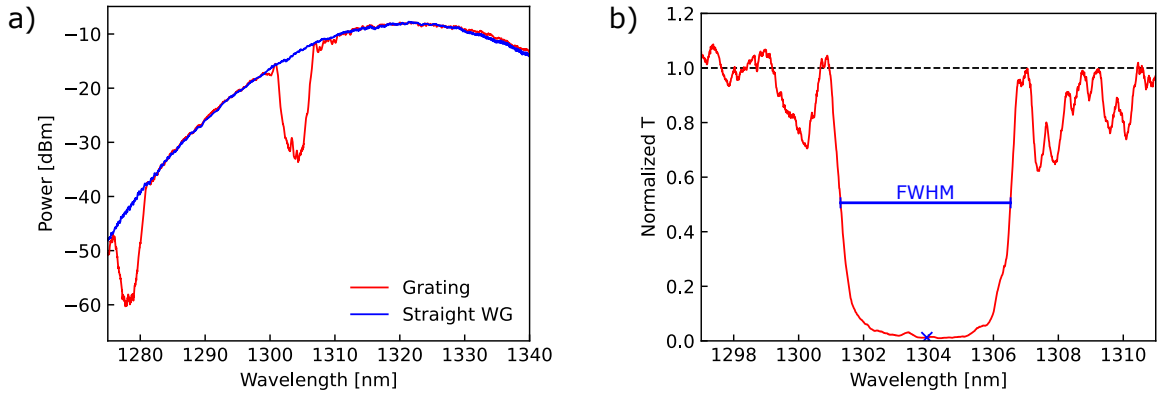

Figure 4.6: Measured transmittance spectrum of a back-mirror posts DBR (die 4). a) Raw measurement of the DBR transmittance spectrum compared with that of a straight waveguide. b) Linear power units transmittance spectrum of the DBR normalized to the straight waveguide transmisison (zoomed-in view of the transmisison drop at 1304 nm). The transmittance minimum at the Bragg wavelength and the FWHM are indicated by the blue cross and line.

A zoomed-in view of the transmission drop at 1304 nm is shown in Fig. 4.6.b. where the grating signal is normalized to the signal of the straight waveguide and converted to linear power units. The experimental Bragg wavelength, FWHM and transmittance at the Bragg wavelength T(λ_B) derived from this spectrum are respectively 1304.0 nm, 5.2 nm and 0.044. The aggregated values for all nine dies are given in Table 4.1. Despite the shorter length as compared with simulations, high reflectivities are still obtained at the Bragg wavelength, with the mean transmittance being 0.057. From R_{peak} = 1 - 0.015 = 0.985 and the equation for the Bragg grating peak reflectivity (Eq. (2.36)), this would indicate an experimental coupling coefficient κ = 280 cm^{-1}.

Table 4.1: Summary of the posts DBR characterization results.

Die	λ_B [nm]		FWHM [nm]		T(λ_B)	
	BM	FM	BM	FM	BM	FM
1	1307.9	1307.4	5.2	9.3	0.008	0.57
2	1304.9	1302.6	5.0	7.6	0.019	0.55
3	1304.9	1303.7	5.2	8.0	0.016	0.64
4	1304.0	1303.5	5.2	8.5	0.012	0.64
5	1301.2	1301.0	5.2	7.9	0.014	0.72
6	1304.2	1304.9	5.3	9.0	0.016	0.69
7	1305.3	1305.7	5.1	9.9	0.018	0.71
8	1302.6	1302.7	5.2	8.7	0.016	0.71
9	1306.2	1306.9	5.0	8.5	0.014	0.75
Mean	1304.6	1304.3	5.2	8.6	0.015	0.66
Standard deviation	1.8	2.0	0.11	0.7	0.003	0.065

The transmittance spectrum of a front-mirror posts DBR is shown in Fig. 4.7. The pattern of this grating is identical to that of the back-mirror, and they only differ in length, with the front-mirror being 25 µm long. As for the back-mirror, two transmission drops can be observed. The Bragg wavelength is 1303.5 nm, and the transmittance at this wavelength is 0.64, determined by filtering-out the high-frequency ripples observed in the spectrum. These ripples are attributed to Fabry-Perot effects in the system. Their period is 0.7 nm, associated to a cavity length of 280 µm according to Eq. (1.17). This is approximately the distance between the DBR and grating coupler. From Eq. (2.36), T(λ_B) = 0.65 indicates an experimental coupling coefficient of 267 cm^{-1}. The experimental values for the front and back-mirror are close and both larger than the value simulated in section 2.4.2, which was 125 cm^{-1}. This is attributed to the angle of inclination in the posts etching, resulting in a wider base than drawn on the photomasks and reported on the HM, as it was illustrated by Fig.3.33. Since the mode is localized in the 165 nm-thick slab, it mainly interacts with the base of the posts, hence being strongly affected by the posts base widening. Due to the coupling coefficient being larger, and the gratings lengths being shorter than in simulations, the experimental FWHM are also larger than simulated, with 8.6 nm and 5.2 nm for the front and back-mirrors respectively, compared with the theoretical estimations of 5.0 and 3.0 nm.

Variations in the Bragg wavelength are observed from one die to the other, but gratings from the same dice tend to exhibit very close Bragg wavelengths. The variations in the Bragg wavelength are attributed to slight inhomogeneities in the SOI thickness, which affect the effective index of the supported modes.

The sidewall corrugations DBR were tested using the four-channel fiber-array measurement setup of Fig. 4.5.b. Fig. 4.8 show the raw measurement data, linear power units reflectivity and transmittance signals normalized to the reference signal, and a zoomed-in view of the spectra

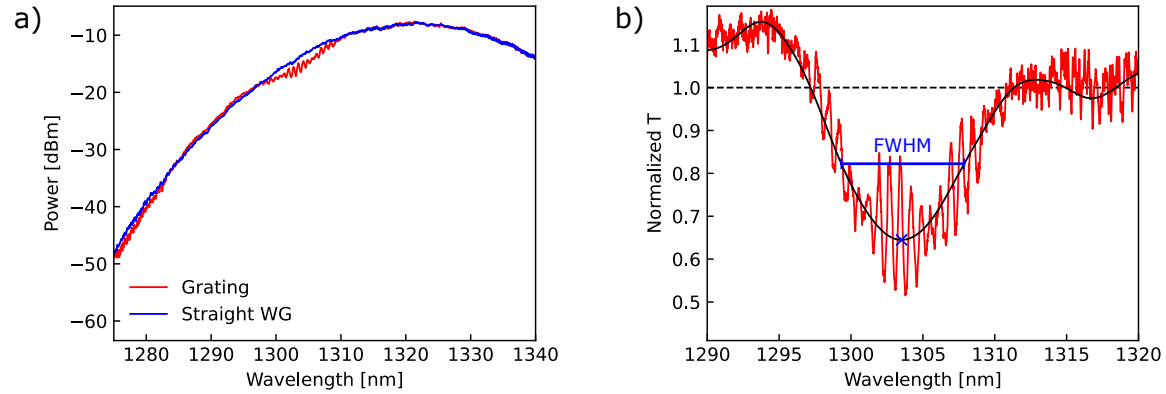

Figure 4.7: Measured transmittance spectrum of the front-mirror posts DBR (die 4). a) Raw measurement of the DBR transmittance spectrum compared with that of a straight waveguide. b) Linear power units transmittance spectra of the DBR normalized to the straight waveguide transmisison (zoomed-in view of the transmisison drop at 1304 nm). The black curve is obtained by filtering-out the noise using a low-pass Butterworth filter. The Bragg wavelength transmittance minimum and the FWHM are indicated by the blue cross and line.

around the Bragg wavelength of the back-mirror.

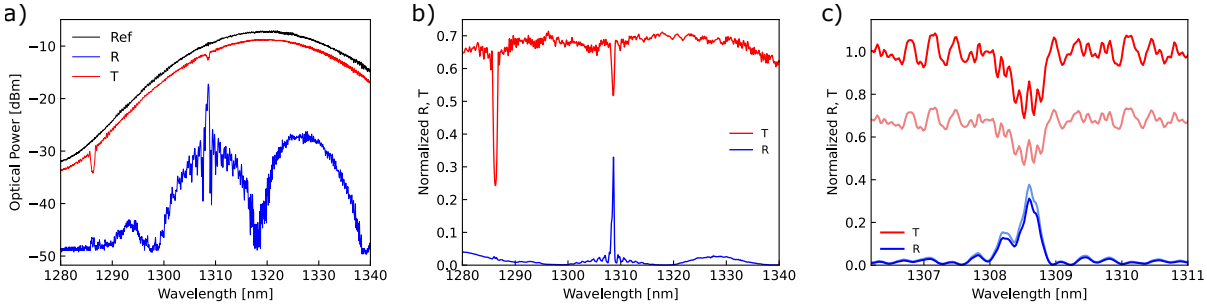

Figure 4.8: Reflectivity and transmittance spectra of the back-mirror sidewall corrugations DBR (die 8), measured using the four-channel fiber-array measurement setup of Fig. 4.5.b. a) Raw data from the reference, transmission and reflection channels. b) Linear power units reflectivity and transmittance spectra of the DBR normalized to the reference signal (plus a 3 dB onset to the reflectivity signal due to crossing the directional coupler twice). c) Zoomed-in view of the reflection peak at 1309 nm. Light colors: data normalized to the reference signal as in (b). Vivid colors: data normalized to the enveloppe of the transmission signal.

Two drops are observed in the transmission spectrum, as for the posts DBR. The transmission drop at the Bragg wavelength (1309 nm) is associated with a reflection peak, which is absent for the transmission drop at 1286 nm. However, this observation must be taken with care as it is possibly caused by the extremely low intensity of the reflectivity signal at this wavelength, close to the photodiode detection limit. This could prevent the reading of a potential reflectivity peak at this wavelength. Normalizing the transmittance and reflectivity signals to the reference signal, with a 3 dB onset applied to the reflectivity signal due to crossing the DC twice, the reflectivity at the Bragg wavelength is 0.38. However, the normalized transmittance away from the Bragg wavelength is only about 0.7, which is likely caused by differences in the coupling coefficient between the four fibers of the fiber-array and their grating couplers, and by the 50:50 DC imbalance. In Fig. 4.8.c, we plotted a zoomed-in version of Fig. 4.8.b. (light colors) around the Bragg wavelength. To fix the normalization issue, we also included a plot of the signal normalized to the envelope of the transmission spectrum (vivid colors).Table 4.2 presents the

Table 4.2: Summary of the sidewall corrugations back-mirror DBR characterization results.

Die	λ_B [nm]	FWHM [nm]	R(λ_B)
2	1308.44	0.48	0.27
4	1308.62	0.50	0.34
6	1308.52	0.37	0.30
7	1308.55	0.55	0.26
8	1308.60	0.30	0.38
Mean	1308.55	0.44	0.31
Standard deviation	0.060	0.09	0.04

characterization results for the nine tested dies. The mean reflectivity at the Bragg wavelength is 0.31, indicating an experimental coupling coefficient κ = 16 cm^{-1}, compared to 71 cm^{-1} as planned in design. This can be partly attributed to the angle of inclination of the sidewalls etching, reducing the index contrast. In addition, the rounded shape of the corrugations can further reduce the coupling coefficient. For instance, the coupling coefficient of a grating with sinusoidal effective index variations is reduced by a factor $\pi/4$ as compared to a grating with step-like effective index variations [160].

Regarding the front-mirror sidewall corrugations DBR, it has no reflection peak or transmission drop across the whole spectrum. This would indicate that the coupling coefficient is too low to produce any significant reflection.

To summarize this section, we have characterized the fabricated SOI posts and sidewall corrugations DBR. The fabricated posts DBR were shorter than on design but still exhibited high-enough reflectivities, owing to larger coupling coefficients than theoretically predicted. The larger coupling coefficients are attributed to the angle of inclination of the SOI etch, widening the posts at their base. The sidewall corrugations DBR, by contrast, exhibited lower coupling coefficients than on design. Despite setting the grating average width to a high value (2 µm) to maximize the corrugations width giving a specified coupling coefficient (see Fig. 2.34), the amplitude of the sidewall corrugations was still considerably tiny and the corrugations

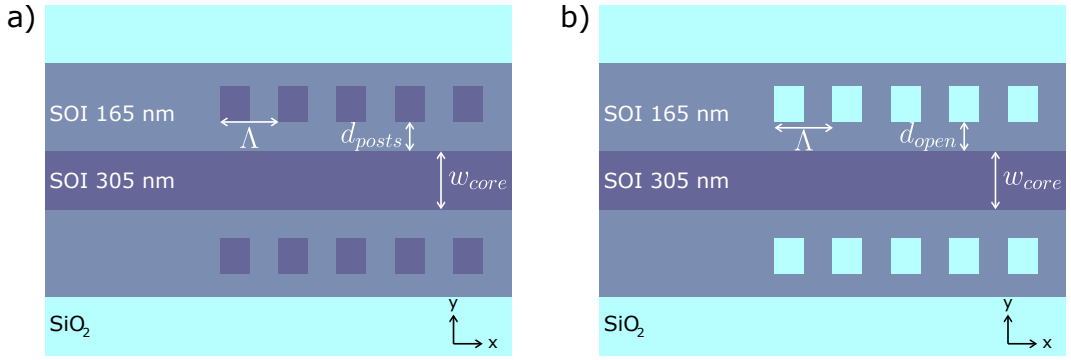

Figure 4.9: Schematic of the recommended Bragg gratings with improved fabrication robustness and control over the coupling coefficient. a) Rib waveguide with side posts. b) Rib waveguide with side slab openings.

were difficult to properly define by lithography and etching. Based on these results, our recommendation for future designs is to use the more robust posts approach, and placing the posts at a chosen distance d_{posts} away from the core of a rib waveguide, to reach lower and controlled coupling coefficients as illustrated in Fig. 4.9.a. Alternatively, instead of posts, opening can be created in the SOI slab to create negative $\Delta\tilde{n}$ index variations (Fig. 4.9.b).

4.2.2. Characterization of Loop Mirrors for Membrane Lasers

The front loop mirror, using a 90:10 DC (theoretical reflectivity R = 0.36) and the back-mirror, using a 50:50 DC (theoretical reflectivity R = 0.36), were characterized using the four-channel fiber-array measurement setup. From the coupling coefficients measured for the fabricated DC (89.8:10.2 and 44.1:55.9), we expect experimental reflectivities of 0.366 and 0.986.

Fig. 4.10 shows the measurement results for the front loop mirror, with the raw data displayed in Fig. 4.10.a, and the normalized reflectivity and transmittance signals in Fig. 4.10.b. The normalized reflectivity is close to the theoretical value of 0.36 at 1310 nm, and exhibits moderate variations over the 1280–1340 nm range. Subnanometer-period ripples are observed for all channels, resulting from parasitic Fabry-Perot interferences. From the variation of their period for the different channels, they appear to arise from cavities formed by the loop mirror and the grating coupler of each channel. Additional longer period (12 nm) variations are observed in the reflectivity signal. Since the DC coupling factor is a monotonic function of the wavelength [195], these variations are likely not related to actual variations of the loop mirror reflectivity, but should be associated to other effects.

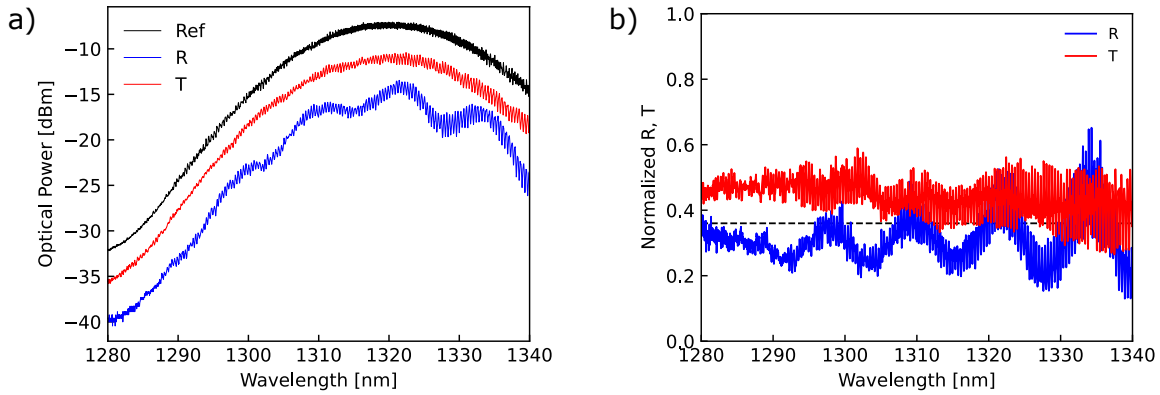

Figure 4.10: Measured reflectivity and transmittance spectra of the loop interferometer front-mirror. a) Fiber-array raw signal from the reference, reflection and transmission channels. b) reflectivity and transmittance signals normalized to the reference signal (plus a 3 dB onset to the reflectivity signal due to crossing the directional coupler twice). The black dashed line corresponds to the theoretical reflectivity (R = 0.36).

The back loop mirror, using the 50:50 DC, offers a close to unity reflectivity, relatively stable over the 1280–1340 nm range, with similar ripples as observed in the spectrum of the front loop mirror.

In essence, building on the DC available from the PDK, the loop-mirrors are reliable mirrors, exhibiting the expected reflection and transmission properties. The deviation between the DC experimental coupling coefficients (89.8:10.2 and 44.1:55.9) and their nominal values (90:10 and

50:50) has a meagre influence on the mirrors reflectivities. Such mirrors have no spectral filtering abilities and the spectral dependence of the DC coupling coefficients is hardly observed in the reflectivity and transmittance spectra. Accordingly, these mirrors cannot be used to realize single-mode lasers, but their reliability is an asset for the realization of III-V on silicon laser prototypes.

4.3. Characterization of Lateral Current Injection devices on a GaAs substrate

This section reports on the characterization of the first generation of lateral current injection devices prototypes, fabricated on a GaAs substrate as described in section 3.3.1. A schematic of these devices is given in Fig. 4.11. The III-V membrane is optically isolated from the substrate by an AlGaAs cladding, also serving the purpose of a barrier for free carriers.

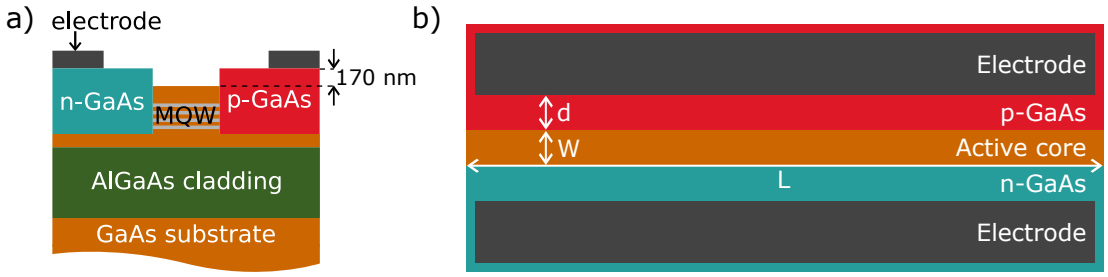

Figure 4.11: a) Cross-sectional schematic of a diode from the first generation of prototypes on a GaAs substrate, as fabricated, with the doped regions being 170 nm thicker than the intrinsic core. b) Top-view illustrating the design parameters: length (L), active region width (W) and distance between the electrodes and the active region (d).

However, as already discussed in section 3.3.1, due to issues with calibrating the selective area growth of GaAs, the doped regions are 170 nm thicker than the intrinsic core (Fig. 4.11.a), when they should have been 130 nm thinner to form a rib waveguide (see section 2.2.2). In the fabricated structure, no mode is supported by the intrinsic core since it would leak to the doped slab. Without guiding, there cannot be optical feedback, which is required for lasing. Yet, these prototypes which already played an important role in the fabrication developments can also give valuable information on current injection and recombination mechanisms.

4.3.1. Electrical Characterization

Here, we focus on the electrical characterization of the fabricated devices. The three wafers constituting this lot used differing doping levels in their p-i-n structure. Wafer 2, exhibiting intermediary doping levels, was scrapped before the end of its processing, leaving us with wafer 1, the most strongly doped, and wafer 3, the least doped. Conventional laser diodes use larger doping concentrations at the metal-semiconductor interface to ensure an ohmic contact is obtained, and reduce the contact resistance, while lower concentrations are used close to the gain medium to reduce optical losses. Since it is unpractical to have concentration gradients in lateral current injection devices, the target doping concentrations for wafer 1 (4.3) reproduce

those of typical metal-semiconductor interfaces, and those of wafer 3 reproduce those used closer to the gain medium [128].

TLM measurements were performed to evaluate which doping levels would be suitable for practical lateral current injection devices. First, these measurements were performed with the two probes setup, using the same probes for both current injection and voltage sensing. For wafer 1, large contact resistances were obtained and exhibited a certain extent of instability, in particular related to the pressure applied with the probe. As a result, the coefficients of determination for the fittings of $R_t(d)$ according to Eq. (4.1) were not satisfying: $R^2 = 0.967$ for the n-contact, and $R^2 = 0.984$ for the p-contact. This tends to indicate a large resistance between the probe and electrode. Accordingly, the TLM measurements were repeated in the four probes setup, giving more consistent results.

Fig. 4.12.a. and c. presents the I-V curves measured for the five electrodes spacings, for the n and p-contacts. The corresponding R_t are plotted as a function of the electrodes spacing in Fig. 4.12.b. and d, with much better coefficients of determination than using the two probes setup (0.999 for the n-contact and 0.991 for the p-contact). The deduced sheet resistance, contact resistance and contact resistivity are summarized in Table. 4.3. In particular, the measured contact resistances for the n and p contacts are 0.30 Ω and 0.98 Ω respectively, compared with 4.3 Ω and 1.9 Ω measured with the two-probes setup. This would indicate probe-electrode resistances of 4.0 Ω and 0.9 Ω for the n and p contacts respectively. This value is particularly high for the n-electrode, which could be explained by the poor structure of the electrode, as we had observed in section 3.3.2 (see Fig. 3.12). The sheet resistance of the p-GaAs layer grown on wafer 1 is lower than that of the n-GaAs, which is unexpected since the hole mobility is lower than that of electrons [44], [50]. This is possibly due to a parallel conduction path in the AlGaAs cladding layers exhibiting a residual carbon doping.

For wafer 3, fabricated with lower doping levels, the VI curves of the TLM structures on the p-doped GaAs exhibit a Schottky diode behavior, indicating that the doping level is insufficient for our application. The TLM structures for the n-contact were measured with the two probes setup and exhibited an ohmic behavior. Fitting the $R_t(d)$ data according to Eq. (4.1) (coefficient of determination $R^2 = 0.999$), we obtained the results given in Table. 4.3. Due to the two probes setup, the contact resistance, transfer length and contact resistivity are probably overestimated.

The VI characteristics of the devices of wafer 1 were measured, and three examples are illustrated in Fig. 4.13. The threshold voltage (V_{th}) and series resistance (R_s) of the diodes were estimated by fitting the VI curves (dashed lines of Fig. 4.13). The threshold voltage is identical for all devices, at 1.05 V. This is expected since the threshold voltage is determined by the quasi-Fermi level separation at the junctions constituting the diode [29], which does not depend on the diodes geometry. On the contrary, the diode series resistance is greatly affected by its design. Due to the actual geometry of the fabricated devices differing from the design dimensions by up to 2 μm because of issues with the alignment of the lithography masks (see for instance Fig. 3.12), we cannot conduct an extensive numerical analysis of the relationship

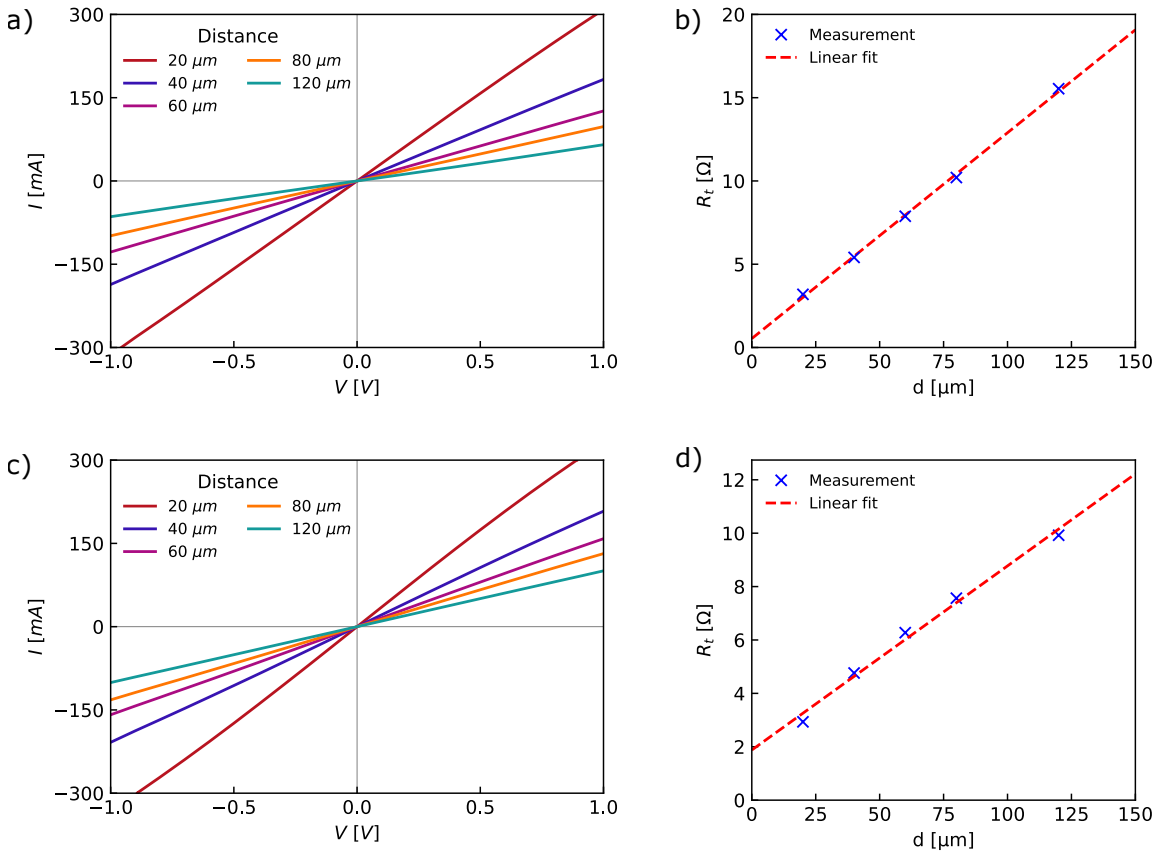

Figure 4.12: Four-probes TLM measurement results for the n-doped GaAs (a-b) and p-doped GaAs (c-d) of wafer 1. a) and c) Raw I-V data. b) and d) Corresponding resistance (R_t) versus electrode separation results, with linear fitting according to Eq. (4.1) (the associated coefficients of determination are R^2 = 0.999 for the n-contact (b) and 0.991 for the p-contact (d)).

Table 4.3: TLM measurements results, measured using the four probes setup for wafer 1, and the two probes setup for wafer 3.

Wafer	Doping type / target conc. [cm^{-3}]	R_c [Ω]	R_{sh} [Ω/□]	L_t [μm]	ρ_c [Ω.cm^{-2}]
1	n / 5×10^{18}	0.30	25	2.5	1.5×10^{-6}
	p / 1×10^{19}	0.98	14	14	2.7×10^{-6}
3	n / 2×10^{18}	3.1	35	18	1.1×10^{-4}
	p / 2×10^{18}	Non-ohmic			

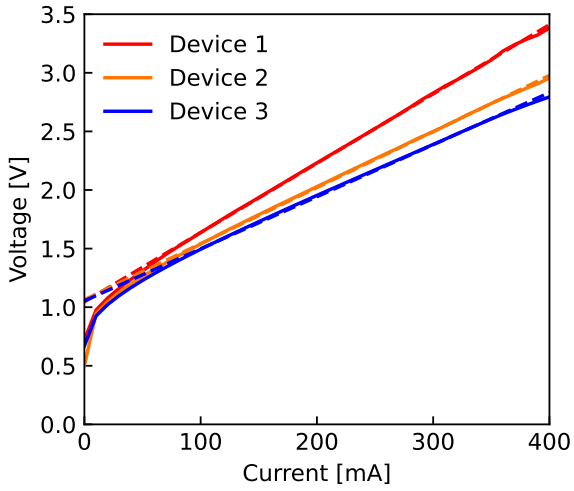

Figure 4.13: VI measurements (full line) and fittings (dashed) for three fabricated devices from wafer 1. The devices dimensions on design are: (1) L = 1 mm, w = 10 µm and d = 5 µm; (2) L = 2 mm, w = 4 µm and d = 5 µm; (3) L = 3 mm, w = 2 µm and d = 2 µm. From the fittings, we obtain V_{th} = 1.05 V for all three devices and R_s = 5.9 Ω (1), 4.8 Ω (2) and 4.4 Ω (3).

between the devices geometry and their series resistance. However, we do observe that reducing the active region width and distance between the electrode and active region, and increasing the device length tends to decrease the series resistance, as expected. For instance the device 1 of Fig. 4.13, which is short (L = 1 mm) and wide (W = 10 µm and d = 5 µm) exhibits a larger series resistance (R_s = 5.9 Ω) than device 3 (R_s = 4.4 Ω), which is longer (L = 3 mm) and narrower (W = 2 µm and d = 2 µm).

4.3.2. Electro-optical Characterization

Electro-optical characterizations were performed on the devices of wafer 1, aiming at demonstrating and studying the electrical pumping of the MQW.

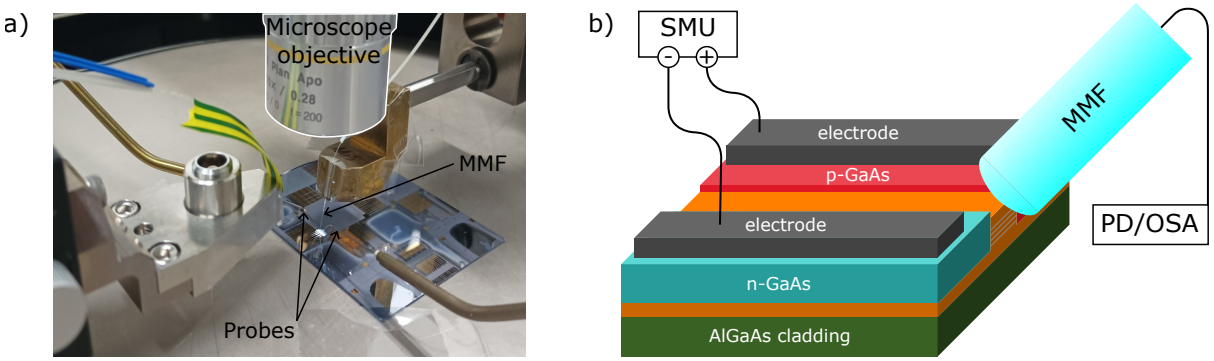

Figure 4.14: Prober measurement setup for the electro-optical characterization of the devices. (a) Photograph and (b) schematic. Probes connected to a source-measure unit (SMU) are used to inject current through the diode and measure the associated voltage. A MMF is used to collect a part of the scattered emitted light for analysis using a photodiode or OSA.

The measurement setup is illustrated in Fig. 4.14 where the wafer is placed on a Cascade Microtech Elite 300 probe system so that each device can be tested semi-automatically. Electrical

probes connected to a source-measure unit are used to bias the diode and inject current. A microscope objective allows observing the device under test with a visible-light or IR (Si) camera, and an optical fiber collects a small part of the scattered light at the device facet. A MMF fiber is used since its larger core diameter allows for collecting more light, but still, only a fraction of the emitted light is collected. This setup allows for qualitative measurements aimed at demonstrating current injection and light emission, which is a first mandatory step. More quantitative measurements would require preparing laser chips to collect emitted light with an integrating sphere.Since at this stage we target qualitative measurements, the devices are tested on the probe system.

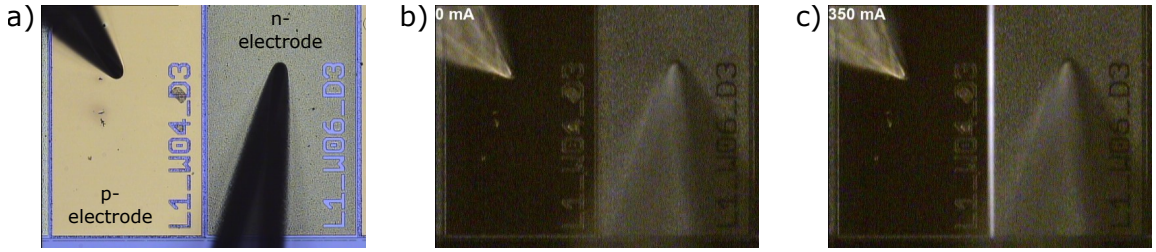

Figure 4.15: Optical microscope photograph of a device and probes captured with a visible light camera (a) and IR (Si) camera, for pump currents of 0 mA (b) and 350 mA (c) showing light emission resulting from electrical pumping of the device.

Our first observation is that light is emitted by the structure when an electrical current is injected into it, as illustrated by the optical microscope images displayed in Fig. 4.15. This observation is supported by plots of the collected optical power as a function of pump current (L-I curves) illustrated in Fig. 4.16 for three devices chosen to represent the diversity of design geometries. Three regions can be identified in the L-I curves, with almost no light being emitted up to 100 mA, followed by a turn-on of the light emission and finally a quasi-linear increase of the output power starting from about 300 mA. The differential external quantum efficiency of the devices increases from one identified region to the next, meaning that the ratio of radiative to non-radiative recombination increases. Looking at the recombination mechanisms presented in section 1.2.1, we have that the rate of non-radiative SRH recombination scales linearly with the free carrier density while the rate of radiative recombination scales quadratically with the free carrier density. Accordingly, the increase of a LED efficiency with increasing current can be linked with a so-called saturation of the nonradiative recombination paths at high injection currents, as radiative recombination becomes predominant when the free carriers density increases [191], [198]. For our devices, this happens close to 200 mA, which could indicate a large density of nonradiative centers. No speckle is observed with the camera, nor is there any kink in the L-I curves, indicating that the devices did not lase (see section 1.1.3). This was expected since, as we have already discussed, the structure does not support any guided mode due to the lateral doped regions being thicker than the active core.

Interestingly, while excessively increasing the pump voltage of laser diodes usually causes electrical breakdown through the semiconductor, in our devices, it instead caused melting of the electrode at the probe-electrode junction. Using the IR camera, we also observed a non-uniform

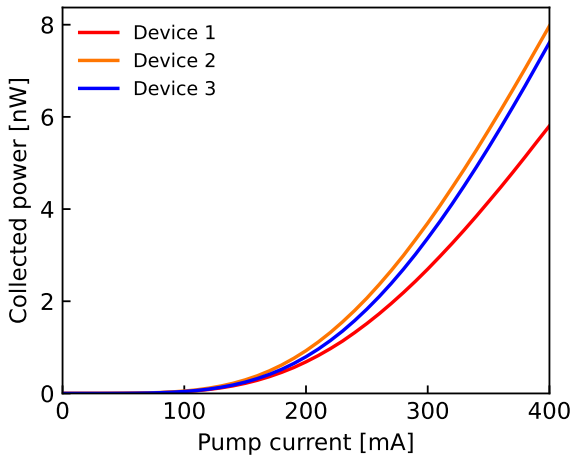

Figure 4.16: Light collected versus CW pump current (CW-L-I curves) for three fabricated devices. The devices dimension on design are given in Table. 4.4.

Table 4.4: Design parameters: length (L), active region width (W) and distance between the electrodes and the active region (d) for the three devices of Fig. 4.16–4.18, and minimum/maximum values used in the design of experiment (DOE).

Device	L [mm]	W [µm]	d [µm]
1	2	2	3
2	2	6	3
3	2	10	1
DOE min/max	1/3	1/10	1/5

distribution of the light intensity over the length of the active region, with the maxima being located at the closest point to the probe placed on the n-GaAs electrode. These observations are attributed to the poor structure of the electrode on the n-GaAs, as we had already observed (see Fig. 3.12), which could hamper current conduction through the electrode. This issue was solved for the lot of devices fabricated on Si, which fabrication was presented in section 3.4.1.

To better identify the sources of light emission, the electroluminescence spectra of those devices were recorded for various injection currents, as displayed in Fig. 4.17. For all three devices, two peaks are clearly identified, close to 870 nm (1.42 eV) and 910 nm (1.36 eV). They respectively correspond to photons emitted from radiative recombination in the GaAs and in the MQW.

The measurement noise was filtered out using a second order low-pass Butterworth filter, so the positions and relative intensity of the GaAs and MQW peaks could be more clearly identified. For all three devices, the signal corresponding to recombination in the GaAs dominated over recombination in the MQW, as illustrated by Fig. 4.18.a. The former could take place either in the SCH, in the doped region (more likely in the p-doped region due to the larger electrons mobility as compared with holes) or in the substrate. From Fig. 4.18.a, we observe that the relative contribution from the MQW increases as the pump current increases. We also note that device 1 exhibits a significantly lower relative MQW contribution. It is the device with the

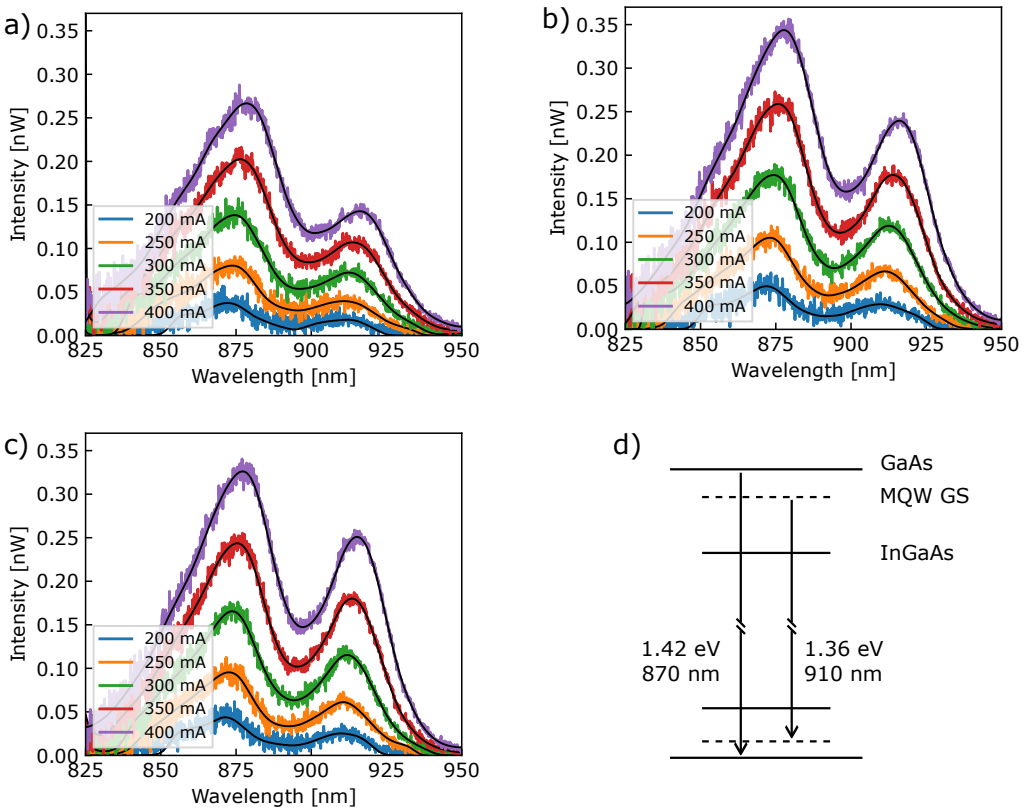

Figure 4.17: Optical emission spectra of devices 1 (a), 2 (b) and 3 (c) for pump currents ranging from 200 mA to 400 mA. The black curves correspond to the measurement data filtered using a second order low-pass Butterworth filter to suppress measurement noise. d) Schematic band diagram illustrating the origin of the two emission peaks visible in the spectra: recombination in the MQW (around 910 nm — 1.36 eV) and in the bulk GaAs (around 870 nm — 1.42 eV).

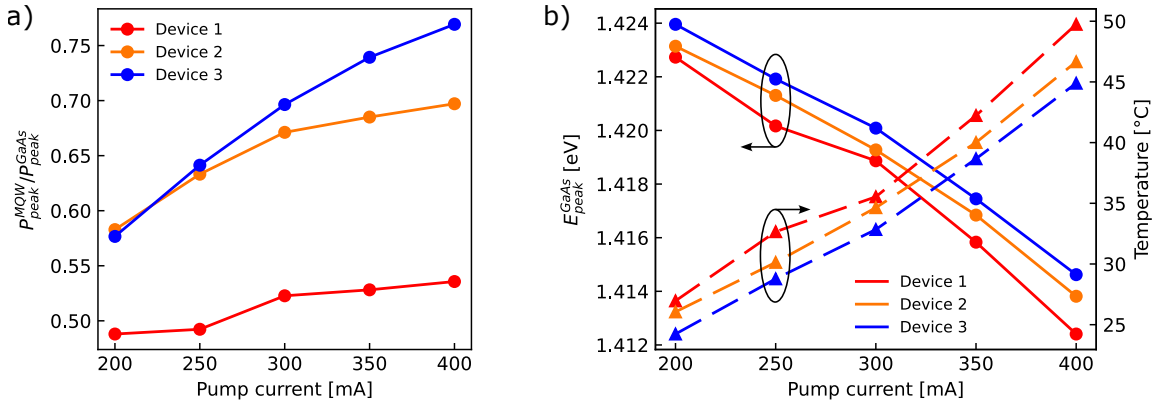

Figure 4.18: Analysis of the electroluminescence spectra of the three devices. a) Ratio of the peak power of the MQW emission to that of the GaAs emission. b) Wavelength shift of the GaAs emission peak as a function of the injection current (dots), and corresponding temperature (triangles) obtained from the Varshni equation (Eq. (4.4)).

narrowest active region, with 2 µm on design as compared to 6 µm and 10 µm for devices 2 and 3 respectively. This could indicate recombination taking place in the p-doped region due to electrons leakage.

As the pump current is increased, a redshift of both the GaAs and MQW emission peaks is observed. It is attributed to the reduction of the materials bandgap with increasing temperatures, as described by the Varshni equation presented in section 4.1.4. Accordingly, we used the Varshni equation 4.4 and the measured energies of the GaAs peaks to estimate the temperature of the active region as a function of the pump current. The result is shown in Fig. 4.18.b. At 200 mA, the calculated temperatures range between 24 ℃ (device 3) and 27 ℃ (device 1), increasing to 45 ℃ (device 3) to 50 ℃ (device 1) at 400 mA. These results are consistent with the measured series resistance, with device 1 exhibiting the highest temperature and largest series resistance (5.9 Ω) and device 3 the lowest heating and series resistance (4.4 Ω).

To summarize this section, we have characterized the first generation of lateral current injection diode prototypes, fabricated on a GaAs substrate. In section 3.3.1, we saw that they played a major role for technological developments since they evidenced deviations in the selective area growth of GaAs preventing the fabrication of rib waveguide structures, which were later corrected. Besides, electrical and electro-optical characterizations have been performed in this chapter. From an electrical perspective, we observed that the p-doping concentration of wafer 1 was required to realize ohmic contacts on p-GaAs, and we chose to use the doping levels of wafer 1 for both the n and p-contacts of later prototypes. In addition, we have demonstrated light emission resulting from electrical pumping of the devices, including at the MQW wavelength, proving electrical pumping of the MQW.These results mark an important first step before the realization of lateral current injection devices on silicon.

4.4. Lateral Current Injection Devices on Silicon

This section presents the characterization results for the devices using a III-V membrane bonded on bulk oxidized silicon and with etched or as-cleaved facets. The devices geometry is shown in Fig. 4.19, showing the design parameters: active region length (L) and width (W), and distance between the electrodes and active region (d). For this lot, a better alignment of the photomasks

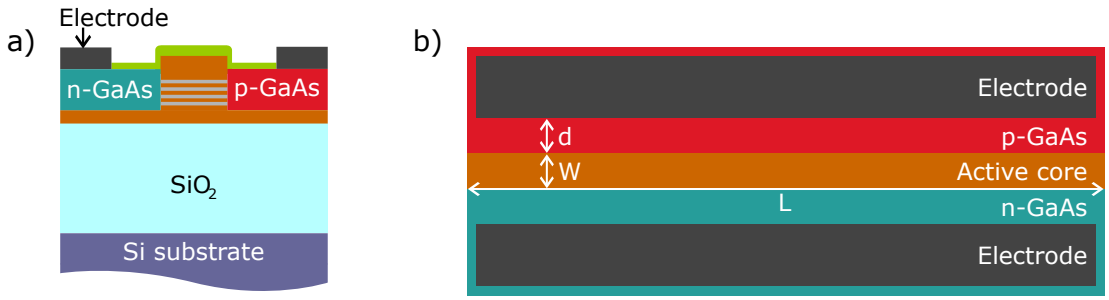

Figure 4.19: Schematic of a prototype device with III-V bonded on oxidized Si. a) Transverse cross-section. b) Top-view. Devices can differ in length (L), active region width (W) and distance between the electrodes and the active region (d).

was achieved so the fabricated structures exhibit a much better agreement with design than those fabricated on a GaAs substrate.

Six wafers constitute this lot with the only difference between them being the use of a SiN adhesion-enhancing at the III-V–bonding dielectric interface as described in section 3.4.1, for wafers 7, 9 and 17.

4.4.1. Electrical Characterization

The electrical contacts and sheet resistance were assessed by TLM measurements, using the two probes setup, on all six wafers. The I-V(d) characteristics and deduced R_t(d) curves are shown in Fig. 4.20.a. and b. for the p-contact, and Fig. 4.20.c. and d. for the n-contact. The measurement results for the six wafers are summarized in Table. 4.5.

These results are consistent from one wafer to another. The average contact resistance for the n-contact is 1.1 Ω with a standard deviation (σ) of 0.07 Ω, while the p-contact yields an average resistance of 2.8 Ω with σ = 0.23 Ω. The larger contact resistance as compared to wafer 1 of the devices fabricated on a GaAs substrate, which was grown to have the same level of doping, is likely due to the probe-contact resistance in two-probes setup. Specifically, the n-GaAs exhibits an average sheet resistance of 36 Ω/□ (σ = 1.4 Ω/□), slightly larger than the results

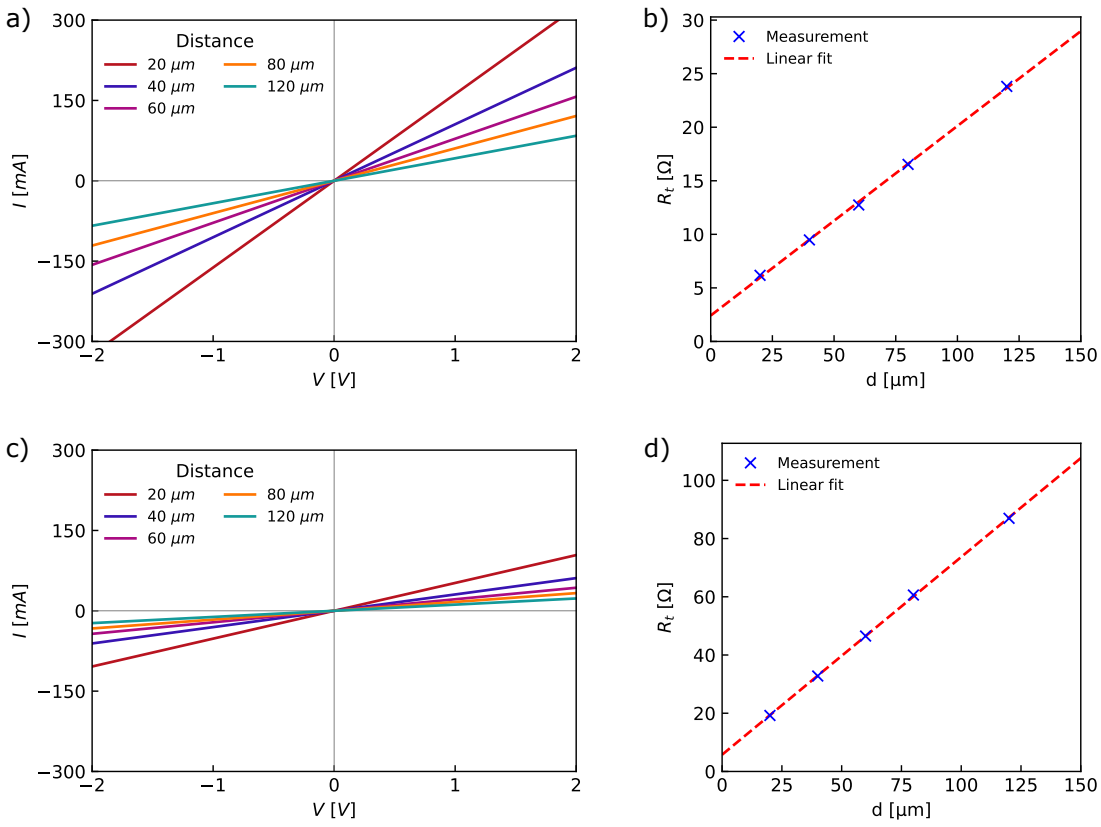

Figure 4.20: Two-probes TLM measurement results for the n-doped GaAs (a-b) and p-doped GaAs (c-d) of wafer 1. a) and c) Raw I-V measurements. b) and d) Corresponding resistance (R_t) versus electrode separation results, with linear fitting according to Eq. (4.1) (the associated coefficients of determination are R^2 = 0.9991 for the n-contact (b) and 0.9999 for the p-contact (d)).

Table 4.5: TLM measurements results for the devices with III-V bonded on oxidized Si, obtained with a two probes setup.

Wafer	Doping type	R_c [Ω]	R_{sh} [Ω/□]	L_t [µm]	ρ_c [Ω.cm^{-2}]
1	n	1.2	35	6.8	1.7×10^{-5}
	p	2.9	136	4.2	2.4×10^{-5}
3	n	1.2	35	6.8	1.6×10^{-5}
	p	2.9	119	5.0	2.9×10^{-5}
7	n	1.2	35	6.6	1.5×10^{-5}
	p	2.5	136	3.7	1.8×10^{-5}
9	n	1.0	38	5.1	1.0×10^{-5}
	p	2.9	110	5.3	3.2×10^{-5}
15	n	1.1	38	5.5	1.2×10^{-5}
	p	3.0	106	5.6	3.3×10^{-5}
17	n	1.1	37	6.0	1.3×10^{-5}
	p	2.4	111	4.3	2.1×10^{-5}

of the previous section. This is mainly due to the reduced thickness of the doped material regrowth. Conversely, the p-GaAs presents a notably higher sheet resistance, averaging 120 Ω/□ (σ = 12 Ω/□). This was expected and in agreement with typical observations owing to the lower hole mobility relative to that of electrons [44], [50].

The I-V characteristics of all diodes from the centermost die of wafer 7 were measured, with two typical curves displayed in Fig. 4.21. A total of ninety-six devices were tested, and three of them were rejected due to exhibiting an open circuit behavior.

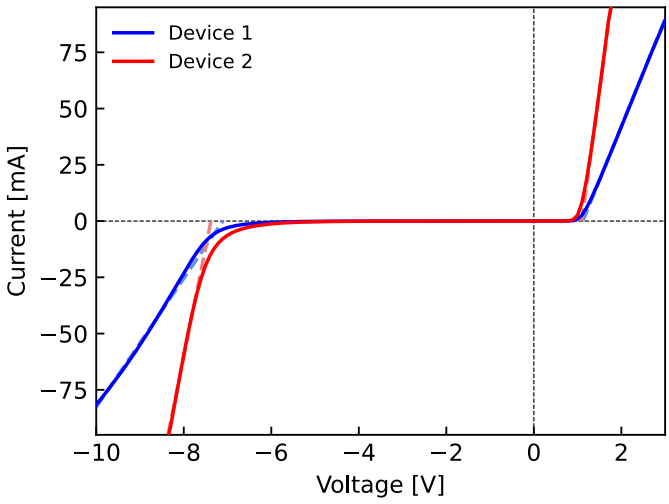

Figure 4.21: I-V measurements (full line) and linear fittings (dashed) for two devices. The devices dimensions on the masks are given in Table. 4.6. From fitting of the I-V curves, we obtain V_{th} = 1.11 V for both device and R_s = 21 Ω (1) and 7.3 Ω (2).

As for the previous section, the threshold voltage is independent of the device geometry,

Table 4.6: Design parameters: length (L), active region width (W) and distance between the electrodes and the active region (d) for the devices of Fig. 4.21 and Fig. 4.24–4.26, and minimum/maximum values used in the design of experiment (DOE).

Device	L [mm]	W [µm]	d [µm]
1	1	6	5
2	3	2	3
3	1.5	2	3
DOE min/max	1/3	1/10	1/5

and exhibits an average value of 1.11 V with with σ = 0.02 V.

The dependence of the series resistance on the device geometry could be studied more extensively for these devices than those fabricated on a GaAs substrate. This is allowed by the fine alignment of the photomasks, meaning that the designed geometries are well transferred to fabricated devices, and by the improved n-electrodes as compared to the previous section.

In order to make explicit the relationship between the device geometry and its series resistance, and to gain a better comprehension of the factors contributing to the series resistance, we have decomposed the measured series resistance in terms of contributions from the two probe-electrode resistance (R_{probes}), n and p contact resistance ($R_{c,tot}$), n and p doped regions (R_{doped}), and intrinsic zone region (R_i). The total series resistance is written as

$$R_s = R_{probes} + R_{c,tot} + R_{doped} + R_i \tag{4.5}$$

The contact resistance $R_{c,tot}$ varies as the inverse of device or contact length [190]. The dependence of the doped (resp. intrinsic) regions is considered proportional to the distance from the electrode to the intrinsic core (resp. intrinsic core width) and inversely proportional to the diode length. Accordingly, we propose the following equation for R_s:

$$R_s = R_{probes} + \alpha\frac{1}{L} + \beta\frac{d}{L} + \gamma\frac{W}{L} \tag{4.6}$$

with α, β and γ fitting parameters. It must be noted that with this setup, we cannot distinguish between the contributions from the n and p contact resistances, nor between the n and p doped regions. However, from the TLM measurements, we know that the n and p-contacts should contribute for 22% and 78% of $R_{c,tot}$ respectively. Similarly, the n and p-doped regions should contribute for 23% and 77% of R_{doped} respectively. Fitting over our dataset of ninety-three devices, we obtain R_{probes} = 5.57 Ω, α = 4.36× 10^{-4} Ω.m, β = 1.22 × 10^2 Ω and γ = 2.36 × 10^3 Ω. The coefficient of determination is R^2 = 0.994, indicating a satisfying fit considering the uncertainty on the actual devices dimensions. A comparison between the measurements and fitting is illustrated in Fig. 4.22, also exhibiting the influence of the three design parameters (d, W and L) on the series resistance.

From the fitting parameters and these curves, we observe that the main contribution to the

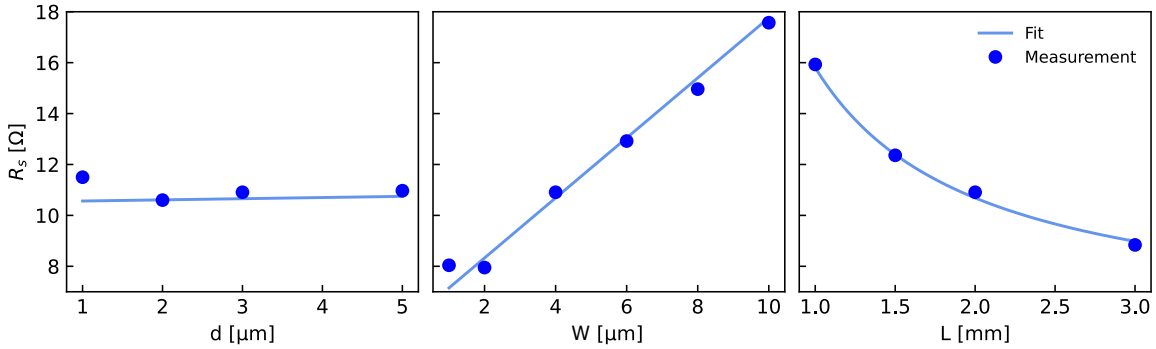

Figure 4.22: Influence of the geometry of the devices on their series resistance: measurement results and fitting according to Eq. (4.6). Unless it is the parameter under study, the distance between the electrode and intrinsic core, active core width and length of the devices are respectively 3 µm, 4 µm and 2 mm.

series resistance, apart from R_{probes}, comes from the intrinsic active region width. In addition to the simulation results presented in Fig. 2.29 — which indicated the optimum active region width to be ≤ 1 µm — this result is another motivation to target narrow active regions, as it is done in state-of-the art membrane lasers [31]. In contrast, owing to the high doping levels, the distance between the contacts and the active region has a fairly limited influence on the series resistance.

4.4.2. Electro-optical Characterization

Electro-optical characterizations of the fabricated devices were performed on prober, as illustrated in Fig.4.23.a. for the devices with etched facets, or on cleaved samples. Similar to the previous section, an optical fiber was used to collect a part of the emitted light.

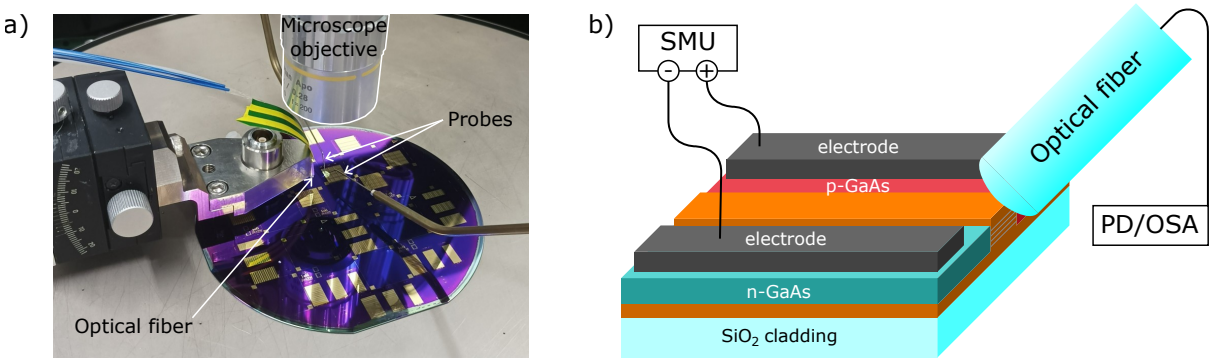

Figure 4.23: Prober measurement setup. (a) Photograph and (b) schematic.

The light versus pump current density (L-J) curves of three devices are shown in Fig. 4.24, for pump currents up to 230 mA (device 1) or 300 mA (devices 2 and 3). The three selected devices aim at representing variations in devices geometry, with device 1 being short and wide while devices 2 and 3 are narrower, with distinct lengths (see Table. 4.6). The optical power collected by the optical fiber is very low, about an order of magnitude lower than for the devices fabricated on a GaAs substrate. We attribute this to the modifications of the selective area growth of GaAs, giving a better selectivity and control of the grown thickness, creating a guiding structure with

a lower fraction of scattered light.

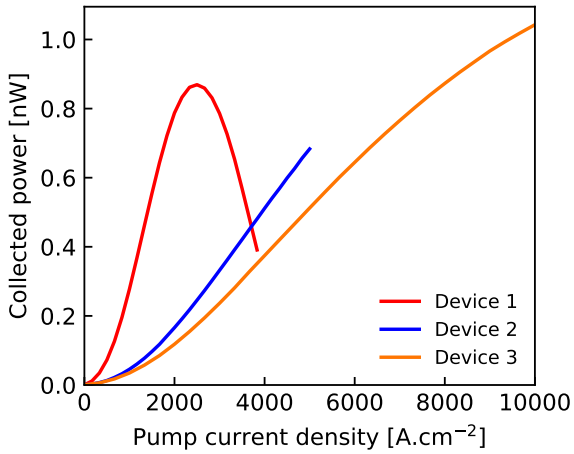

Figure 4.24: Collected optical power versus CW pump current density for three fabricated devices with etched facets. Devices 1 and 2 are the same as presented in Fig. 4.21. The dimensions of all three devices (on the mask) are given in Table. 4.6. The maximum current density corresponds to 300 mA for devices 2 and 3, and 230 mA for device 1 due to roll-over.

Compared with the previous lot, we also observe that the light emission turns on at much lower pump currents. This observation suggests an earlier saturation of the nonradiative recombination paths, likely due to a reduced density of nonradiative recombination centers.

However, we observe a roll-over of the optical power at high injection currents. It is particularly visible for device 1, also exhibiting the largest series resistance due to its wide intrinsic region and short length. For device 3, less resistive due to its narrower intrinsic region but still quite short, the differential efficiency just begins to decrease at 10000 A.cm^{-2} (300 mA), while device 3, the least resistive, does not exhibit any indications of roll-over up to 5000 A.cm^{-2} (300 mA). Since the III-V membrane lies on a thermally insulating SiO_2 layer, it was expected that the devices would have a high thermal impedance and self-heating could lead to roll-over. To confirm this hypothesis, we also studied the pump current-dependent emission spectra.

The emission spectra of the three devices are shown in Fig. 4.25. For all devices, the GaAs signal is much weaker than that from the MQW, and it is often hardly identifiable from the measurement noise. It was already visible from the PL spectra of the epitaxial stacks at the beginning of the processing that the GaAs signal was much weaker for this epitaxy. This could be owed to the lower energy levels of the QW, permitting a stronger confinement of the free carriers.

Due to the low to null GaAs signal, the analysis of self-heating cannot be performed from the position of the GaAs peaks. Besides, we cannot directly relate the signal from the QW emission to the active region temperature due to the quantized nature of the QW energy eigenstates. However, since the energy eigenstates have a given offset from the bandgap energy, the temperature variations can be computed from the derivative of the Varshni equation

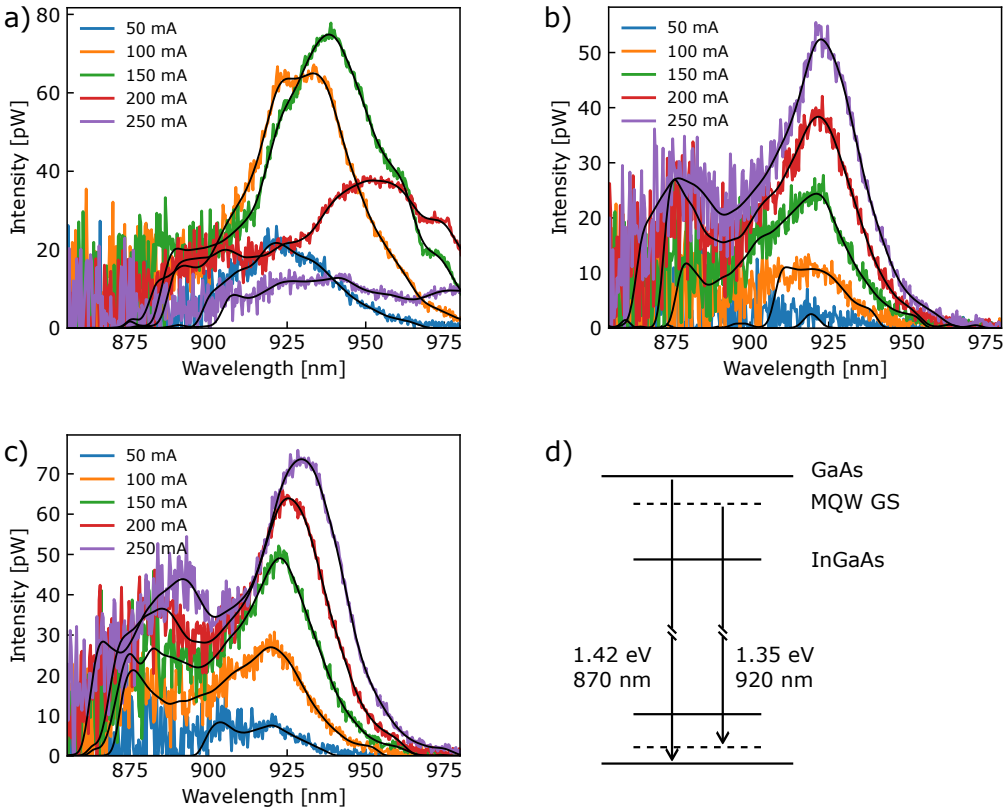

Figure 4.25: Optical emission spectra for three fabricated devices, measured at various CW pump currents. The devices are the same as presented in Fig. 4.24 (design parameters given in Table 4.6). The black curves correspond to the measurement data filtered using a second order low-pass Butterworth filter to suppress measurement noise. d) Schematic band diagram illustrating the origin of the two emission peaks visible in the spectra: recombination in the MQW (around 920 nm — 1.35 eV, decreasing in energy as the pump current is increased) and in the bulk GaAs (around 870 nm — 1.42 eV).

(Eq. (4.4)). We obtain:

$$\frac{\partial E_g}{\partial T} = -\frac{\alpha T\,(2\beta + T)}{(\beta + T)^2} \tag{4.7}$$

Expecting that other parameters not represented by the Varshni equation could also influence the shift of the MQW peak wavelength, for instance band filling or the difference between the thermal expansion coefficients of the different materials, we benchmarked this derivative method with the devices fabricated on a GaAs substrate (spectra of Fig. 4.17). With β = 225 K and α = 0.5 meV [193], [199], the derived increase in temperature from 250 mA to 400 mA for device 1, 2 and 3 fabricated on GaAs substrate are respectively 19 K, 17 K and 17 K , compared to 17 K, 17 K and 16 K obtained from the direct application of the Varshni equation to the GaAs peaks. This indicates that the derivative of the Varshni equation can be applied to the MQW peaks to determine the variations of the active region temperature with a high-enough degree of confidence.

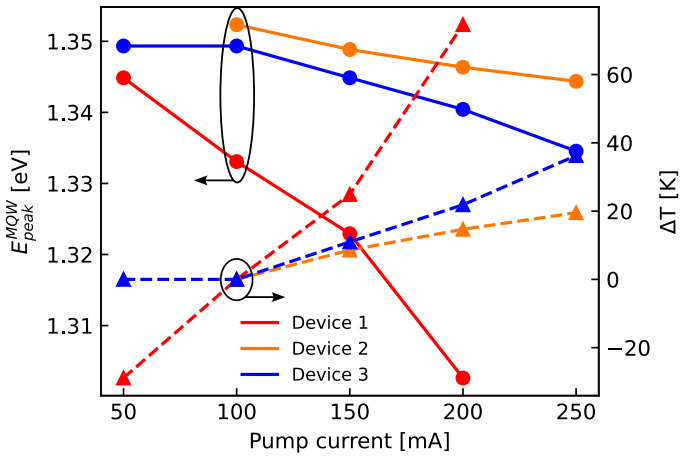

Figure 4.26: Shift of the MQW emission peak wavelength as a function of the pump current, and temperature variation inferred from the derivative of the Varshni equation (Eq. (4.7)). The devices under test are the same as in Fig. 4.24 (design parameters given in Table 4.6).

For the devices on a Si substrate, Fig. 4.26 shows the position of the MQW emission peak as a function of the injection current, along with the inferred temperature variations (the reference ΔT = 0 K is taken at 100 mA). The temperature increase is particularly high for device 1, with over 100 K of self-heating from 50 mA to 200 mA. This explains the dramatic roll-over observed in the L-J curve of this device (Fig. 4.24). For devices 2 and 3, which have lower series resistances, the temperature increase is more moderate, with 20 K and 30 K from 100 mA to 250 mA for device 2 and 3 respectively. Again, it is consistent that device 3, which exhibits signs of an imminent roll-over at 300 mA, has the highest temperature increase of the two devices. Due to its shorter length, it also has the highest series resistance.

In state-of-the art membrane lasers, the issue of a high thermal impedance is counterbalanced by typical low threshold currents [50].

To increase the pump current while mitigating self-heating, cleaved samples were tested in the pulsed pumping regime, replacing the source-measure unit with a voltage pulse generator.

The length of the devices, set by the cleavage planes, is measured to be 1994 µm, and the two selected devices were chosen to have narrow intrinsic region width to reduce their series resistance. They have w = 1 µm and d = 1 µm, and w = 2 µm and d = 3 µm. Fig. 4.27, shows

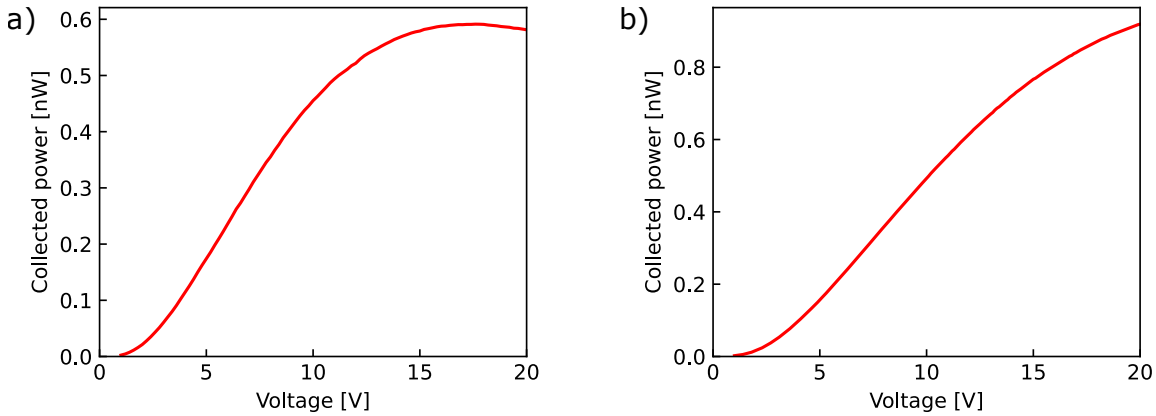

Figure 4.27: LV curves measured in the pulsed pumping regime on cleaved samples with (a) L = 1994 µm, w = 1 µm and d = 1 µm, pulse width 1 µs and frequency 10 kHz (duty cycle 0.01) and (b) L = 1994 µm, w = 2 µm and d = 3 µm, pulse width 0.5 µs and frequency 200 kHz (duty cycle 0.1).

the LV curves obtained in the pulsed pumping regime for these two devices. From Eq. (4.6), the corresponding pump currents at 20 V are 2.7 A (a) and 2.3 A (b). The pulses width and frequency are 1 µs and 10 kHz, giving a 0.01 duty cycle for Fig. 4.27.a, and 0.5 µs and 200 kHz (duty cycle 0.1) for Fig. 4.27.b. For both curves, no lasing behavior is observed, even at the higher pump voltages. Fig. 4.27.a. still exhibits roll-over, which could indicate the pulse duration of 1 µm is enough for the device to heat, despite the pulses pattern being similar to other reports from the literature (see for instance reference [63]: 1 µs pulse width and 0.01 duty cycle). The heating we observe in our conditions could be attributed to the high command voltage, small device volume, and increased electrical and thermal impedance.

4.4.3. Further Prospects

Owing to the good morphological characterizations and promising electro-optical characterization results, these devices exhibit great potential for the understanding of their operation, and potentially, for lasing. Indeed, the MQW provide light emission, and according to optical simulations, the thickness difference between the intrinsic core and the doped regions provides the optical guiding required for feedback. Due to the limited time we had during the frame of thesis, we could not push the devices characterizations further. However, the characterization of these devices is still ongoing.

Lasing is achieved when the optical gain compensates the propagation and mirrors losses, giving two potential levers to reach lasing. For as-cleaved samples, the facets reflectivity calculated from Eq. (2.30) for a GaAs–air interface is 30%. Hence, to reduce mirror losses, Al_2O_3/Si reflective coatings using will be applied to one or both facets of the cleaved samples. In addition, low temperature characterizations will be performed to reduce the thermal noise and ensure the free-carriers are confined to the lower energy states of the QW, which will increase

the optical gain. The sample temperature can be reduced to about 50 K. Reference [200] showed that carrier freezeout is not an issue in highly doped GaAs, down to temperatures of at least 80 K.

To quantify the propagation losses and the modal gain as a function of the pump current, and gain better insight into the device operation, the mode-sum method could also be used. In the mode-sum method, the Fabry-Perot spectrum of the biased device under test is recorded with an OSA, and the net optical gain is computed from the ratio of the optical intensity integrated over one FSR to the minimum of the intensity over the same FSR [201]. An advantage of the mode-sum method over, for instance, the cutback method, is that it can be performed below the lasing threshold, using the amplified spontaneous emission (ASE) spectrum of the device under test. The net modal gain versus pump current of the device under test is obtained by this method. Combining it with a transparency current measurement, one can retrieve the material gain versus pump current, and the propagation losses of the device under test, as done in reference [128]. The knowledge of the relationship between the pump current and the optical gain and propagation losses can be highly valuable in understanding the functioning of the fabricated devices.

4.5. Chapter summary

In summary, the devices which fabrication was presented in Chapter 3 were characterized from an electro-optical perspective in this chapter.

We first introduced the characterization setup and methods, such as the TLM, analysis of the L-I-V characteristic and electroluminescence spectra.

Next, the passive SOI components, in particular mirrors, were characterized. Posts DBR performed well, although with a larger coupling coefficient than on design, while the sidewall corrugations DBR had a much reduced coupling coefficient as compared with design. The reasons behind these differences were discussed, and based on these observations, we recommend using side-posts or side-openings DBR in future designs, for improved reliability and control over the coupling coefficient of the grating. Loop mirrors, building on mature DC from the PDK, exhibited the expected reflectivity and transmittance over a wide bandwidth. The SOI wafers are yet to receive the III-V stacks in order to demonstrate hybrid III-V/SOI membrane lasers. Comparing the photoluminescence spectra of the QD (Fig. 3.17.b) with the posts DBR (Figs. 4.6–4.7) and loop mirrors (Fig. 4.10) spectra indicates that these mirrors would effectively form an optical cavity providing optical feedback for stimulated emission towards lasing action.

Following that, we presented the results of the characterization of the lateral current injection devices fabricated on a GaAs substrate. These devices played a major role in the improvement of the fabrication conditions, but suffered from several issues limiting their potential as functional devices. Still, they provided important information on the doping levels of the epitaxial regrowth required to obtain ohmic contacts and a diode behavior. Light-emission upon electrical pumping of the devices was demonstrated, albeit without lasing. The analysis of the emission spectra

indicated light emission from recombination in the MQW, and mainly, from recombination in the GaAs.

Moving on to devices comprising a III-V membrane bonded on oxidized silicon, we could perform a more advanced analysis of impact of the diodes geometry on their characteristics, and in particular on their series resistance, found to be mainly impacted by the active region width. RT CW pumping L-I curves showed no evidence of lasing, and roll-over caused by self-heating was observed for the devices with the higher series resistance at high pump currents. Pulsed operation helped mitigating roll-over, but still no lasing was observed. Analysis of the pump current-dependent emission spectra indicated GaAs emission was strongly reduced for these devices as compared to those fabricated on a GaAs substrate, and that self-heating was stronger due to the insulating oxide layer. The characterization of these devices is still ongoing, and prospects are discussed.

5

Conclusion and Outlook

Within the context of increasing data communication volumes, this thesis aimed at providing a new type of on-chip laser for integrated optics applications. The proposed solution consists of InAs DWELL membrane lasers on silicon. With a predicted high energy efficiency and ability to operate in high-temperature conditions, these lasers could make co-packaged optics and optical network-on-chip a viable solution to extend optical communications to shorter distances.

5.1. Summary

The main results of this work can be divided in three main axes, namely: the development of a QD laser model, the design, fabrication and characterization of SOI passive components for integrated membrane lasers, and finally, the design, fabrication and characterization of light-emitting membrane diodes on silicon.

The QD laser model presented in Chapter 2 provides a new understanding of the operation of p-doped QD laser, in particular at high temperatures [108]. Especially, we found that npp Auger recombination plays an important role in the observed increase of the RT threshold and characteristic temperature of p-doped QD laser. By focusing on steady-state operation, we were able to find semi-analytical solutions to the model, dramatically reducing the computation time as compared to finite difference simulations. With this new tool in hand, we optimized the design of p-doped QD laser for operation at high temperatures. Compared with unintentionally doped QD laser, p-doped laser performed better with shorter cavities, and optimized p-doped devices could achieve lower RT thresholds than the unintentionally doped ones. In particular, we have simulated InAs QD membrane lasers with a 300 μm-long and 1 μm-wide active medium comprising 4 DWELL layers and a p-doping level corresponding to 10 extra holes per dot. The simulation results indicate that these lasers could exhibit submilliamp thresholds up to 60 ℃, and deliver more than 1 mW of output power for temperatures up to 110 ℃.

In designing the SOI passive components for membrane laser, we have focused on reducing

the complexity and number of specific steps compared with conventional lasers on silicon. So far, laser on silicon fabricated at CEA-LETI required localized thickening of the SOI for coupling light from the III-V to the SOI, and a specific lithography level for the partial etching of the SOI waveguides to realize Bragg gratings. By imposing an appropriate thickness for the III-V membrane, we were able to design III-V to SOI couplers without requiring thickening of the SOI nor tapering of the III-V. Designed couplers have a theoretical transmission of 97% and a length of 100 µm. For the Bragg reflectors requiring no specific lithography level, two designs were explored, namely sidewall corrugations and posts Bragg reflectors. The SOI circuits were fabricated on the 300 mm CEA-LETI platform, but the III-V could not bonded during the time of this thesis. Characterization of the Bragg reflectors indicates that the best results are obtained with the posts Bragg reflectors, although they suffer from an excessively large coupling factor. We suggest using side-posts Bragg reflectors to address this issue.

The fabrication of III-V membrane devices on Si was a great challenge since it required a complete transformation of the process-flow for the III-V fabrication. New processes were developed to fabricate the lateral current injection p-i-n diodes by plasma etching of the III-V membrane, chemical surface preparation and selective area growth of doped GaAs. Optimization of the processes was required to yield fine control of the etching depth and growth thickness and selectivity. Lateral current injection p-i-n diodes were successfully fabricated on III-V substrates as well as on silicon, following direct oxide bonding of the III-V epitaxial stack. The interfaces between the active stack and the selectively grown GaAs were observed at the atomic scale by STEM, and electrical characterizations of the fabricated diodes were performed. Both STEM images and electrical characterizations indicate defect-free interfaces. Following optimization of the fabrication process, the III-V membrane could be processed into rib waveguide structures, a requirement for the realization of laser diodes. Light emission was demonstrated upon electrical pumping of the fabricated diodes comprising InGaAs MQW. Electroluminescence spectra indicate emission from the MQW, as well as parasitic emission from the GaAs, which was reduced for the devices fabricated on silicon. These results pave the way for the realization of InAs QD membrane laser on silicon, and open many captivating prospects.

5.2. Outlook

In the short term, ongoing works initiated within the frame of this thesis could deliver important results. Although we have provided a fabrication pathway and demonstrated light emission from electrically pumped GaAs-based lateral current injection diodes on silicon, lasing action still needs to be demonstrated. This may be achieved through further characterization of the fabricated devices, as discussed in section 4.4.3. In particular, the deposition of highly reflective coatings on the facets of selected samples, and low-temperature characterization of these samples could favour lasing behavior. Besides, the fabrication of hybrid III-V on silicon devices using InAs QD is still in progress. Already characterized Bragg reflectors and loop interferometer mirrors fabricated in the SOI could provide the feedback necessary to attain lasing action, or

membrane microdisks could prove to be an efficient cavity. Some of these devices could also use AlGaAs doped regions to improve optical confinement and prevent free carriers leakage, as proposed in section 2.2.2.

Once lasing action will be demonstrated, the focus could be put on improving the performance of these lasers. In particular, it would be highly valuable to compare the results of the characterization of QD membrane laser with predictions from our model. These results could be used to refine the model, and potentially enrich it by studying, for instance, the dynamic behavior of QD membrane laser. This model was not ready for use yet when the hybrid III-V on silicon devices were designed. With this model now available, we have a new tool to improve the design of these lasers. Other improvements to the hybrid membrane lasers have already been discussed in Chapter 2 and 4. Especially, the use of side posts Bragg gratings could improve the performance and reliability of Bragg gratings. Besides, III-V/SOI optical couplers with a narrower output width could still achieve complete coupling of the optical mode from the III-V to the SOI waveguide while mitigating issues mentioned in Chapter 2. Design improvements could target not only the figures of merit describing continuous-wave operation, but also dynamic properties, since membrane lasers have already been demonstrated to provide superior ability for direct modulation [31].

Finally, the fabrication process should be optimized to tend towards industrial requirements. In this view, the III-V wafer or die bonding approach benefits from excellent maturity — in particular at CEA-LETI — is compatible with CMOS processing tools, and facilitates the realization of hybrid III-V on silicon devices. However, as we have already discussed, it is associated with a limited III-V material use efficiency. This raises the question: how could III-V membrane lasers be fabricated in a more material efficient way? Direct epitaxy would be challenging to use for the realization of membrane laser, since both blanket heteroepitaxy and aspect ratio trapping require rather thick III-V stacks. Lateral aspect ratio trapping could be a working solution, but it is not enough mature yet. In addition, the requirement of growing laterally several tens of micrometers of III-V material would lead to huge precursor consumption. The micro-transfer printing technology is compatible with the realization of III-V membrane laser on silicon, and offers many benefits. Finally, large diameter GaAs on silicon substrates as have already been demonstrated for InP [91] could give the best results in terms of scaling and throughput, while requiring little modifications as compared to the process-flow presented in this thesis. For instance, the epitaxial stack could be grown on the GaAs on silicon substrates before bonding on processed SOI wafers. From this point on, the process-flow developed in this thesis could be transferred to large diameter wafers.

To close this thesis, InAs DWELL membrane laser are a promising solution to address the recent challenges in optical data communications and silicon photonics. With this works, we hope to provide tools helping to fabricate and better understand such devices.

List of Publications

Journal Papers

- M. Chobé and K. Hassan, "Steady-State Semi-Analytical Modeling of p-Doped Quantum Dot Lasers Thermal Characteristics and Extrapolation to Membrane Lasers," *IEEE Journal of Quantum Electronics*, vol. 60, no. 1, pp. 1-9, Feb. 2024. DOI: 10.1109/JQE.2023.3342180.

Conference Proceedings

- M. Chobé, H. Hijazi, M. Martin, S. Barbet, R. Thibon, C. Jany, T. Baron and K. Hassan, "Investigation of InAs Quantum Dot Membrane Lasers for on-chip Communications: Simulation and Integration Prospects," in *2023 International Conference on Solid State Devices and Materials (SSDM2023)*, Sept. 2023.
- T. Baron, V. Letka, H. Hijazi, M. Chobé, L. Mallet-Dida, M. Martin, J. Moeyaert, N. Massara, J. Mignot, J. Richy, C. Licitra, R. Thibon, S. Barbet, D. Mouloua, F. Boeuf, C. Jany, and K. Hassan, "Monolithic integration of GaAs based compounds on silicon platform for photonic and optoelectronic devices," in *Proc. SPIE PC12890, Smart Photonic and Optoelectronic Integrated Circuits 2024*, March 2024. DOI: 10.1117/12.3000351.

Patents

- M. Chobé, K. Hassan, and C. Dupré, "Optoelectronic device comprising a III-V semiconductor membrane laser source forming a lateral p-i-n junction," US20230318263A1, Oct. 2023.

References

[1] CISCO, *Cisco Global Cloud Index: Forecast and Methodology, 2016–2021*, 2018.

[2] CISCO, *Cisco Annual Internet Report (2018–2023)*, 2020.

[3] IEEE, *International Roadmap for Devices and Systems: 2022*.

[4] E. Masanet *et al.*, "Recalibrating global data center energy-use estimates," *Science*, vol. 367, no. 6481, pp. 984–986, Feb. 2020. DOI: 10.1126/science.aba3758.

[5] K. M. U. Ahmed, M. H. J. Bollen, and M. Alvarez, "A Review of Data Centers Energy Consumption and Reliability Modeling," *IEEE Access*, vol. 9, pp. 152 536–152 563, 2021. DOI: 10.1109/ACCESS.2021.3125092.

[6] M. Koot and F. Wijnhoven, "Usage impact on data center electricity needs: A system dynamic forecasting model," *Appl. Energy*, vol. 291, p. 116 798, 2021. DOI: 10.1016/j.apenergy.2021.116798.

[7] J. W. Goodman *et al.*, "Optical interconnections for VLSI systems," *Proc. IEEE*, vol. 72, no. 7, pp. 850–866, Jul. 1984. DOI: 10.1109/PROC.1984.12943.

[8] M. R. Feldman *et al.*, "Comparison between optical and electrical interconnects based on power and speed considerations," en, *Appl. Opt.*, vol. 27, no. 9, p. 1742, May 1988. DOI: 10.1364/AO.27.001742.

[9] D. Miller, "Device Requirements for Optical Interconnects to Silicon Chips," *Proc. IEEE*, vol. 97, no. 7, pp. 1166–1185, Jul. 2009. DOI: 10.1109/JPROC.2009.2014298.

[10] Y. Han *et al.*, "Recent advances in light sources on silicon," *Adv. Opt. Photon.*, vol. 14, no. 3, pp. 404–454, Sep. 2022. DOI: 10.1364/AOP.455976.

[11] T. Alexoudi *et al.*, "Optics in Computing: From Photonic Network-on-Chip to Chip-to-Chip Interconnects and Disintegrated Architectures," *J. Light. Technol.*, vol. 37, no. 2, pp. 363–379, Jan. 2019. DOI: 10.1109/JLT.2018.2875995.

[12] C. Minkenberg *et al.*, "Co-packaged datacenter optics: Opportunities and challenges," *IET Optoelectron.*, vol. 15, no. 2, pp. 77–91, 2021. DOI: 10.1049/ote2.12020.

[13] *Cisco Transceiver Modules - Cisco 400G QSFP-DD Cable and Transceiver Modules Data Sheet*, en. AVAILABLE: https://www.cisco.com/c/en/us/products/collateral/interfaces-modules/transceiver-modules/datasheet-c78-743172.html (visited on 06/04/2024).

[14] *Intel® Silicon Photonics 400G DR4 QSFP-DD Optical Transceiver - Product Specifications*. AVAILABLE: https://www.intel.com/content/www/us/en/products/sku/135329/intel-silicon-photonics-400g-dr4-qsfpdd-optical-transceiver/specifications.html (visited on 06/04/2024).

[15] S. Sun *et al.*, "CLEAR: A Holistic Figure-of-Merit for Post- and Predicting Electronic and Photonic-based Compute-system Evolution," *Sci. Reports*, vol. 10, no. 1, p. 6482, Apr. 2020. DOI: 10.1038/s41598-020-63408-7. (visited on 07/08/2024).

[16] Y. Thonnart *et al.*, "POPSTAR: A Robust Modular Optical NoC Architecture for Chiplet-based 3D Integrated Systems," in *2020 Design, Automation & Test in Europe Conference & Exhibition*, 2020, pp. 1456–1461. DOI: 10.23919/DATE48585.2020.9116214.

[17] A. H. Atabaki *et al.*, "Integrating photonics with silicon nanoelectronics for the next generation of systems on a chip," en, *Nature*, vol. 556, no. 7701, pp. 349–354, Apr. 2018. DOI: 10.1038/s41586-018-0028-z.

[18] R. Soref and J. Larenzo, "All-silicon active and passive guided-wave components for λ = 1.3 and 1.6 μm," *IEEE J. Quantum Electron.*, vol. 22, no. 6, pp. 873–879, Jun. 1986. DOI: 10.1109/JQE.1986.1073057.

[19] S. Shekhar *et al.*, "Roadmapping the next generation of silicon photonics," en, *Nat. Commun.*, vol. 15, no. 1, p. 751, Jan. 2024. DOI: 10.1038/s41467-024-44750-0. (visited on 06/06/2024).

[20] W. Bogaerts *et al.*, "Nanophotonic Waveguides in Silicon-on-Insulator Fabricated With CMOS Technology," *J. Light. Technol.*, vol. 23, no. 1, p. 401, Jan. 2005. DOI: 10.1109/JLT.2004.834471.

[21] Q. Wilmart *et al.*, "A Complete Si Photonics Platform Embedding Ultra-Low Loss Waveguides for O- and C-Band," *J. Light. Technol.*, vol. 39, no. 2, pp. 532–538, Jan. 2021. DOI: 10.1109/JLT.2020.3030123. (visited on 06/05/2024).

[22] S. Bernabé *et al.*, "Silicon photonics for terabit/s communication in data centers and exascale computers," en, *Solid-State Electron.*, vol. 179, p. 107 928, May 2021. DOI: 10.1016/j.sse.2020.107928.

[23] L. Chrostowski and M. E. Hochberg, *Silicon photonics design*, en. Cambridge: Cambridge university press, 2015.

[24] C. Dragone, "An N*N optical multiplexer using a planar arrangement of two star couplers," *IEEE Photonics Technol. Lett.*, vol. 3, no. 9, pp. 812–815, Sep. 1991. DOI: 10.1109/68.84502.

[25] F. Horst *et al.*, "Cascaded Mach-Zehnder wavelength filters in silicon photonics for low loss and flat pass-band WDM (de-)multiplexing," *Opt. Express*, vol. 21, no. 10, pp. 11 652–11 658, May 2013. DOI: 10.1364/OE.21.011652.

[26] A. G. Griffith *et al.*, "Silicon-chip mid-infrared frequency comb generation," en, *Nat. Commun.*, vol. 6, no. 1, p. 6299, Feb. 2015. DOI: 10.1038/ncomms7299.

[27] D. Thomson *et al.*, "Roadmap on silicon photonics," en, *J. Opt.*, vol. 18, no. 7, p. 073 003, Jun. 2016. DOI: 10.1088/2040-8978/18/7/073003.

[28] R. Sapienza, "Determining random lasing action," en, *Nat. Rev. Phys.*, vol. 1, no. 11, pp. 690–695, Nov. 2019. DOI: 10.1038/s42254-019-0113-8.

[29] L. A. Coldren, S. W. Corzine, and M. Mashanovitch, *Diode lasers and photonic integrated circuits* (Wiley series in microwave and optical engineering 218), 2nd ed. Hoboken, N.J: Wiley, 2012.

[30] J. C. Norman *et al.*, "The Importance of p-Doping for Quantum Dot Laser on Silicon Performance," *IEEE J. Quantum Electron.*, vol. 55, no. 6, pp. 1–11, Dec. 2019. DOI: 10.1109/JQE.2019.2941579.

[31] S. Yamaoka *et al.*, "Directly modulated membrane lasers with 108 GHz bandwidth on a high-thermal-conductivity silicon carbide substrate," *Nat. Photonics*, vol. 15, no. 1, pp. 28–35, Jan. 2021. DOI: 10.1038/s41566-020-00700-y.

[32] K. Takeda *et al.*, "Few-fJ/bit data transmissions using directly modulated lambda-scale embedded active region photonic-crystal lasers," en, *Nat. Photonics*, vol. 7, no. 7, Jul. 2013. DOI: 10.1038/nphoton.2013.110.

[33] E. Commission, *The European Green Deal*, en, 2019. AVAILABLE: https://eur-lex.europa.eu/legal-content/EN/TXT/?qid=1596443911913&uri=CELEX:52019DC0640#document2 (visited on 06/16/2024).

[34] A. SG Andrae, "New perspectives on internet electricity use in 2030," *Eng. Appl. Sci. Lett.*, vol. 3, no. 2, pp. 19–31, 2020.

[35] J. C. T. Bieser and L. M. Hilty, "Assessing Indirect Environmental Effects of Information and Communication Technology (ICT): A Systematic Literature Review," en, *Sustainability*, vol. 10, no. 8, p. 2662, Aug. 2018. DOI: 10.3390/su10082662.

[36] S. Lange, J. Pohl, and T. Santarius, "Digitalization and energy consumption. Does ICT reduce energy demand?" en, *Ecol. Econ.*, vol. 176, p. 106 760, Oct. 2020. DOI: 10.1016/j.ecolecon.2020.106760.

[37] N. Moreau *et al.*, "Could Unsustainable Electronics Support Sustainability?" en, *Sustainability*, vol. 13, no. 12, p. 6541, Jun. 2021. DOI: 10.3390/su13126541.

[38] A. Luers *et al.*, "Will AI accelerate or delay the race to net-zero emissions?" *Nature*, vol. 628, no. 8009, pp. 718–720, Apr. 2024. DOI: 10.1038/d41586-024-01137-x.

[39] U. Gupta *et al.*, "Chasing Carbon: The Elusive Environmental Footprint of Computing," en, *IEEE Micro*, vol. 42, no. 4, pp. 37–47, Jul. 2022. DOI: 10.1109/MM.2022.3163226.

[40] T. Pirson *et al.*, "The Environmental Footprint of IC Production: Review, Analysis, and Lessons From Historical Trends," *IEEE Trans. on Semicond. Manuf.*, vol. 36, no. 1, pp. 56–67, Feb. 2023. DOI: 10.1109/TSM.2022.3228311.

[41] W. Shockley and W. T. Read, "Statistics of the Recombinations of Holes and Electrons," *Phys. Rev.*, vol. 87, no. 5, pp. 835–842, Sep. 1952. DOI: 10.1103/PhysRev.87.835.

[42] R. N. Hall, "Electron-Hole Recombination in Germanium," *Phys. Rev.*, vol. 87, no. 2, pp. 387–387, Jul. 1952. DOI: 10.1103/PhysRev.87.387.

[43] T. Visser *et al.*, "Confinement factors and gain in optical amplifiers," *IEEE J. Quantum Electron.*, vol. 33, no. 10, pp. 1763–1766, 1997. DOI: 10.1109/3.631280.

[44] S. M. Sze and K. K. Ng, *Physics of semiconductor devices*, 3rd ed. Hoboken, N.J: Wiley-Interscience, 2007.

[45] D. Liang and J. E. Bowers, "Recent progress in lasers on silicon," *Nat. Photonics*, vol. 4, no. 8, pp. 511–517, Aug. 2010. DOI: 10.1038/nphoton.2010.167.

[46] H. Mathieu and H. Fanet, *Physique des semiconducteurs et des composants électroniques*, 6è édition. Dunod, 2009.

[47] Z. I. Alferov and R. F. Kazarinov, "Semiconductor laser with electric pumping," Russian, Mar. 1963.

[48] H. Kroemer, "A proposed class of hetero-junction injection lasers," *Proc. IEEE*, vol. 51, no. 12, pp. 1782–1783, Dec. 1963. DOI: 10.1109/PROC.1963.2706.

[49] V. Y. Aleshkin *et al.*, "Monolithically integrated InGaAs/GaAs/AlGaAs quantum well laser grown by MOCVD on exact Ge/Si(001) substrate," *Appl. Phys. Lett.*, vol. 109, no. 6, Aug. 2016. DOI: 10.1063/1.4961059.

[50] T. Aihara *et al.*, "Membrane buried-heterostructure DFB laser with an optically coupled III-V/Si waveguide," *Opt. Express*, vol. 27, no. 25, pp. 36 438–36 448, 2019. DOI: 10.1364/OE.27.036438.

[51] T. Kageyama *et al.*, "Extremely high temperature (220°C) continuous-wave operation of 1300-nm-range quantum-dot lasers," in *2011 Conference on Lasers and Electro-Optics Europe and 12th European Quantum Electronics Conference*, May 2011. DOI: 10.1109/CLEOE.2011.5943701.

[52] J. C. Norman, R. P. Mirin, and J. E. Bowers, "Quantum dot lasers—History and future prospects," *J. Vac. Sci. & Technol. A*, vol. 39, no. 2, p. 020 802, Mar. 2021. DOI: 10.1116/6.0000768.

[53] L. Goldstein *et al.*, "Growth by molecular beam epitaxy and characterization of InAs/GaAs strained-layer superlattices," *Appl. Phys. Lett.*, vol. 47, no. 10, pp. 1099–1101, Nov. 1985. DOI: 10.1063/1.96342.

[54] B. A. Joyce and D. D. Vvedensky, "Self-organized growth on GaAs surfaces," *Mater. Sci. Eng. R: Reports*, vol. 46, no. 6, pp. 127–176, Dec. 2004. DOI: 10.1016/j.mser.2004.10.001.

[55] V. M. Ustinov *et al.*, "InAs/InGaAs quantum dot structures on GaAs substrates emitting at 1.3 μm," *Appl. Phys. Lett.*, vol. 74, no. 19, pp. 2815–2817, May 1999. DOI: 10.1063/1.124023.

[56] J. M. Ramirez *et al.*, "III-V-on-Silicon Integration: From Hybrid Devices to Heterogeneous Photonic Integrated Circuits," *IEEE J. Sel. Top. Quantum Electron.*, vol. 26, no. 2, pp. 1–13, Mar. 2020. DOI: 10.1109/JSTQE.2019.2939503.

[57] P. Kaur *et al.*, "Hybrid and heterogeneous photonic integration," *APL Photonics*, vol. 6, no. 6, p. 061 102, Jun. 2021. DOI: 10.1063/5.0052700.

[58] N. Li *et al.*, "Integrated Lasers on Silicon at Communication Wavelength: A Progress Review," *Adv. Opt. Mater.*, vol. 10, no. 23, p. 2 201 008, 2022. DOI: 10.1002/adom.202201008.

[59] G. Roelkens *et al.*, "Micro-transfer printing for heterogeneous si photonic integrated circuits," *IEEE J. Sel. Top. Quantum Electron.*, vol. 29, pp. 1–14, 2023. DOI: 10.1109/JSTQE.2022.3222686.

[60] S. Lourdudoss, "Heteroepitaxy and selective area heteroepitaxy for silicon photonics," *Curr. Opin. Solid State Mater. Sci.*, Photonic Nanostructure Materials, Processing and Characterization, vol. 16, no. 2, pp. 91–99, Apr. 2012. DOI: 10.1016/j.cossms.2012.01.003.

[61] S. Adachi, *Properties of semiconductor alloys: group-IV, III-V and II-VI semiconductors*. Chichester, U.K: Wiley, 2009.

[62] M.-L. Touraton, "Direct epitaxy of III-V semiconductors on silicon substrate for photonic devices," Ph.D. dissertation, Université Grenoble Alpes, 2020.

[63] S. Chen *et al.*, "Electrically pumped continuous-wave III–V quantum dot lasers on silicon," *Nat. Photonics*, vol. 10, no. 5, pp. 307–311, May 2016. DOI: 10.1038/nphoton.2016.21.

[64] J. Norman *et al.*, "Electrically pumped continuous wave quantum dot lasers epitaxially grown on patterned, on-axis (001) Si," *Opt. Express*, vol. 25, no. 4, pp. 3927–3934, Feb. 2017. DOI: 10.1364/OE.25.003927.

[65] Y. Shi *et al.*, "Novel adiabatic coupler for III-V nano-ridge laser grown on a Si photonics platform," *Opt. Express*, vol. 27, no. 26, pp. 37 781–37 794, Dec. 2019. DOI: 10.1364/OE.27.037781.

[66] M. Martin *et al.*, "Toward the III–V/Si co-integration by controlling the biatomic steps on hydrogenated Si(001)," *Appl. Phys. Lett.*, vol. 109, no. 25, p. 253 103, Dec. 2016. DOI: 10.1063/1.4972394.

[67] Y. Wan *et al.*, "1.3 μm submilliamp threshold quantum dot micro-lasers on Si," *Optica*, vol. 4, no. 8, pp. 940–944, Aug. 2017. DOI: 10.1364/OPTICA.4.000940.

[68] K. Volz *et al.*, "GaP-nucleation on exact Si (001) substrates for III/V device integration," *J. Cryst. Growth*, vol. 315, no. 1, pp. 37–47, 2011. DOI: 10.1016/j.jcrysgro.2010.10.036.

[69] S. Chen *et al.*, "Electrically pumped continuous-wave 1.3 μm InAs/GaAs quantum dot lasers monolithically grown on on-axis Si (001) substrates," *Opt. Express*, vol. 25, no. 5, pp. 4632–4639, 2017. DOI: 10.1364/OE.25.004632.

[70] C. Shang *et al.*, "A Pathway to Thin GaAs Virtual Substrate on On-Axis Si (001) with Ultralow Threading Dislocation Density," *physica status solidi (a)*, vol. 218, no. 3, p. 2 000 402, 2021. DOI: https://doi.org/10.1002/pssa.202000402.

[71] C. Shang *et al.*, "Electrically pumped quantum-dot lasers grown on 300 mm patterned Si photonic wafers," *Light. Sci. & Appl.*, vol. 11, no. 1, p. 299, 2022. DOI: 10.1038/s41377-022-00982-7.

[72] W.-Q. Wei *et al.*, "Monolithic integration of embedded iii-v lasers on soi," *Light. Sci. & Appl.*, vol. 12, no. 1, p. 84, 2023. DOI: 10.1038/s41377-023-01128-z.

[73] R. Cipro *et al.*, "Low defect InGaAs quantum well selectively grown by metal organic chemical vapor deposition on Si(100) 300 mm wafers for next generation non planar devices," *Appl. Phys. Lett.*, vol. 104, no. 26, p. 262 103, Jul. 2014. DOI: 10.1063/1.4886404.

[74] B. Kunert *et al.*, "III/V nano ridge structures for optical applications on patterned 300 mm silicon substrate," *Appl. Phys. Lett.*, vol. 109, no. 9, p. 091 101, Aug. 2016. DOI: 10.1063/1.4961936.

[75] Y. Han *et al.*, "Selectively Grown III-V Lasers for Integrated Si-Photonics," *J. Light. Technol.*, vol. 39, no. 4, pp. 940–948, Feb. 2021. DOI: 10.1109/JLT.2020.3041348.

[76] H. Schmid *et al.*, "Template-assisted selective epitaxy of III–V nanoscale devices for co-planar heterogeneous integration with Si," *Appl. Phys. Lett.*, vol. 106, no. 23, p. 233 101, Jun. 2015. DOI: 10.1063/1.4921962.

[77] J. Zhang *et al.*, "Transfer-printing-based integration of a III-V-on-silicon distributed feedback laser," *Opt. Express*, vol. 26, no. 7, pp. 8821–8830, Apr. 2018. DOI: 10.1364/OE.26.008821.

[78] R. Baets and A. Rahim, "Heterogeneous integration in silicon photonics: Opportunities and challenges: Opinion," *Opt. Mater. Express*, vol. 13, no. 12, pp. 3439–3444, Dec. 2023. DOI: 10.1364/OME.509531.

[79] T. Shimizu *et al.*, "High density hybrid integrated light source with a laser diode array on a silicon optical waveguide platform for inter-chip optical interconnection," in *8th IEEE International Conference on Group IV Photonics*, 2011, pp. 181–183. DOI: 10.1109/GROUP4.2011.6053756.

[80] H. Lu *et al.*, "Flip-chip integration of tilted vcsels onto a silicon photonic integrated circuit," *Opt. Express*, vol. 24, no. 15, pp. 16 258–16 266, Jul. 2016. DOI: 10.1364/OE.24.016258.

[81] H. Yang *et al.*, "Transfer-printed stacked nanomembrane lasers on silicon," en, *Nat. Photonics*, vol. 6, no. 9, pp. 615–620, Sep. 2012. DOI: 10.1038/nphoton.2012.160.

[82] S. Keyvaninia *et al.*, "Demonstration of a heterogeneously integrated III-V/SOI single wavelength tunable laser," *Opt. Express*, vol. 21, no. 3, pp. 3784–3792, Feb. 2013. DOI: 10.1364/OE.21.003784.

[83] A. Fang *et al.*, "Electrically pumped hybrid AlGaInAs-silicon evanescent laser," *Opt. Express*, vol. 14, no. 20, pp. 9203–9210, 2006. DOI: 10.1364/OE.14.009203.

[84] R. Jones *et al.*, "Heterogeneously integrated InPSilicon photonics: Fabricating fully functional transceivers," *IEEE Nanotechnol. Mag.*, vol. 13, no. 2, pp. 17–26, 2019. DOI: 10.1109/MNANO.2019.2891369.

[85] D. Pasquariello and K. Hjort, "Plasma-assisted InP-to-Si low temperature wafer bonding," *IEEE J. Sel. Top. Quantum Electron.*, vol. 8, no. 1, pp. 118–131, Jan. 2002. DOI: 10.1109/2944.991407.

[86] H. Moriceau *et al.*, "Overview of recent direct wafer bonding advances and applications," *Adv. Nat. Sci. Nanosci. Nanotechnol.*, vol. 1, no. 4, p. 043 004, Feb. 2011. DOI: 10.1088/2043-6262/1/4/043004.

[87] F. Fournel *et al.*, "Water Stress Corrosion in Bonded Structures," en, *ECS J. Solid State Sci. Technol.*, vol. 4, no. 5, P124, Feb. 2015. DOI: 10.1149/2.0031505jss.

[88] F. Niklaus *et al.*, "Adhesive wafer bonding," *J. Appl. Phys.*, vol. 99, no. 3, p. 031 101, Feb. 2006. DOI: 10.1063/1.2168512.

[89] S. Keyvaninia *et al.*, "Ultra-thin DVS-BCB adhesive bonding of III-V wafers, dies and multiple dies to a patterned silicon-on-insulator substrate," *Opt. Mater. Express*, vol. 3, no. 1, pp. 35–46, Jan. 2013. DOI: 10.1364/OME.3.000035.

[90] S. Uvin *et al.*, "1.3 μm InAs/GaAs quantum dot DFB laser integrated on a Si waveguide circuit by means of adhesive die-to-wafer bonding," *Opt. Express*, vol. 26, no. 14, pp. 18 302–18 309, Jul. 2018. DOI: 10.1364/OE.26.018302.

[91] B. Ghyselen *et al.*, "Large-Diameter III–V on Si Substrates by the Smart Cut Process: The 200 mm InP Film on Si Substrate Example," *physica status solidi (a)*, vol. 219, no. 4, p. 2 100 543, 2022. DOI: 10.1002/pssa.202100543.

[92] T. Christopoulos *et al.*, "On the calculation of the quality factor in contemporary photonic resonant structures," *Opt. Express*, vol. 27, no. 10, pp. 14 505–14 522, May 2019. DOI: 10.1364/OE.27.014505.

[93] S. Skalsky *et al.*, "Heterostructure and Q -factor engineering for low-threshold and persistent nanowire lasing," en, *Light. Sci. & Appl.*, vol. 9, no. 1, p. 43, Mar. 2020. DOI: 10.1038/s41377-020-0279-y.

[94] A. Röhm, *Dynamic Scenarios in Two-State Quantum Dot Lasers*. Springer Fachmedien Wiesbaden, 2015. DOI: 10.1007/978-3-658-09402-7.

[95] J. Van Campenhout *et al.*, "Electrically pumped InP-based microdisk lasers integrated with a nanophotonic silicon-on-insulator waveguide circuit," *Opt. Express*, vol. 15, no. 11, pp. 6744–6749, May 2007. DOI: 10.1364/OE.15.006744.

[96] D. Liang *et al.*, "Integrated finely tunable microring laser on silicon," en, *Nat. Photonics*, vol. 10, no. 11, pp. 719–722, Nov. 2016. DOI: 10.1038/nphoton.2016.163.

[97] S. L. McCall *et al.*, "Whispering-gallery mode microdisk lasers," *Appl. Phys. Lett.*, vol. 60, no. 3, pp. 289–291, Jan. 1992. DOI: 10.1063/1.106688.

[98] S. Wirths *et al.*, "Room-Temperature Lasing from Monolithically Integrated GaAs Microdisks on Silicon," *ACS Nano*, vol. 12, no. 3, pp. 2169–2175, Mar. 2018. DOI: 10.1021/acsnano.7b07911.

[99] B. Ellis *et al.*, "Ultralow-threshold electrically pumped quantum-dot photonic-crystal nanocavity laser," *Nat. Photonics*, vol. 5, no. 5, pp. 297–300, 2011. DOI: 10.1038/nphoton.2011.51.

[100] K. Takeda *et al.*, "Optical links on silicon photonic chips using ultralow-power consumption photonic-crystal lasers," EN, *Opt. Express*, vol. 29, no. 16, pp. 26 082–26 092, Aug. 2021. DOI: 10.1364/OE.427843.

[101] T. Okamoto *et al.*, "Optically pumped membrane BH-DFB lasers for low-threshold and single-mode operation," *IEEE J. Sel. Top. Quantum Electron.*, vol. 9, no. 5, pp. 1361–1366, Sep. 2003. DOI: 10.1109/JSTQE.2003.819495.

[102] Y. Jiao *et al.*, "InP membrane integrated photonics research," en, *Semicond. Sci. Technol.*, vol. 36, no. 1, p. 013 001, Dec. 2020. DOI: 10.1088/1361-6641/abcadd.

[103] K. Papatryfonos *et al.*, "Refractive indices of MBE-grown $Al_xGa_{1-x}As$ ternary alloys in the transparent wavelength region," *AIP Adv.*, vol. 11, p. 025 327, Feb. 2021. DOI: 10.1063/5.0039631.

[104] N. P. Diamantopoulos *et al.*, "60 GHz Bandwidth Directly Modulated Membrane III-V Lasers on SiO_2/Si," *J. Light. Technol.*, pp. 1–1, 2022. DOI: 10.1109/JLT.2022.3153648.

[105] B. Szelag *et al.*, "Hybrid III–V/Silicon technology for laser integration on a 200-mm fully CMOS-compatible silicon photonics platform," *IEEE J. Sel. Top. Quantum Electron.*, vol. 25, no. 5, pp. 1–10, 2019. DOI: 10.1109/JSTQE.2019.2904445.

[106] E. H. Sargent and J. M. Xu, "Lateral injection lasers," en, *Int. J. High Speed Electron. Syst.*, vol. 09, no. 04, p. 38, 1998. DOI: 10.1142/S0129156498000397.

[107] T. Okumura *et al.*, "Lateral current injection GaInAsP/InP laser on semi-insulating substrate for membrane-based photonic circuits," EN, *Opt. Express*, vol. 17, no. 15, pp. 12 564–12 570, Jul. 2009. DOI: 10.1364/OE.17.012564.

[108] M. Chobé and K. Hassan, "Steady-State Semi-Analytical Modeling of p-Doped Quantum Dot Lasers Thermal Characteristics and Extrapolation to Membrane Lasers," *IEEE J. Quantum Electron.*, vol. 60, no. 1, pp. 1–9, Feb. 2024. DOI: 10.1109/JQE.2023.3342180.

[109] M. Sugawara *et al.*, "Effect of homogeneous broadening of optical gain on lasing spectra in self-assembled $In_xGa_{1-x}As$/GaAs quantum dot lasers," *Phys. Rev. B*, vol. 61, no. 11, pp. 7595–7603, Mar. 2000. DOI: 10.1103/PhysRevB.61.7595.

[110] T. Berg *et al.*, "Ultrafast gain recovery and modulation limitations in self-assembled quantum-dot devices," *IEEE Photonics Technol. Lett.*, vol. 13, no. 6, pp. 541–543, 2001. DOI: 10.1109/68.924013.

[111] A. Markus and A. Fiore, "Modeling carrier dynamics in quantum-dot lasers," *physica status solidi (a)*, vol. 201, no. 2, pp. 338–344, 2004. DOI: 10.1002/pssa.200303965.

[112] A. Fiore and A. Markus, "Differential Gain and Gain Compression in Quantum-Dot Lasers," *IEEE J. Quantum Electron.*, vol. 43, no. 4, pp. 287–294, Apr. 2007. DOI: 10.1109/JQE.2006.890399.

[113] D. O'Brien *et al.*, "Sensitivity of quantum-dot semiconductor lasers to optical feedback," *Opt. Lett.*, vol. 29, no. 10, pp. 1072–1074, May 2004. DOI: 10.1364/OL.29.001072.

[114] H. Altug and J. Vučković, "Photonic crystal nanocavity array laser," *Opt. Express*, vol. 13, no. 22, pp. 8819–8828, Oct. 2005. DOI: 10.1364/OPEX.13.008819.

[115] E. A. Viktorov, P. Mandel, and Y. Tanguy, "Electron-hole asymmetry and two-state lasing in quantum dot lasers," *Appl. Phys. Lett.*, p. 4, 2005. DOI: 10.1063/1.1995947.

[116] L. V. Asryan, "Maximum power of quantum dot laser versus internal loss," *Appl. Phys. Lett.*, vol. 88, no. 7, p. 073 107, Feb. 2006. DOI: 10.1063/1.2174103.

[117] M. Rossetti *et al.*, "Modeling the temperature characteristics of InAs/GaAs quantum dot lasers," *J. Appl. Phys.*, vol. 106, no. 2, p. 023 105, Jul. 2009. DOI: 10.1063/1.3176499.

[118] M. Gioannini and M. Rossetti, "Time-Domain Traveling Wave Model of Quantum Dot DFB Lasers," *IEEE J. Sel. Top. Quantum Electron.*, vol. 17, no. 5, pp. 1318–1326, Sep. 2011. DOI: 10.1109/JSTQE.2011.2128857.

[119] M. Rossetti, P. Bardella, and I. Montrosset, "Time-Domain Travelling-Wave Model for Quantum Dot Passively Mode-Locked Lasers," *IEEE J. Quantum Electron.*, vol. 47, no. 2, pp. 139–150, Feb. 2011. DOI: 10.1109/JQE.2010.2055550.

[120] K. Lüdge, *Nonlinear Laser Dynamics From Quantum Dots to Cryptography*. Wiley, 2011.

[121] C. Hantschmann *et al.*, "Understanding the Bandwidth Limitations in Monolithic 1.3 μm InAs/GaAs Quantum Dot Lasers on Silicon," *J. Light. Technol.*, vol. 37, no. 3, pp. 949–955, Feb. 2019. DOI: 10.1109/JLT.2018.2884025.

[122] S. Meinecke *et al.*, "Optical feedback induced oscillation bursts in two-state quantum-dot lasers," *Opt. Express*, vol. 28, no. 3, p. 3361, Feb. 2020. DOI: 10.1364/OE.28.003361.

[123] C. Hantschmann, "Monolithic 1.3 μm InAs/GaAs Quantum Dot Lasers on Silicon: Simulation and Experiment," Ph.D. dissertation, University of Cambridge, Aug. 2020.

[124] A. J. Williamson, L. W. Wang, and A. Zunger, "Theoretical interpretation of the experimental electronic structure of lens-shaped self-assembled InAs/GaAs quantum dots," *Phys. Rev. B*, vol. 62, pp. 12 963–12 977, 19 Nov. 2000. DOI: 10.1103/PhysRevB.62.12963.

[125] S. Fathpour *et al.*, "The role of Auger recombination in the temperature-dependent output characteristics ($T_0 = \infty$) of p-doped 1.3 μm quantum dot lasers," *Appl. Phys. Lett.*, vol. 85, no. 22, pp. 5164–5166, Nov. 2004. DOI: 10.1063/1.1829158.

[126] I. Marko *et al.*, "The role of Auger recombination in InAs 1.3-μm quantum-dot lasers investigated using high hydrostatic pressure," *IEEE J. Sel. Top. Quantum Electron.*, vol. 9, no. 5, pp. 1300–1307, Sep. 2003. DOI: 10.1109/JSTQE.2003.819504.

[127] C. Melnychuk and P. Guyot-Sionnest, "Multicarrier Dynamics in Quantum Dots," *Chem. Rev.*, vol. 121, no. 4, pp. 2325–2372, Feb. 2021. DOI: 10.1021/acs.chemrev.0c00931.

[128] D. Jung *et al.*, "Highly Reliable Low-Threshold InAs Quantum Dot Lasers on On-Axis (001) Si with 87% Injection Efficiency," *ACS Photonics*, vol. 5, no. 3, pp. 1094–1100, Mar. 2018. DOI: 10.1021/acsphotonics.7b01387.

[129] T. S. Sosnowski *et al.*, "Rapid carrier relaxation in $In_{0.4}Ga_{0.6}As$/GaAs quantum dots characterized by differential transmission spectroscopy," *Phys. Rev. B*, vol. 57, R9423–R9426, 16 1998. DOI: 10.1103/PhysRevB.57.R9423.

[130] R. Ferreira and G. Bastard, "Phonon-assisted capture and intradot Auger relaxation in quantum dots," *Appl. Phys. Lett.*, vol. 74, no. 19, pp. 2818–2820, May 1999. DOI: 10.1063/1.124024.

[131] H. Jiang and J. Singh, "Nonequilibrium distribution in quantum dots lasers and influence on laser spectral output," *J. Appl. Phys.*, vol. 85, no. 10, pp. 7438–7442, May 1999. DOI: 10.1063/1.369375.

[132] S. Adachi, "Thermal Properties," in *Properties of Group-IV, III-V and II-VI Semiconductors*, John Wiley & Sons, Ltd, 2005, pp. 23–40. DOI: 10.1002/0470090340.ch2.

[133] J. Gomis-Bresco *et al.*, "InGaAs Quantum Dots Coupled to a Reservoir of Nonequilibrium Free Carriers," *IEEE J. Quantum Electron.*, vol. 45, no. 9, pp. 1121–1128, Sep. 2009. DOI: 10.1109/JQE.2009.2021565.

[134] A. V. Uskov *et al.*, "Auger Capture Induced Carrier Heating in Quantum Dot Lasers and Amplifiers," *Appl. Phys. Express*, vol. 4, no. 2, p. 022 202, Feb. 2011. DOI: 10.1143/APEX.4.022202.

[135] K. Lüdge *et al.*, "Large-Signal Response of Semiconductor Quantum-Dot Lasers," *IEEE J. Quantum Electron.*, vol. 46, no. 12, pp. 1755–1762, Dec. 2010. DOI: 10.1109/JQE.2010.2066959.

[136] J. J. More, B. S. Garbow, and K. E. Hillstrom, *User guide for minpack-1*, Aug. 1980. DOI: 10.2172/6997568.

[137] O. B. Shchekin and D. G. Deppe, "1.3 μm InAs quantum dot laser with $T_0 = 161$ K from 0 to 80 °C," *Appl. Phys. Lett.*, vol. 80, no. 18, pp. 3277–3279, Apr. 2002. DOI: 10.1063/1.1476708.

[138] S. Ghosh *et al.*, "Temperature-dependent measurement of Auger recombination in self-organized $In_{0.4}Ga_{0.6}As$/GaAs quantum dots," *Appl. Phys. Lett.*, vol. 79, no. 6, pp. 722–724, Aug. 2001. DOI: 10.1063/1.1391401.

[139] S. J. Sweeney *et al.*, "Dependence of Threshold Current on QW Position and on Pressure in 1.5 μm InGaAs(P) Lasers," *physica status solidi (b)*, vol. 211, no. 1, pp. 525–531, 1999.

[140] S. Guerber, "Intégration d'un deuxième niveau de guidage photonique par dépôt de sin au-dessus du soi traditionnel," Ph.D. dissertation, Université Paris-Saclay, 2019.

[141] P. Bienstman *et al.*, "Modelling leaky photonic wires: A mode solver comparison," *Opt. Quantum Electron.*, vol. 38, no. 9-11, pp. 731–759, Mar. 2007. DOI: 10.1007/s11082-006-9025-9.

[142] *Waveguide Substrate Loss (FEEM)*. AVAILABLE: https://optics.ansys.com/hc/en-us/articles/4402501341459-Waveguide-Substrate-Loss-FEEM- (visited on 01/12/2024).

[143] M. Chobé, K. Hassan, and C. Dupré, "Optoelectronic device comprising a III-V semiconductor membrane laser source forming a lateral p-i-n junction," US20230318263A1, Oct. 2023.

[144] H. J. Lee *et al.*, "Electron transport and band structure of $Ga_{1-x}Al_xAs$ alloys," *Phys. Rev. B*, vol. 21, no. 2, pp. 659–669, Jan. 1980. DOI: 10.1103/PhysRevB.21.659.

[145] A. K. Saxena, "Electron mobility in $Ga_{1-x}Al_xAs$ alloys," *Phys. Rev. B*, vol. 24, no. 6, Sep. 1981. DOI: 10.1103/PhysRevB.24.3295.

[146] A. Yariv, "Coupled-mode theory for guided-wave optics," *IEEE J. Quantum Electron.*, vol. 9, no. 9, pp. 919–933, Sep. 1973. DOI: 10.1109/JQE.1973.1077767.

[147] X. Sun, H.-C. Liu, and A. Yariv, "Adiabaticity criterion and the shortest adiabatic mode transformer in a coupled-waveguide system," *Opt. Lett.*, vol. 34, no. 3, pp. 280–282, Feb. 2009. DOI: 10.1364/OL.34.000280.

[148] H. A. Haus, *Waves and Fields in Optoelectronics* (Prentice-Hall Series in Solid State Physical Electronics). 1984.

[149] H. Ishikawa, "Fully Adiabatic Design of Waveguide Branches," *J. Light. Technol.*, vol. 25, no. 7, pp. 1832–1840, Jul. 2007. DOI: 10.1109/JLT.2007.899186.

[150] X. Sun and A. Yariv, "Engineering supermode silicon/III-V hybrid waveguides for laser oscillation," *J. Opt. Soc. Am. B*, vol. 25, no. 6, p. 923, Jun. 2008. DOI: 10.1364/JOSAB.25.000923.

[151] T. Ferrotti, "Design, fabrication and characterization of a hybrid III-V on silicon transmitter for high-speed communications," Ph.D. dissertation, Université de Lyon, Dec. 2016.

[152] A. Hardy and W. Streifer, "Coupled mode theory of parallel waveguides," *J. Light. Technol.*, vol. 3, no. 5, pp. 1135–1146, Oct. 1985. DOI: 10.1109/JLT.1985.1074291.

[153] *MODE - EigenMode Expansion (EME) solver introduction*. AVAILABLE: https://optics.ansys.com/hc/en-us/articles/360034396614-MODE-EigenMode-Expansion-EME-solver-introduction (visited on 01/18/2024).

[154] Y. Maeda *et al.*, "Micro-Transfer-Printed Membrane Distributed Reflector Lasers on Si Waveguide Modulated With 50-Gbit/s NRZ Signal," *J. Light. Technol.*, pp. 1–7, 2023. DOI: 10.1109/JLT.2023.3265973.

[155] D. Deppe, H. Huang, and O. Shchekin, "Modulation characteristics of quantum-dot lasers: The influence of p-type doping and the electronic density of states on obtaining high speed," *IEEE J. Quantum Electron.*, vol. 38, no. 12, pp. 1587–1593, Dec. 2002. DOI: 10.1109/JQE.2002.805246.

[156] Z. Zhang *et al.*, "Effects of modulation p doping in InAs quantum dot lasers on silicon," *Appl. Phys. Lett.*, vol. 113, no. 6, p. 061 105, Aug. 2018. DOI: 10.1063/1.5040792.

[157] Y. Wan *et al.*, "High speed evanescent quantum-dot lasers on Si," *Laser & Photonics Rev.*, vol. 15, no. 8, p. 2 100 057, 2021. DOI: 10.1002/lpor.202100057.

[158] H. Liu *et al.*, "High-performance three-layer 1.3-μm InAs-GaAs quantum-dot lasers with very low continuous-wave room-temperature threshold currents," *IEEE Photonics Technol. Lett.*, vol. 17, no. 6, pp. 1139–1141, 2005. DOI: 10.1109/LPT.2005.846948.

[159] M. Born and E. Wolf, *Principles of Optics: Electromagnetic Theory of Propagation, Interference and Diffraction of Light*, 7th ed. Cambridge University Press, 1999.

[160] X. Wang, "Silicon Photonic Waveguide Bragg Gratings," Ph.D. dissertation, University Of British Columbia, 2013. DOI: 10.14288/1.0165738.

[161] T. Dupont, "Réalisation de sources laser III-V sur silicium," Ph.D. dissertation, Université de Lyon, 2011.

[162] A. Descos, "Conception, fabrication et réalisation de sources lasers hybrides III-V sur silicium," Ph.D. dissertation, Université de Lyon, 2014.

[163] H. Duprez, "From design to characterization of hybrid III-V on silicon lasers for photonic integrated circuits," Ph.D. dissertation, Université de Lyon, 2016.

[164] L. Pang, "Inverse lithography technology: 30 years from concept to practical, full-chip reality," *J. Micro/Nanopatterning, Materials, Metrol.*, vol. 20, no. 03, Aug. 2021. DOI: 10.1117/1.JMM.20.3.030901.

[165] C. Xiang *et al.*, "High-performance lasers for fully integrated silicon nitride photonics," *Nat. Commun.*, vol. 12, no. 1, p. 6650, Nov. 2021. DOI: 10.1038/s41467-021-26804-9.

[166] X. Wang *et al.*, "Precise control of the coupling coefficient through destructive interference in silicon waveguide Bragg gratings," *Opt. Lett.*, vol. 39, no. 19, p. 5519, Oct. 2014. DOI: 10.1364/OL.39.005519.

[167] J. D. Joannopoulos *et al.*, *Photonic crystals: molding the flow of light*, 2nd edition. Princeton Oxford: Princeton University Press, 2008.

[168] A. Takagi, K. Jinguji, and M. Kawachi, "Wavelength Characteristics of (2 x 2) Optical Channel-Type Directional Couplers with Symmetric or Nonsymmetric Coupling Structures," *J. Light. Technol.*, vol. 10, no. 6, 1992. DOI: 10.1109/50.143072.

[169] C. Zhang *et al.*, "Hybrid quantum-dot microring laser on silicon," *Optica*, vol. 6, no. 9, pp. 1145–1151, Sep. 2019. DOI: 10.1364/OPTICA.6.001145.

[170] J. E. Ayers *et al.*, *Heteroepitaxy of semiconductors: theory, growth, and characterization*. CRC press, 2016.

[171] M. Heiß *et al.*, "Growth mechanisms and optical properties of GaAs-based semiconductor microstructures by selective area epitaxy," *J. Cryst. Growth*, vol. 310, no. 6, pp. 1049–1056, 2008. DOI: 10.1016/j.jcrysgro.2007.12.061.

[172] O. Kayser *et al.*, "Control of selective area growth of inp," *J. Cryst. Growth*, vol. 112, no. 1, pp. 111–122, 1991. DOI: 10.1016/0022-0248(91)90916-S.

[173] K. Hiruma, T. Haga, and M. Miyazaki, "Surface migration and reaction mechanism during selective growth of GaAs and AlAs by metalorganic chemical vapor deposition," *J. Cryst. Growth*, vol. 102, no. 4, pp. 717–724, 1990. DOI: 10.1016/0022-0248(90)90836-A.

[174] F. Olsson *et al.*, "Large mask area effects in selective area growth," *J. Cryst. Growth*, vol. 289, no. 1, pp. 24–30, 2006. DOI: 10.1016/j.jcrysgro.2005.10.130.

[175] B. Wang *et al.*, "Principles of Selective Area Epitaxy and Applications in III–V Semiconductor Lasers Using MOCVD: A Review," *Crystals*, vol. 12, no. 7, 2022. DOI: 10.3390/cryst12071011.

[176] B. He *et al.*, "Vertical nanostructure arrays by plasma etching for applications in biology, energy, and electronics," *Nano Today*, vol. 8, no. 3, pp. 265–289, 2013. DOI: 10.1016/j.nantod.2013.04.008.

[177] Y. Pu, "Plasma etch equipment," in *Handbook of Integrated Circuit Industry*, Y. Wang *et al.*, Eds. Springer Nature Singapore, 2024, pp. 1441–1493. DOI: 10.1007/978-981-99-2836-1_68.

[178] K. Racka-Szmidt *et al.*, "A review: Inductively coupled plasma reactive ion etching of silicon carbide," *Materials*, vol. 15, no. 1, 2022. DOI: 10.3390/ma15010123.

[179] K. Nojiri, *Dry Etching Technology for Semiconductors*. Springer International Publishing, 2015. DOI: 10.1007/978-3-319-10295-5.

[180] P. Vigneron *et al.*, "Advanced and reliable GaAs/AlGaAs ICP-DRIE etching for optoelectronic, microelectronic and microsystem applications," *Microelectron. Eng.*, vol. 202, pp. 42–50, Dec. 2018. DOI: 10.1016/j.mee.2018.09.001.

[181] M. V. Lebedev *et al.*, "Etching of GaAs(100) with Aqueous Ammonia Solution: A Synchrotron-Photoemission Spectroscopy Study," en, *The J. Phys. Chem. C*, vol. 114, no. 49, pp. 21 385–21 389, Dec. 2010. DOI: 10.1021/jp104321e.

[182] U. Schnakenberg *et al.*, "NH4OH-based etchants for silicon micromachining: Influence of additives and stability of passivation layers," *Sensors Actuators A: Phys.*, vol. 25, no. 1, pp. 1–7, Oct. 1990. DOI: 10.1016/0924-4247(90)87001-Y.

[183] M.-L. Touraton *et al.*, "Selective epitaxial growth of AlGaAs/GaAs heterostructures on 300 mm Si(001) for red optical emission," *Thin Solid Films*, vol. 721, p. 138 541, Mar. 2021. DOI: 10.1016/j.tsf.2021.138541.

[184] P. Demeester, P. Van Daele, and R. Baets, "Growth behavior during nonplanar metalorganic vapor phase epitaxy," *J. Appl. Phys.*, vol. 63, no. 7, pp. 2284–2290, Apr. 1988. DOI: 10.1063/1.341042.

[185] C. Bryce and D. Berk, "Kinetics of GaAs Dissolution in H2O2–NH4OH–H2O Solutions," *Ind. & Eng. Chem. Res.*, vol. 35, no. 12, pp. 4464–4470, 1996. DOI: 10.1021/ie960278t.

[186] M. Lu and H. Huang, "Interfacial energy release rates of SiN/GaAs film/substrate systems determined using a cyclic loading dual-indentation method," *Thin Solid Films*, vol. 589, pp. 822–830, Aug. 2015. DOI: 10.1016/j.tsf.2015.07.027.

[187] Y. Watanabe *et al.*, "Characterization of SiO_2/GaAs interface structures using spectroscopic ellipsometry," *Thin Solid Films*, vol. 233, no. 1, pp. 236–239, 1993. DOI: 10.1016/0040-6090(93)90098-A.

[188] P. Lee *et al.*, "Sub-atmospheric chemical vapor deposition (sacvd) of teos-ozone usg and bpsg," in *Seventh International IEEE Conference on VLSI Multilevel Interconnection*, 1990, pp. 396–398. DOI: 10.1109/VMIC.1990.127910.

[189] G. Reeves and H. Harrison, "Obtaining the specific contact resistance from transmission line model measurements," *IEEE Electron Device Lett.*, vol. 3, no. 5, pp. 111–113, May 1982. DOI: 10.1109/EDL.1982.25502.

[190] L. Basset *et al.*, "In depth analysis of transfer length method application on passivated contacts under illumination," *Sol. Energy Mater. Sol. Cells*, vol. 230, p. 111 255, Sep. 2021. DOI: 10.1016/j.solmat.2021.111255.

[191] M. Meneghini *et al.*, "A review on the reliability of gan-based leds," *IEEE Trans. on Device Mater. Reliab.*, vol. 8, no. 2, pp. 323–331, 2008. DOI: 10.1109/TDMR.2008.921527.

[192] J. Gaudy, "Lasers III-V sur Si pour Lidar FMCW à 1550 nm," Ph.D. dissertation, Université Grenoble Alpes, 2023.

[193] I. Vurgaftman, J. R. Meyer, and L. R. Ram-Mohan, "Band parameters for III–V compound semiconductors and their alloys," *J. Appl. Phys.*, vol. 89, no. 11, pp. 5815–5875, Jun. 2001. DOI: 10.1063/1.1368156.

[194] Y. Varshni, "Temperature dependence of the energy gap in semiconductors," *Physica*, vol. 34, no. 1, pp. 149–154, 1967. DOI: 10.1016/0031-8914(67)90062-6.

[195] K. Hassan *et al.*, "Robust silicon-on-insulator adiabatic splitter optimized by metamodeling," *Appl. Opt.*, vol. 56, no. 8, pp. 2047–2052, Mar. 2017. DOI: 10.1364/AO.56.002047.

[196] Z. Lu *et al.*, "Broadband silicon photonic directional coupler using asymmetric-waveguide based phase control," *Opt. Express*, vol. 23, no. 3, pp. 3795–3808, Feb. 2015. DOI: 10.1364/OE.23.003795.

[197] M. Ibsen *et al.*, "Sinc-sampled fiber Bragg gratings for identical multiple wavelength operation," *IEEE Photonics Technol. Lett.*, vol. 10, no. 6, pp. 842–844, 1998. DOI: 10.1109/68.681504.

[198] P. N. Grillot *et al.*, "Sixty Thousand Hour Light Output Reliability of AlGaInP Light Emitting Diodes," *IEEE Trans. on Device Mater. Reliab.*, vol. 6, no. 4, pp. 564–574, 2006. DOI: 10.1109/TDMR.2006.887416.

[199] D. K. Gaskill *et al.*, "Band-gap determination by photoreflectance of InGaAs and InAlAs lattice matched to InP," *Appl. Phys. Lett.*, vol. 56, no. 13, pp. 1269–1271, Mar. 1990. DOI: 10.1063/1.102533.

[200] M. L. Lovejoy, M. R. Melloch, and M. S. Lundstrom, "Temperature dependence of minority and majority carrier mobilities in degenerately doped GaAs," *Appl. Phys. Lett.*, vol. 67, no. 8, pp. 1101–1103, Aug. 1995. DOI: 10.1063/1.114974.

[201] D. T. Cassidy, "Technique for measurement of the gain spectra of semiconductor diode lasers," *J. Appl. Phys.*, vol. 56, no. 11, pp. 3096–3099, Dec. 1984. DOI: 10.1063/1.333867.

A

Determination of the Excitation Times for the Rate Equation Model

In the QD laser model presented in section 2.1, the impact of temperature on the emission properties of the laser derives from the temperature-dependent distribution of the free-carriers among available energy levels. This appendix gives more details on the calculation of the free-carriers excitation time as a function of their relaxation time and temperature so that at thermal equilibrium, the free carrier distribution would follow the Fermi-Dirac distribution.

The Detailed Balance Condition

The detailed balance condition is our starting point for the expression of excitation times as a function of capture and relaxation times. It states that in the absence of external perturbation and recombination and at thermal equilibrium, all capture and relaxation processes must be balanced with the reverse excitation processes [131]:

$$\frac{w_{bulk}^{e,h}}{\tau_{c,QW}^{e,h}} = \frac{w_{QW}^{e,h}}{\tau_{e,QW}^{e,h}} \tag{A.1}$$

$$\frac{w_{QW}^{e,h}\left(1-f_{ES2}^{e,h}\right)}{\tau_{c,dot}^{e,h}} = \rho\nu_{ES2}\frac{f_{ES2}^{e,h}}{\tau_{e,ES2}^{e,h}} \tag{A.2}$$

$$\frac{f_{ES2}^{e,h}\left(1-f_{ES1}^{e,h}\right)}{\tau_{r,ES2}^{e,h}} = \frac{\nu_{ES1}}{\nu_{ES2}}\frac{f_{ES1}^{e,h}\left(1-f_{ES2}^{e,h}\right)}{\tau_{e,ES1}^{e,h}} \tag{A.3}$$

$$\frac{f_{ES1}^{e,h}\left(1-f_{GS}^{e,h}\right)}{\tau_{r,ES1}^{e,h}} = \frac{\nu_{GS}}{\nu_{ES1}}\frac{f_{GS}^{e,h}\left(1-f_{ES1}^{e,h}\right)}{\tau_{e,GS}^{e,h}} \tag{A.4}$$

Which, isolating τ_e, rewrites:

$$\tau_{e,QW}^{e,h} = \tau_{c,QW}^{e,h} \frac{w_{QW}^{e,h}}{w_{bulk}^{e,h}} \tag{A.5}$$

$$\tau_{e,ES2}^{e,h} = \tau_{c,dot}^{e,h} \rho \nu_{ES2} \frac{f_{ES2}^{e,h}}{1 - f_{ES2}^{e,h}} \frac{1}{w_{QW}^{e,h}} \tag{A.6}$$

$$\tau_{e,ES1}^{e,h} = \tau_{r,ES2}^{e,h} \frac{\nu_{ES1}}{\nu_{ES2}} \frac{f_{ES1}^{e,h}}{1 - f_{ES1}^{e,h}} \frac{1 - f_{ES2}^{e,h}}{f_{ES2}^{e,h}} \tag{A.7}$$

$$\tau_{e,GS}^{e,h} = \tau_{r,ES1}^{e,h} \frac{\nu_{GS}}{\nu_{ES1}} \frac{f_{GS}^{e,h}}{1 - f_{GS}^{e,h}} \frac{1 - f_{ES1}^{e,h}}{f_{ES1}^{e,h}} \tag{A.8}$$

The different terms are detailed in the following sections.

Thermal Equilibrium Distribution

At thermal equilibrium, the occupation probability for a state i is given by the Fermi-Dirac distribution:

$$f_i = \frac{1}{1 + exp\left(\frac{E_i - E_F}{k_B T}\right)} \tag{A.9}$$

Rearranging yields a simplified expression for the recurring ratio:

$$\frac{1 - f_i}{f_i} = \exp\left(\frac{E_i - E_F}{k_B T}\right) \tag{A.10}$$

Bi-QW Carriers Density

The density of carriers in the bi-QW is obtained by integrating over the energy space the product of the 2D density of states and occupation probabilities:

$$\begin{aligned}
w_{QW}^{e,h} &= \int_{E_{QW}}^{\infty} N(E) f(E)\, dE \\
w_{QW}^{e,h} &= \int_{E_{QW}}^{\infty} \frac{m^{e,h}}{\pi\hbar^2} \frac{1}{1 + exp\left(\frac{E - E_F}{k_B T}\right)} dE \\
w_{QW}^{e,h} &= \frac{-k_B T m^{e,h}}{\pi\hbar^2} \int_{E_{QW}}^{\infty} \frac{-1}{k_B T} \frac{exp\left(-\frac{E - E_F}{k_B T}\right)}{1 + exp\left(-\frac{E - E_F}{k_B T}\right)} dE \\
w_{QW}^{e,h} &= \frac{m^{e,h} k_B T}{\pi\hbar^2}\, ln\left[1 + exp\left(\frac{E_F - E_{QW}}{k_B T}\right)\right]
\end{aligned} \tag{A.11}$$

Besides, this allows expressing the electron and hole quasi-Fermi levels $E_f^{e,h}$ as functions of

w_{QW} [122], which we will use later on:

$$E_F^{e,h} = E_{QW} + k_B T \, ln \left[exp \left(\frac{w_{QW}^{e,h} \pi \hbar^2}{m^{e,h} k_B T} \right) - 1 \right] \tag{A.12}$$

GaAs Spacers Carriers Density

Assuming a Boltzmann distribution in the conduction band (a straightforward analogy can be used for the valence band), the density of free electrons is expressed as:

$$\begin{aligned} n &= \int_{E_C}^{\infty} N_C(E) \, f(E) \, dE \\ n &= \int_{E_C}^{\infty} N_C(E) \exp\left(-\frac{E - E_F}{k_B T} \right) dE \\ n &= \exp\left(-\frac{E_C - E_F}{k_B T} \right) \int_{E_C}^{\infty} N_C(E) \exp\left(-\frac{E - E_C}{k_B T} \right) dE \\ n &= N_C \, \exp\left(-\frac{E_C - E_F}{k_B T} \right) \end{aligned} \tag{A.13}$$

With:

$$N_C = \int_{E_C}^{\infty} N_C(E) \exp\left(-\frac{E - E_C}{k_B T} \right) dE \tag{A.14}$$

Besides, in a bulk material [46]:

$$N_C(E) = \frac{1}{2\pi^2} \left(\frac{2m^e}{\hbar^2} \right)^{3/2} \sqrt{E - E_C} \tag{A.15}$$

Thus:

$$N_C = \frac{1}{2\pi^2} \left(\frac{2m^e}{\hbar^2} \right)^{3/2} \int_{E_C}^{\infty} \sqrt{E - E_C} \, \exp\left(-\frac{E - E_C}{k_B T} \right) dE \tag{A.16}$$

The integral is quite complex to solve and we will not dive into the details here. After a variable change, integrating by parts and using the Gaussian integral, we obtain:

$$N_C = \frac{1}{\sqrt{2}} \left(\frac{m^e k_B T}{\pi \hbar^2} \right)^{3/2} \tag{A.17}$$

Thus, at thermal equilibrium:

$$w_{GaAs}^e = n \, t_{GaAs} = t_{GaAs} \frac{1}{\sqrt{2}} \left(\frac{m^e k_B T}{\pi \hbar^2} \right)^{3/2} \exp\left(-\frac{E_C - E_F}{k_B T} \right) \tag{A.18}$$

Rearranging the Detailed Balance Results

Plugging equations A.10, A.11 and A.18 back into equations A.5–A.8:

$$\tau_{e,QW}^{e,h} = \tau_{c,QW}^{e,h} w_{QW}^{e,h} \frac{\sqrt{2}}{t_{GaAs}} \left(\frac{\pi \hbar^2}{m^{e,h} k_B T} \right)^{3/2} \exp\left(\frac{E_{GaAs} - E_F}{k_B T} \right) \tag{A.19}$$

$$\tau_{e,ES2}^{e,h} = \tau_{c,dot}^{e,h} \rho \nu_{ES2} \exp\left(-\frac{E_{ES2} - E_F}{k_B T} \right) \frac{1}{w_{QW}^{e,h}} \tag{A.20}$$

$$\tau_{e,ES1}^{e,h} = \tau_{r,ES2}^{e,h} \frac{\nu_{ES1}}{\nu_{ES2}} \exp\left(\frac{E_{ES2} - E_{ES1}}{k_B T} \right) \tag{A.21}$$

$$\tau_{e,GS}^{e,h} = \tau_{r,ES1}^{e,h} \frac{\nu_{GS}}{\nu_{ES1}} \exp\left(\frac{E_{ES1} - E_{GS}}{k_B T} \right) \tag{A.22}$$

Where the expression A.12 is used to compute the quasi Fermi levels.

Résumé en Francais

Introduction

Les liens optiques sont aujourd'hui largement utilisés pour les communications de données longue et courte distance, en remplacement des liens électriques souffrant notamment de résistances et capacités parasites qui limitent leurs performances. La co-intégration de circuits optiques et électroniques doit permettre de réduire plus encore les interconnexions électroniques afin d'améliorer les performances et réduire la consommation énergétique des centres de calcul et des outils de communications associés [9]. En particulier, la photonique sur silicium qui s'appuie sur la maturité des procédés de fabrication CMOS est une solution bas coût et facilement intégrable avec l'électronique pour répondre à ce besoin [19]. Cependant, du fait de son gap indirect, le silicium n'est pas un candidat idéal pour l'émission de lumière. Les lasers III-V intégrés sur silicium permettent de répondre à cette problématique.

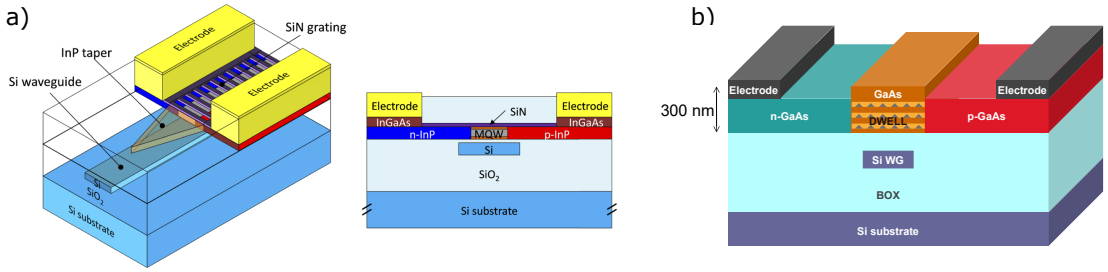

Figure A.1: a) Schémas en perspective (gauche) et coupe transversale (droite) de lasers DFB à membrane semiconductrice InP couplée à un guide d'onde SOI. D'après [50]. b) Schéma (non à l'échelle) de laser à membrane à boîtes quantiques InAs sur silicium tel que nous cherchons à fabriquer et modéliser dans cette thèse.

Parmi les différents types de lasers III-V sur silicium, cette thèse s'intéresse plus spécifiquement aux lasers dits à membrane III-V, comme illustrés en Fig. A.1. Ceux-ci se distinguent par l'utilisation d'une couche fine de matériaux III-V, de l'ordre de quelques centaines de nanomètres d'épaisseur (contre quelques micromètres pour les lasers conventionnels), comprise entre des matériaux de faible indice de réfraction [50]. Cela leur confère plusieurs avantages, notamment un confinement optique amélioré malgré un volume réduit de matériau à gain, permettant une meilleure efficacité énergétique et de meilleures performances en modulation directe [31]. En outre, l'épaisseur réduite du III-V est compatible avec un procédé standard de back-end CMOS et facilite l'intégration sur silicium sur isolant (SOI) standard. L'épaisseur réduite du III-V nécessite un schéma d'injection du courant latérale, utilisant une diode p-i-n horizontale, comme illustré en Fig. A.1. Plus précisément, nous cherchons à simuler, concevoir, fabriquer et caractériser des lasers à membrane III-V utilisant des boîtes quantiques d'InAs come matériau à

gain, tels qu'illustrés en Fig. A.1.b. En effet, grâce au confinement électronique des porteurs libres dans les trois dimensions de l'espace, les lasers à boîtes quantiques bénéficient entre autres de courants de seuil plus faibles, d'une capacité à opérer à plus haute température ainsi qu'une moindre sensibilité aux réflections parasites en comparaison aux lasers à puits quantiques [52].

Modélisation

Une partie de cette thèse a été dédiée à la simulation et conception de ces lasers. La Fig. A.2 illustre les différents éléments composant une diode laser intégrée sur silicium, que nous avons simulés dans cette thèse.

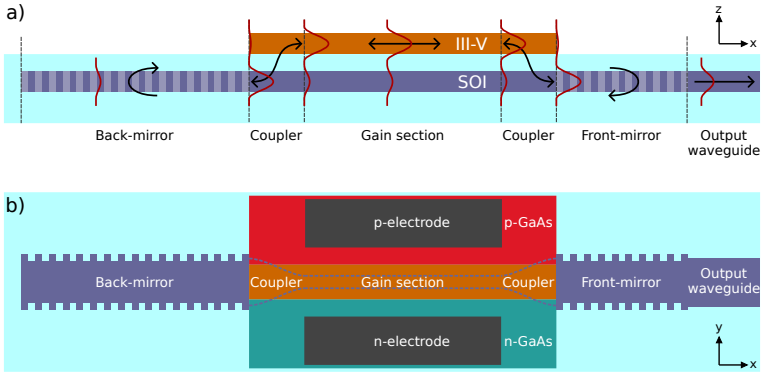

Figure A.2: Schéma en coupe longitudinale (a) et vue de dessus (b) des composants principaux d'une diode laser DBR sur silicium : un milieu amplificateur, des coupleurs optiques III-V/SOI, deux miroirs (qui jouent également le rôle de filtres spectraux) et un guide d'onde de sortie.

S'il existe plusieurs outils commerciaux pour la simulation de lasers à puits quantiques, les lasers à boîtes quantiques représentent une technologie moins mature, pour laquelle nous ne disposons pas de tels outils. En nous appuyant sur l'état de l'art [110], [111], [121], [122], nous avons mis au point un modèle à équations de taux afin d'y pallier et de contribuer à une meilleure compréhension de ces lasers. Dix équations de taux décrivent l'évolution temporelle de la population des électrons et trous libres peuplant les niveaux d'énergie de la bande de conduction et de valence du système, comme illustré en Fig. A.3, tandisqu'une autre équation de taux décrit l'évolution spatio-temporelle de la densité de photon. Les taux de transition entre ces niveaux sont dépendants de la température du laser, ce qui permet de rendre compte de l'influence de ce paramètre sur les propriétés d'émission du laser. Notamment, du fait du faible écart entre leurs niveaux d'énergie, les trous libres ont tendance à se thermaliser plus rapidement que les électrons, et déserter le niveau fondamental (GS) au profit des niveaux excités, ce qui augmente le courant de seuil et diminue l'efficacité du laser. Un dopage de type p modéré de la zone active permet de compenser partiellement ce phénomène et améliorer le comportement des lasers à haute température, au prix d'un courant de seuil augmenté à température ambiante [30]. Des hypothèses proposées pour expliquer l'augmentation du courant de seuil à température ambiante et sa faible évolution avec la température sont : l'augmentation du taux de recombinaison Auger dans le niveau fondamental [125], et les pertes

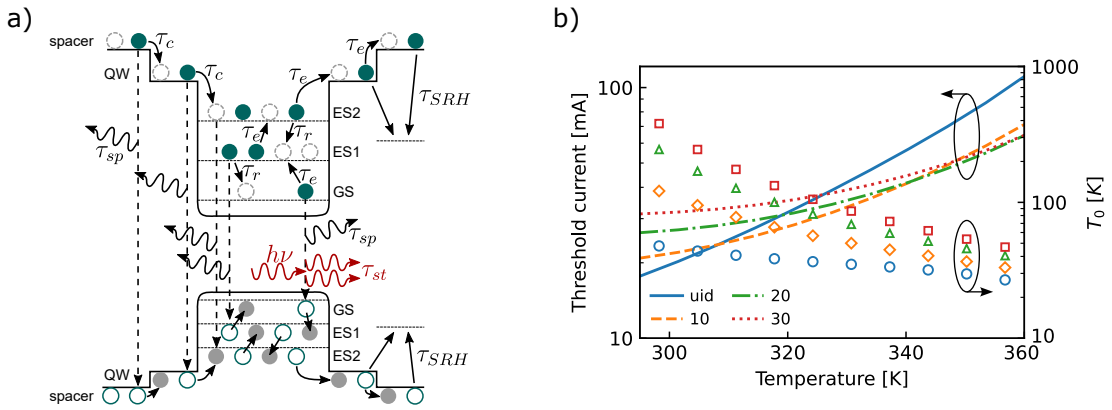

Figure A.3: a) Diagramme de niveaux d'énergie des bandes de conduction et de valence pris en compte dans le modèle à équations de taux, et transitions entre ces niveaux. b) Simulation de la dépendence en température du courant de seuil et de la température caractéristique T_0 de lasers non-intentionellement dopés et avec des niveaux de dopage-p correspondant à 10, 20 et 30 trous supplémentaires par boîte quantique. Dispositifs simulés d'après la référence [30].

optiques dues à l'absorption inter-bandes de valence (IVBA) [30]. Notre modèle se démarque par la prise en compte de ces deux effets. En nous focalisant sur le comportement sous pompage continu des lasers, nous avons également pu proposer une solution semi-analytique au modèle, beaucoup plus efficace en ressources de calcul qu'une résolution de type différences finies, et tout aussi précise. Une évaluation de notre modèle sur des résultats expérimentaux de la litérature démontre sa précision et sa représentation fidèle des effets du dopage p, comme illustré en Fig. A.3.b. Nous observons également que l'influence observée du dopage p est principalement due aux recombianisons Auger de type npp.

Par ailleurs, nous avons simulé et conçu des lasers à membrane hybride III-V/SOI. Le guidage optique dans le matériau III-V est obtenu en formant le III-V en guide arête (ou rib), comme illustré en Fig. A.4, avec une différence d'épaisseur de 50 nm entre le coeur du guide comprenant le matériau émissif et le slab dopé. Nous avons également proposé dans la référence [143] d'utiliser de l'AlGaAs contenant de 10% à 15% d'Al pour former les zones dopées, afin d'améliorer le confinement optique et électronique.

En choisissant de manière appropriée l'épaisseur de la membrane III-V, il est possible de transformer le mode hybride de manière à ce qu'il soit entièrement localisé dans le SOI, en travaillant seulement sur la largeur du guide SOI et sans nécessiter son épaississement comme cela peut être nécessaire pour des lasers conventionnels [105]. Pour une épaisseur de membrane III-V de 310 nm, nous avons pu concevoir des coupleurs III-V/SOI présentant une transmission simulée de 97% pour une longueur de 100 µm, comme illustré en Fig. A.5. Le profil de ces coupleurs a été calculé en se basant sur le critère d'adiabaticité de Sun et Yariv [147].

Enfin, les cavités laser ont été complétées par des miroirs conçus dans le SOI. En particulier, des laser utilisent des réseaux de Bragg (DBR) basés sur des variations périodiques de l'indice de réfraction au long de la propagation de la lumière de manière à obtenir une réflectivité controllée à une longueur d'onde choisie. Cela permet de filtrer certains modes de la cavité afin d'obtenir un laser monomode. Certains DBR sont fabriqués par gravure partielle du sommet du

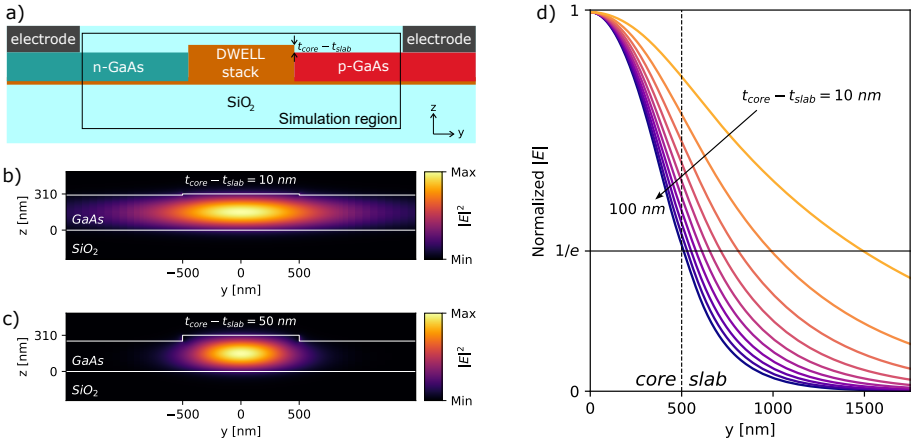

Figure A.4: Simulation en coupe transversale du mode TE0 (longueur d'onde 1310 nm) d'un guide d'onde GaAs en arête. a) Schéma de la structure simulée. b, c) Champs électriques simulés pour des différences de hauteur entre le coeur du guide et le slab de 10 nm et 50 nm. d) Champ électrique dans un plan horizontal pour des différences de hauteur entre le coeur du guide et le slab variant de 10 nm à 100 nm.

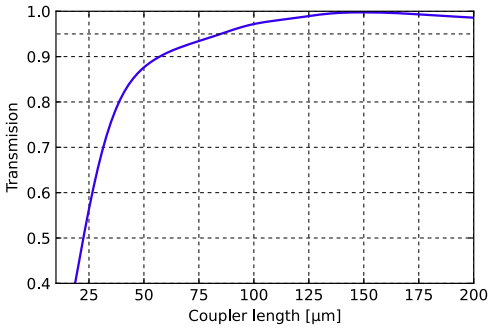

Figure A.5: Transmisison simulée (longueur d'onde 1310 nm) d'un coupleur III-V/SOI en fonction de la longueur du coupleur.

guide SOI, ce qui nécessite un niveau de lithographie supplémentaire par rapport aux standards. Ici, nous avons conçu des DBR par corrugations latérales du guide SOI ou en formant des guides SOI avec des plots centraux, sans utiliser d'autres niveaux de lithographie que les niveaux standards. Des cavités à rétroaction distribuée (DFB), pour lesquelles le réseau est situé le long du milieu à gain, ont également été conçues sur ce modèle. Par ailleurs, nous proposons une architecture de laser microdisque à membrane III-V couplés à un guide SOI.

Suite à cela, nous avons pu appliquer le modèle à équations de taux aux lasers à membrane à boîtes quantiques InAs. Nous trouvons qu'une cavité de 300 µm de long avec une zone de gain de 1 µm de large comprenant 4 plans de boîtes quantiques (DWELL) et un dopage p correspondant à 10 trous par boîte quantique donne un bon compromis entre les performances à température ambiante et à haute température. En particulier, les résultats de simulation (Fig. A.6) indiquent un courant de seuil inférieur à 1 mA jusqu'à 60 °C, et une puissance optique de sortie supérieure à 1 mW jusqu'à 110 °C. Ces résultats confirment le potentiel des lasers à membrane à boîtes quantiques InAs pour des applications de communications de données.

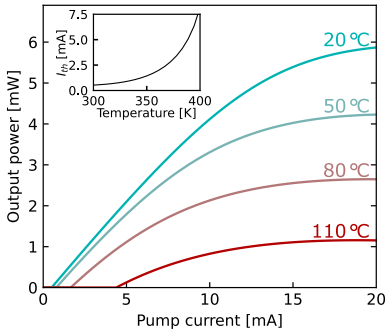

Figure A.6: Courbes LI d'un laser à membrane à boîtes quantiques InAs de géométrie optimisée, simulées pour différentes températures. Insert: dépendence en température du courant de seuil.

Fabrication

Le procédé de fabrication de lasers à membrane à boîtes quantiques InAs sur silicium est illustré en Fig. A.7. Il commence par l'épitaxie d'une couche d'arrêt de gravure (ESL) et de l'empilement III-V sur substrat GaAs de 100 mm de diamètre, suivie d'un dépôt diélectrique et sa planarisation, ou non, selon le procédé choisi (Fig. A.7.a). Ensuite, le substrat III-V est reporté par collage direct sur un substrat SOI 300 mm contenant la circuiterie passive, fabriquée par ailleurs (Fig. A.7. b, c). Le substrat GaAs et l'ESL sont retirés par meulage (grinding) et gravure chimique, puis le substrat est détouré à 100 mm (Fig. A.7.d). La structure p-i-n est fabriquée par gravure plasma du III-V utilisant un masque dur (HM) suivie d'une préparation de surface chimique et croissance sélective de GaAs dopé p (Fig. A.7. e, f). Puis le même enchaînement est répété pour le GaAs dopé n (Fig. A.7.g). Finalement, les contacts métalliques sont réalisés et le mesa peut être gravé (Fig. A.7.h). Ce procédé de fabrication est très différent de celui de diodes lasers conventionelles, pour lesquelles la structure p-i-n est fabriquée par épitaxie successive des matériaux n, i et p. La fabrication de jonctions p-i-n horizontales par gravure et épitaxie sélective, qui plus est sur GaAs collé sur silicium, présente donc un véritable défi technologique.

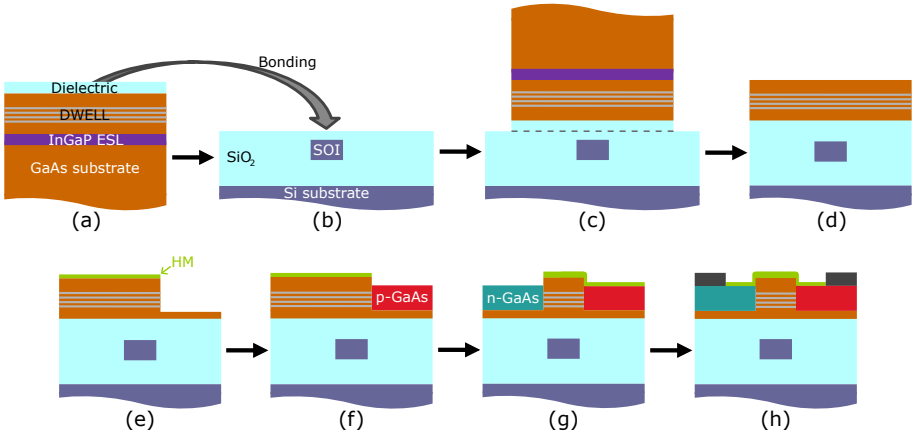

Figure A.7: Procédé de fabrication de lasers à membrane à boîtes quantiques InAs sur silicium.

Des études préliminaires ont porté sur le collage de GaAs sur silicium, et sur la préparation de surface de GaAs post-gravure pour la réprise d'épitaxie sélective. Nous avons observé

qu'un enchaînement de désoxydation de surface utilisant une solution de NH_4OH suivie d'une réoxydation à l'ozone sec et d'une seconde désoxydation permet de significativement réduire la rugosité des reprises d'épitaxie (rugosité RMS de 0,14 nm contre 8,25 nm pour le témoin). Des premières structures diodes à injection de courant latérale ont ensuite été fabriquées sur substrat GaAs, utilisant des puits quantiques InGaAs comme matériau émissif. La membrane diode est isolée optiquement et électriquement du substrat GaAs par une couche d'AlGaAs. Une image MEB des composants fabriqués est présentée en Fig. A.8.a. La jonction p-i-n horizontale est clairement visible, ainsi que les contacts métalliques sur GaAs-p et GaAs-n. Cependant, des défauts d'épaisseur de reprise d'épitaxie sont à noter, car le GaAs-p et GaAs-n dépassent de la zone i quand ils auraient dû être moins épais afin de former un guide en arête. En outre, des défauts de sélectivité sont observés, alors que des cristaux de GaAs ont crû sur la zone i, pourtant masquée. En dehors des zones du masque comportant les diodes, ce manque de sélectivité était significativement plus marqué dû à la présence de larges zones masquées. Cela a dégradé les marques d'alignement, réduisant la précision de la lithographie des niveaux suivants, d'où un désaccord géométrtique entre les dessins et diodes fabriquées. Un nouveau jeu de masques a été dessiné, où des damiers ont été ouverts dans les larges zones précédemment masquées. Les paramètres de l'épitaxie ont également été revus, avec notamment une température du suscepteur plus faible et une augmentation du flux de dilution. Ces modifications ont permis d'obtenir la sélectivité voulue, et le temps de croissance a également été recalibré afin de donner l'épaisseur de reprise d'épitaxie désirée. La Fig. A.8.b. illustre le témoin ayant permis d'aboutir à ces paramètres optimisés.

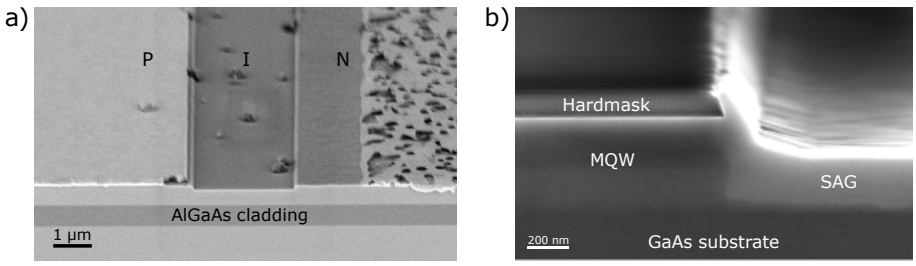

Figure A.8: a) Image MEB d'un prototype fabriqué sur substrat GaAs (échantillon clivé). b) Image MEB d'une interface de reprise d'épitaxie du lot ayant servi à la correction des paramètres de l'épitaxie sélective (échantillon clivé).

Après correction des paramètres d'épitaxie, un nouveau lot a été fabriqué pour lequel des épitaxies III-V contenant des puits quantiques InGaAs et des boîtes quantiques InAs ont été reportées sur silicium oxydé. Deux procédés de collage ont été mises en œuvre, le premier utilisant un dépôt diélectrique fin sur le III-V, ne nécéssitant pas de planarisation, tandis que et le deuxième utilisant un dépôt plus épais suivi d'une planarisation par polissage mécano-chimique (CMP). Si les épitaxies de puits quantiques ont pû être collées par les deux procédés, la topographie induite par les boîtes quantiques nécessite le recours à la seconde méthode avec CMP pour obtenir une surface suffisament plane pour le collage. Pour des raisons de délais, seules les plaques collées par le procédé sans CMP ont pû être conduites

au terme de leur fabrication. Après collage et retrait du substrat GaAs et ESL, le procédé de fabrication est similaire à celui des premiers prototypes fabriqués sur substrat GaAs, avec les paramètres d'épitaxie sélective optimisés. Les facettes des miroirs ont été gravées chimiquement. L'imagerie au MEB des échantillons fabriqués montre un meilleur accord entre le design et les dispositifs finaux (Fig. A.9.a). En outre, une image de résolution atomique réalisée au microscope électronique en transmission à balayage (STEM) montre la continuité cristalline entre le matériau intrinsèque et la reprise d'épitaxie (Fig. A.9.b).

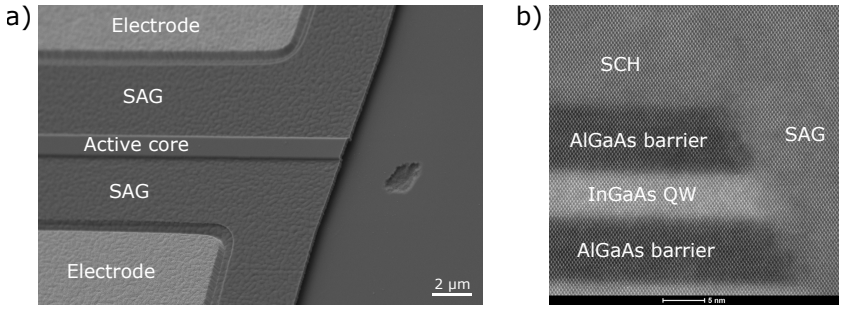

Figure A.9: a) Image MEB des prototypes fabriqués sur silicium. b) Image STEM (résolution atomique) de l'interface latérale de reprise d'épitaxie.

Enfin, les composants passifs ont été fabriqué sur la plateforme de photonique sur silicium standard du CEA-LETI. Leur fabrication n'est pas détaillée ici, mais des images MEB de guides d'ondes SOI et miroirs de Bragg fabriqués sont visibles en Fig. A.10. Pour des raisons de délais de fabrication, nous n'avons pas pu reporter les épitaxies III-V sur ces plaques SOI durant le temps de ce travail de thèse.

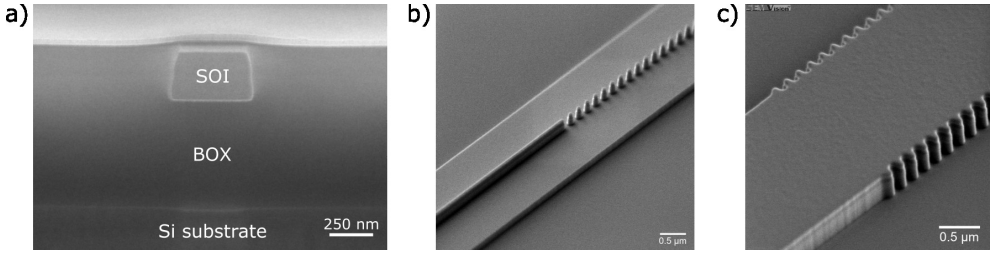

Figure A.10: Images MEB des composants SOI : (a) guides rubans encapsulés, (b) miroirs de Bragg à plots centraux et (c) corrugations latérales, avant encapsulation.

Caractérisation

Les composants fabriqués ont été caractérisés du point de vue électrique et électro-optique, afin de quantifier leurs performances et mieux comprendre leur fonctionnement.

Tout d'abord, pour les miroirs de Bragg, nous observons que les meilleurs résultats sont obtenus dans la version à plots centraux, dont les spectres de transmission sont illustrés en Fig. A.11. Ceux-ci présentent malgré-tout un coefficient de couplage très élevé qui limite les performances atteignables, notamment en finesse de la réponse spectrale. Les miroirs de Bragg à corrugations latérales ont, de leur côté, obtenu des coefficients de couplage en deçà de ceux visés.

Cela est attribué à un lissage des corrugations (dont les dimensions étaient très aggressives) à la lithographie. Une géométrie de miroirs de Bragg à plots latéraux, présentant un guide en arête avec des plots déportés dans le slab, permettrait de mieux contrôler le coefficient de couplage des miroirs fabriqués.

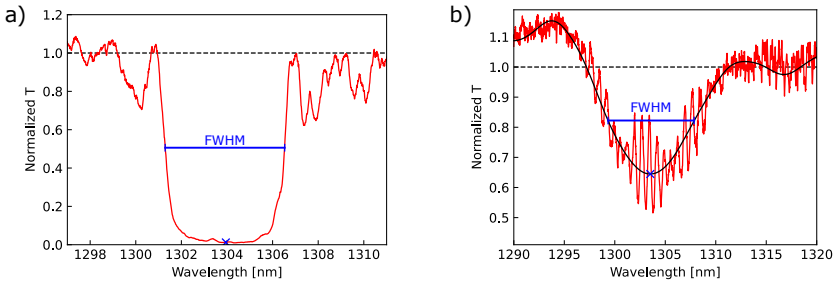

Figure A.11: Spectres de transmission mesurés des miroirs de Bragg à plots centraux arrière (a) et avant (b). Les croix et lignes bleues indiquent le minimum de transmisison et la largeur à mi-hauteur.

Les prototypes fabriqués sur substrat GaAs ont été caractérisés sous pompage électrique. Les courbes courant-tension (non présentées ici) montrent un comportement de diode conforme aux attentes, sans chute de tension due aux interfaces de reprise d'épitaxie, ce qui indique également leur qualité. Afin de caractériser les propriétés d'émission optique des diodes, une fibre optique est placée à la verticale des diodes, collectant une partie de la lumière émise diffractée. Les courbes de puissance optique collectée en fonction du courant de pompe (L-I, Fig. A.12.a) démontrent l'émission de lumière résultant du pompage électrique de ces structures, sans toutefois d'effet laser, ce qui était attendu car la forme de guide en arête ciblée n'a pas été obtenue. Par ailleurs, deux pics sont clairement identifiables dans le spectre d'émission de ces diodes (Fig. A.12.a) : un vers 870 nm correspondant à des recombinaisons parasites dans le GaAs, et un vers 910 nm correspondant à des recombinaisons dans les puits quantiques. Nous démontrons donc la fabrication de diodes p-i-n à injection de courant latérale et le pompage électrique de puits quantiques dans ces structures.

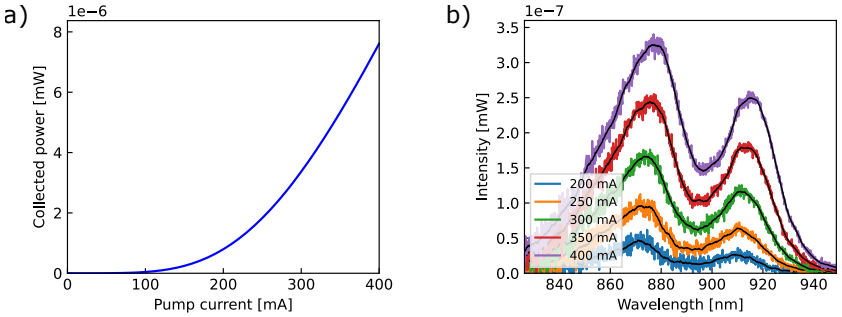

Figure A.12: Puissance optique collectée en fonction du courant de pompe (courbe L-I, a) et spectres d'électroluminescence pour des courant de pompe variables (b) d'un composant fabriqué sur substrat GaAs de dimensions sur design : L = 2 mm, w = 10 µm et d = 1 µm.

Les composants fabriqués sur substrat silicium ont été caractérisés de manière analogue, et la Fig. A.13 présente deux exemples de courbes L-J et spectres d'émisison. Pour ces composants, une structure de guide d'onde a été obtenue, ce qui explique la plus faible intensité du signal

collecté. Les dispositifs illustrés ont été pompés jusqu'à 4 kA.cm^{-2} et 10 kA.cm^{-2} (ou 230 mA et 300 mA). Si l'émission de lumière est observée dès des courants de pompes faibles que pour les prototypes sur GaAs, probablement grâce à une plus faible densité de centre de recombinaisons non-radiatives, l'effet laser n'est pas non plus observé. Lorsque les courants de pompe augmentent, on observe une saturation de la puissance émise due à l'échauffement du laser. Ce phénomène est particulièrement marqué pour les dispositifs présentant une résistance électrique série élevée tels que device 1, c'est à dire ceux présentant une zone active intrinsèque plus large, et ceux de longueur réduite. Une quantification de leur échauffement sous pompage électrique continu a été menée à partir de l'équation de Varshni et de la mesure du décalage du pic d'émission des MQW en fonction de l'intensité du courant de pompe. Pour device 1, le plus résistif, on note un échauffement très marqué du milieu actif, soit 100 °C de 50 mA à 200 mA, contre 30 °C de 100 mA à 250 mA pour device 2. Ces échauffements marqués s'expliquent par la couche de SiO_2 sur laquelle repose la membrane III-V, agissant comme un isolant thermique. Pour d'autres lasers à membrane III-V de la littérature, cet effet est peu gênant grâce aux courants de seuil faibles [50]. Des mesures ont été réalisées en régime pulsé afin de limiter cet auto-échauffement, mais n'ont pas donné de résultats probants. Par ailleurs, les spectres d'émission montrent, pour ces dispositifs, une intensité du signal GaAs relative au signal MQW significativement réduite en comparaison des premiers prototypes fabriqués sur substrat GaAs.

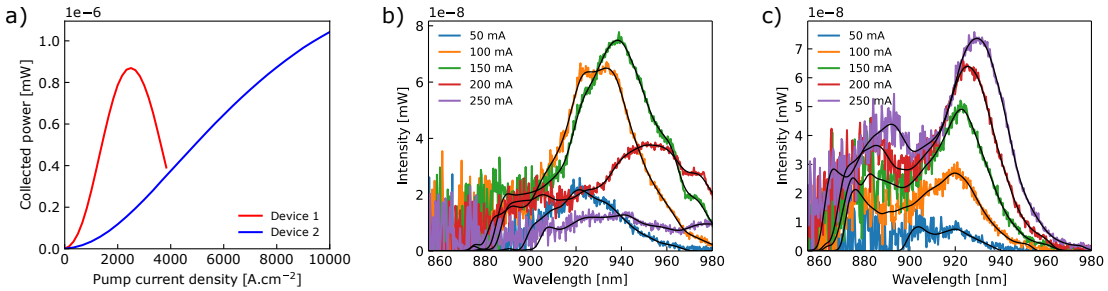

Figure A.13: Puissance optique collectée en fonction de la densité de courant de pompe (courbe L-J, a) et spectres d'électroluminescence pour des courant de pompe variables (b, c) de composant fabriqués sur silicium, de dimensions sur design : L = 1 mm, w = 6 µm et d = 5 µm (device 1 et b), et L = 1.5 mm, w = 2 µm et d = 3 µm (device 2 et c).

La caractérisation de ces composants est toujours en cours afin de démontrer l'effet laser. En particulier, des traitements réflectifs Al_2O_3/Si vont être appliqués sur les facettes de barrettes laser, puis ces composants seront caractérisés à basse température.

Conclusion

En résumé, nous avons modélisé et conçu des lasers à membrane à boîtes quantiques InAs sur silicium. Un procédé de fabrication a été avancé pour la réalisation de ces lasers, et des prototypes ont été fabriqués, démontrant l'émission de lumière par pompage électrique de diodes à membrane III-V sur silicium. L'effet laser n'a pas encore été observé, mais des travaux sont toujours en cours afin de l'atteindre.

Design, fabrication and characterization of microlasers for data communications

The exponential growth of data flows over the recent decades has increased the pressure on interconnections between computing and communication systems. In this context, silicon photonics has concentrated significant interest in transferring the benefits of photonics closer to the ASICs through on-board modules, co-packaged optics, or optical network-on-chip. However, silicon faces limitations, particularly in light emission, necessitating innovative solutions and advanced materials. Bandwidth density, energy efficiency, and high-temperature operation of optical sources are crucial for integrating photonics and electronics.

In this context, we investigate III-V membrane lasers on silicon using InAs quantum dots (QDs) as the emissive material. These lasers feature a thin III-V stack, just a few hundred nanometers thick, sandwiched between low refractive index dielectric layers, allowing for high optical confinement factors while minimizing the laser volume. This results in low threshold currents, high modulation speeds, and facilitates co-integration with silicon-on-insulator (SOI) photonic circuits and standard microelectronic back-end-of-line processes.

In this thesis, we simulated and designed hybrid lasers featuring a III-V membrane coupled to an SOI photonic circuit. We developed an electro-optical model of quantum dot lasers, focusing on their high-temperature behavior and the mechanisms by which the p-doping of the active region can influence it. Applying this model to InAs QD III-V membrane lasers confirms their potential for optical interconnect applications. We also proposed an integration pathway for the fabrication of these devices. Prototypes fabricated on silicon substrates confirm the feasibility of this approach and were used to demonstrate light emission in GaAs-based membrane diodes. Morphological characterizations, especially using electron microscopy, and electro-optical measurements of the fabricated components provide deeper insights into their operation.

Modélisation, fabrication et caractérisation de microlasers pour les communications de données

La croissance exponentielle des flux des données au cours des dernières décennies a accentué la pression sur les interconnexions entre systèmes de calcul et de communications. Dans ce contexte, la photonique sur silicium suscite un grand intérêt pour transférer en masse les bénéfices de la photonique au plus près des ASIC, via des modules bord-de-puce, l'optique co-packagée ou des réseaux optiques sur une puce. Mais le silicium présente aussi des lacunes, notamment pour l'émission de lumière, et nécessite le recours à des solutions innovantes et matériaux avancés. En particulier, la densité de bande passante, efficacité énergétique et capacité à opérer à haute température des sources optiques sont des figures de mérite importantes pour la co-intégration de la photonique et de l'électronique.

Dans ce contexte, nous nous intéressons à des microlasers à membrane III-V sur silicium utilisant des boîtes quantiques (QD) d'InAs comme matériau émissif. Ces lasers se distinguent par un empilement III-V fin (quelques centaines de nanomètres) compris entre des couches de matériaux diélectriques à faible indice de réfraction, permettant d'obtenir des confinements optiques élevés tout en minimisant le volume du laser. Cela donne accès à des courants de seuil faibles, des vitesses de modulation élevées et facilite la co-intégration avec un circuit photonique en SOI (silicium sur isolant) et avec un back-end standard de la microélectronique.

Dans le cadre de cette thèse, nous avons simulé et conçu des lasers hybrides comportant une membrane III-V couplée à un circuit photonique en SOI. Un modèle électro-optique de lasers à boites quantiques a notamment été développé, mettant l'accent sur le comportement à haute température de ces lasers, et les mécanismes par lesquels il peut être influencé par un dopage p de la zone active. L'application de ce modèle à des lasers à membrane III-V comportant des QD d'InAs confirme le potentiel de ces lasers pour des applications d'interconnexions optiques. En outre, une voie d'intégration a été avancée pour la fabrication de ces dispositifs. Des prototypes fabriqués sur substrat de silicium confirment la faisabilité de cette approche et ont permis de démontrer l'émission de lumière dans des diodes à membrane à base de GaAs. Les caractérisations morphologiques (utilisant notamment la microscopie électronique) et électro-optiques des composants fabriqués permettent de mieux comprendre leur fonctionnement.